

# **Lode gold mineralisation in the Neoproterozoic granitoids of Batouri, southeastern Cameroon**

Doctoral Thesis  
(Dissertation)

to be awarded the degree of  
*Doctor rerum naturalium* (Dr. rer. nat.)

submitted by

**Asaah Victor Akwinga**

from Wum, Cameroon

approved by the Faculty of Energy and Economic Sciences,  
Clausthal University of Technology

Date of oral examination  
7<sup>th</sup> May 2010

*Chairperson of the Board of Examinations:* Prof. Dr.-Ing. Daniel Goldmann

*Chief Reviewer:* Prof. Dr. Bernd Lehmann

*Reviewer:* Prof. Dr. Kurt Mengel

This dissertation was undertaken at the Mineral Resources Department of  
the Technical University of Clausthal

This thesis is dedicated to:

My father

**Atu Moses Asaah**

and

my mother

**Angawah Cecilia Asaah**

## **ABSTRACT**

The Batouri gold district is located in southeastern Cameroon, within the Neoproterozoic granitoids of the Central African Fold Belt (CAFB). Gold mineralisation occurs as veins along N35°-trending, steeply dipping shear zones, which cut the granitoids and define a 13 km-long mineralised corridor of variable width (100 m to 1 km). Two types of gold ores occur at Batouri: vein ore (0.04 to >30 g/t) and wall-rock ore (up to 19 g/t). Four successive ore mineral assemblages were distinguished: (1) pyrite I; (2) pyrite II, arsenopyrite, chalcopyrite and pyrrhotite; (3) sphalerite, tetrahedrite, chalcopyrite, galena, pyrite III and gold; and (4) marcasite, greenockite, bornite, covellite, goethite, Mn oxides and gold. Primary gold occurs either as invisible gold within pyrite (all generations of pyrite) and arsenopyrite, or as visible gold along cavities and fractures in pyrite, arsenopyrite and quartz.

Hydrothermal mineral assemblages and their associated fluid inclusions point to reducing aqueous–carbonic mineralising fluids with near-neutral pH (~5.5), in which gold was transported predominantly as the bisulfide complex  $\text{Au}(\text{HS})_2^-$ . Wall-rock sulfidation likely destabilised this complex and triggered the precipitation of gold-bearing sulfides and, subsequently, native gold. Ore deposition occurred at temperatures decreasing from >420 to ~250°C, with visible gold possibly deposited at ~250°C. U–Pb dating of zircon, Ar–Ar dating of K-feldspar and bulk rock K-feldspar granite indicate that granitoid emplacement occurred between 640 and 620 Ma. Ar–Ar dating of hydrothermal white mica does not yield a definitive age for the hydrothermal event. However, it indicates that gold mineralisation occurred earlier than 480 Ma. The gold-mineralising fluid sources are not defined, but thermal events associated with the Pan-African orogeny and granite magmatism may have driven large-scale circulation of fluids in the crust, which were subsequently channelised by ductile–brittle deformation structures to form the gold lodes. Based on the geotectonic setting and geological controls, gold mineralisation at Batouri is orogenic.

## **ACKNOWLEDGEMENT**

Foremost on the list of many who contributed one way or the other to the success of this work is my supervisor Prof. Bernd Lehmann, without whose patience and constructive criticisms, this endeavour would not have been successful. My co-supervisor Prof. Kurt Mengel was very helpful with thesis review, and was always willing to go the extra mile. Prof. Cheo Emmanuel Suh from the University of Buea, Cameroon, suggested this project and helped with field supervision and review. Critical review from Dr. Richard Goldfarb, USGS Denver, greatly improved the quality of this work. Worthy of note is the academic guidance and reviews received from Dr. Basem A. Zoheir and Dr. Alexandre R. Cabral, which helped shape my thinking.

Dr. Eike Gierth assisted with ore microscopy, as did Dr. Karl Strauß for mineralogy and petrography, and Dr. Alfons M. Van den Kerkhof for fluid inclusion studies. Dr. Akinlolu F. Abimbola and Dr. N. V. Chalapathi Rao reviewed parts of this thesis. Dr. Dirk Frei helped with U-Ub dating of zircon, Dr. Ray Burgess, with Ar-Ar dating of K-feldspar, K-feldspar granite bulk rock and white mica. LA-ICP-MS analysis on pyrite and arsenopyrite was done by Dr. Helene Brätz.

Mr. Ulf Hemmerling prepared the polished, polished-thin and doubly polished sections; Mr. Klaus Hermann helped with electron microprobe analysis; and Mr. Fred Türck was constantly available to assist with computer and office logistical matters. Our secretaries, Mrs. Helga Vollbrecht and Mrs. Elvira Schulze, were always available and helpful. Colleagues at the Mineral Resources Department of TU Clausthal, Dr. Jens Wittenbrink, Dr. Farhad Mohammad Torab, Dr. Kouadio Etienne Assie, Dr. Mohammad Ali Nekouvaght Tak, Mr. Daniel Hennig, Mr. Jasmi Hafiz, Miss. Hongying Qu, Mr. Lingang Xu and Miss. Stephanie Lohmeier, were a great source of encouragement.

The unfailing love and support of my father Mr. Atu Moses Asaah, and my mother Mrs. Angawah Cecilia Asaah; my sisters Miss. Keng Florence

## ACKNOWLEDGEMENT

Asaah, Mrs. Ambang Sarah Shey, Mrs. Okwaomah Ofuibit Helen and Mrs. Angacobi Sharon Ngwaso; my brothers Mr. Abiambe Martin Asaah, Mr. Tantoh Daniel Asaah, Mr. Ateghe Job Asaah and Mr. Bah Donald Asaah, as well as Mr. Shey Germanus Nge, Mr. Agyingi Enyiawah Samson and the rest of my family; sustained me in good as well as in difficult times.

This work benefited from financial support from the German Academic Exchange Service (DAAD: Deutscher Akademischer Austauschdienst), in the form of a full PhD scholarship. It also benefited from financial support from the Institute for Mineralogy and Mineral Resources, TU Clausthal. Two research grants were provided by the Newmont Mining Corporation and the Hugh E. McKinstry Fund, through their collaboration with the Society of Economic Geologists (SEG). A travel grant to a conference in Johannesburg was jointly provided by SEG and the Geological Society of South Africa. An additional stipend was granted by the Society for Geology Applied to Mineral Deposits (SGA). Logistical support in the field was provided by African Aura Resources Ltd (now African Aura Mining Inc).

To the above-mentioned individuals and corporate bodies, as well as to my many friends and relatives, who supported me one way or the other through these years, but whose names have been unavoidably omitted, I say THANK YOU!

Finally, I thank God for the gift of life, and for His constant love.

## **TABLE OF CONTENTS**

CERTIFICATION .....	iv
DEDICATION .....	v
ABSTRACT .....	vi
ACKNOWLEDGEMENT .....	vii
TABLE OF CONTENTS .....	iv
TABLE OF FIGURES .....	xiii
LIST OF TABLES .....	xvii
<b>CHAPTER 1: INTRODUCTION.....</b>	<b>1</b>
1.1    Background.....	1
1.2    Problem and objectives .....	2
1.3    Methods .....	3
1.3.1    Fieldwork and sample preparation .....	3
1.3.2    Whole-rock geochemical analyses .....	4
1.3.3    Electron-microprobe analyses .....	4
1.3.4    Laser ablation-inductively coupled plasma-mass spectrometry ...	5
1.3.5    Isotope geochemistry.....	6
1.3.6    Fluid inclusion studies.....	7
1.4    Geographical setting.....	8
1.4.1    Location and accessibility .....	8
1.4.2    Climate and vegetation.....	9
1.4.3    Relief and drainage .....	11
1.4.4    Soil .....	13

## TABLE OF CONTENTS

1.5 Geological setting .....	14
1.5.1 Regional geological overview.....	14
1.5.2 Ore deposits in Cameroon.....	28
1.6 Summary .....	30
<b>CHAPTER 2: GEOLOGY OF THE STUDY AREA.....</b>	<b>31</b>
2.1 Introduction .....	31
2.2 Petrographic descriptions of major plutonic rocks .....	34
2.3 Geochemistry .....	39
2.4 Deformation structures .....	47
2.5 Discussion .....	53
2.5.1 Magmatic evolution.....	53
2.5.2 Source rock characteristics and tectonic setting.....	54
2.5.3 The role of magmatism in gold mineralisation .....	56
2.6 Summary .....	57
<b>CHAPTER 3: HYDROTHERMAL ALTERATION.....</b>	<b>59</b>
3.1 Introduction .....	59
3.2 Alteration zones.....	60
3.2.1 The proximal zone: quartz–white mica–carbonate–pyrite.....	60
3.2.2 The distal zone: chlorite–quartz–white mica–epidote–carbonate–pyrite.....	60
3.3 Alteration mineral chemistry.....	61
3.3.1 Chlorite mineral chemistry and geothermometry .....	62

## TABLE OF CONTENTS

3.3.2 Mineral chemistry of white mica.....	67
3.3.4 Carbonate mineral chemistry .....	71
3.3.3 Apatite mineral chemistry .....	73
3.3.5 Iron sulfide minerals.....	75
3.4 Interpretation and discussion .....	77
3.5 Summary .....	80
<b>CHAPTER 4: MINERALOGICAL AND PHYSICO-CHEMICAL ASPECTS OF GOLD MINERALISATION.....</b>	<b>81</b>
4.1 General description of gold-mineralised veins .....	81
4.2 Ore mineralogy and sulfide chemistry .....	83
4.2.1 Ore mineralogy .....	83
4.2.2 Sulfide chemistry.....	87
4.3 Gold textures and chemistry.....	92
4.4 Interpretation of ore chemistry and paragenesis.....	98
4.5 Constraints on temperature and sulfur fugacity.....	105
4.6 Reconnaissance fluid inclusion studies.....	105
4.6.1 Introduction.....	105
4.6.2 Fluid inclusion petrography .....	106
4.6.3 Microthermometry .....	107
4.6.4 Interpretation and discussion of fluid inclusion data.....	109
4.7 Gold transport and deposition mechanism.....	111
4.8 Summary .....	115

## TABLE OF CONTENTS

<b>CHAPTER 5: GEOCHRONOLOGY .....</b>	<b>116</b>
5.1    Introduction .....	116
5.2    U–Pb dating of granites at Kambélé mines .....	116
5.2.1    Interpretation of U–Pb geochronology .....	123
5.3    Ar–Ar dating of Bougogo granites and hydrothermal muscovite from the Dimako mining sites.....	124
5.3.1    Interpretation of Ar–Ar geochronology .....	125
5.4    Discussion of U–Pb and Ar–Ar geochronology.....	131
5.5    Summary .....	133
<b>CHAPTER 6: CONCLUSIONS AND RECOMMENDATIONS .....</b>	<b>134</b>
6.1    Conclusions .....	134
6.1    Recommendations .....	136
<b>REFERENCES.....</b>	<b>137</b>
<b>APPENDIX.....</b>	<b>153</b>

## TABLE OF FIGURES

<b>Figure 1.1:</b> Location map of Batouri showing the road map of Cameroon with an inset of the map of Africa, the road map of the East Region of Cameroon and the road map of Batouri, showing artisanal mining sites.	10
<b>Figure 1.2:</b> Semi-deciduous forest, which covers the southern parts of Batouri.....	12
<b>Figure 1.3:</b> Guinean savannah-type vegetation, which covers the northern parts of Batouri.. ..	13
<b>Figure 1.4:</b> Pre-drift reconstruction of western Gondwanaland, showing potential correlations between west-central Africa and northeastern Brazil.....	18
<b>Figure 1.5:</b> Geology of south-eastern Cameroon.. ..	22
<b>Figure 1.6:</b> Map of Cameroon showing the Cameroon Volcanic Line and the sedimentary basins.....	26
<b>Figure 2.1:</b> K-feldspar granite outcrop at Ndoumembe.....	32
<b>Figure 2.2:</b> Sketch geological map of Batouri, showing the distribution of rock outcrops.. ..	33
<b>Figure 2.3:</b> Classification of studied rocks based on modal mineralogy. ....	34
<b>Figure 2.4:</b> K-feldspar granite samples from Djira II at Batouri.....	35
<b>Figure 2.5:</b> Syeno-monzogranite samples from Bougogo, Kambélé III and Dimako in Batouri. ....	37
<b>Figure 2.6:</b> Granodiorite samples from Kambélé III at Batouri.. ..	38
<b>Figure 2.7:</b> Tonalite samples from Kombo at Batouri.....	39
<b>Figure 2.8:</b> Major and trace element geochemical classification plots for a suite of plutonic rocks from Batouri.....	42
<b>Figure 2.9:</b> Magmatic evolution of Batouri granitoids, as portrayed by Ta versus TiO <sub>2</sub> and Zr/Hf versus Zr plots.. ..	43
<b>Figure 2.10:</b> Harker diagrams for plutonic rocks from the Batouri area... ..	45
<b>Figure 2.11:</b> Plots showing trace-element distribution in the Batouri granitoids.. ..	46

## TABLE OF FIGURES

<b>Figure 2.12:</b> Deformation structures at Batouri.....	49
<b>Figure 2.13:</b> Transmitted-light photomicrograph showing shear fabric in the wall-rock adjacent to gold-bearing veins and veinlets.. .....	50
<b>Figure 2.14:</b> Gold distribution patterns in the soils of Batouri. ....	51
<b>Figure 2.15:</b> Structural map of Batouri, showing the main shear zones....	52
<b>Figure 2.16:</b> A model of the post-collisional stage of the Central African Fold Belt and the Congo Craton.....	55
<b>Figure 2.17:</b> Sketch illustration of the tectonic setting of the most common gold deposit types.. .....	57
<b>Figure 3.1:</b> Transmitted-light photomicrographs, showing plastic deformation in wall-rock. ....	60
<b>Figure 3.2:</b> Transmitted-light photomicrographs, showing textures in hydrothermal chlorite.. .....	63
<b>Figure 3.3:</b> Bivariate plots of the chemical components of chlorite.....	65
<b>Figure 3.4:</b> Composition of chlorite in samples from the altered wall-rock at Kambélé. ....	66
<b>Figure 3.5:</b> Histogram showing the estimated formation temperatures of chlorite from the proximal and distal zones of the wallrock.. .....	67
<b>Figure 3.6:</b> Composition of white mica from the hydrothermal alteration zones at the Batouri gold prospect.. .....	70
<b>Figure 3.7:</b> Correlation plot of $(Al^{iv}+Al^{vi})$ and $(Si+Mg^{2+}+Fe^{2+})$ for hydrothermal white mica from Batouri. ....	71
<b>Figure 3.8:</b> Transmitted-light photomicrographs, showing carbonate veins with pyrite and associated hydrothermal quartz and white mica.. .....	72
<b>Figure 3.9:</b> Classification of carbonates from Batouri. ....	73
<b>Figure 3.10:</b> Back-scattered electron images showing microtextures in carbonates.....	73
<b>Figure 3.11:</b> Transmitted-light photomicrographs, showing hydrothermal apatite intergrown with carbonate, white mica, chlorite and sulfides... ..	74
<b>Figure 3.12:</b> Ternary plot of the atomic proportions of F, Cl and OH of hydrothermal apatite from the Batouri gold deposit.....	75

## TABLE OF FIGURES

<b>Figure 3.13:</b> Transmitted-light photomicrograph, back-scattered electron image and reflected-light photomicrographs, showing the replacement of biotite, magnetite and titano-magnetite by iron sulfides.. .....	76
<b>Figure 3.14:</b> Schematic of the wall-rock alteration processes at Batouri, showing alteration zones and the ionic inputs that characterise each alteration type.. .....	80
<b>Figure 4.1:</b> Quartz samples from gold-bearing veins at Batouri.....	82
<b>Figure 4.2:</b> Reflected- and transmitted-light photomicrographs showing microstructures in quartz from gold-bearing veins.. .....	83
<b>Figure 4.3:</b> Reflected-light photomicrographs, showing modes of occurrence of pyrite associated with gold mineralisation at Batouri.....	85
<b>Figure 4.4:</b> Reflected-light photomicrographs, showing textures in second-generation sulfides.....	86
<b>Figure 4.5:</b> Reflected-light photomicrographs, showing microtextures in third generation sulfides.. .....	87
<b>Figure 4.6:</b> The composition of pyrite, arsenopyrite and pyrrhotite from Batouri lodes, as given by electron-microprobe analyses. .....	91
<b>Figure 4.7:</b> The distribution of As, Bi and Au in the pyrite phases and arsenopyrite from Batouri.....	92
<b>Figure 4.8:</b> Reflected-light photomicrographs and back-scattered electron image showing modes of occurrence of gold in primary quartz veins at Batouri.. .....	94
<b>Figure 4.9:</b> Reflected-light photomicrographs, showing modes of occurrence of gold in quartz strongly affected by supergene fluids.....	95
<b>Figure 4.10:</b> Reflected-light photomicrographs, of placer- and vein-derived gold from Batouri.....	96
<b>Figure 4.11:</b> Scatter diagrams showing the compositional variations in gold and electrum from Batouri.....	98
<b>Figure 4.12:</b> Schematic showing the selective leaching of silver from the electrum rim of a gold grain. ....	101
<b>Figure 4.13:</b> Paragenetic assemblages of minerals associated with Au-bearing veins at Batouri.....	104

## TABLE OF FIGURES

<b>Figure 4.14:</b> Temperature and sulfur fugacity estimation based on sulfide assemblage and the composition of arsenopyrite from the Batouri deposit.....	106
<b>Figure 4.15:</b> Transmitted-light photomicrographs, showing fluid inclusion textures in quartz from gold-bearing veins at Batouri.....	108
<b>Figure 4.16:</b> Histogram showing homogenisation temperatures of aqueous-carbonic inclusions in quartz samples from gold-mineralised veins at Batouri.....	109
<b>Figure 4.17:</b> Solubility of the major Au complexes in acid hydrothermal fluids at variable pressures.....	113
<b>Figure 4.18:</b> The solubility of Au(I) bisulfide complex species in aqueous solution as a function of pH at 400 °C and 600 bars.. ..	114
<b>Figure 5.1:</b> Back-scattered images of selected analysed GC zircon grains. Laser pits are about 40 µm in diameter.....	118
<b>Figure 5.2:</b> Back-scattered images of selected analysed HR zircon grains. Laser pits are about 40 µm in diameter.....	119
<b>Figure 5.3:</b> Wetherill concordia diagram depicting results for 30 U–Pb spot measurements of zircon grains obtained from stream sediments in the mining area by LA–SF–ICP–MS.....	122
<b>Figure 5.4:</b> Wetherill concordia diagram depicting results for 24 U–Pb spot measurements of zircon grains obtained from host rock by LA–SF–ICP–MS.....	123
<b>Figure 5.5:</b> Ar–Ar age spectra for K-feldspar and alkali-feldspar granite sampled at the Bougogo outcrop located in northern Batouri.. ..	128
<b>Figure 5.6:</b> Ar–Ar age spectra for muscovite from saprolite and weathered wall-rock at the Dimako mine. ....	130
<b>Figure 6.1:</b> Block diagram illustrating the genetic model for gold mineralisation proposed for Batouri.....	136

## LIST OF TABLES

Table 1.1: Summary of selected mineral deposits in Cameroon .....	29
<b>Table 3.1:</b> Representative electron-microprobe analyses of chlorite from altered wall-rock at Batouri.. ..	64
<b>Table 3.2:</b> Representative electron-microprobe analyses of white mica from altered wall-rock at Batouri.. ..	69
<b>Table 3.3:</b> XRF chemical analyses of weathered hydrothermal white mica used for Ar–Ar dating .....	70
<b>Table 3.4:</b> Representative electron microprobe analyses of carbonate from quartz-carbonate veins and altered wallrock at Kambélé. ....	72
<b>Table 4.1:</b> Representative electron microprobe analyses of hydrothermal apatite from altered wall-rock at Batouri.....	74
<b>Table 4.2:</b> Partial results of electron microprobe analyses of pyrite, arsenopyrite, chalcopyrite and pyrrhotite. ....	89
<b>Table 4.3:</b> Partial results of LA-ICP-MS analyses of pyrite and arsenopyrite from Batouri lodes. ....	91
<b>Table 4.4:</b> Summary of electron-microprobe analyses of vein and placer gold from Batouri. ....	97
<b>Table 5.1:</b> LA-SF-ICP-MS U-Pb zircon analytical data for GC samples from Kambélé in Batouri, Cameroon. ....	120
<b>Table 5.2:</b> LA-SF-ICP-MS U-Pb zircon analytical data for HR samples from Kambélé in Batouri, Cameroon. ....	121
<b>Table 5.3:</b> $^{40}\text{Ar}$ - $^{39}\text{Ar}$ stepped heating data for K-feldspar from Batouri....	126
<b>Table 5.4:</b> $^{40}\text{Ar}$ - $^{39}\text{Ar}$ stepped heating data for granite from Batouri.....	127
<b>Table 5.5:</b> $^{40}\text{Ar}$ - $^{39}\text{Ar}$ stepped heating data for weathered hydrothermal white mica from Batouri.....	129

# **CHAPTER 1: INTRODUCTION**

## **1.1 Background**

Gold has been mined artisanally in eastern and northern Cameroon since 1934 (Gazel and Gérard, 1954). Mining is focused on alluvial and eluvial deposits, but weathered quartz veins are worked as well. The current annual production of gold in Cameroon is estimated at 1,500 kg (George, 2009), but no reliable historical gold production data exist. In addition, literature on primary gold mineralisation in Cameroon is extremely scarce. Nevertheless, recent studies (Milési *et al.*, 2006; Suh *et al.*, 2006) and figures from on-going exploration work by gold exploration companies, such as African Aura Mining Inc., suggest that Cameroon is prospective for gold.

Located in eastern Cameroon (Figure 1.1), Batouri has been one of the main sites for artisanal gold mining in the country for more than 70 years. The gold occurs in shear zone lodes and associated wall-rock, along a 13 km-long mineralised corridor, which cross-cut granitoid rocks. Milési *et al.* (2006) estimated the resource potential of the Batouri gold district to be at least 15 tonnes Au. In 2006, African Aura Resources Ltd. (now African Aura Mining Inc.) acquired the Batouri concession from the previous license holder SeQued, which is a Germany-based geological consulting service and exploration company. Exploration is currently being done by African Aura Mining at an advanced stage. Exploration pits and boreholes along the shear zone yielded high-grade rock samples (as much as 66g/t Au; African Aura Mining, 2009). Gold distribution patterns in soil along this shear zone define two high-priority target areas, namely the Dem-Bote-Kambélé-Mboscoro and the Mongonam-Dimako areas (Figure 1.1).

The geology of Cameroon is not well documented, and the mineral sector has, in the past, suffered neglect due to poor infrastructure and an unattractive 1964 mining code. However, a 2001 mining legislation, which offers mining companies a 5-year tax holiday and free transfer of capital out of the country, has proven to be a potent incentive for foreign investment, as

Cameroon has become an attractive destination for major mining companies. These companies are currently targeting previously known occurrences of various mineral commodities including bauxite, iron ore, cobalt, nickel, uranium, manganese, rutile, gold, diamond, and industrial minerals (Newman, 2008). Cameroon is hoping that its burgeoning mineral sector will attract investments worth \$10 billion and create 27,000 jobs in the next few years (Kinnaird, 2008; Newman, 2008).

### 1.2 Problem and objectives

Structural and geochemical features of gold-mineralised shear zones cutting granitoids in many parts of the world are well documented in the literature (see summary in Gosselin and Dubé, 2005 and references therein). These studies have enabled the precise identification of temporal and spatial systematics of gold mineralisation relative to magmatic and tectonic events. No similar information exists on gold mineralisation in Cameroon. The present research is a descriptive study aimed at providing petrographic information and geochemical data on gold mineralisation at Batouri. In order to achieve this objective, the following aspects were approached:

- i. Study of field relationships between the host granitoids and distribution and geometry of the auriferous quartz lodes,
- ii. Study of the mineral composition and geochemistry of the host granitoids,
- iii. Study of the paragenesis of both ore and gangue minerals of the Batouri gold mineralisation,
- iv. Determination of age of gold mineralisation by dating hydrothermal minerals that are intimately associated with the sulfide-gold assemblage,
- v. Use of mineral thermometers and fluid inclusion data for estimating the physico-chemical conditions of gold deposition.

## 1.3 Methods

### 1.3.1 Fieldwork and sample preparation

Fieldwork was accomplished during three field campaigns, and the geological map was compiled from field data, exploration maps showing gold distribution in the regolith, and a topographic sheet at a scale of 1:50,000. About 150 rock samples were collected from outcrops, open pits and drill cores for petrographic and petrochemical studies. Sampling sites were located using GPS readings. Gold concentrates were obtained from a mineralised vein at Dimako and a placer deposit at Kambélé; concentrates of hydrothermal muscovite came from a mineralised vein at Dimako; and concentrates of zircon were recovered from a mineralised vein and the placer deposit at Kambélé. Dimensions and structural orientations of mineralized veins were measured by means of a compass-clinometer and a measuring tape. The sample locations are given in Appendix 1.

Rock samples were crushed at the University of Yaounde, Cameroon, and pulverised with an agate shatter box at the Technical University of Clausthal (TUC), Germany. The rock powders were analyzed for major and trace elements. Regular and thin polished sections for petrographic studies and electron-microprobe analyses were prepared at TUC, as well as doubly polished thin sections for fluid inclusion studies (preparator: Ulf Hemmerling). Eighty zircon grains were hand-picked from two heavy-mineral concentrates with the aid of a pair of magnifying lenses, and dated at the Geological Survey for Denmark. Concentrates of hydrothermal muscovite from Dimako and K-feldspar from Bougogo, as well as K-feldspar granite (whole-rock) from Bougogo, were dated at the University of Manchester, UK. Ore microscopy and petrography were performed on the rock samples in order to examine their mineralogy, hydrothermal alteration, and microtextures, as well as to classify them.

### 1.3.2 Whole-rock geochemical analyses

Chemical analyses were performed on the pulverised rocks samples in order to investigate the chemical characteristics of the different rock units. Major and some trace elements ( $\text{SiO}_2$ ,  $\text{TiO}_2$ ,  $\text{Al}_2\text{O}_3$ ,  $\text{Fe}_2\text{O}_3$ ,  $\text{MnO}$ ,  $\text{MgO}$ ,  $\text{CaO}$ ,  $\text{Na}_2\text{O}$ ,  $\text{K}_2\text{O}$ ,  $\text{P}_2\text{O}_5$ ,  $\text{Rb}$ ,  $\text{Ba}$ ,  $\text{Th}$ ,  $\text{Nb}$ ,  $\text{Sr}$ ,  $\text{Nd}$ ,  $\text{Zr}$ ,  $\text{Y}$ , and  $\text{V}$ ) were determined by X-ray fluorescence spectrometry (XRF) on lithium-metaborate fused disks at the Federal Institute for Geosciences and Natural Resources (Bundesanstalt für Geowissenschaften und Rohstoffe, BGR) in Hanover. Further analyses for trace elements were performed at Activation Laboratories Ltd. in Ontario, Canada. Lanthanum, Ce, Hf, Sm, Eu, Yb, Lu and Au were analysed by instrumental neutron activation analysis (INAA) [1D Enhanced (Au+34) package]; Hg was analysed by cold vapour flow injection mass spectrometry [Hg-FIMS; Code 1G package]; and inductively coupled plasma spectrometry (ICP) and inductively coupled plasma mass spectrometry (ICPMS) were employed in the analysis of Zn, Pb, Fe, As, S, Cu, Mo, Ag and Sb, after aqua regia extraction [AR-MS and AR-ICP (Ultratrace 2 package)]. See Appendix 2 for the analytical data.

### 1.3.3 Electron-microprobe analyses

The mineral chemistry of selected ore and associated gangue minerals were determined by means of a CAMECA SX100 electron microprobe at TUC (analysts: Mr. Klaus Herrmann and Asaah Victor Akwinga). Geothermobarometry and information on the nature of hydrothermal mineralisation were obtained from the resulting data. Backscattered-electron (BSE) images demonstrating microscopic textures were also obtained.

Measuring conditions for carbonate, chlorite, apatite and muscovite were 15 kV accelerating voltage, 20 nA beam current, and 2–10  $\mu\text{m}$  beam diameter. Reference materials and X-ray lines for carbonate analysis were: kaersutite for Na K<sub>a</sub>, K K<sub>a</sub>, Ti K<sub>a</sub> and Fe K<sub>a</sub>; pyrope for Mg K<sub>a</sub>; K-feldspar for Al K<sub>a</sub> and Si K<sub>a</sub>; dolomite for Ca K<sub>a</sub>; almandine for Mn K<sub>a</sub>; eskolaite for Cr K<sub>a</sub>.

and chromite for V K<sub>a</sub>. Reference materials and X-ray lines for chlorite analysis were: kaersutite for Na K<sub>a</sub> and Ca K<sub>a</sub>; hornblende for Mg K<sub>a</sub>; K-feldspar for Al K<sub>a</sub>, Si K<sub>a</sub> and K K<sub>a</sub>; chloroapatite for Cl K<sub>a</sub>; rutile for Ti K<sub>a</sub>; metallic manganese for Mn K<sub>a</sub>; haematite for Fe K<sub>a</sub>; chromite for V K<sub>a</sub>; eskolaite for Cr K<sub>a</sub> and barite for Ba L<sub>a</sub>. For apatite analysis reference materials and X-ray lines were: apatite for F K<sub>a</sub> and P K<sub>a</sub>; kaersutite for Mg K<sub>a</sub> and Ca K<sub>a</sub>; chloroapatite for Cl K<sub>a</sub>. Those for muscovite analysis were: kaersutite for Na K<sub>a</sub>, Mg K<sub>a</sub>, Ti K<sub>a</sub>, Fe K<sub>a</sub>, Ca K<sub>a</sub> and K K<sub>a</sub>; apatite for F K<sub>a</sub> and P K<sub>a</sub>; K-feldspar for Al K<sub>a</sub>; rhodonite for Mn K<sub>a</sub>; albite for Si K<sub>a</sub>; barite for Ba L<sub>a</sub>; celestine for Sr L<sub>a</sub>; chloroapatite for Cl K<sub>a</sub> and almandine for Cr K<sub>a</sub>. The complete analytical data is shown in Appendix 3.

Measuring conditions for sulfides were 30 kV accelerating voltage, 300 nA beam current, and usually 2–10 µm beam diameter. Reference materials and X-ray lines used were: CuFeS<sub>2</sub> for S K<sub>a</sub>, Cu K<sub>a</sub> and Fe K<sub>a</sub>; ZnS for Zn K<sub>a</sub>; PbS for Pb L<sub>β</sub>; GaAs for As L<sub>a</sub>; Ag for Ag L<sub>a</sub>; metallic Au for Au L<sub>a</sub>; metallic Ni for Ni K<sub>a</sub>; metallic Co for Co K<sub>a</sub>; metallic Sb for Sb L<sub>a</sub> and CdS for Cd K<sub>a</sub>. Detection limits (in wt.%) were approximately: 0.04 for S, Zn and Sb; 0.01 for Cu; 0.03 for Fe; 0.2 for Pb; 0.006 for As and Ag; 0.004 for Au; 0.002 for Ni; 0.008 for Co and 0.1 for Cd. Measuring conditions for native gold and electrum were 25 kV accelerating voltage, 100 nA current beam and 1 µm beam diameter, with reference materials and X-ray lines as follows: Ag for Ag L<sub>a</sub>; Au for Au L<sub>a</sub>; HgTe for Hg L<sub>a</sub> and Te L<sub>a</sub>. Detection Limits (in wt. %) were approximately: 0.09 for Ag, 0.1 for Au, 0.07 for Hg and 0.04 for Te. See Appendix 4 for the complete analytical data.

### **1.3.4 Laser ablation-inductively coupled plasma-mass spectrometry**

Electron-microprobe analyses of pyrite and arsenopyrite indicated concentrations of refractory gold near the detection limit (40 ppm). In order to confirm that these readings were not just effects of background noise, laser ablation-inductively coupled plasma-mass spectrometry, LA-ICP-MS,

with a Au detection limit of 0.01 ppm, was performed on the same pyrite and arsenopyrite samples.

The LA-ICP-MS analyses were performed at the University of Erlangen, Germany (analyst: Dr. Helene Brätz). Measurements were done using a single collector quadrupole AGILENT 7500i ICP-MS equipped with a 266 nm Merchantek LUV 266x laser, with argon as a carrier gas. The reference material Po724 B2 SRM (Sulfide standard, Memorial University Newfoundland) was used for external calibration. On-line data reduction was done with GLITTER Version 3.0 for LA-ICP-MS by Macquarie Research Ltd (2000). The laser beam was fired at 10 Hz repetition rate with energy ranging from 0.15 to 0.28 mJ/pulse. The error for a single measurement was <10% ( $1\sigma$ ). The spot size was 30  $\mu\text{m}$ , and the acquisition time for S and Au was 10 and 50 ms, respectively. The detection limit for gold was 0.01–0.02 ppm. There was no reference material available for Cu, As, Te, and Bi, and these were measured as relative concentrations in counts per second (cps). The complete analytical data is shown in Appendix 5.

### **1.3.5 Isotope geochemistry**

#### *U-Pb isotope analysis*

The U-Pb isotope analyses on zircon were performed at the Geological Survey of Denmark and Greenland (GEUS), Copenhagen (analyst: Dr. Dirk Frei). The objective was to determine the age of crystallisation of the host granitoids. Polished sections of zircon grains, set in epoxy-filled blocks (diameter: 2.5 cm), were cleaned with ethanol and deionised water in an ultrasonic bath to remove surface lead contamination. Backscattered electron (BSE) and cathodoluminescence (CL) images were obtained by means of a Philips XL 40 scanning electron microscope at GEUS in order to study the internal structure of the zircon crystals and to select homogeneous parts for U-Pb isotope analysis. The U-Pb isotope analyses were performed using a single collector laser ablation-magnetic sector field-inductively coupled plasma-mass spectrometry (LA-SF-ICP-MS) at GEUS.

Details of this analytical procedure can be found in Frei and Gerdes (2009). The raw data were processed using an Excel sheet, and concordia ages and concordia plots were obtained using Isoplot/Ex 3.00 software. All ages are reported at the  $2\sigma$  level of uncertainty.

#### *Ar–Ar isotope analysis*

The Ar–Ar isotope analyses of K-feldspar obtained from the K-feldspar granite at Bougogo, granite bulk rock (Bougogo), and hydrothermal white mica (lode vein at Dimako) were done by the stepped heating technique at the University of Manchester, UK (Analyst: Dr. Ray Burgess), in order to date the magmatic events and hydrothermal gold mineralisation. The mineral separates and bulk-rock sample were cleaned, weighed, wrapped in aluminium foil, and encapsulated in quartz vials together with the neutron fluence monitor Hb3gr ( $t = 1073.6 \pm 5.3$  Ma, Jourdan *et al.*, 2006). Nuclear irradiation was carried out in position B2W of the SAFARI-1 reactor at Pelindaba, South Africa, using a fast neutron flux of  $\sim 2 \times 10^{18}$  n cm $^{-2}$ . The J value determined from Hb3gr was  $0.01010135 \pm 0.0000027$  ( $2\sigma$ ). The irradiated samples were step-heated in a Ta-resistance furnace over the temperature interval of 500 to 1600°C, using 30 minutes heating steps. During heating, Ar was purified using a Zr-Al getter at 450°C and transferred to an MS1 mass spectrometer for isotope measurements. The data obtained were corrected for mass discrimination (calibrated using atmospheric argon), radioactive decay, and neutron interference corrections. See Burgess *et al.* (2004) for further experimental details. The Ar–Ar ages were determined from an age spectrum diagram, using the ISOPLOT/Ex 3.23 software (Ludwig, 2003). All ages are reported at the  $2\sigma$  level of uncertainty.

#### **1.3.6 Fluid inclusion studies**

Microthermometric measurements of fluid inclusions were conducted at Universität Göttingen and TUC (analysts: Dr. Alfons M. van den Kerkhof and Asaah Victor Akwinga). Doubly polished ( $\sim 220$   $\mu\text{m}$ ) sections of three

auriferous vein samples were subjected to microthermometric measurements using a Linkam 600 freezing-heating stage (operation range of -196°C to +600°C), with thermal control unit TMS-94 mounted on a Zeiss binocular microscope. Freezing was achieved using liquid nitrogen and heating was supplied by thermal resistor components in the freezing-heating stage. Freezing rates were very fast (-100°C/min), whereas heating rates were greatly reduced when approaching expected phase changes. The rapid freezing was done to avoid metastability and the slow heating, to ensure accuracy in determining temperatures at which phase changes occurred. The data obtained were used to determine the physico-chemical characteristics of the mineralising fluid. The computer software program of Bakker (2003) was used to determine salinities and densities of the inclusions based on water volume fraction estimates and data obtained from the microthermometric measurements. This software program utilises equations of state by Duscheck *et al.* (1990).

### 1.4 Geographical setting

#### 1.4.1 Location and accessibility

Cameroon is often referred to as the “hinge of Africa” for its central location in the continent of Africa (Figure 1.1). It traverses the boundary between West and Central Africa, covering an area of 475,440 km<sup>2</sup> (including 2,730 km<sup>2</sup> of water). Cameroon shares land boundaries with Nigeria (1,690 km) to the west, Chad (1,094 km) to the north and east, Central African Republic (797 km) to the east, Congo (523 km) to the east and south, and Gabon (298 km) and Equatorial Guinea (189 km) to the south. Cameroon is bound to the southwest by the Atlantic Ocean and it has a 402-km-long coastline (CIA, 2009). Cameroon is also known as “Africa in miniature” because it represents the confluence of Africa’s rich geographic and cultural diversity.

Batouri is located in southeastern Cameroon (Figure 1.1). It belongs to the geopolitical East Region of Cameroon (formerly East Province) and serves as the administrative headquarters of the Kadei Division. It is the second

largest municipality in the Region, after Bertoua, the regional capital. Access from the capital city Yaoundé is by a 349-km-long, well-maintained combination of tarmac and laterite road.

The study is limited to the prospective areas near Kambélé and Dimako (Figure 1.1). Access within the mining areas is by tracks and forest roads.

### **1.4.2 Climate and vegetation**

Extending from the semi-arid north to the southern dense equatorial rain forests, the territory of Cameroon traverses the tropical and equatorial climatic zones of Africa. Topographic variations and the Atlantic Ocean along the southwestern coastline locally modify these regional climates, imposing different sub-climatic conditions and vegetation types in different parts of the country that are reminiscent of the entire range of vegetation types found on the African continent (Achoundong, 2007; Tsaléfac, 2007). Generally, precipitation increases and vegetation gets denser from north to south and Cameroon's more than 8,000 floral species (Achoundong, 2007) constitute an ecological paradise that is home to a broad diversity of fauna, including several endemic species.

The Batouri area has a wet, subequatorial climate that is greatly influenced by the Congo forest (Tsaléfac, 2007). To the north of Batouri, it quickly changes into a drier Guinean savannah-type climate. There is a corresponding abrupt change in vegetation from a semi-deciduous forest (Figure 1.2) to Guinean savannah (Figure 1.3). This scenario places Batouri within a transition zone. Batouri experiences two annual climatic seasons; a wet season from mid-March to mid-November and a dry season during the remaining part of the year. North-south annual migration of the Intertropical Convergent Zone influences seasonal variations. This zone is defined as the front where the northeast Harmattan and southwest Monsoon winds meet (Ngwa, 1978; Tsaléfac, 2007). Peak rainfall is usually in October, when precipitation reaches 251 mm. The average annual precipitation is

## CHAPTER 1: INTRODUCTION

1,524 mm and temperatures are fairly constant at about 22.5°C throughout the year (Tsaléfac, 2007).

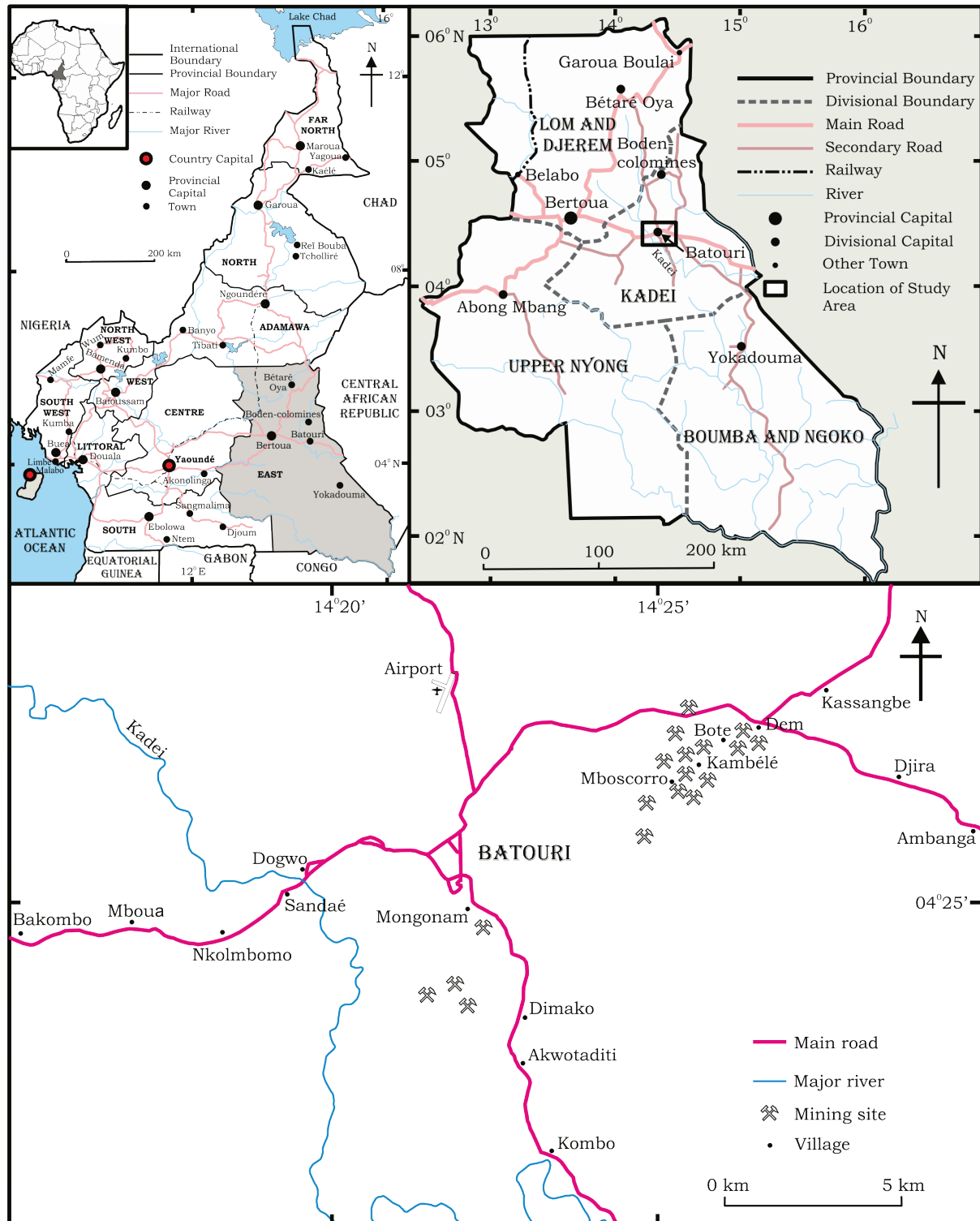


**Figure 1.1:** Location map of Batouri showing the road map of Cameroon with an inset of the map of Africa (top left), the road map of the East Region of Cameroon (top right) and the road map of Batouri, showing artisanal mining sites (bottom).

### **1.4.3 Relief and drainage**

The most prominent topographic feature of the Cameroonian landscape is the 1,600-km-long, Y-shaped chain of intraplate alkaline volcanoes known as the Cameroon Volcanic Line (CVL), which diagonally traverses Cameroon's territory, extending from the Atlantic island of Pagalu through the Gulf of Guinea into the interior of the African continent (Fitton and Dunlop, 1985; Fitton, 1987; Halliday *et al.*, 1988; Lee *et al.*, 1996; Suh *et al.*, 2003; Peive, 2007). It consists of high rising volcanic edifices which include the Mandara Mountains (1,442 m) in the north; the Poli (2,049 m), Mbang (1,923 m), and Mambila Mountains (2,460 m) in north-central (Adamawa) region; and the Bamenda (3,008 m) and Bamboutous (2,740 m) Highlands, and the Manengouba (2,396 m) and Cameroon (4,095 m) Mountains in the western part of the country (Tchawa, 2007).

These mountains have numerous hot springs and crater lakes (Ngako, 2007). Some of these crater lakes host large chambers of magmatic gases, mainly carbon dioxide, which have been released in the past, leaving a trail of destruction in their wake. Examples are the Lake Monoun and Lake Nyos gas disasters that occurred in 1984 and 1986, respectively, and resulted in the loss of thousands of lives (Sigurdsson *et al.*, 1987; Shanklin, 1989). Mount Cameroon is the only active volcano of the Cameroon Volcanic Line. It is a massive strato volcano, which lies on the southwestern coast of Cameroon, and rises from the coastal rainforest with a base that measures  $35 \times 50$  km. More than 100 fissure-controlled cinder cones occur along the flanks of the mountain, as well as in the summit region and the surrounding lowlands (Woolley, 2001; Suh *et al.*, 2003; Schlüter, 2006; Wandji *et al.*, 2009).

Altitude drops rapidly northwards of the Cameroon volcanic line into the northern basins of Cameroon. A plateau (650 to 900 m), which covers an estimated one-third of the total area of Cameroon, dominates the southern parts of the country. However, there are strips of lowland along Cameroon's

southwest coast (Douala, Kribi-Campo and Rio-del-Rey Basins), as well as in the west (Mamfe Basin), and southeast (Dja Basin) (Tchawa, 2007).

Batouri lies on the Southern Cameroon Plateau at elevations between 550 to 700 m. The area consists of gently rolling hills that are occasionally interrupted by elevated residual basement cores. The hills are generally erosional landforms, commonly terminating in entrenching river valleys. These valleys form a dendritic drainage system and the rivers flow into the main Kadei River (Figure 1.1), which empties into the Congo Basin further south.



**Figure 1.2:** Semi-deciduous forest, which covers the southern parts of Batouri. Photograph was taken from the granite outcrop at Domenam.



**Figure 1.3:** Guinean savannah-type vegetation (in the background), which covers the northern parts of Batouri. In partial view is a sanctuary built on the granite outcrop at Bougogo.

#### 1.4.4 Soil

Soils in Cameroon vary from place to place depending on the bedrock, climate and topography. The combination of bedrock geology and climate strongly affects soil structure and fertility, and consequently influences local populations depending on the productivity of these soils for agriculture. The soils in the south and south-central regions have developed on basement rocks and are affected by high precipitation, resulting in deep weathering and extensive leaching. They are red, ferrallitic, permeable and low in plant nutrients, but are physically very stable (Yerima and Ranst, 2005). Volcanic soils in the western regions of Cameroon along the Cameroon Volcanic Line, which also experience high precipitation, are very fertile. In fact, population densities in the areas covered by volcanic soils are the highest in the

country. These soils are dark, aerieable and good for agriculture, but are not as physically stable as the soils developed on the basement rocks.

Devastating landslides and mudflows frequently occur on the slopes of hills and mountains along the Cameroon Volcanic Line. These mass movements are the consequences of a combination of factors, such as steep slopes, high precipitation, deforestation, poor agricultural practices and earthquakes, sometimes induced by volcanic eruptions (Ayonghe *et al.*, 2004; Zogning *et al.*, 2007). Earthquake-triggered underwater landslides have been implicated for the lethal gas bursts from Monoun and Nyos lakes (Sigurdsson *et al.*, 1987). This hypothesis has, however, been challenged in more recent studies (Kusakabe *et al.*, 1989; Tabod *et al.*, 1992; Cotel, 1999; Rice, 2000; Schmid *et al.*, 2004), where thermal instabilities in the lake water column and gas chamber pressure have been invoked as more credible causes.

In the northern part of the country, where precipitation is much lower, soils are less developed, have not suffered much leaching, are fertile, and range in colour from grey to brown. Soils developed on sedimentary rocks display variable permeabilities and physical stabilities depending on the underlying bed rock type.

At Batouri, soil has developed on granitoid basement rocks and weathering is very deep, with a regolith that is more than 30 m thick. The soil is a ferralitic, red and highly leached. A very hard protective cuirass has formed over the soil and, in some places (e.g. Mongonam, Figure 1.1), it hinders artisanal mining activities. Due to excessive leaching, the soil is not fertile.

### 1.5 Geological setting

#### 1.5.1 Regional geological overview

Batouri is situated within the Adamawa–Yadé domain (Toteu *et al.*, 2004; Van Schmus *et al.*, 2008), or the poorly defined Central Domain (Tanko

Njiosseu *et al.*, 2005) of the Neoproterozoic mobile belt of Africa, which is also known as the Central African Fold Belt (CAFB; Toteu *et al.*, 2001, 2004) or the North Equatorial Fold Belt (NEFB; Nzenti *et al.*, 1988). Bounded to the west by the West African Craton and to the south by the Congo Craton (Figure 1.4), the CAFB is the southernmost part of the conceptual pre-Neoproterozoic Saharan “metacraton”, which occupied the north-central part of Africa, i.e. the entire region of the African continent extending north of the Congo Craton and east of the West African Craton (Abdelsalam *et al.*, 2002; Van Schmus *et al.*, 2008). The CAFB and the Congo Craton are the two major lithostructural domains that make up the Precambrian basement of Cameroon. Together, they cover about 80% of the total surface area of Cameroon (Figure 1.5a).

The Congo Craton outcrops in the south of the country, whereas the Central African Mobile Belt outcrops north of the Congo Craton (Figure 1.4). These lithostratigraphic domains record a crustal history that spans the period from Mesoarchaean (~3000 Ma, Toteu *et al.*, 1994) to Neoproterozoic (580 Ma, Toteu *et al.*, 2001). Analogous domains have been recognised across the Atlantic in the northeastern corner of Brazil. In pre-drift reconstructions of western Gondwanaland (Figure 1.4), lateral continuity of lithologies and geological structures exist between the CAFB and the Borborema Province in northeastern Brazil, as well as a correlation between the Congo Craton and the São Francisco Craton (Van Schmus *et al.*, 1995, 2008; Toteu *et al.*, 2001; de Wit *et al.*, 2008).

### *The Congo Craton*

The Congo Craton in Cameroon consists of two rock suites, namely the Archaean Ntem Complex and the Palaeoproterozoic Nyong Series (Toteu *et al.*, 1994). The Archaean Ntem Complex comprises the oldest rock units of the Congo Craton and is predominantly made up of Archaean rocks that were partially reworked during the Palaeoproterozoic Transamazonian cycle (Toteu *et al.*, 1994; Tchameni *et al.*, 2001; Tanko Njiosseu *et al.*, 2005). The

oldest rocks here belong to 3100 Ma greenstone belts and include metagraywacke, banded iron formation (BIF), sillimanite-bearing paragneiss, and amphibolite, now preserved as xenoliths in younger intrusive complexes (Shang *et al.*, 2007; Van Schmus *et al.*, 2008). Intrusive rocks dominate the Ntem Complex, and consist of charnockites and a variety of other rocks, which define a tonalite–trondhjemite–granite (TTG) suite (Nédélec *et al.*, 1990; Toteu *et al.*, 1994; Shang *et al.*, 2004a, 2004b, 2007). The TTG suite is the product of a major crust-forming event that occurred from 2900–2825 Ma; the oldest members being charnockitic rocks and the youngest, tonalitic rocks (Shang *et al.*, 2007). Abundant gneissic and migmatitic structures in the TTG are indicative of late- to post-tectonic partial melting events between 2700 and 2500 Ma, which affected both the TTG and greenstone terranes (Kornprobst *et al.*, 1976; Nédélec *et al.*, 1990; Nsifa and Riou, 1990; Tchameni *et al.*, 2001; Van Schmus *et al.*, 2008). Cross-cutting dolerite dykes represent the last phase of magmatic activity in the Ntem Complex (Toteu *et al.*, 1994; Tchameni *et al.*, 2000; Shang *et al.*, 2007).

Four major deformation episodes have been identified in the Ntem Complex. The first episode, characterised by vertical foliation and stretching, is associated with the emplacement of Mesoarchaean granites. The second deformation episode, marked by sinistral shear zones trending N0°–45°E, correlates with partial melting of TTG and BIF that generated various granites during the Neoarchaean (Tchameni *et al.*, 2000; Shang *et al.*, 2007). It has been suggested that the Ntem Complex later underwent regional metamorphism associated with the Eburnean-Transamazonian orogeny (Toteu *et al.*, 1994; Shang *et al.*, 2004a). Retrogressed rocks at the northern margin of Ntem Complex are thought to have later been affected by low-grade metamorphism linked to the Pan-African orogeny (Shang *et al.*, 2004b, 2007).

The Palaeoproterozoic Nyong Series crops out west of the Ntem Complex (Figure 1.5a). It is part of the Palaeoproterozoic Transamazonian belt, which once extended from west-central Africa to northeastern Brazil, a

## CHAPTER 1: INTRODUCTION

consequence of the Eburnean-Transamazonian collision ca. 2100 Ma of the Congo and the São Francisco cratons (Toteu *et al.*, 1994; Feybesse *et al.*, 1998; Penaye *et al.*, 2004; Lerouge *et al.*, 2006). The Nyong Series is the most important sequence of Palaeoproterozoic crust in Cameroon. It consists mainly of high-grade gneissic rocks, including biotite-hornblende gneiss, charnockite, garnet-amphibole-pyroxenite and BIF. Intrusions of weakly metamorphosed diorite, granodiorite, and syenite cut rocks of the Nyong Series, along with post-tectonic dolerite in places (Toteu *et al.*, 1994; Lerouge *et al.*, 2006).

The Nyong Series was previously thought to represent a Neoproterozoic (Pan-African) or Palaeoproterozoic reactivation of the western corner of the Archaean Ntem Complex (Lasserre and Soba, 1976; Feybesse *et al.*, 1986). However, later studies by Toteu *et al.* (1994) and Lerouge *et al.* (2006) revealed a Palaeoproterozoic sedimentary origin of the series, which was subsequently thrust onto the Ntem Complex during the Eburnean-Transamazonian orogeny, leading to granulite-facies metamorphism of the underthrust rocks and related plutonism. The Pan-African orogeny (~600 Ma) partially overprinted the Palaeoproterozoic history, being best observed to the north of the Nyong Series and in the Pan African belt where blocks of Palaeoproterozoic crust are widespread (Tanko Njiosseu *et al.*, 2005).

## CHAPTER 1: INTRODUCTION

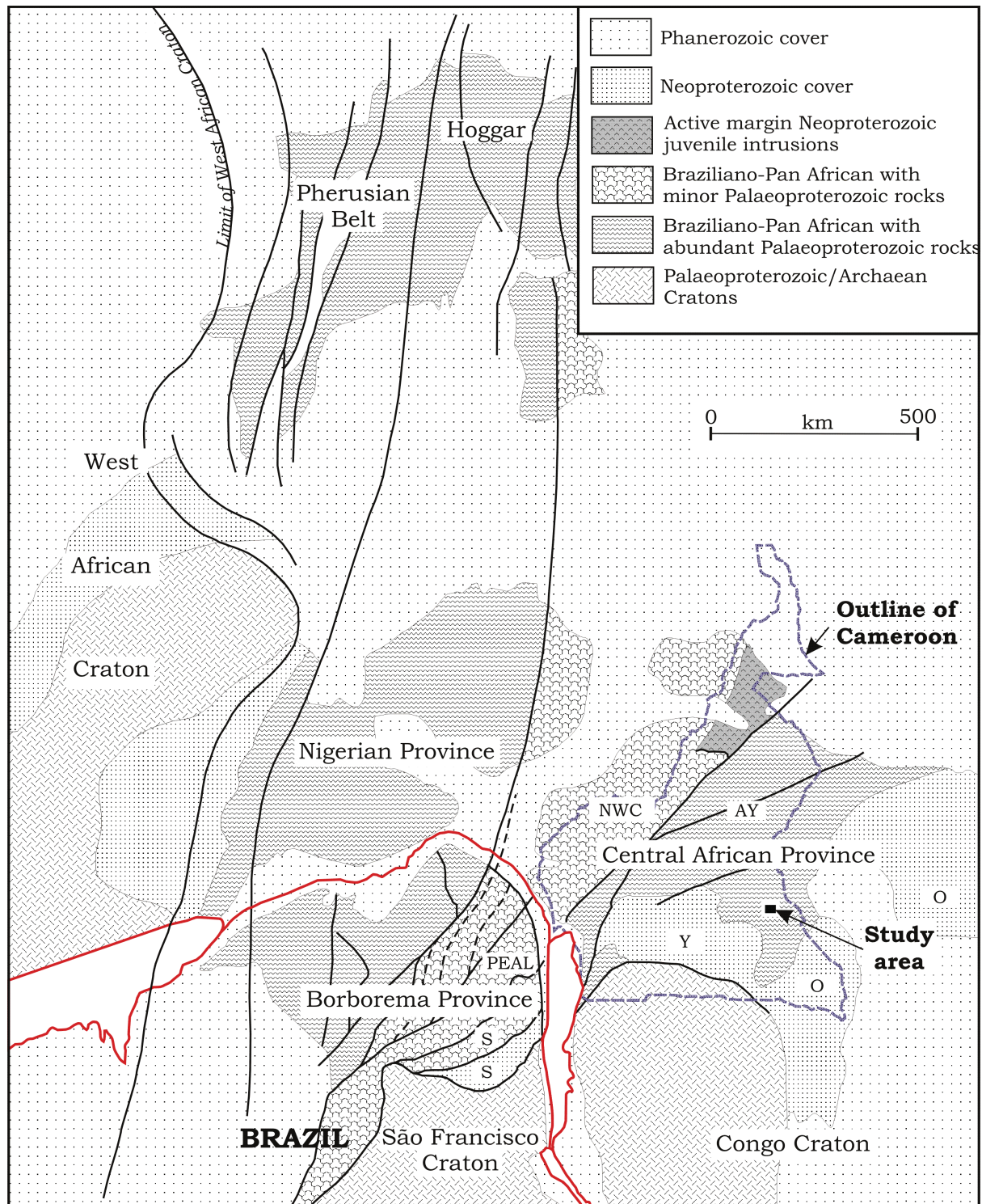


**Figure 1.4:** Pre-drift reconstruction of western Gondwanaland, showing potential correlations between west-central Africa and northeastern Brazil. Modified after van Schmus *et al.* (2008). The red line marks the continental divide. NWC, Northwestern Cameroon domain; AY, Adamawa-Yadé domain; Y, Yaoundé domain; O, Oubagouide fold belt; PEAL, Pernambuco-Alagoas domain; S, Sergipano domain.

### *The Central African Fold Belt*

The CAFB is a major collisional belt that spans the region from the eastern limits of the West African Craton to East Africa (Toteu *et al.*, 2006a; Van Schmus *et al.*, 2008). It underlies eastern Nigeria, Cameroon, Chad, and Central African Republic, and extends as far east as Sudan and Uganda (Toteu *et al.*, 2006a). The evolution of this belt is poorly understood (Toteu *et al.*, 2004; Van Schmus *et al.*, 2008), but it is generally believed that the CAFB evolved during the Neoproterozoic collision of the West African Craton with the Congo Craton (Toteu *et al.*, 2004). Toteu *et al.* (2004) have proposed a three-phase evolution, beginning with an ill-defined pre-collisional history accompanied by the emplacement of pre-tectonic calc-alkaline granitoids (670–660 Ma); a syn-collisional stage, which induced crustal thickening, high-grade metamorphism, calc-alkaline magmatism (640–610 Ma), and tectonism; and a post-collisional stage concomitant with nappe formation, retrograde metamorphism, sub-alkaline magmatism (600–570 Ma), molasse basin development, high-level alkaline magmatism (545 Ma), and shearing. Three lithostructural domains have been identified in the Pan-African fold belt in Cameroon: the Yaoundé, Adamawa-Yadé, and Northwestern Cameroon domains (Toteu *et al.*, 2004; Van Schmus *et al.*, 2008).

The Yaoundé domain consists of a large tectonic nappe that was thrust southwards onto the Congo craton during the Pan-African collisional tectonics between 616 and 580 Ma (Nzenti *et al.*, 1988; Toteu *et al.*, 1994, 2004, 2006b; Van Schmus *et al.*, 2008). The domain is analogous to the Gbayas and Sergipano nappes in Central African Republic and Brazil, respectively. Three major groups have been identified in this domain: the Yaoundé, Mbalmayo, and Bafia Groups. Thrust slices of metasedimentary and metaplutonic rocks dominate the Yaoundé and Mbalmayo Groups, whereas the Bafia Group is poorly studied (Toteu *et al.*, 2006b; Van Schmus *et al.*, 2008). Late- to post-deformation intrusions are absent in the Yaoundé Group (Toteu *et al.*, 2006b). The provenance of the metasedimentary rocks is controversial, but current interpretations (Toteu *et al.*, 1994, 2001) hold that

the detrital material was derived from juvenile Palaeoproterozoic and Neoproterozoic sources in the southern parts of the Adamawa-Yadé domain. Toteu *et al.* (2006c) determined that the meta-sedimentary units in the Yaoundé domain are not older than 626 Ma, an age constrain that is similar to the Sergipano domain in Brazil.

The Adamawa-Yadé domain extends east of the Tcholliré-Banyo fault (Figure 1.5a). It is dominated by 640–610 Ma, syn- to late-collisional high-K calc-alkaline granitoids, which intrude high-grade gneisses (Toteu *et al.*, 2004; Tanko Njiosseu *et al.*, 2005; Van Schmus *et al.*, 2008). This domain is dissected by large NE-striking transcurrent faults thought to be extensions of the major shear zones of north-eastern Brazil (Figure 1.4). Toteu *et al.* (2004) classified the rocks of the Adamawa-Yadé domain into three main groups: (a) large supracrustal blocks of Palaeoproterozoic metasedimentary rocks and orthogneiss with contributions from an Archaean crust similar to the Ntem Complex, (b) 612–600 Ma, low- to medium-grade metasedimentary and metavolcanoclastic rocks (Toteu *et al.*, 2006c); and (c) 640–610 Ma syn- to late-tectonic granitoids of transitional composition and crustal origin (Toteu *et al.*, 2004; Van Schmus *et al.*, 2008).

Radiometric age data for the southern part of the Adamawa-Yadé domain, where the study area is situated, is scanty. The available data are shown in Figure 1.5b. The data show detrital zircon ages as old as 2.8 Ga and Sm-Nd depleted mantle model ages ( $T_{DM}$ ) of 2.2 to 1.4 Ga. This indicates that this area may be underlain by Archaean crust affected by the Transamazonian orogeny. The Adamawa-Yadé domain extends eastwards into Central African Republic, where it is known as the Yadé massif.

The Northwestern Cameroon domain is located to the west of the Tchollire-Banyo Fault (TBF in Figure 1.5a), and extends along the western border of Cameroon into eastern Nigeria. Rock types belonging to this domain include: (a) Neoproterozoic medium- to high-grade schists and gneisses preserved in the ~700 Ma rocks of the Poli series, (b) Pan-African

(660–580 Ma) pre-, syn-, to post-tectonic calc-alkaline granitoids (diorite, granodiorite and granite); (c) post-tectonic alkaline granitoids; and (d) low-grade sedimentary and volcanic basin sequences (Toteu *et al.*, 2004; Van Schmus *et al.*, 2008).

Four deformation phases ( $D_1$ ,  $D_2$ ,  $D_3$  and  $D_4$ ) have been described in the CAFB (Toteu *et al.*, 2004).  $D_1$  is characterised by flat-lying foliations associated with isoclinal folds, and  $D_2$  by tight and upright folds with vertical axial planes trending NNE–SSW to NE–SW, and shear zones trending N–S to NW–SE. Both  $D_1$  and  $D_2$  are believed to have been formed between 640 and 610 Ma, by the same E–W syncollisional regional compressive stresses associated with crustal thickening and delamination of subcrustal lithospheric mantle.  $D_3$  and  $D_4$  are defined by NE–SW to N–S sinistral and WNW–ESE to NE–SW dextral shear zones, respectively. These shear zones were formed between 600 and 570 Ma by compressive stresses associated with the post-collisional nappe formation and uplift (Toteu *et al.*, 2004).

## CHAPTER 1: INTRODUCTION

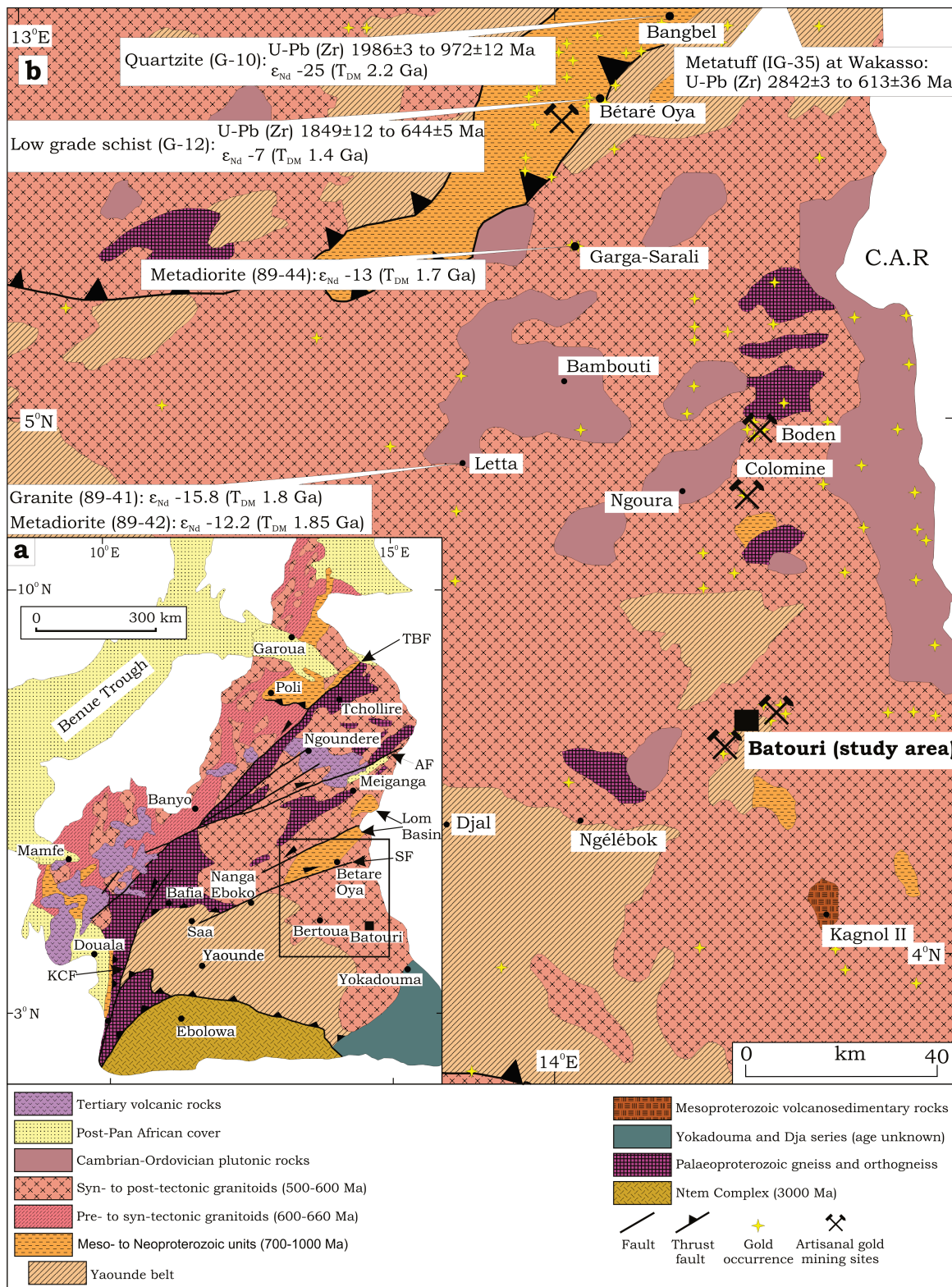


**Figure 1.5:** Geology of south-eastern Cameroon. (a) Geological map of Cameroon (modified after Toteu et al., 2001). The Central African Shear Zone is defined by a system of NE-trending faults comprising Tchollire-Banyo Fault (TBF), Adamawa Fault (AF), Sanaga Fault (SF) and Kribi-Campo Fault (KCF). (b) Regional geological map of southeastern Cameroon, showing geochronological and model ages, artisanal gold mining sites and other reported gold indications (Toteu et al., 2001, 2006c; Milési et al., 2004).

### *The Phanerozoic geology*

The Phanerozoic geology of Cameroon consists of poorly defined Cambrian to Ordovician plutonic rocks (Milési *et al.*, 2004), Cretaceous to Quaternary sedimentary formations, Tertiary plutonic complexes and Tertiary to Recent volcanic complexes (Halliday *et al.*, 1988; Maurin and Guiraud, 1990; Brownfield and Charpentier, 2006; Ngako, 2007; Peive, 2007). The sedimentary formations are spatially restricted to the coastal (Rio-del-Rey, Douala and Kribi-Campo) and continental (Mamfe, Garoua, Koum, Vina, Mbere and Njerem) basins (Figure 1.6), where their oldest members (basal sandstones and conglomerates) unconformably overlie the basement complex (Maurin and Guiraud, 1990; Mateer *et al.*, 1992; Brownfield and Charpentier, 2006).

The coastal basins are passive margin basins formed in the Early Cretaceous (ca. 123 Ma) as a result of the opening of the South Atlantic Ocean, which began in the Jurassic when Africa rifted from South America (Pauken and Thompson, 1991; Oba, 2001; Schlüter, 2006), and contain sedimentary rocks of predominantly marine origin (Mateer *et al.*, 1992). The continental basins, on the other hand, are synsedimentary troughs genetically related to the Benue Trough in eastern Nigeria (Figure 1.6), and host sedimentary rocks of continental origin (Maurin and Guiraud, 1990; Mateer *et al.*, 1992). The Benue Trough is also believed to be a site of the Jurassic continental break-up of southern Gondwana, formed through crustal rifting propagated along existing zones of weakness, but which failed to develop into an ocean (Fitton, 1980; Eseme *et al.*, 2002; Kamguia *et al.*, 2005).

With the exception of the Chad Basin, which is a Quaternary basin, sedimentation in the continental basins ended during the Cretaceous. Palaeontological evidence (Mateer *et al.*, 1992) indicates that the oldest formations in continental basins are Barremian–Aptian, found in the Vina, Babour-Figuil, Mayo Oulo-Lérè, Hama Koussous and Koum Basins (Figure

## CHAPTER 1: INTRODUCTION

1.6). Rocks in the Garoua, Lame, Mbere, and Njerem Basins are mainly Albo-Aptian to Cenomano-Turonian, and correspond to the Bimi sandstone of northeastern Nigeria (Maurin and Guiraud, 1990; Mateer *et al.*, 1992). Sedimentation in the Mamfe Basin was short-lived, between Aptian and Albian, and resulted in the deposition of sandstones, mudstones, organic-rich shales, limestones, and conglomerates, which have been grouped into an upper and a lower formation (Eseme *et al.*, 2002; Ndougsa-Mbarga *et al.*, 2007). Sedimentary formations in these inland basins contain a variety of fossil fauna and flora, including dinosaurs (Maurin and Guiraud, 1990; Mateer *et al.*, 1992; Ngako, 2007). These basins are important for hosting hydrocarbon reservoirs and deposits of phosphates, sulfates, chlorides, gypsum, limestone, vivianite (Ngako, 2007), and gemstones.

The coastal basins (Rio-del-Rey, Douala and Kribi-Campo) are a string of continental shelf basins, which form part of the Aptian salt basin of equatorial West Africa (Edwards and Bignell, 1988), also known as the West-Central Coastal Province of West Africa (Brownfield and Charpentier, 2006). They consist of coastal and offshore areas from Namibia to Cameroon. Sedimentation along the Cameroon, Gabon, and Equatorial Guinea coasts occurred in three phases (Oba, 2001); syn-rift, transitional, and post-rift phases.

Syn-rift formations in Cameroon (Lower Mundeck or “Basal Sandstone”) unconformably overlie the Precambrian basement, and consist of continental conglomerates and marls (Ntamak-Nida *et al.*, 2008). Deposition of these formations probably occurred in the early Aptian.

Post-rift sedimentation along the Cameroon coast range from late Aptian to Holocene. Transitional evaporites, precipitated in the late Aptian, thin out and disappear northwestwards in the Douala Basin (Oba, 2001; Brownfield and Charpentier, 2006), and mark the transition between the syn-rift (Lower Mundeck) and post-rift (Upper Mundeck, Mungo, Logbadjeck, Logbaba, N’kapa, Souellaba, Matanda, and Wouri) sedimentation

## CHAPTER 1: INTRODUCTION

(Brownfield and Charpentier, 2006; Ntamak-Nida *et al.*, 2008). The oldest member of post-rift formations (Upper Mundeck) consists of continental shales, marls, sandstones, and carbonates (Meyers *et al.*, 1996; Brownfield and Charpentier, 2006; Ntamak-Nida *et al.*, 2008).

Late Cretaceous (Mungo or Logbadjeck, and Logbaba) formations along these coastal basins were deposited in marine environments ranging from deep anoxic to shallow oxygenated (Meyers *et al.*, 1996). Rock types deposited here include siltstones, organic-rich shales, carbonates and sandstones. Tertiary to Quaternary (N'kapa, Souellaba, Matanda, and Wouri) formations consist mainly of prograding deltaic and turbidite deposits (Meyers *et al.*, 1996; Brownfield and Charpentier, 2006). Erosional surfaces (unconformities) observed along contacts between Mundeck–Mungo (Cenomanian), Mungo–Logbaba (Campano–Maastrichtian), Logbaba and N'kapa (Maastrichtian–Palaeocene), and N'kapa and Souellaba (Eocene–Oligocene) Formations (Brownfield and Charpentier, 2006) represent erosional hiatuses (Meyers *et al.*, 1996). Hypovolcanic dykes and basaltic rocks, similar to rocks found on Mount Cameroon, occur within the sandstones in the Matanda and Wouri Formations (Meyers *et al.*, 1996; Kamguia *et al.*, 2005).

Hydrocarbon source rocks in the coastal basins of Cameroon span the Early Cretaceous to Miocene. Aptian evaporites in the Douala Basin have been suggested to be interbedded with lacustrine source rocks (Tamfu *et al.*, 1995). Source rocks abound in the Late Albian to Maastrichtian, especially in the Mungo and Logbadjeck Formations, consisting mainly of marls and organic-rich shales. Palaeocene to Miocene formations are particularly prospective for Type II and III Kerogens. Miocene source rocks containing Type III kerogens have TOC of 1 to 2 wt. %, and are associated with gas fields (Brownfield and Charpentier, 2006). Proven reservoirs include the Early Cretaceous Mundeck, Late Cretaceous Logbaba, and Tertiary N'Kapa and Souellaba Formations (Luzzi-Arbouille *et al.*, 2009). Despite the high

## CHAPTER 1: INTRODUCTION

propensity of Cameroon's sedimentary basins for significant hydrocarbon reserves, they remain underexplored (Brownfield and Charpentier, 2006).

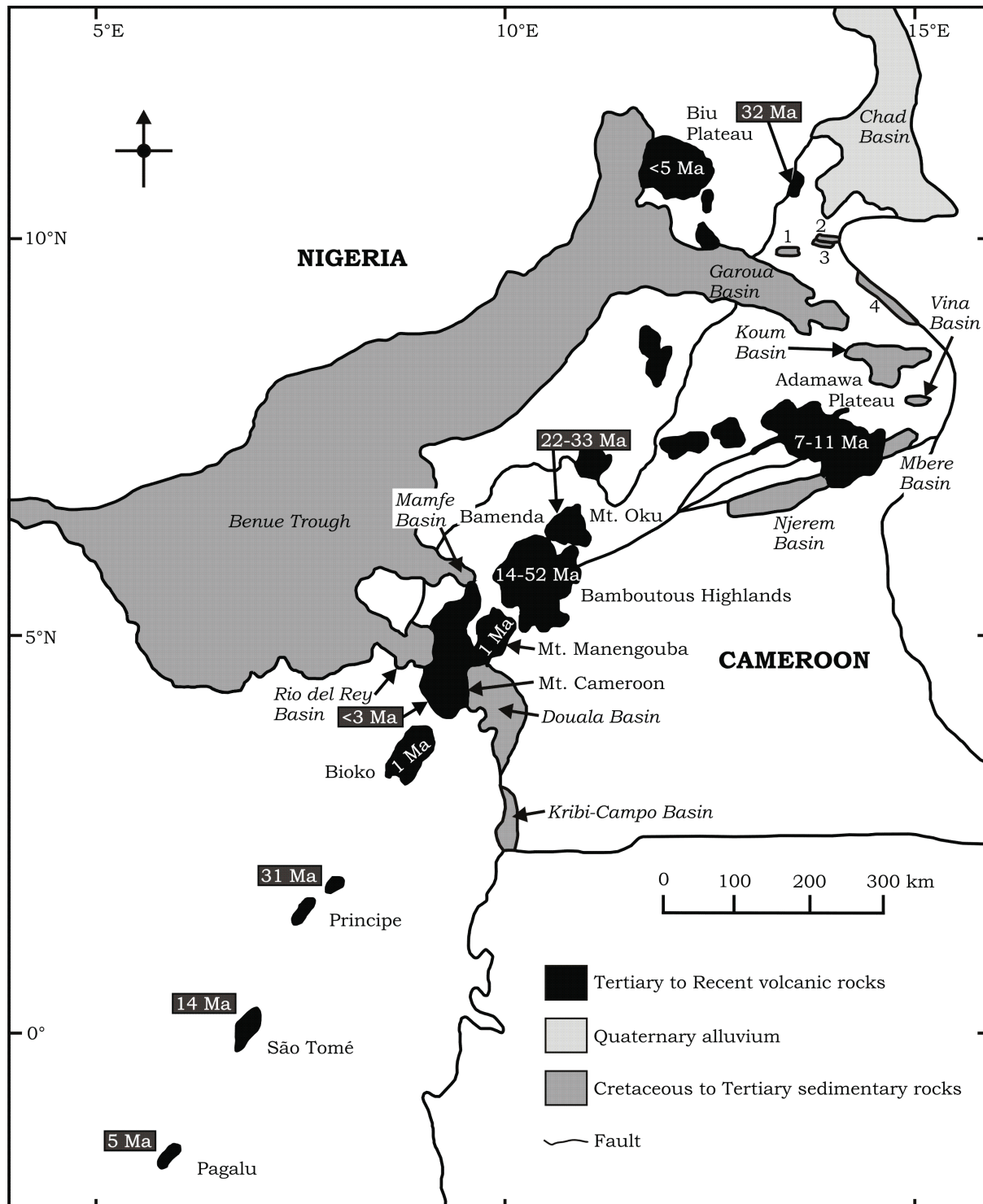


**Figure 1.6:** Map of Cameroon showing the Cameroon Volcanic Line (with ages of volcanoes) and the sedimentary basins (Fitton, 1987; Maurin and Guiraud, 1990; Marzoli *et al.*, 2000; Moundi *et al.*, 2007). 1: Hama Koussou Basin, 2: Figuil Basin, 3: Mayo Oulo Basin, 4: Lame Basin.

The Tertiary plutonic complexes and overlying Tertiary to Recent volcanic complexes have formed along a megashear zone that trends 30° NE (Nkouathio *et al.*, 2008). This line (Figure 1.6) forms a major geological province on the Cameroon landscape, made up of >60 high-level continental anorogenic ring complexes, and 12 main volcanic centres (Wandji *et al.*, 2009) consisting of a continental and an oceanic segments (Figure 1.6). This unique feature of the line has generated much interest because it makes it ideal for studying changes that occur in mantle magmas as they rise through continental crust (Fitton, 1987).

The continental plutonic complexes, which occur along the 1000 km stretch from Mount Cameroon to Lake Chad, and consist of rocks such as gabbro, syenite and alkali granite, range in age from 66–30 Ma (Fitton and Dunlop, 1985; Moreau *et al.*, 1987; Ghogomu *et al.*, 1989; Fitton and Underhill, 2009). These complexes contain anomalous concentrations of lead, zinc, tin, niobium, tantalum, uranium, and thorium (Ngako, 2007).

Volcanism along this line began at 52 Ma (Moundi *et al.*, 2007) and has continued to this day. The volcanic edifices differ in size, age, and lithology, varying from mildly alkaline basaltic and nephelinitic to trachytic and rhyolitic (Woolley, 2001; Schlüter, 2006). Chemical (mean chemical and Sr-Nd isotopic compositions) similarities between the lavas of the continental and oceanic segments have provoked suggestions that they have a common and homogeneous magma source probably located in the asthenosphere (Fitton and Dunlop, 1985; Halliday *et al.*, 1988). The continental segment has large strato-volcanoes and central-type volcanic massifs, with occasional calderas, collapsed plains occupied by monogenetic volcanoes and flood basalts, and volcanic necks and plugs (Nkouathio *et al.*, 2008).

The origin of the Cameroon Volcanic Line (CVL) is still a debated question, but there now seems to be agreement among workers that it developed as a result of mantle upwelling along a lithospheric fracture zone,

after intracontinental extension (Nkouathio *et al.*, 2008). Noting the striking resemblance in shape between the CVL and the Benue Trough, Fitton (1980) evoked a genetic link between Volcanic Line the Benue Trough. The current debate revolves around the type of mantle dome responsible for forming the Volcanic Line (hotspot or hot line), and the upwelling mechanism (Nkouathio *et al.*, 2008).

### 1.5.2 Ore deposits in Cameroon

#### *Gold*

Primary gold deposits in Cameroon occur in the northern, southern, and eastern parts of the country. Bétaré Oya, Boden-Colomine (Figure 1.1) and Batouri are important artisanal gold mining sites in the east. Gold mineralisation in these districts occurs along NE–SW-trending major shear zones that cut Neoproterozoic metavolcanic and metasedimentary rocks (Bétaré Oya), the contacts between these rocks and the Pan-African granitoid massifs of variable size (Boden-Colomine) (Suh *et al.*, 2006), or the granitoid bodies (Batouri). Milesi *et al.* (2006) proposed resource estimates for these gold districts as follows: ~20 t Au in Bétaré Oya, ~12 t Au in Boden-Colomine, and ~15 t Au at Batouri. However, these estimates are purely speculative since no detailed study on distribution and controls of these gold deposits were conducted.

In the north, two gold districts, located at Tcholliré and Rey Boubia, (Figure 1.1) are coincident with the NE–SW-trending Tcholliré shear zone (African Aura Mining, 2009). The geology of this area consists of Neoproterozoic magmatic rocks intruding Palaeoproterozoic (Birimian) supracrustal rocks. The lithologic and structural controls of gold mineralisation are still poorly defined (Milési *et al.*, 2006). In the south, gold mineralisation in the Djoum-Akonolinga and Ntem districts (Figure 1.1) is associated with Archaean to Palaeoproterozoic greenstone belts, BIF, and ultramafic rocks, which have been deformed by NNE–SSW- and E–W- (Djoum-Akonolinga), as well as N–S-trending (Ntem), shear zones and faults

## CHAPTER 1: INTRODUCTION

(African Aura Mining, 2009). The discovery of these gold occurrences, even with minimal geological study, suggests that Cameroon is highly prospective for gold.

### *Other mineral commodities in Cameroon*

Substantial deposits of diamond, bauxite, cobalt, iron ore, nickel, cassiterite, uranium, rutile, and nepheline have been found in many sites in Cameroon. A summary of the most important deposits and their resource estimates are shown in Table 1.1.

Table 1.1: Summary of selected mineral deposits in Cameroon

Mineral commodity	Locations	Reserve estimate	Deposit types	References
Diamond	Mobilong	3.78 billion carats	Conglomerate and alluvium	Gentry (2009)
Bauxite	Minim-Martap, Ngoundal & Fongo Tongo.	3 Gt (39–47 % Al <sub>2</sub> O <sub>3</sub> , 1–3.6 % Si).	Residual deposits on Palaeogene to Quaternary volcanics.	Milési <i>et al.</i> (2006), Gentry (2009).
Co-Ni-Mn	Nkamouna, Mada, Kondong, Messea, North Mang, Rapodjombo and South Mang.	225 Mt (0.24% Co, 1.22% Mn, 0.72% Ni).	Laterite deposit hosted by Neoproterozoic (?) mafic-ultramafic magma complex.	Milési <i>et al.</i> (2006), Newman (2008), Gentry (2009).
Iron ore	Mbalam, Kribi and Nkout	Mbalam >800 Mt. (35–60 % Fe) Kribi ~330 Mt. (30 % Fe) Nkout (not defined).	Archaeon-Palaeoproterozoic (?) BIF in greenstone belts.	Newman (2008), Ngako (2007), Milési <i>et al.</i> (2006), African Aura Mining (2009), Gentry (2009).
Uranium	Kitongo, Lolodorf, Teubang, and Bantadje.	Kitongo=13,125 t. Lolodorf=1,200 t. Teubang (not defined). Bantadje=~10,000 t.	Mid-Proterozoic vein-related granite- metasediment contact, conglomerate and sandstone, microdiorite.	Newman, (2008), African Aura Mining (2009), Mega Uranium (2009).
Rutile	Akonolinga	2.6 Mt.	Quaternary alluvium reworked from Neoproterozoic Yaounde nappe (micaschist & gneiss).	Milési <i>et al.</i> (2006), Ngako (2007).
Nepheline	Eboundja	800 Mt.	Quaternary alluvium reworked from Neoproterozoic nepheline-bearing-syenite.	Milési <i>et al.</i> (2006), Ngako (2007).
Tin	Mayo Darle	17 targets with one world class deposit.	Granitoids	Gentry (2009)
Wolframite	Goutchoumi	ca. 4,500 t.	Fault-related orogenic Neoproterozoic granite.	(Milési <i>et al.</i> , 2006).

## 1.6 Summary

The present study is aimed at generating petrological, structural and geochemical information important for characterisation of primary gold mineralisation at Batouri to optimise exploration. Batouri is situated within the Adamawa-Yadé domain of the Neoproterozoic Central African Fold Belt, and is underlain by granitoids. Gold occurrence at Batouri is coincidental with a 13 km long NE-trending ductile-brittle shear zone.

## **CHAPTER 2: GEOLOGY OF THE STUDY AREA**

### **2.1 Introduction**

The Batouri area has had very limited geological study. Besides the on-going gold exploration programme that is being conducted by African Aura Mining Inc, the work done by Suh *et al.* (2006) is the only previous attempt at describing the bedrock geology and primary gold mineralisation of the Batouri deposit. The rock types in the area include K-feldspar granite, syeno-monzogranite, granodiorite and tonalite. Enclaves of monzonite, quartz monzodiorite and quartz diorite occur in these rocks, with the exception of K-feldspar granite. However, biotite-gneiss enclaves (Figure 2.1a and b) are ubiquitous in area, occurring in all the rock outcrops in the area. Aplitic granite (Figure 2.1c and d) and pegmatite dykes intrude K-feldspar granite, while barren quartz veins intrude all rock types in the area. Detailed petrogenetic study of the enclaves is beyond the scope of the present work, but the biotite-gneiss enclaves may be fragments of underlying Palaeoproterozoic–Archaean basement rocks, or Neoproterozoic high-grade metasedimentary rocks, which are believed to have been invaded by these granitoids (Toteu *et al.*, 1994, 2004, 2006c; Van Schmus *et al.*, 2008).

The weathering profile is very deep at Batouri and rock outcrops are sparcely distributed. Sampling was, therefore, not systematic, but followed the distribution of the outcrops. Because the geology of Batouri is largely unknown, sampling was not limited to areas of known gold occurrence, but covered the whole Batouri area (See sample map in Appendix 1). Most of the samples were gotten from the surface of the outcrops, but only samples without obvious overprint from weathering were collected. A sketch geological map showing outcrop distribution is shown on Figure 2.2. Although barren veins intrude all rock types in the Batouri area, granodiorite and syeno-monzogranite are the main hosts of the lodes.

## CHAPTER 2: GEOLOGY OF THE STUDY AREA

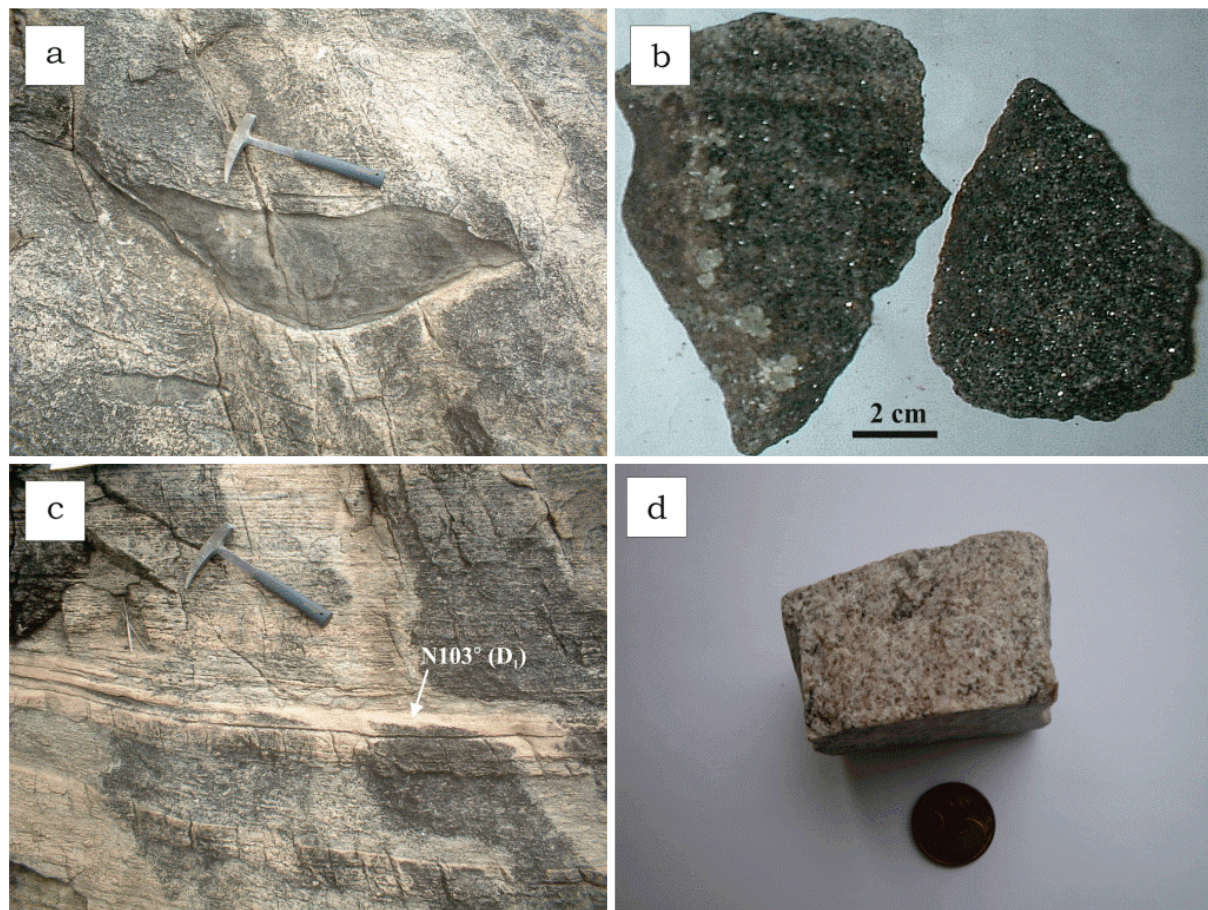


**Figure 2.1:** K-feldspar granite outcrop at Ndoumembe. **(a)** biotite-gneiss enclave in K-feldspar granite. **(b)** Samples of biotite-gneiss. **(c)** Aplitic granite dykes in K-feldspar granite. **(d)** A sample of aplitic granite. The Hammer is 30 cm long and the 5 Euro coin has a diameter of 2 cm.

## CHAPTER 2: GEOLOGY OF THE STUDY AREA

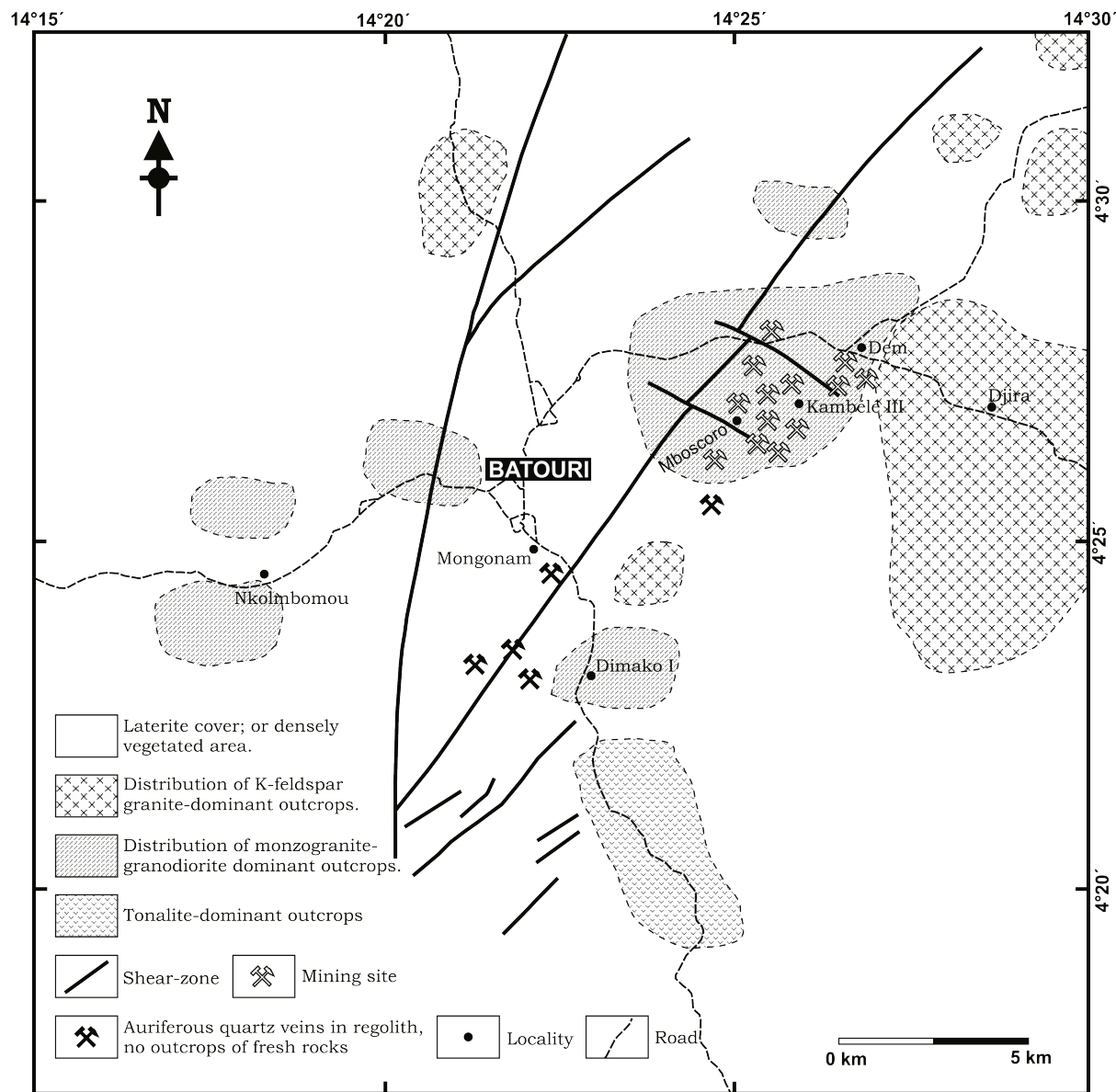


**Figure 2.2:** Sketch geological map of Batouri, showing the distribution of rock outcrops. Syenogranite occurs in monzogranite- and K-feldspar-dominant outcrops. K-feldspar granite-dominant outcrops are truncated by aplite dykes. The map is modified from African Aura Mining (2009).

The classification of the studied rocks based on modal mineralogy, following the IUGS procedure (Streckeisen, 1974), is shown in Figure 2.3. Rocks outcropping in the Batouri area display a wide mineral compositional range from alkali-feldspar granite to tonalite. Biotite and hornblende contents of granite vary greatly from almost absent in alkali-feldspar granite to abundant in syeno- and monzogranite. The IUGS classification scheme for granitoid rocks does not take into account the mafic contents. Hence

rocks plotting in the ‘granite’ field in Figure 2.3 have significantly variable mafic mineral contents. Alkali granite, which plots in the ‘granite’ field of Figure 2.3, has  $\leq 10$  of its feldspar content being plagioclase.

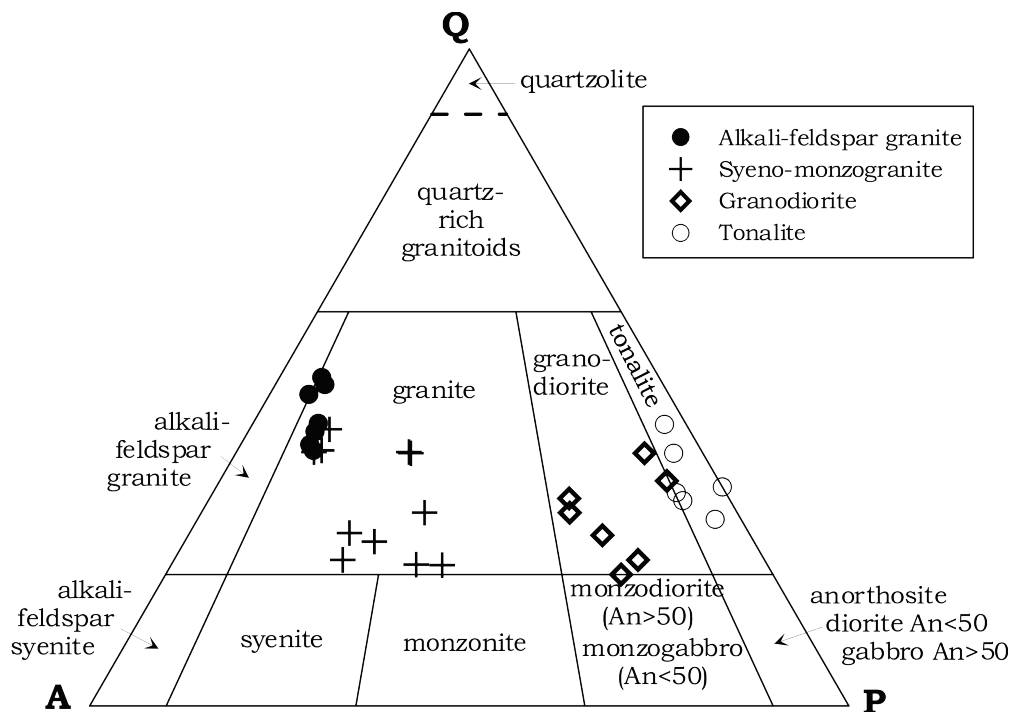


**Figure 2.3:** Classification of studied rocks based on modal mineralogy.

## 2.2 Petrographic descriptions of major plutonic rocks

### K-feldspar granite

K-feldspar granite (Figure 2.4) occurs as a fine- to coarse-grained rock, exhibiting a pink to gray colour and is composed essentially of K-feldspar (40–46 %), quartz (35–46 %), plagioclase (5–9 %), biotite (<1–10 %) and hornblende (<1–3 %). Accessory minerals include zircon, apatite, ilmenite, magnetite and muscovite. Microcline is secondary after orthoclase, and microperthitic microcline occurs as fine- to coarse-grained crystals now partially sericitised. Quartz occurs as fine- to coarse-grained xenomorphic grains with irregular grain boundaries, and exhibits undulatory extinction. Fine-grained recrystallised quartz grains adorn the margins of coarser quartz. In the foliated granite (Figure 2.4c and d), plastically deformed quartz grains have been drawn into ribbons. The long axes of the quartz

## CHAPTER 2: GEOLOGY OF THE STUDY AREA

ribbons are aligned parallel to the direction of shear. Plagioclase occurs as fine- to medium-grained crystals interstitial between K-feldspar and quartz. Myrmekitic texture is common along K-feldspar-plagioclase grain boundaries. Other interstitial minerals include K-feldspar and quartz, biotite, hornblende and the accessory minerals. Zircon and apatite are idiomorphic and occur as inclusions in hornblende, biotite, feldspar and quartz.

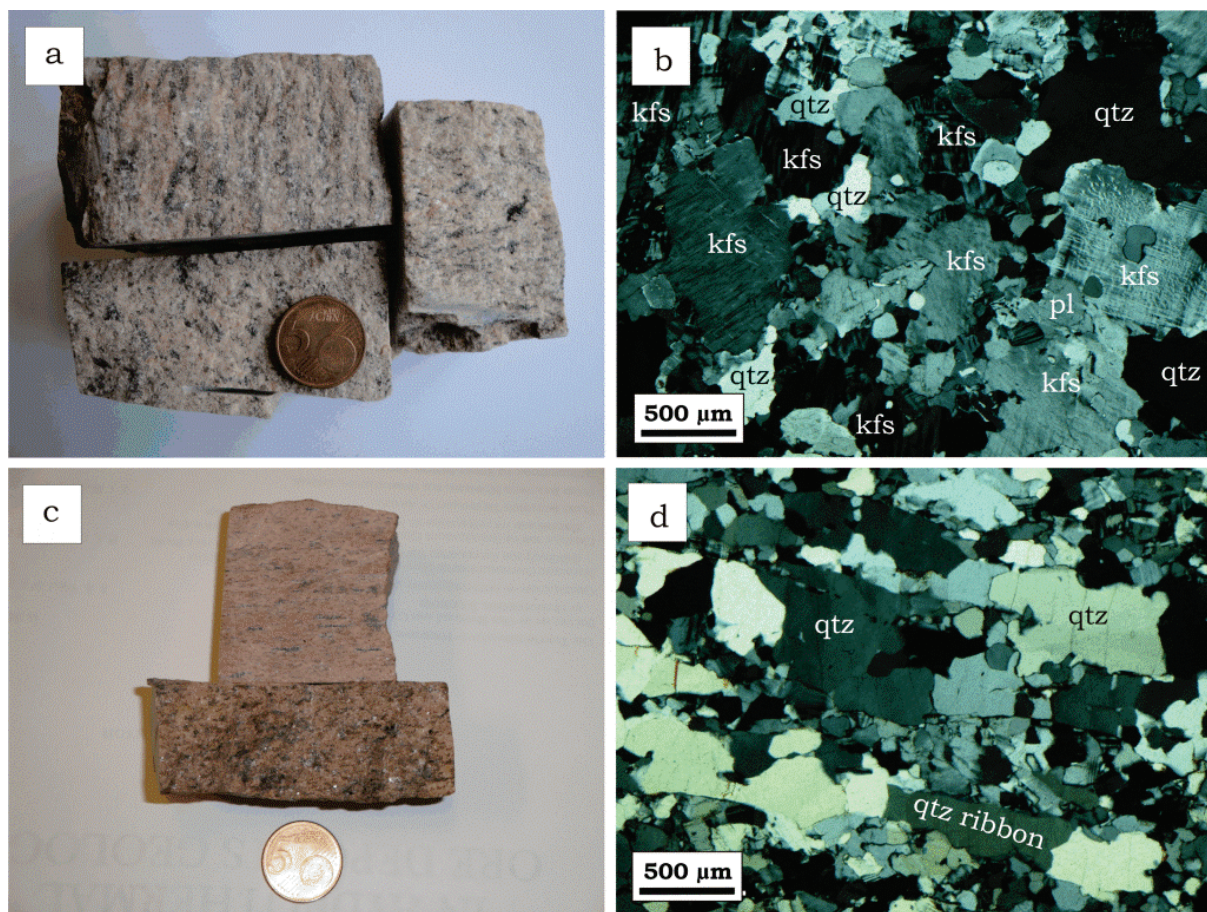


**Figure 2.4:** K-feldspar granite samples from Djira II at Batouri. **(a)** Hand specimens of undeformed K-feldspar granite. **(b)** Transmitted-light photomicrograph (crossed nicols) of one of the samples in (a). Quartz in this sample appears to be mostly isotropic (i.e. not affected by ductile deformation). **(c)** Hand specimens of deformed K-feldspar granite. **(d)** Transmitted-light photomicrograph (crossed nicols) of one of the samples in (c). Quartz in this sample shows prominent planar anisotropy (tectonic foliation). kfs: K-feldspar, qtz: quartz, pl: plagioclase.

### ***Syeno-monzogranite***

Syeno-monzogranite is similar to K-feldspar granite, except for its lower K-feldspar, and higher plagioclase, biotite and hornblende contents (Figure 2.5a-b). In places, the monzogranite resembles granodiorite in hand specimen and mineralogical composition (Figure 2.5c-d). At Dimako, syenogranite is banded, displaying alternating dark and light zones (Figure 2.5e-f). The mineral compositional ranges are: K-feldspar (10–50 %), quartz (10–40 %), plagioclase (5–30 %), biotite (2–30 %), hornblende (<1–65 %). In these rocks, minor clino-pyroxene is present in the hornblende-rich domains. Accessory minerals include zircon, apatite, rarely observed garnet, magnetite, ilmenite, titanite, muscovite, epidote, chlorite and carbonate.

### ***Granodiorite***

Granodiorite is medium- to coarse-grained, and exhibits parallel alignment of interstitial biotite flakes in places (Figure 2.6). It is composed of plagioclase (15–55 %), quartz (10–30 %), K-feldspar (5–30 %), biotite (5–30 %), hornblende (<1–30 %) and accessory apatite, titanite, opaques, zircon and carbonate (<1–8 %). Plagioclase is medium- to coarse-grained, hypidiomorphic to xenomorphic and weakly sericitised. Inclusions in plagioclase consist of zircon, apatite and biotite. Quartz occurs as intergranular mosaics of strained and sutured grains, elongate ribbons displaying undulatory extinctions, and K-feldspar replacements. K-feldspar includes microperthitic microcline and orthoclase. Generally, K-feldspar occurs as medium- to coarse-grained, anhedral crystals, relatively unaltered and contains quartz inclusions. Biotite occurs as fine-grained, subhedral, pleochroic green to reddish brown flakes partly altered to chlorite. These flakes are interstitial between plagioclase, quartz, K-feldspar and hornblende. Hornblende occurs as coarse-grained, subhedral prismatic crystals, interstitial between plagioclase crystals. It alters to chlorite in places (Figure 2.6b). Titanite occurs as subhedral to euhedral crystals, interstitial to plagioclase, quartz and K-feldspar. Hydrothermal minerals

## CHAPTER 2: GEOLOGY OF THE STUDY AREA

such as coarse-grained apatite (~1 mm in length), sulfides and carbonate increase with greater proximity to the auriferous veins.

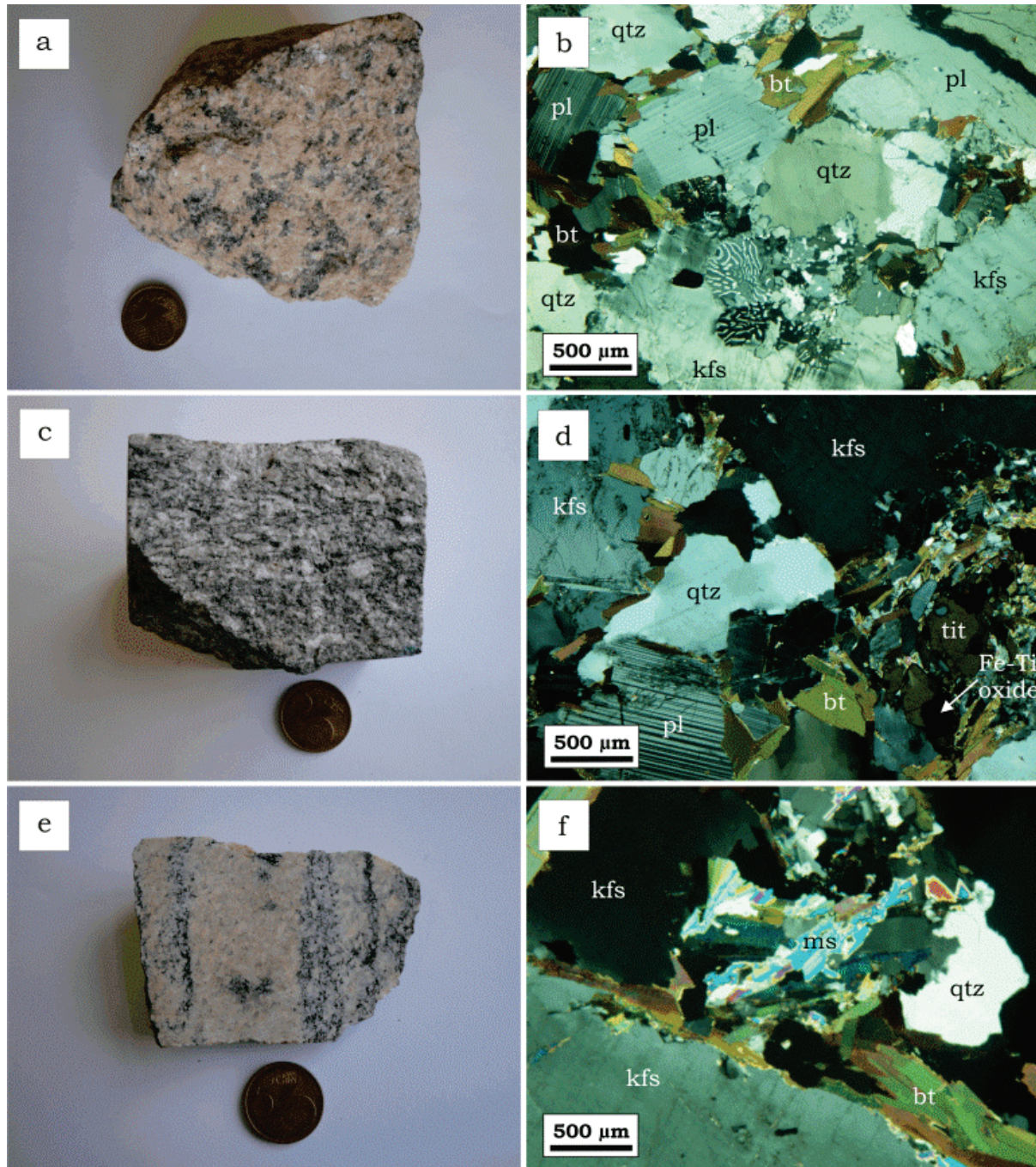


**Figure 2.5:** Syeno-monzogranite samples from Bougogo, Kambélé III and Dimako in Batouri. **(a)** Hand specimen of syenogranite from Bougogo. **(b)** Transmitted-light photomicrograph (crossed nicols) of the sample in (a). **(c)** Hand specimen of monzogranite from Kambélé III. **(d)** Transmitted-light photomicrograph (crossed nicols) of the sample in (c). **(e)** Hand specimen of banded syenogranite from Dimako. **(f)** Transmitted-light photomicrographs (crossed nicols) of the sample in (e). This sample displays prominent mineralogical banding, with alternating melanocratic and leucocratic bands. pl: plagioclase, ms: muscovite, tit: titanite, bt: biotite.

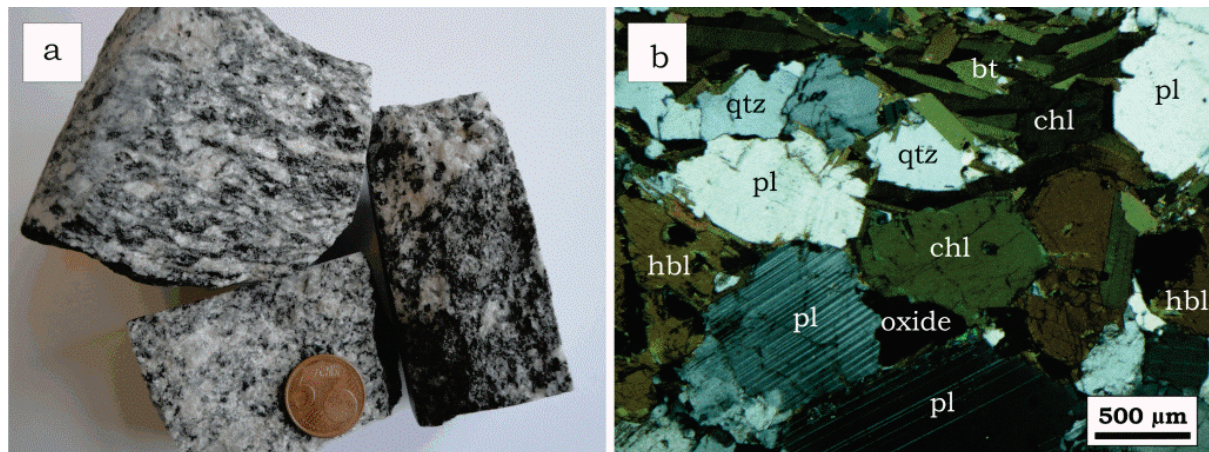


**Figure 2.6:** Granodiorite samples from Kambélé III at Batouri. **(a)** Hand specimens of Granodiorite from Kambélé III. **(b)** Transmitted-light photomicrograph (crossed nicols) of the sample in (a). hbl: hornblende, chl: chlorite.

### Tonalite

Tonalite occurs as fine- to coarse-grained rock (Figure 2.7), composed essentially of plagioclase, quartz, biotite, hornblende and subordinate K-feldspar with minor titanite. Plagioclase occurs as medium- to coarse-grained subhedral crystals, mantled by biotite. The plagioclase contains inclusions of zircon and apatite. Quartz occurs as fine- to coarse-grained xenomorphic crystals displaying undulatory extinctions. Fine-grained quartz mantles K-feldspar and fills spaces between plagioclase crystals. K-feldspar occurs as fine- to medium anhedral crystals interstitial between plagioclase and quartz. Biotite occurs as fine- to medium-grained subhedral, green to reddish brown crystals interstitial between plagioclase and hornblende, partially altered to chlorite. Hornblende is coarse-grained, brownish in colour and anhedral, partially altered to chlorite. Titanite exists as a fine- to medium grained euhedral mineral interstitial between plagioclase, hornblende, biotite and quartz.

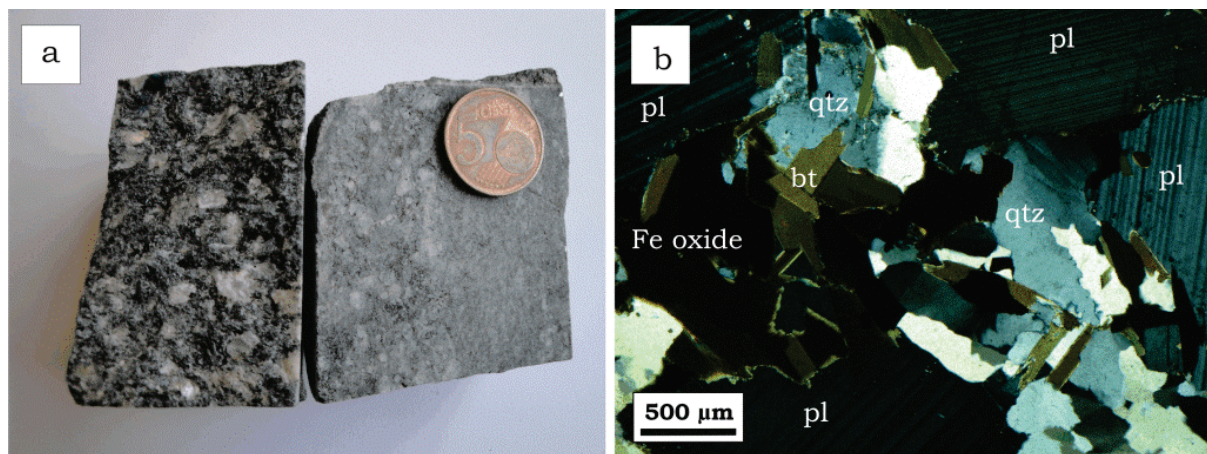


**Figure 2.7:** Tonalite samples from Kombo at Batouri. **(a)** Hand specimens of tonalite from Kombo. **(b)** Transmitted-light photomicrograph (crossed nicols) of one of the samples in (a).

### 2.3 Geochemistry

Representative rock samples, without obvious overprint by hydrothermal alteration and/or weathering, were analysed for major- and trace-elements. The analytical data are presented in Appendix 2a. According to this data, the rocks display a wide compositional range for major-elements: ~60–78 wt % SiO<sub>2</sub>, ~12–17 wt % Al<sub>2</sub>O<sub>3</sub>, 2–6 wt % K<sub>2</sub>O, 0.6–6 wt %  $\Sigma$ Fe<sub>2</sub>O<sub>3</sub>, ~3–4 wt % Na<sub>2</sub>O, 0.4–5 wt % CaO and <0.01–3 wt % MgO.

According to the classification scheme of MacDonald and Katsura (1964), which measures total alkalis (Na<sub>2</sub>O+K<sub>2</sub>O) relative to SiO<sub>2</sub> content to distinguish between alkaline and subalkaline rocks, the Batouri rocks are firmly rooted in the subalkaline field (Figure 2.8a). The K-feldspar granite samples show silica contents of 75–78 wt %, syeno-monzogranite: 69–73 wt %, granodiorite: 65–68 wt %, and tonalite displays the lowest silica contents: 60–62 wt %.

Peccerillo and Taylor (1976) proposed a further classification of subalkaline rocks on the basis of their K<sub>2</sub>O as opposed to SiO<sub>2</sub> content. Applying the field boundaries and nomenclature of Rickwood (1989) to this classification scheme, the Batouri granitoids plot in the high-K calc-alkaline field (Figure 2.8b).

## CHAPTER 2: GEOLOGY OF THE STUDY AREA

In the AFM plot (which measures the proportions of alkali earth metals against Fe and Mg to determine differentiation trends), the Batouri rocks display a calc-alkaline differentiation trend, with K-feldspar granite plotting close to the alkali apex of the AFM diagram. The field boundaries of Irvine and Baragar (1971) was adopted (Figure 2.8c).

Classification of rocks based on the concept of alumina saturation employs the Shand indices A/NK versus A/CNK on the diagram of Maniar and Piccoli (1989), where A/NK is defined as molar  $\text{Al}_2\text{O}_3/\text{Na}_2\text{O}+\text{K}_2\text{O}$  and A/CNK as molar  $\text{Al}_2\text{O}_3/\text{CaO}+\text{Na}_2\text{O}+\text{K}_2\text{O}$ . For the Batouri granitoids, K-feldspar granite and syeno-monzogranite plot marginally in the peraluminous field, while granodiorite and tonalite range in composition from peraluminous to slightly metaluminous, with all samples clustering within the “I-type” field (Figure 2.8d). All the rocks cluster around the metaluminous/peraluminous boundary.

On the classification diagram for normative An-Ab-Or of O'Connor (1965), which is used for felsic rocks with more than 10% normative quartz, K-feldspar granite plots in the granite field, syeno-monzogranite also plots in granite field but a few samples plot in the granodiorite field. Granodiorite and tonalite plot in the granodiorite field, although two tonalite samples plot on the granodiorite-tonalite boundary line (Figure 2.8e).

High magnetic susceptibility was recorded in the Batouri granitoids, ranging from  $4.07 \times 10^{-3}$  SI units for leucocratic rocks to as high as  $49.1 \times 10^{-3}$  SI units for melanocratic rocks.

The Ta-Yb discrimination plot of Pearce *et al.* (1984; Figure. 2.8f), for determining the tectonic settings of rocks, reveals that the Batouri granitoids are volcanic arc-related. Tantalum is severely depleted in these rocks as shown in Figure 2.9a. Most of the rock samples have Ta below the detection limit of 0.5 ppm (dashed line in Figure 2.9a), except for two leucogranite (K-feldspar granite and syenogranite) samples, which show enrichment with respect to lower and upper crustal abundances. In Figure

## CHAPTER 2: GEOLOGY OF THE STUDY AREA

2.9a, Ta values below the detection limit are plotted as half the value of the detection limit (i.e. 0.25 ppm). Tonalite has the highest, and K-feldspar granite the lowest Ti contents.

In Figure 2.9b, Zr/Hf ratios are plotted against Zr in order to portray the magmatic evolution of the rocks, as Hf generally displays a stronger tendency to concentrate in granitic melts than Zr. For the analysed samples, a strong fractionation of Hf is observed in tonalite, and there is some superposition between granodiorite and tonalite. Syeno-monzogranite and K-feldspar granite display high scatter.

## CHAPTER 2: GEOLOGY OF THE STUDY AREA

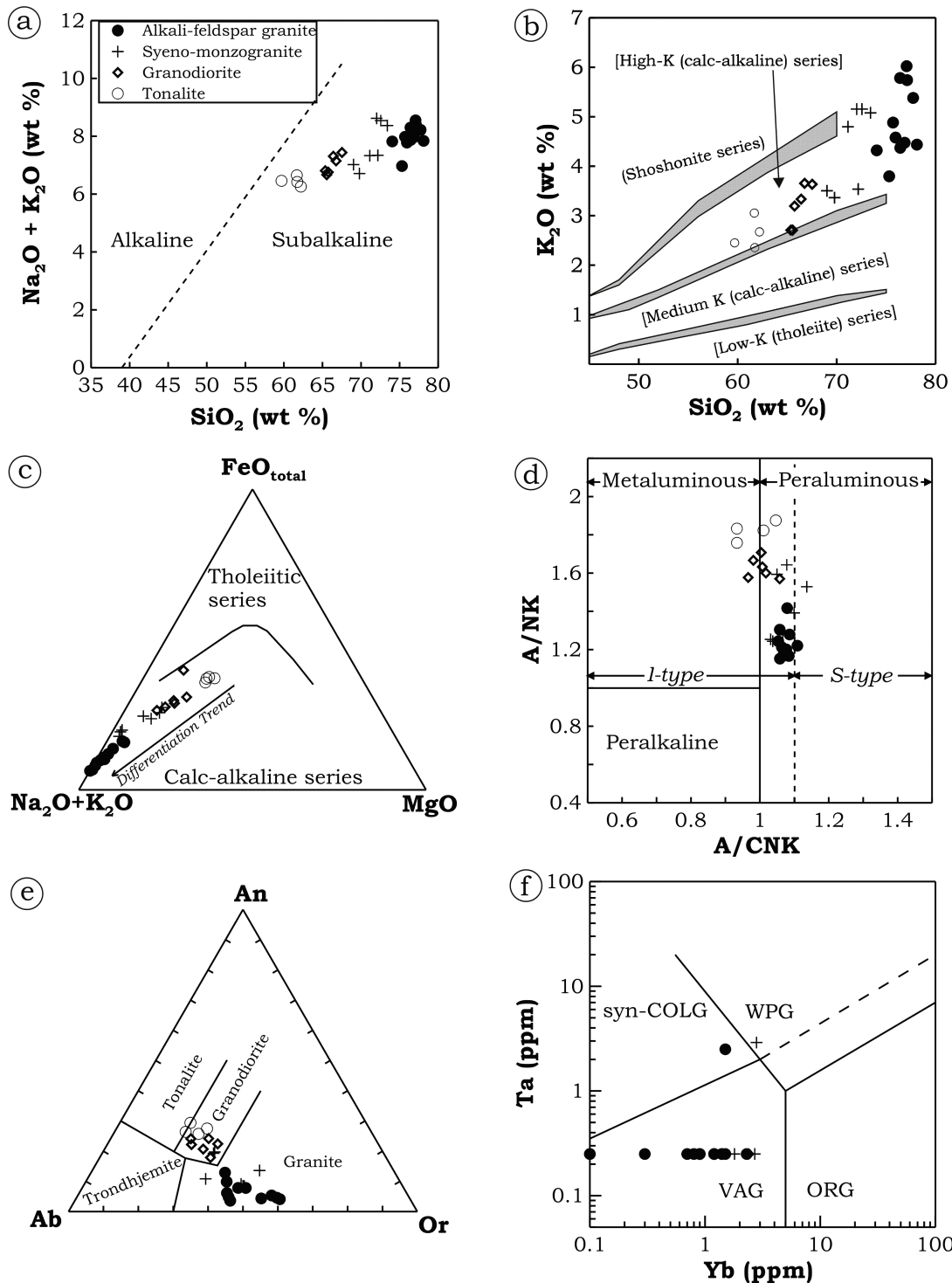


**Figure 2.8:** Major and trace element geochemical classification plots for a suite of plutonic rocks from Batouri. **(a)**  $\text{Na}_2\text{O} + \text{K}_2\text{O}$  versus  $\text{SiO}_2$  diagram of MacDonald and Katsura (1964), showing subalkaline compositions. **(b)**  $\text{K}_2\text{O}$  versus  $\text{SiO}_2$  diagram of Peccerillo and Taylor (1976), showing high-K contents. **(c)** AFM diagram of Irvine and Baragar (1971), showing a calc-alkaline magma differentiation trend. **(d)**  $\text{A}/\text{NK}$  versus  $\text{A}/\text{CNK}$  diagram of Maniar and Piccoli (1989), showing igneous origins. **(e)** Ab-An-Or classification diagram of O'Connor (1965). **(f)** Discrimination diagram of Pearce *et al.* (1984), showing a volcanic arc setting. Syn-COLG: syn-collisional granitoid, WPG: within plate granitoid, VAG: volcanic arc granitoid, ORG: oceanic ridge granitoid.

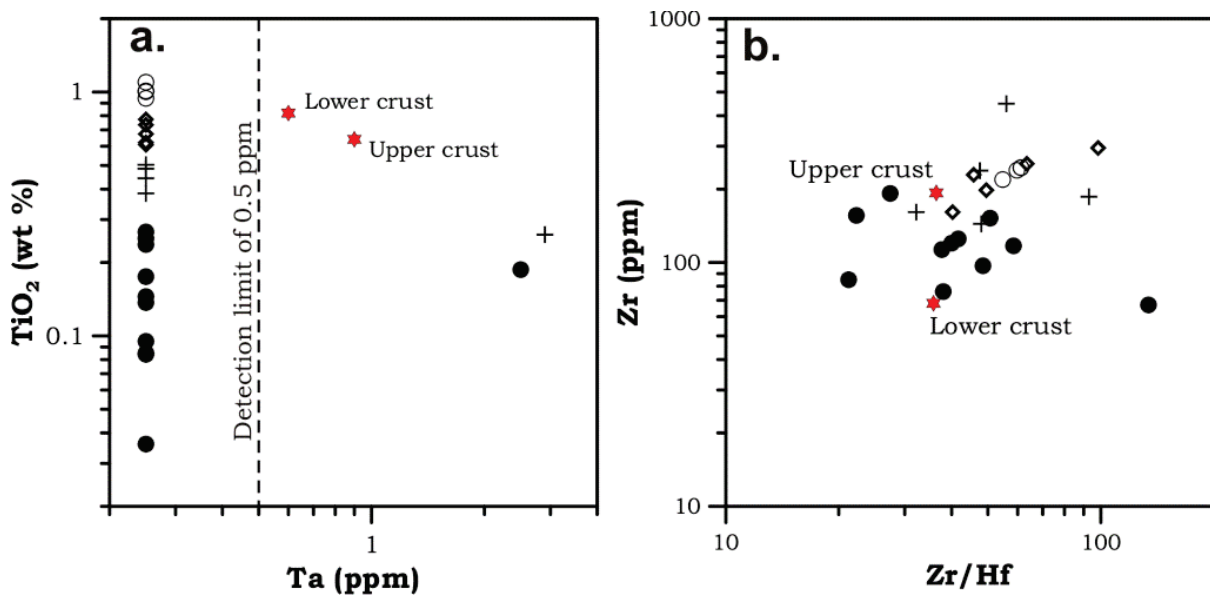


**Figure 2.9:** Magmatic evolution of Batouri granitoids, as portrayed by (a)  $\text{Ta}$  versus  $\text{TiO}_2$  and (b)  $\text{Zr}/\text{Hf}$  versus  $\text{Zr}$  plots. Rudnick and Gao's (2005) upper and lower crustal values for  $\text{TiO}_2$ ,  $\text{Ta}$ ,  $\text{Zr}$  and  $\text{Hf}$  were used for reference purposes. Symbols are same as in Figure 2.8.

$\text{Na}_2\text{O}/\text{K}_2\text{O}$  ratios are generally low (0.42–1.72), with alkali-feldspar granite displaying the lowest and tonalite the highest ratios. Conversely, tonalite exhibits the lowest  $\text{Na}_2\text{O}/\text{CaO}$  ratio (0.80–0.99) and alkali-feldspar granite the highest (1.98–7.78). On Harker diagrams (Figure 2.10) the abundances of  $\text{TiO}_2$ ,  $\text{Al}_2\text{O}_3$ ,  $\text{MnO}$ ,  $\text{MgO}$ ,  $\text{CaO}$ ,  $\text{Na}_2\text{O}$ ,  $\Sigma\text{Fe}_2\text{O}_3$  and  $\text{P}_2\text{O}_5$  decrease with increasing  $\text{SiO}_2$ . However,  $\text{K}_2\text{O}$  correlates positively with  $\text{SiO}_2$ .

The  $\text{Rb}/\text{Sr}$  and  $\text{Rb}/\text{Ba}$  ratios exhibited by these rocks are 0.08–5.69 and 0.04–1.61, respectively. The highest  $\text{Rb}/\text{Sr}$  and  $\text{Rb}/\text{Ba}$  ratios are displayed by K-feldspar granite while tonalite shows the lowest ratios. The rocks are characterised by high contents of  $\text{Ba}$  (113–2290 ppm),  $\text{Rb}$  (68–207 ppm),  $\text{Th}$  (6–39 ppm), and low contents of  $\text{Zr}$  (67–295 ppm).  $\text{Sr}$  (32–932 ppm) and  $\text{V}$  (<5–120 ppm) display wide concentration ranges. On Harker diagrams, abundances of  $\text{Ba}$ ,  $\text{Sr}$ ,  $\text{V}$ , and  $\text{Zr}$  tend to decrease with increasing  $\text{SiO}_2$ , while  $\text{Rb}$  abundances increase with increasing  $\text{SiO}_2$ . However, the relationship between  $\text{Ba}$  and  $\text{SiO}_2$  is far less defined in tonalite, granodiorite and syeno-monzogranite than in K-feldspar granite.

## CHAPTER 2: GEOLOGY OF THE STUDY AREA

Normalisation of trace-elements against primordial mantle reveals significant depletion of Ba in K-feldspar granite with respect to neighbouring elements Rb and Th, as shown in the multi-element spider diagram in Figure 2.11. The rocks generally display depletions in U, Nb, and P. They also show variable total REE contents, from 36 to 240 ppm, and display slight to very strong LREE enrichment on chondrite-normalised REE patterns. Alkali-feldspar granite exhibits strong variations in the REEs.

## CHAPTER 2: GEOLOGY OF THE STUDY AREA

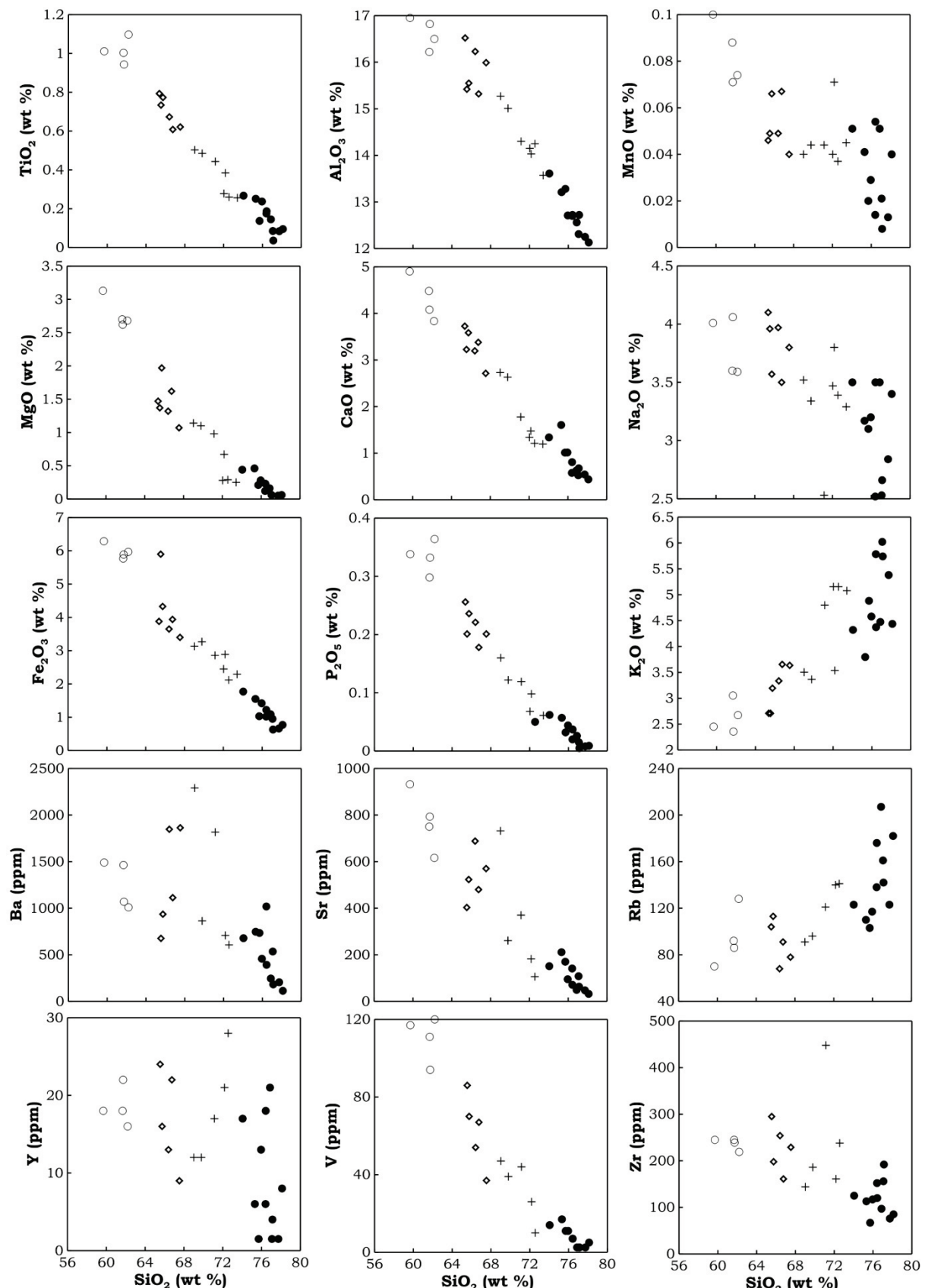


**Figure 2.10:** Harker diagrams for plutonic rocks from the Batouri area. Symbols are same as in Figure 2.8.

## CHAPTER 2: GEOLOGY OF THE STUDY AREA

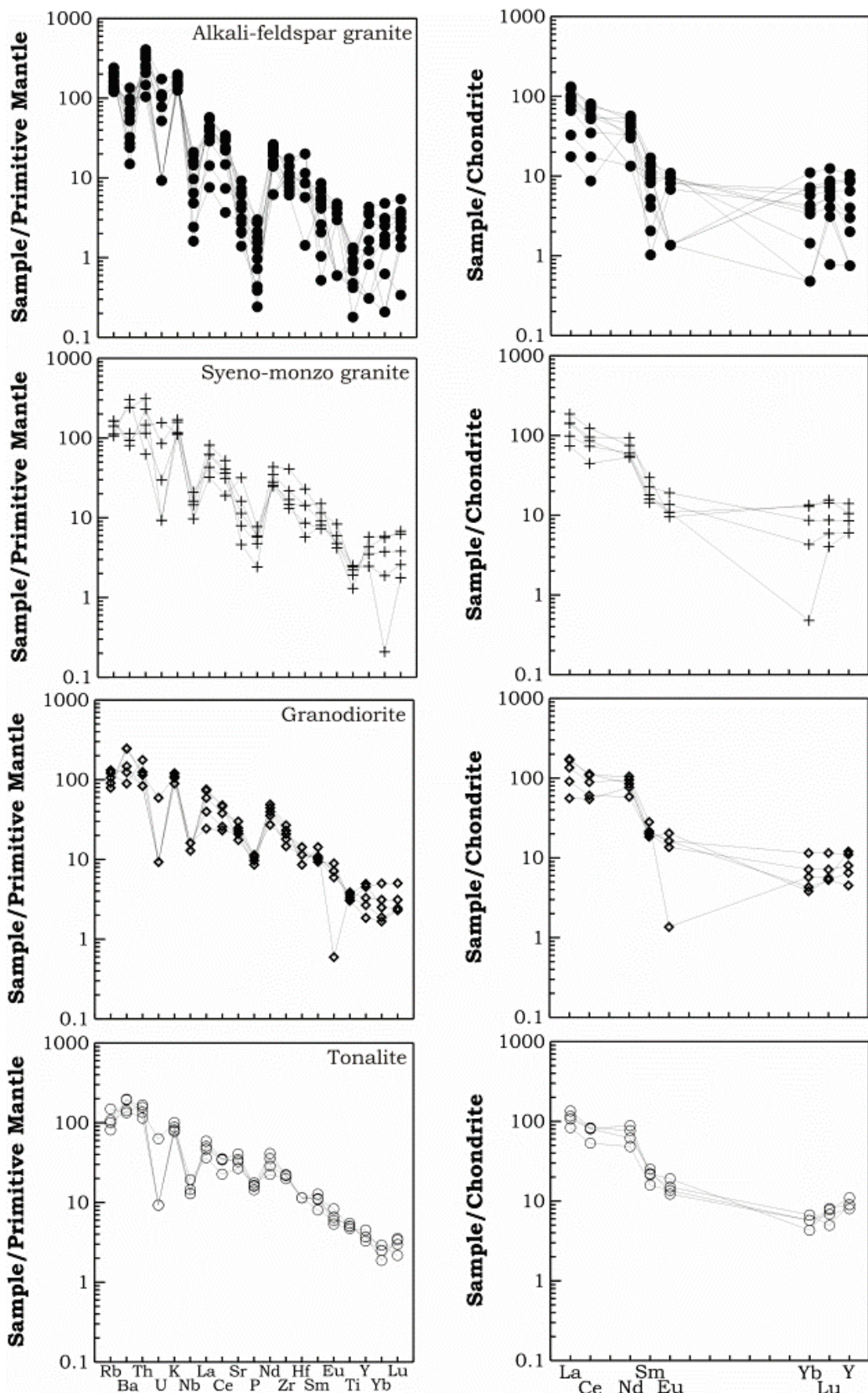


**Figure 2.11:** Plots showing trace-element distribution in the Batouri granitoids. The concentration values have been normalised to primitive mantle for the multi-element spider plots, and chondrite for the rare earth element plots. Symbols are same as in Figure 2.8.

## 2.4 Deformation structures

Structural elements in the Batouri area include numerous variably dipping regional-, meso- and microscale fault-vein sets mainly trending NNE–SSW, NE–SW, ENE–WSW and ESE–WNW. The patterns of the intersecting veins define three major deformation phases. These deformation phases are pre-, syn- and post-gold mineralisation, here designated D<sub>1</sub>, D<sub>2</sub> and D<sub>3</sub>, respectively. The early deformation phase (D<sub>1</sub>) is characterised by ESE–WNW, SE–NW and SSE–NNW trending faults associated with aplitic granite intrusions. These intrusions are abundant in K-feldspar granite (Figures 2.1c and 2.12a), but are rare in syeno-monzogranite and granodiorite, except in close proximity to K-feldspar granite. These aplitic intrusions range in width from a few millimetres to tens of centimetres. In places, they occur as a set of parallel near-horizontal dykes which appear to define local foliation (Figure 2.1c).

The most important structural feature of the Batouri area is the 13 km-long, NE-trending, sinistral shear zone associated with gold mineralisation, which mainly cuts granodiorite and syeno-monzo granite plutons, and defines D<sub>2</sub> deformation. The width of the shear zone (including associated secondary structures) ranges from 100 m to 1 km. The shear zone and associated secondary structures hosts several sets of gold-bearing quartz veins, mostly trending NNE–SSW, NE–SW, ENE–WSW and NW–SE, and dipping steeply northwest and southeast. These veins vary from 10 to 70 cm in thickness (Figure 2.12c) and are discontinuous. Individual segments of the veins attain strike lengths in scales of 10s of metres. The veins consist essentially of white, rose and smoky quartz varieties, as well as carbonates. Gold mineralisation occurs both in the veins (0.04 to >30 g/t) and the wallrock (0.4 to 18.5 g/t; Appendix 2b). The ore-zones also include a complex network of gold-bearing veinlets, displaying variable strike and dip directions (Figure 2.12d). Evidence of crystal-plasticity and shearing is expressed as bent twin lamellae in plagioclase (Figure 2.13a), sub-parallel

## CHAPTER 2: GEOLOGY OF THE STUDY AREA

fractures in plagioclase (Figure 2.13b), sigmoidal fabric in quartz ribbons (Figure 2.13c and d), and pressure shadows.

Secondary NW–SE-trending faults also associated with D<sub>2</sub> deformation are coincidental with high-grade gold mineralisation (Figure 2.14). The secondary deformation structures were mapped at Kambélé by geophysical survey methods (commissioned by African Aura Mining Inc.), but they are not well represented by veins in the regolith (to which this study was limited). However, D<sub>2</sub> deformation generally defines a major N35°-trending ductile–brittle shear zone (Figure 2.15).

D<sub>3</sub> deformation is marked by near-horizontal barren quartz veins which displace the lodes in places. These barren veins are widespread in the Batouri area and are probably related to similarly-oriented pegmatite dykes occurring at Bougogo and Amedobi. They range in thickness from a few millimetres to 14 metres, mostly striking ENE–WSW. The barren quartz varies from white, grey to smoky in colour. It is generally massive, but in places it forms coarse-grained euhedral to subhedral crystals projecting inwards to a central vug. Where the central vug is absent it is filled by finer-grained euhedral to subhedral quartz crystals. Barren veins also host clusters of well-formed gold-poor pyrite crystals (Suh *et al.*, 2006). In places, the veins clearly occupy mesoscale brittle–ductile shear zones (e.g. Figure 2.12b).

## CHAPTER 2: GEOLOGY OF THE STUDY AREA

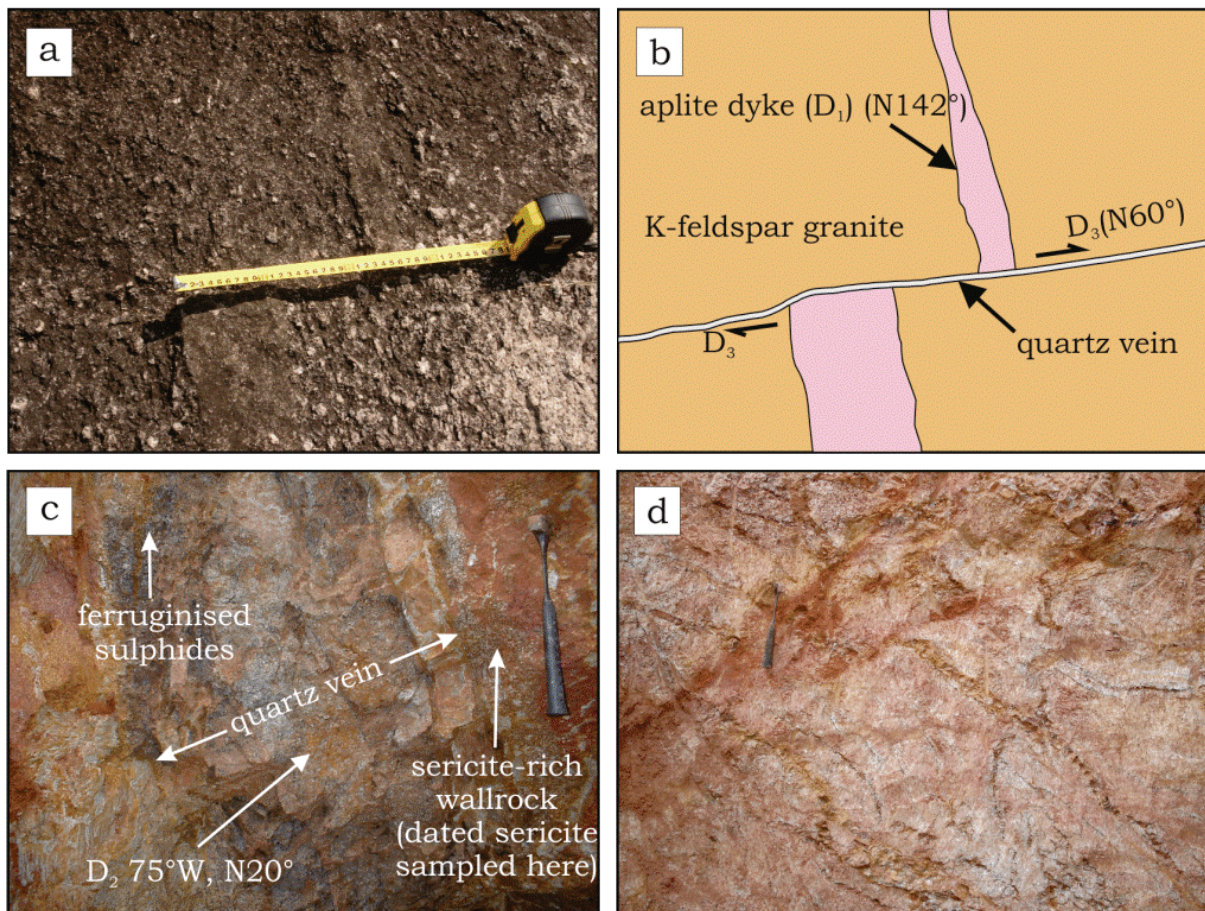


**Figure 2.12:** Deformation structures at Batouri. **(a)** Outcrop of K-feldspar granite intruded by an aplite dyke and a quartz vein, which are obscured by weathering. **(b)** Key to the outcrop shown in (a), where aplite dyke ( $D_1$ ) is truncated and displaced by barren quartz vein ( $D_3$ ). **(c)** Close-up view of a lode vein at Dimako ('open pit'). **(d)** Network of gold-bearing veinlets exposed at a pit in Kambélé III. These veinlets emanate from a larger vein (not shown). The dated zircon (HR) was sampled at this location.

## CHAPTER 2: GEOLOGY OF THE STUDY AREA

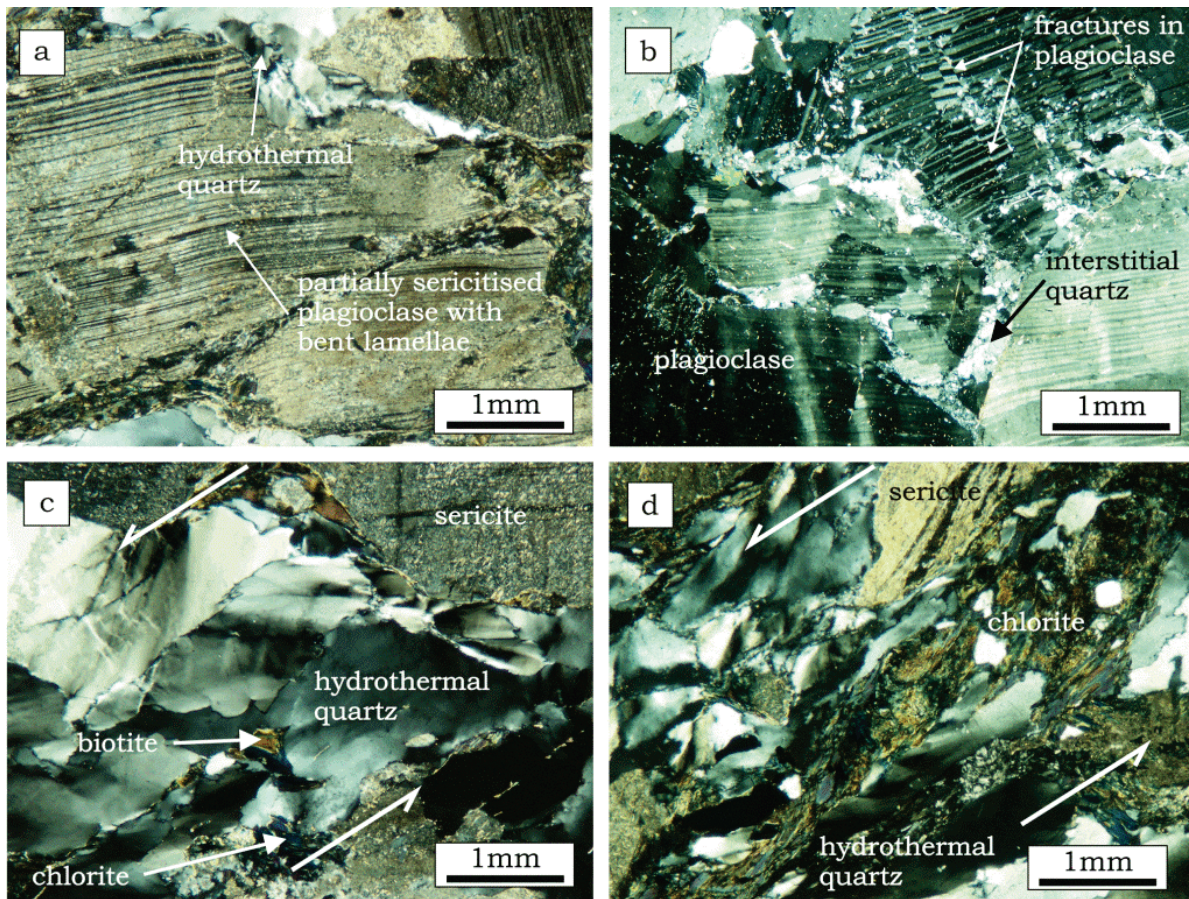


**Figure 2.13:** Transmitted-light photomicrograph (crossed nicols) showing shear fabric in the wall-rock adjacent to gold-bearing veins and veinlets. **(a)** Bending of twin lamellae in partially altered plagioclase. This microstructural feature points to crystal plasticity of the granitic country rock during the emplacement of the quartz veins. **(b)** Coarse-grained plagioclase crystals displaying bending and dextral displacement of twin lamellae, indicative of ductile-brittle deformation. **(c)** and **(d)** Sigmoidal-shaped quartz ribbons displaying sub-parallel fractures and undulatory extinctions. These microstructures imply sinistral shearing and crystal plasticity.

## CHAPTER 2: GEOLOGY OF THE STUDY AREA

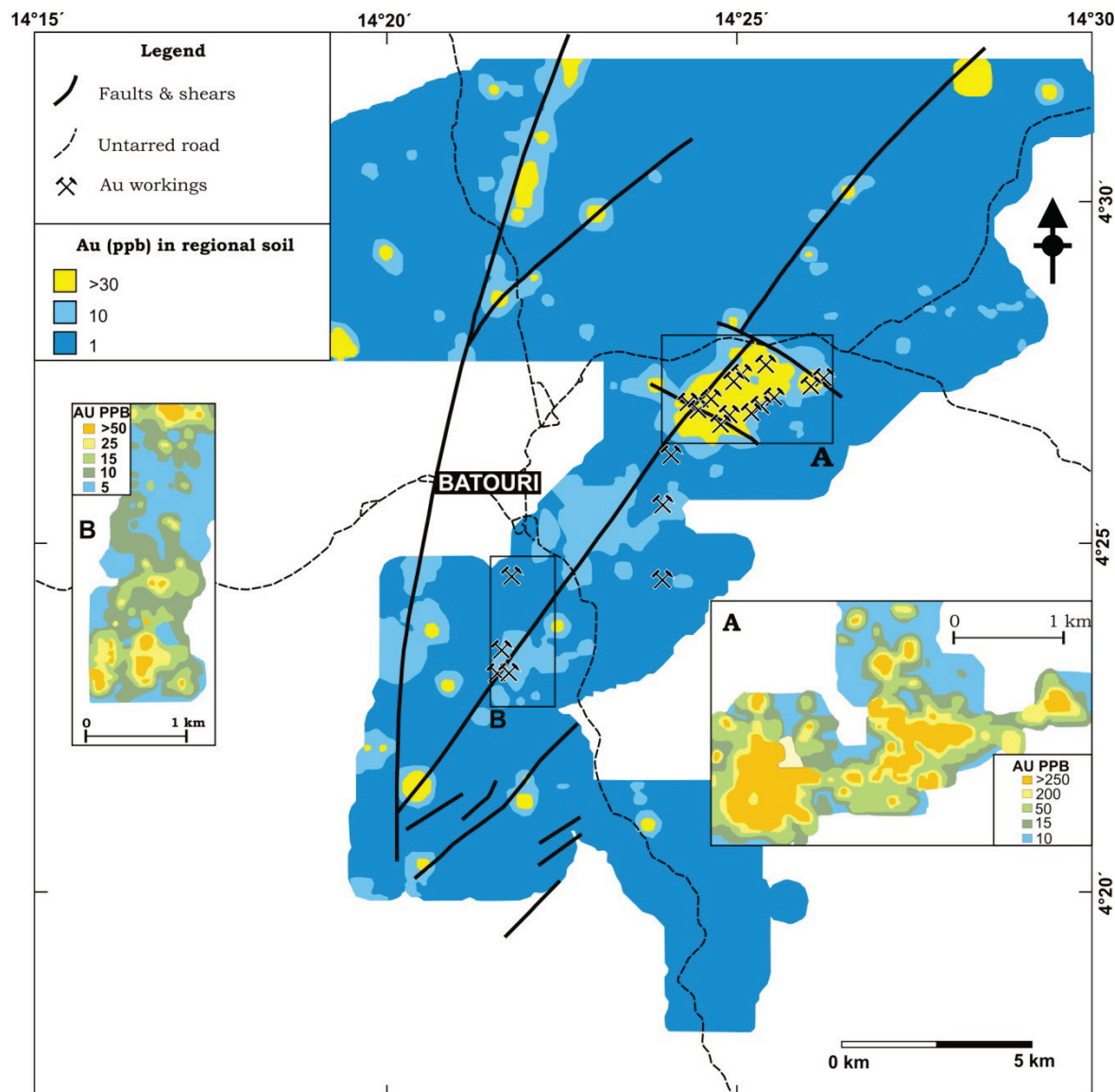


**Figure 2.14:** Gold distribution patterns in the soils of Batouri. The gold anomalies are spatially associated with shear zones. Inset A shows the distribution of gold in the soil at the Dem-Bote-Kambélé-Mboscoro area, while inset B shows the distribution in the Mongonam-Dimako area. Modified after African Aura Mining (2009).

## CHAPTER 2: GEOLOGY OF THE STUDY AREA

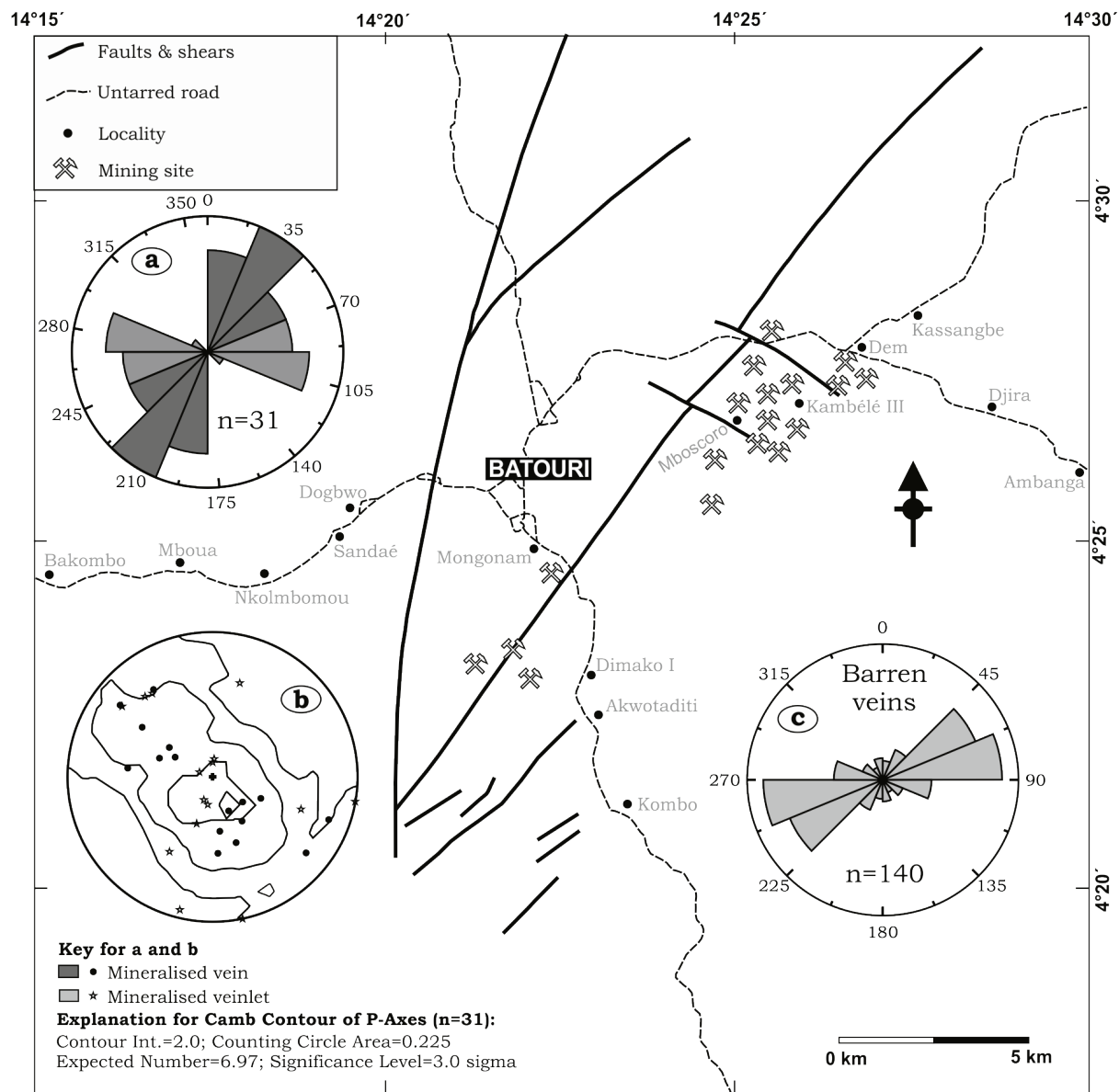


**Figure 2.15:** Structural map of Batouri, showing the main shear zones. **(a)** Rose diagram showing strike directions of mineralised veins (dark grey) and veinlets (light grey). The mineralised veins dominantly trend N35°. The veinlets display variable orientations, mainly ENE-WSW and ESE-WNW. SE-NW-oriented secondary faults at the Kambélé-Mboscoro area are coincidental with high grade ores (see Figure 2.14). **(b)** Contour plot of the poles to the mineralised veins and veinlets. The orientation of the contours indicate a N35° strike direction of the shear zone. **(c)** Rose diagram showing strike directions of barren veins in the Batouri prospect, which are dominated by NE-SW and ENE-WSW oriented veins.

## 2.5 Discussion

### 2.5.1 Magmatic evolution

The Batouri granitoids display characteristics of I-type, high-K calc-alkaline series magma, with a metaluminous to slightly peraluminous character (Figure 2.8). On Harker diagrams (Figure 2.10), the abundances of TiO<sub>2</sub>, Al<sub>2</sub>O<sub>3</sub>, MnO, MgO, CaO, Na<sub>2</sub>O, ΣFe<sub>2</sub>O<sub>3</sub> and P<sub>2</sub>O<sub>5</sub> decrease with increasing SiO<sub>2</sub>. These trends are consistent with those expected for magmatic evolution through fractional crystallisation of plagioclase, ferromagnesian minerals, Fe-Ti oxides, titanite and apatite. The positive correlation between K<sub>2</sub>O and SiO<sub>2</sub> indicates the persistence of K-feldspar to the late stages of crystallisation. The negative correlations of SiO<sub>2</sub> with Ba and Sr suggest fractionation of K-feldspar and plagioclase, respectively (e.g. Njanko *et al.*, 2006; Zhu *et al.*, 2009). However, the relationship between Ba and SiO<sub>2</sub> is far less defined in tonalite, granodiorite and syeno-monzogranite than in K-feldspar granite. This implies that K-feldspar fractionation only became an important differentiation process during the crystallisation of the Batouri granite. The Batouri rocks show a negative correlation between Zr and SiO<sub>2</sub> (Figure 2.10), and lower Zr/Hf ratios in the leucocratic than the more melanocratic rocks. The Zr/Hf ratios reflects the tendency of Hf to be more concentrated than Zr in granitic melts (Zaraisky *et al.*, 2009), due to fractional crystallisation of Zircon.

The high magnetic susceptibilities ( $4.07 \times 10^{-3}$ – $49.1 \times 10^{-3}$  SI units) recorded from Batouri granitoids indicate that they belong to the magnetite series *sensu* Ishihara *et al.* (1977). There is a decrease in the magnetic susceptibility toward the more evolved leucocratic rocks. Such a decrease implies fractional crystallisation of magnetite. The decreasing abundance of V with increasing SiO<sub>2</sub> further points to magnetite fractionation.

The presence of enclaves in the Batouri granitoids could indicate assimilation of older rocks. The linear magmatic trends and the clustering of the rocks around the metaluminous–peraluminous boundary (Figure 2.8d)

indicate a co-magmatic origin (e.g. Heinhorst *et al.*, 1996; Zoheir *et al.*, 2008) for the Batouri granitoids. Tonalite and granodiorite partially plot in the metaluminous field, while monzo-syenogranite and K-feldspar granite all plot in the peraluminous field (Figure 2.8d). This trend is characteristic of a metaluminous parent magma, which underwent closed-system fractional crystallisation of ferromagnesian minerals (e.g. Cawthorn and Brown, 1976; Barbarin, 1996; Zen, 2003).

### 2.5.2 Source rock characteristics and tectonic setting

The rocks generally display depletions in U, Nb, P and HREEs (Figure 2.11), which is a feature of melts generated at oceanic crust–continental crust subduction zones (Wilson, 1989; Thirlwall *et al.*, 1994). However, partial melting experiments on crustal rocks, conducted by Roberts and Clemens (1993), suggest that high-K, I-type granitoid magmas can only be derived from the partial melting of hydrous, calc-alkaline to high-K calc-alkaline, mafic to intermediate metagneous rocks in the crust. The presence of magnetite indicates that partial melting occurred under oxidising conditions. Oxidised melts are typically derived from the lower crust at oceanic crust–continent crust subduction-zone settings. The extreme depletion of Ta in these rocks could be indicative of the existence of residual Ta-bearing minerals such as titanite, rutile, ilmenite, amphibole or garnet at the source during partial melting (Green and Pearson, 1986; Wilson, 1989; De Souza *et al.*, 2007). The depletion of HREEs (Figure 2.11) is suggestive of refractory garnet at the magma source (Rollingson, 1993).

In the Yb versus Ta discrimination diagram (Pearce *et al.*, 1984), the Batouri granitoids plot in the ‘volcanic arc granite’ field (Figure 2.8f). Their high-K, calc-alkaline affinities are also consistent with granitoids intruded at active continental margins (Pearce *et al.*, 1984). These conform with the geodynamic model proposed by Toteu *et al.* (2004), for the Pan-African mobile belt in Cameroon (Figure 2.16). According to this model, the collision between the mobile belt and the northern edge of the Congo Craton resulted

## CHAPTER 2: GEOLOGY OF THE STUDY AREA

in crustal thickening, subcrustal lithospheric delamination, and the upwelling of the asthenosphere. These processes generated excessive heat, which melted crustal rocks at depth and produced the high-K calc-alkaline magmas. Because of the widespread occurrence of granitoids in the Adamawa-Yadé domain with similar chemical features (i.e. high-K, cal-alkaline, metaluminous to peraluminous, I-type affinities), Tchameni *et al.* (2006) have postulated that these granitoids form a regional-scale batholith, which underlies the Adamawa-Yadé domain.

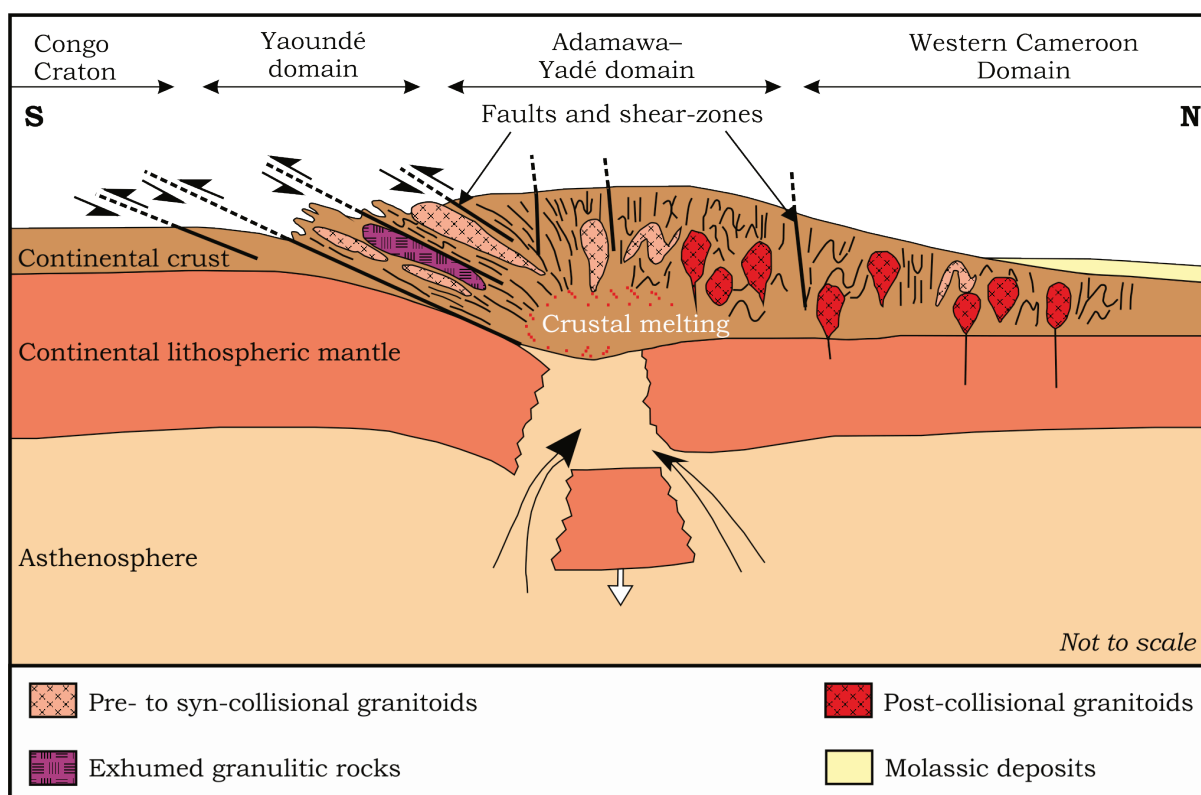


**Figure 2.16:** A model of the post-collisional stage of the Central African Fold Belt and the Congo Craton. The upwelling asthenosphere supplied excessive heat to the lower crust, which melted crustal rocks to generate high-K calc-alkaline granitic magmas. Modified after Toteu *et al.* (2004).

At Batouri, the earliest deformation ( $D_1$ ) is associated with the intrusion of aplite dykes. Aplite is the most evolved rock in the Batouri area, and is assumed to represent the last phase of magmatic activity at Batouri. The major NE-SW shear zone at Batouri, which is associated with gold mineralisation, is the result of sinistral  $D_2$  deformation.  $D_3$  deformation at

Batouri is characterised by the intrusion of barren quartz veins and pegmatite dykes. In places, the quartz veins display crystal growths and central vuggy structures reminiscent of emplacement in dilational fractures. But in other places, they truncate aplite veins and exhibit ductile–brittle dextral shearing. D<sub>2</sub> deformation at Batouri, which is contemporaneous with gold mineralisation, probably correlates with the regional D<sub>3</sub> deformation described by Toteu *et al.*, (2004). Their D<sub>3</sub> deformation is related to post-collisional nappe tectonics, which produced regional fracturing.

### **2.5.3 The role of magmatism in gold mineralisation**

Hypogene gold mineralisation occurs in a variety of tectonic environments (Figure 2.17) where they exist in spatial and temporal association with a great variety of plutonic rock types, predominantly granitoids (Goldfarb *et al.*, 2005). Based on these associations, and supported by geochemical evidence, some workers (e.g. Burrows and Spooner, 1987) have suggested a magmatic source for the gold. Magmatic sources have actually been unequivocally established in deposit types related to alkaline magmatism such as gold-rich porphyry (Jensen and Barton, 2000; Sillitoe, 2000) and epithermal systems (Cooke and Simmons, 2000; Jensen and Barton, 2000); as well as, intrusion-related (Thompson and Newberry, 2000) and gold-bearing skarn deposits (Meinert, 2000).

However, the role of magma in the genesis of other deposit types, notably orogenic gold deposits, is unclear; one possible connection between magma and orogenic gold deposits supposes that igneous intrusions serve as a source of heat that drives ore-forming hydrothermal systems (Goldfarb *et al.*, 2005). Hronsky and Groves (2009) have recently suggested that mantle-derived, gold-enriched alkalic magmas are the ultimate source of gold enrichment in the crust. According to them, gold-rich alkalic magmas are so modified by crustal processes that evidence of their genetic relationship with gold become obscured in many cases.

## CHAPTER 2: GEOLOGY OF THE STUDY AREA

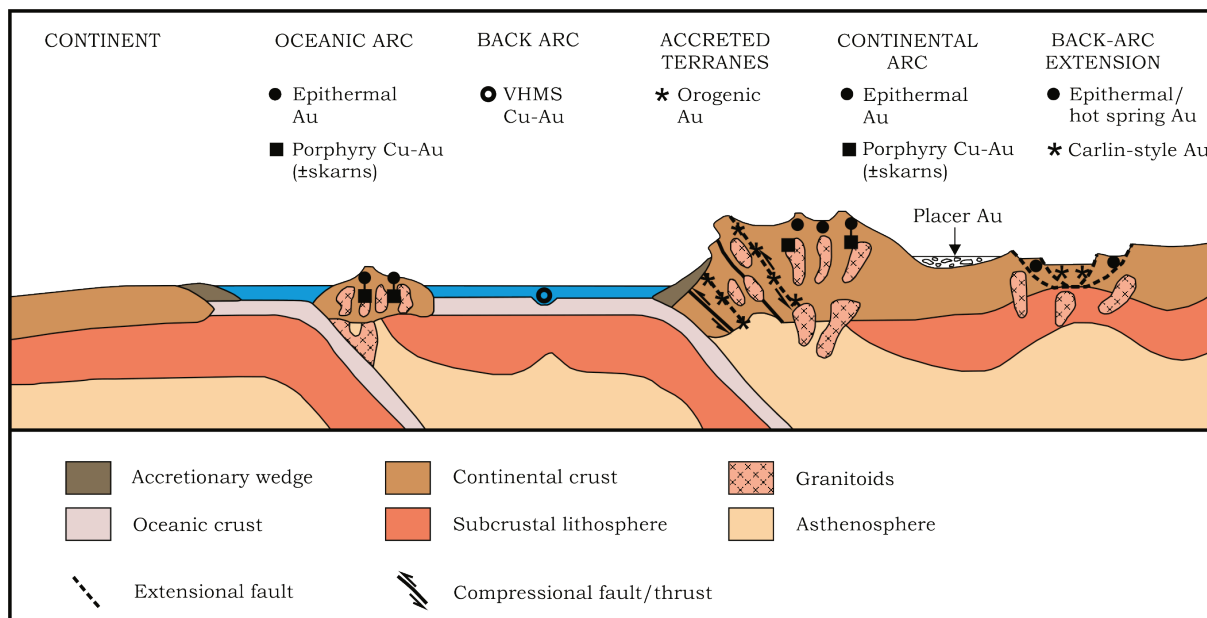


**Figure 2.17:** Sketch illustration of the tectonic setting of the most common gold deposit types. After Groves *et al.* (1998) and Goldfarb *et al.* (2005).

It is believed that the Pan-African orogeny, and associated regional metamorphism and magmatism, generated large-scale movements of ore-bearing fluids in the crust. These fluids were channelised along complex fractures into regional NE-trending shear zones and were responsible for gold and base-metal mineralisation along these structures throughout the Pan-African mobile belt (Pirajno and Jacob, 1988; Goldfarb *et al.*, 2001). Gold mineralisation at Batouri displays structurally-controlled quartz veins that occur in spatial proximity to crustally-derived, oxidised, intermediate to felsic intrusions.

## 2.6 Summary

The geology of Batouri consists of high-K, calc-alkaline granitoids, which intruded gneissic basement rocks in a continental arc tectonic setting. The granitoids belong to the magnetite series and possibly resulted from partial melting of metaigneous crustal rocks. The rocks have been dissected by sets of faults representing at least three major deformation events ( $D_1$ ,  $D_2$  and  $D_3$ ). At least one of these events ( $D_2$ ) was coeval with lode gold

## CHAPTER 2: GEOLOGY OF THE STUDY AREA

mineralisation. The gold occurs in veins and wall-rock, along N35°-trending, steeply dipping shear zones.

## **CHAPTER 3: HYDROTHERMAL ALTERATION**

### **3.1 Introduction**

Hydrothermal alteration involves a series of chemical reactions, which seek to establish chemical equilibrium between invading hydrothermal solutions and wall-rock. These reactions result in mineralogical, chemical and textural changes in the wall-rock (Rose and Burt, 1979; Pirajno, 1992). The changes occur at decreasing intensities with distance away from the vein, imposing a zonation pattern. Hydrothermal processes play a central role in ore deposition because the resultant physico-chemical changes destabilise metal complexes carried in the hydrothermal solutions, culminating in the precipitation of metals. A careful study of wall-rock alteration processes is therefore important in understanding the ore precipitation mechanism and physico-chemical conditions of the hydrothermal system at the time of ore formation (Kishida and Kerrich, 1987).

For the purpose of the present study, core samples of hydrothermally altered wall-rock from depths of 35–100 m, and without obvious supergene overprint, were studied. Microfractures in the wall-rock, genetically linked to the main veins, host thin quartz-carbonate veinlets. The alteration halos around the main veins are wider in the footwalls, but are more symmetrical around the veinlets. The width of the alteration zones varies from vein to vein in scales of millimetres to tens of centimetres. Microscopic studies of the wall-rock samples revealed dextrally rotated feldspar porphyroblasts and asymmetric pressure shadows (Figure 3.1a and b), which suggest that vein emplacement was coeval with plastic deformation. Further microscopic observations revealed that chloritisation, sericitisation, silicification, carbonatisation and sulfidation, are common hydrothermal alteration processes in the vicinity of auriferous veins. Two lateral alteration zones are distinguished around the auriferous quartz veins, namely: (a) a proximal, pervasive quartz–carbonate–muscovite–pyrite zone, which transists

gradationally into (b) a distal chlorite–quartz–muscovite±carbonate±pyrite zone.

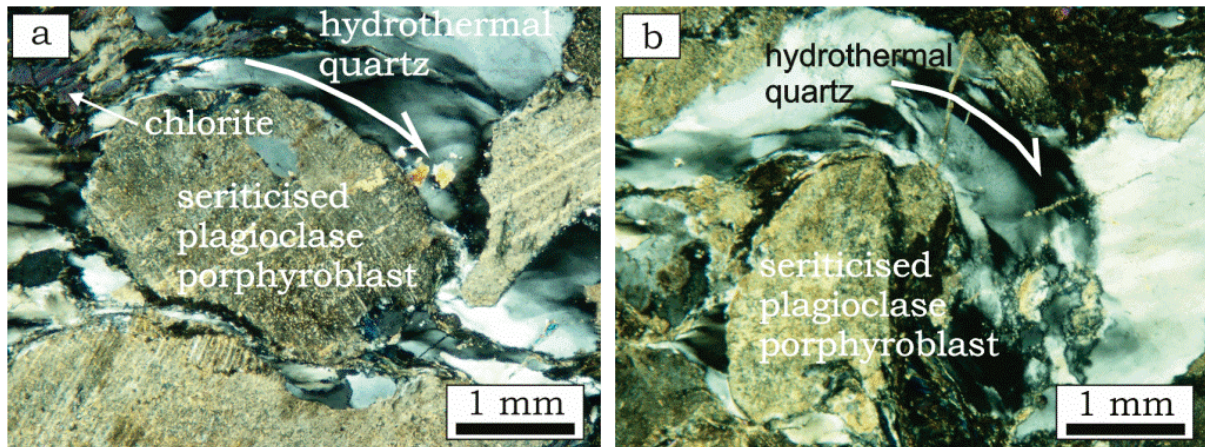


**Figure 3.1:** Transmitted-light photomicrographs (crossed nicols), showing plastic deformation in wall-rock **(a)** Intergranular quartz with chlorite and muscovite flakes replacing original feldspar crystals in the wall-rock, **(b)** Wrapping of quartz implying a dextral rotation of feldspar porphyroblast during quartz invasion.

## 3.2 Alteration zones

### 3.2.1 The proximal zone: quartz–white mica–carbonate–pyrite

The proximal alteration zone is characterised by abundance of white mica, quartz, carbonate and sulfides. Relics of K-feldspar, plagioclase and chlorite occur within masses of white mica. In places, feldspar and chlorite display faint superimposed calcite twinning. Iron sulfides such as pyrite, pyrrhotite and chalcopyrite are intimately associated with partially replaced magnetite, ilmenite and biotite. Rutile occurs alongside ilmenite and pyrite. Carbonate occurs in the proximal zone of the wall-rock as veins or disseminations. Carbonate is also intimately intergrown with pyrite. Coarse-grained apatite is common in the wall-rock. The gold content of the proximal zone ranges from 0.4–18.5 g/t (Appendix 2b).

### 3.2.2 The distal zone: chlorite–quartz–white mica–epidote–carbonate–pyrite

The distal alteration zone is dominated by chlorite, with subordinate amounts of quartz, white mica, carbonate, rutile, pyrite and epidote. Biotite

relics are common in chlorite masses (Figure 3.2a). Chlorite is mostly interstitial, retaining the crystallographic directions of the precursor biotite. Quartz and carbonate occur as anhedral or subhedral grains that are disseminated, clustered or vein-forming. Hornblende is partially replaced along cleavage planes by chlorite and epidote (Figure 3.2b). In places, biotite, plagioclase and subgrains of partially altered hornblende (bottom of Figure 3.2b) display faint calcite twinning. Clusters of fine-grained rutile intergrown with chlorite assume a titanite-like crystal shape (Figure 3.2c). Less common is the occurrence of chlorite as fine-grained disseminations or as veinlets in the quartz–carbonate veins (Figure 3.2d). Marginal alteration of biotite to white mica occurs in places. Plagioclase and K-Feldspars exhibit variable degrees of sericitisation, which proceed along twin planes, fractures and grain boundaries. Plagioclase is more altered than K-feldspar. Coarse-grained apatite (~1.2 mm long) is abundant in this zone. Sulphide such as pyrite, chalcopyrite and pyrrhotite are common in domains rich in biotite. The sulfides are also intergrown with minerals such as magnetite, haematite, ilmenite and chlorite.

### 3.3 Alteration mineral chemistry

Microprobe analyses were performed on chlorite, white mica, apatite, carbonate and sulfides. The chemistry of chlorite is known to be temperature dependent (McDowell and Elders, 1980; Cathelineau and Nieva, 1985; Cathelineau, 1988; Zang and Fyfe, 1995), and will be important here for geothermometric estimations. Chemical compositions and variation trends in the other hydrothermal minerals (white mica, apatite and carbonate) will indicate composition and evolution of the hydrothermal fluids from which they were formed. Because of their genetic association with gold, sulfides are an important group of minerals in most lode gold deposits. In this chapter, discussions on sulfides will focus on their textural relationships with other minerals. Their chemistry will be explored in detail in Chapter 4.

### **3.3.1 Chlorite mineral chemistry and geothermometry**

#### *Chlorite chemistry*

Chlorite was microanalysed and the results of the electron-microprobe analyses are summarised in Table 3.1 (see Appendix 3a for complete results). These results shows a fairly uniform composition,  $\text{SiO}_2$ : 25.6–28.3 wt %;  $\text{TiO}_2$ : 0.06–0.28 wt %;  $\text{Al}_2\text{O}_3$ : 18.2–21.8 wt %;  $\text{FeO}$ : 24.0–29.0 wt %;  $\text{MnO}$ : 0.11–0.39 wt %;  $\text{MgO}$ : 11.7–16.3 wt %;  $\text{CaO}$ : <0.03–0.18 wt %; and  $\text{K}_2\text{O}$ : 0.05–2.47 wt %. The compositions of  $\text{Na}_2\text{O}$ , Cl and F are negligible. There is lack of correlation between  $\text{Fe}/(\text{Fe}+\text{Mg})$  and  $\text{Al}^{\text{iv}}$ ,  $\text{Fe}/(\text{Fe}+\text{Mg})$  and  $\text{Al}^{\text{iv}}/\text{Al}_{\text{tot}}$ ,  $\text{Fe}/(\text{Fe}+\text{Mg})$  and  $\text{Si}/\text{Al}_{\text{tot}}$ , and  $\text{Na}+\text{K}+\text{Ca}$  and T2 (Octahedral valency) (Figure 3.3).  $\text{Fe}/(\text{Fe}+\text{Mg})$  ratios fall within the range 0.45–0.58, whereas  $\text{Al}^{\text{iv}}$  ranges from 1.94 to 2.57 a.p.f.u (atoms per formula unit). According to the classification of Hey (1954), two compositional chlorite types were identified; ripidolite and pycnochlorite (Figure 3.4). With respect to the AIPEA (Association Internationale Pour l'Étude des Argiles) nomenclature of Bayliss (1975) for trioctahedral chlorites as recommended by Bailey (1980), ripidolite and pycnochlorite would be classed as ferroan clinochlore.

#### *Chlorite thermometry*

The variation of  $\text{Al}^{\text{iv}}$  and  $\text{Fe}+\text{Mg}$  content of chlorite with temperature has been widely documented (Cathelineau and Nieva, 1985; Kranidiotis and MacLean, 1987; Cathelineau, 1988; Zang and Fyfe, 1995). Ideas have evolved since the work of McDowell and Elders (1980), who were probably the first to report such compositional relationships with temperature of formation of chlorite, while studying the progressive diagenetic changes that occurred in sheet silicate minerals in the geothermal systems of the Salton Trough of southern California. Cathelineau and Nieva (1985) furthered this concept by developing a chlorite solid-solution geothermometer, based on their investigations of the relationship between chlorite composition and formation temperature in the geothermal systems of Los Azufres in Mexico. They found that the temperature of chlorite formation correlated strongly with  $\text{Al}^{\text{iv}}$  content and very weakly with  $\text{Al}^{\text{vi}}$ . They defined the relationship

between temperature and  $\text{Al}^{\text{iv}}$  by least square regression. This relationship was redefined by Cathelineau (1988) according to equation 1 (page 66).

However,  $\text{Al}^{\text{iv}}$  increases with increase in  $\text{Fe}/(\text{Fe}+\text{Mg})$ , and in the study of Cathelineau (1988) the  $\text{Fe}/(\text{Fe}+\text{Mg})$  values for the studied chlorite range from 0.27 to 0.38. This means that for chlorite formed under the same conditions with higher  $\text{Fe}/(\text{Fe}+\text{Mg})$ ,  $\text{Al}^{\text{iv}}$  will be higher, and so will be the calculated temperatures of formation.

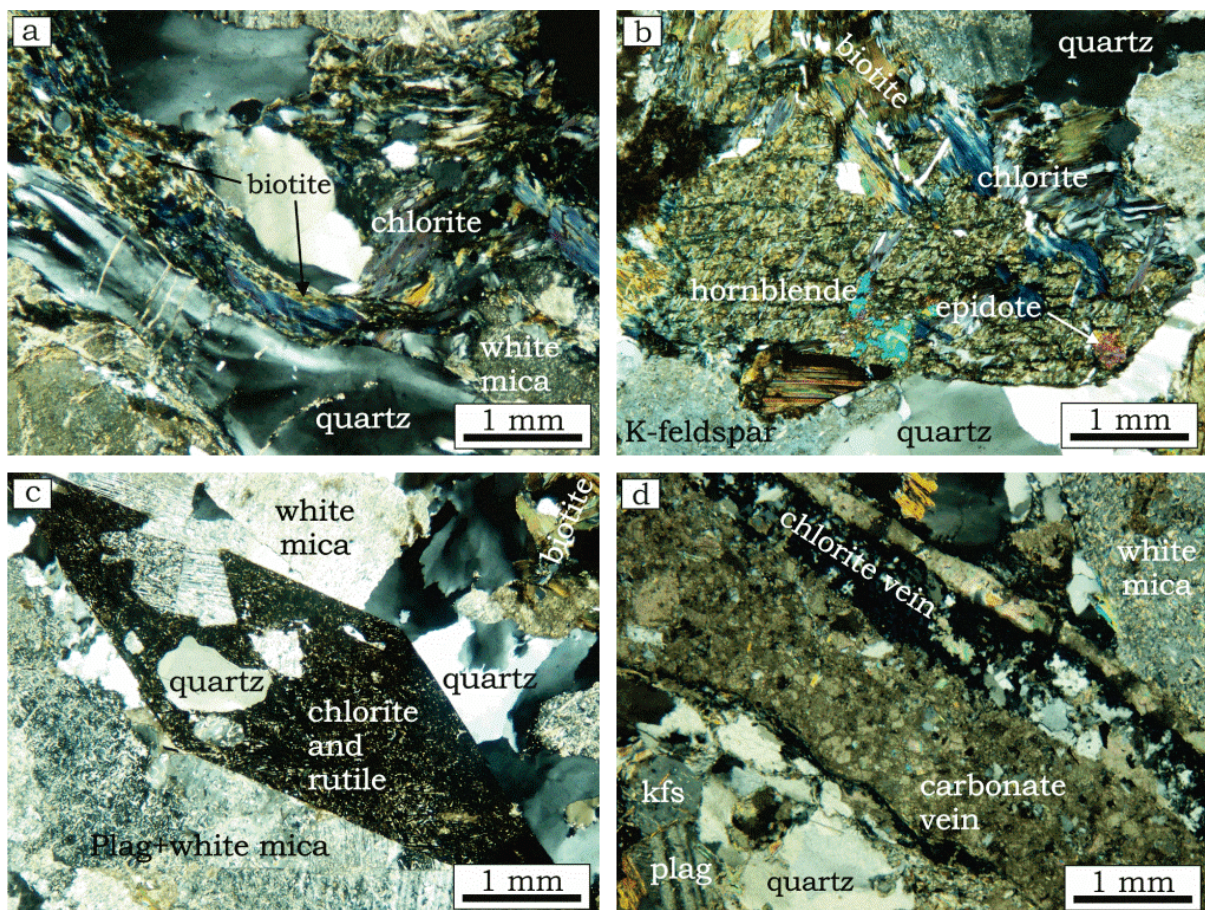


**Figure 3.2:** Transmitted-light photomicrographs (crossed nicols), showing textures in hydrothermal chlorite. **(a)** Chlorite formed by the hydrothermal alteration of biotite, intergrown with hydrothermal quartz ribbons and white mica. **(b)** Hornblende crystal partially altered to chlorite, intergrown with partially altered biotite, K-feldspar and quartz. **(c)** Fine-grained chlorite and rutile pseudomorphically replacing a titanite-like crystal. **(d)** Fine-grained chlorite within carbonate vein. kfs: K-feldspar; plag: plagioclase.

### CHAPTER 3: HYDROTHERMAL ALTERATION

**Table 3.1:** Representative electron-microprobe analyses of chlorite from altered wall-rock at Batouri. Fluorine and chlorine were sought for, but were below the detection limit of 0.03 wt %. Shaded columns are for analyses of chlorite from the distal zone of the wall-rock. General formula for chlorite =  $[R^{2+}, R^{3+}]_{12}^{vi} [Si_{8-x} R_x^{3+}]^{iv} O_{20} (OH)_{16}$ , Where  $R^{2+}$ =Mg, Fe, Mn, Ti, Ni, Zn;  $R^{3+}$ =Al,Fe,Cr; and x (generally) ~ 1-3. FeO represents total iron content.

	1/1	2/1	3/1	4/1	5/1	6/1	7/1	8/1	9/1	10/1
SiO <sub>2</sub> (wt %)	26.64	26.78	28.38	26.44	26.02	25.72	26.98	26.95	26.28	27.06
TiO <sub>2</sub> (wt %)	0.09	0.12	0.17	0.14	0.28	0.21	0.06	0.08	0.09	0.06
Al <sub>2</sub> O <sub>3</sub> (wt %)	20.45	19.68	18.22	19.65	19.71	20.53	20.49	20.18	20.04	20.71
FeO (wt %)	24.62	26.36	26.64	28.16	28.35	27.93	25.09	24.27	26.55	24.03
MnO (wt %)	0.37	0.24	0.24	0.19	0.11	0.16	0.18	0.37	0.29	0.37
MgO (wt %)	15.96	14.93	14.52	13.82	13.91	13.83	14.55	15.77	14.83	16.38
CaO (wt %)	<0.03	0.05	0.14	0.06	0.06	0.05	0.18	0.06	0.04	<0.03
Na <sub>2</sub> O (wt %)	<0.04	0.06	0.06	<0.04	0.07	0.04	0.04	0.05	0.06	<0.04
K <sub>2</sub> O (wt %)	0.08	0.18	0.11	0.11	0.07	0.18	0.21	0.27	0.15	0.05
Cl (wt %)	<0.03	0.03	<0.03	<0.03	<0.03	<0.03	<0.03	<0.03	<0.03	<0.03
F (wt %)	<0.03	<0.03	<0.03	<0.03	<0.03	<0.03	<0.03	<0.03	<0.03	<0.03
<b>TOTAL (wt %)</b>	<b>87.58</b>	<b>87.77</b>	<b>87.84</b>	<b>87.95</b>	<b>87.95</b>	<b>88.03</b>	<b>87.14</b>	<b>87.36</b>	<b>87.70</b>	<b>88.07</b>
O=F, Cl	-	0.01	-	-	-	-	-	-	-	-
<b>TOTAL</b>	<b>87.57</b>	<b>87.76</b>	<b>87.84</b>	<b>87.94</b>	<b>87.95</b>	<b>88.03</b>	<b>87.14</b>	<b>87.36</b>	<b>87.69</b>	<b>88.06</b>
T2	12.52	12.62	12.59	12.72	12.74	12.71	12.60	12.54	12.66	12.39
No Anions	28.00	28.00	28.00	28.00	28.00	28.00	28.00	28.00	28.00	28.00
<b>Formula based on 28 oxygens</b>										
Si	5.55	5.63	5.95	5.60	5.52	5.44	5.66	5.63	5.54	5.58
Ti	0.01	0.02	0.03	0.02	0.04	0.03	0.01	0.01	0.01	0.01
Al <sup>iv</sup>	2.45	2.37	2.05	2.40	2.48	2.56	2.34	2.37	2.46	2.42
Al <sup>vi</sup>	2.58	2.50	2.45	2.50	2.44	2.56	2.73	2.59	2.51	2.62
Al <sub>tot</sub>	5.02	4.87	4.50	4.90	4.93	5.12	5.07	4.97	4.98	5.03
Fe <sup>2+</sup>	4.29	4.63	4.67	4.98	5.03	4.94	4.40	4.24	4.68	4.15
Mn	0.06	0.04	0.04	0.03	0.02	0.03	0.03	0.07	0.05	0.06
Mg	4.96	4.68	4.54	4.36	4.40	4.36	4.55	4.91	4.66	5.04
Ca	-	0.01	0.03	0.01	0.01	0.01	0.04	0.01	0.01	-
Na	-	0.02	0.02	-	0.03	0.02	0.02	0.02	0.03	-
K	0.02	0.05	0.03	0.03	0.02	0.05	0.06	0.07	0.04	0.01
Cl	-	0.01	-	-	-	-	-	-	-	-
<b>TOTAL</b>	<b>19.93</b>	<b>19.95</b>	<b>19.80</b>	<b>19.93</b>	<b>19.98</b>	<b>19.98</b>	<b>19.83</b>	<b>19.91</b>	<b>19.98</b>	<b>19.88</b>
Al <sup>iv</sup> <sub>c1</sub>	2.77	2.72	2.41	2.78	2.85	2.93	2.68	2.70	2.81	2.73
Al <sup>iv</sup> <sub>c2</sub>	2.34	2.24	1.91	2.23	2.31	2.39	2.21	2.26	2.32	2.32
*T°C <sub>Cath</sub>	363	351	300	356	369	381	346	351	366	358
**T°C <sub>K&amp;M</sub>	<b>312</b>	<b>307</b>	<b>273</b>	<b>312</b>	<b>321</b>	<b>329</b>	<b>302</b>	<b>304</b>	<b>316</b>	<b>308</b>
***T°C <sub>Z&amp;F</sub>	266	255	220	255	263	272	252	258	264	264
Fe/(Fe+Mg)	0.46	0.50	0.51	0.53	0.53	0.53	0.49	0.46	0.50	0.45
Al <sup>iv</sup> /Al <sub>tot</sub>	0.49	0.49	0.46	0.49	0.50	0.50	0.46	0.48	0.49	0.48
Si/Al <sub>tot</sub>	1.11	1.15	1.32	1.14	1.12	1.06	1.12	1.13	1.11	1.11
Na+K+2Ca	0.02	0.09	0.12	0.06	0.07	0.09	0.15	0.12	0.09	0.03

\*Cathelineau (1988); \*\*Kranidiotis and MacLean (1987); \*\*\* Zang and Fyfe (1995).

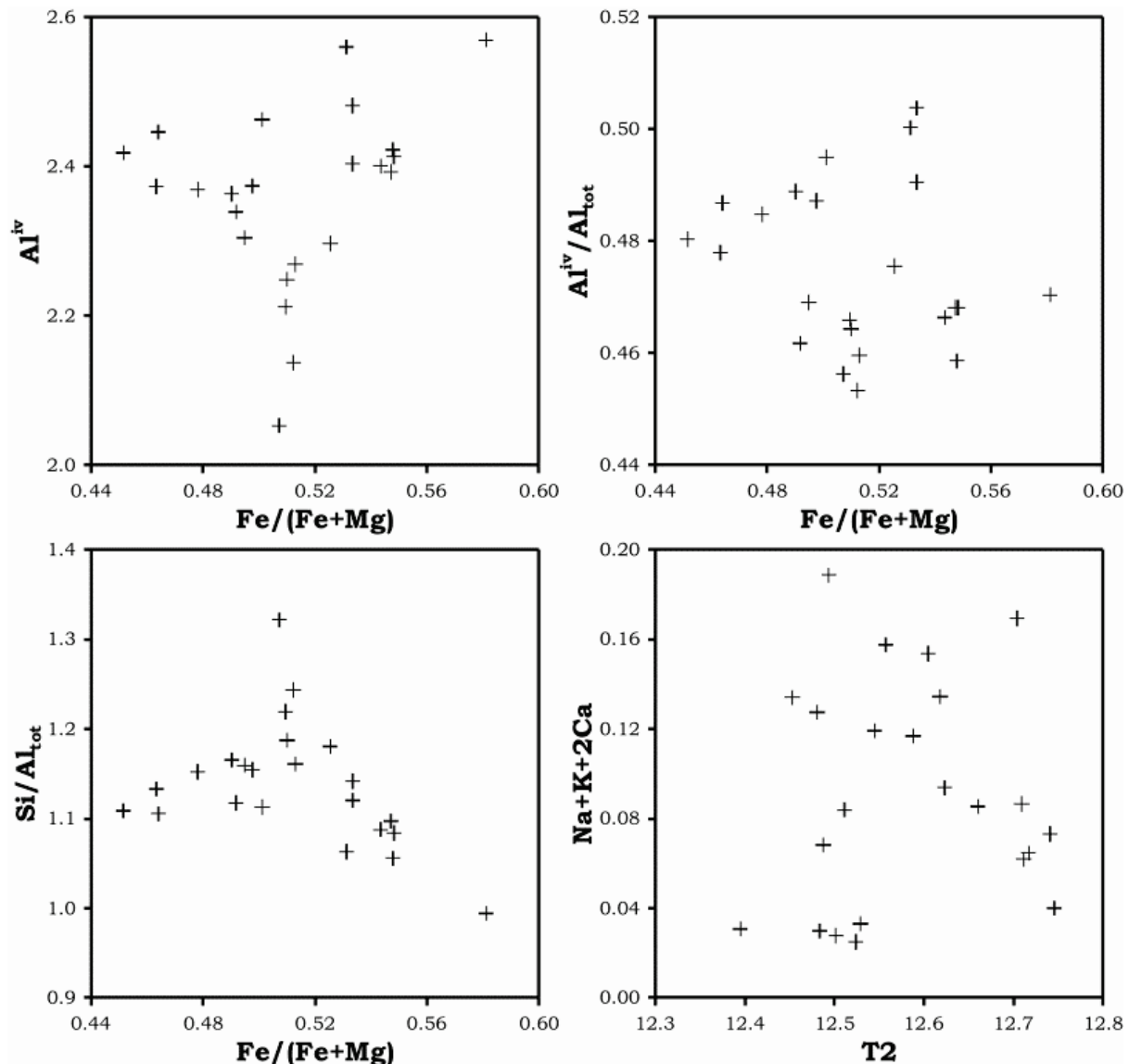


**Figure 3.3:** Bivariate plots of the chemical components of chlorite. No correlation occurs between  $\text{Fe}/(\text{Fe}+\text{Mg})$  and  $\text{Al}^{\text{IV}}$ ,  $\text{Al}^{\text{IV}}/\text{Al}_{\text{tot}}$  and  $\text{Si}/\text{Al}_{\text{tot}}$ , and  $\text{T2}$  (octahedral valency) and  $\text{Na}+\text{K}+2\text{Ca}$ .

In an earlier study, Kranidiotis and MacLean (1987) applied a correction for  $\text{Al}^{\text{IV}}$  referred to here as  $\text{Al}_{\text{c1}}^{\text{IV}}$  (Equation 2) to a re-arranged version of the equation of Cathelineau and Nieva (1985) (Equation 3), for chlorite [ $\text{Fe}/(\text{Fe}+\text{Mg})=0.18-0.64$ ] from the Phelps Dodge massive sulphide deposit in Matagami, Quebec. Zang and Fyfe (1995) applied a different correction for  $\text{Al}^{\text{IV}}$  for hydrothermal chlorite with high  $\text{Fe}/(\text{Fe}+\text{Mg})$  ratios (0.43–0.81), from the Igarapé Bahia gold deposit in Carajás, Brazil. This correction, referred to here as  $\text{Al}_{\text{c2}}^{\text{IV}}$ , is shown in Equation 4.

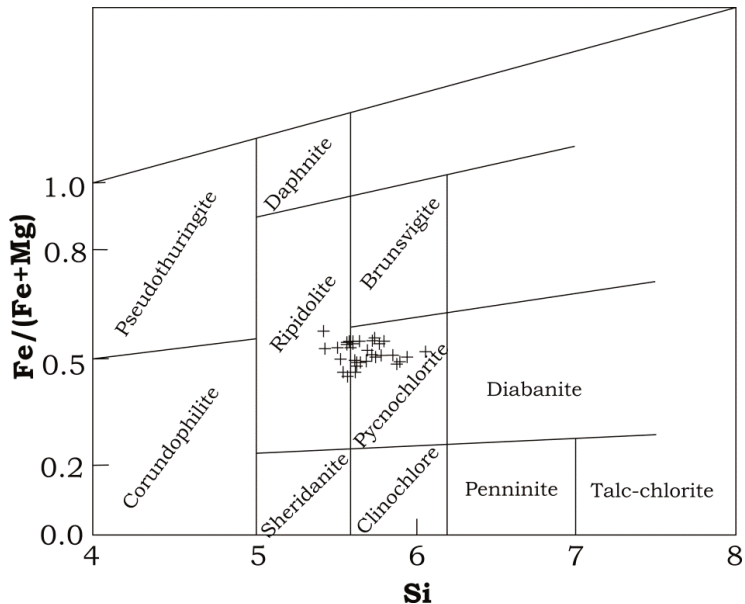


**Figure 3.4:** Composition of chlorite in samples from the altered wall-rock at Kambélé (fields boundaries after Hey, 1954).

$$T[^\circ C] = 106Al_{\frac{IV}{C}} + 18 \dots \dots \dots \dots \dots \dots \dots \dots [3]$$

Klein *et al.* (2007) recommended that the selection of the appropriate geothermometer in any study should be contingent upon the consistency between the Al<sup>iv</sup> and Fe/(Fe+Mg) contents of the chlorite being studied and those of chlorite used in the calibration of the geothermometer. In the case of chlorite from Batouri, the Al<sup>iv</sup>: 2.05–2.57 and Fe/(Fe+Mg): 0.45–0.58 contents fall within the compositional range of chlorites used by Kranidiotis and MacLean (1987). This implies that the calculated temperatures of formation (273–333°C) for chlorite from Batouri using the geothermometer of Kranidiotis and MacLean (1987) represent the best approximation (Table 3.1; Appendix 3a). Fine-grained chlorite from the proximal zone of the wall-

rock yields temperatures from 333 to 312°C, while coarse-grained chlorite from the distal zone yields temperatures from 308 to 273°C (Figure 3.5).

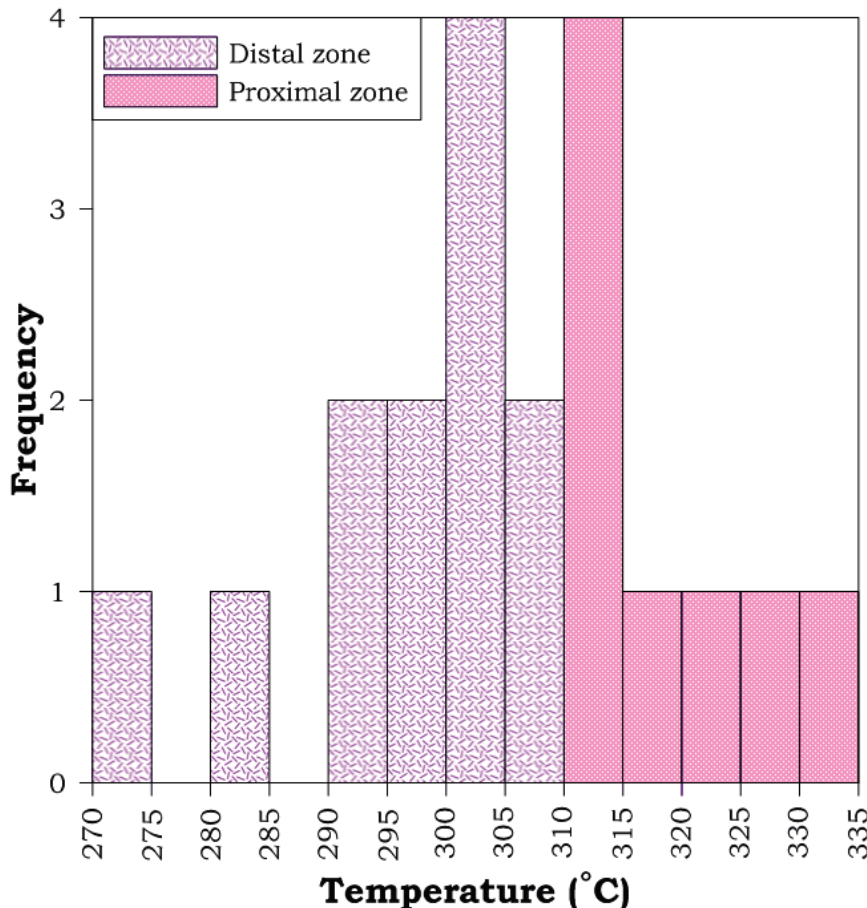


**Figure 3.5:** Histogram showing the estimated formation temperatures of chlorite from the proximal and distal zones of the wallrock. Chlorite from the proximal zone yields higher temperatures of formation than that from the distal zone. This implies that the temperature of formation of chlorite decreased with increasing distance from the vein.

### 3.3.2 Mineral chemistry of white mica

White mica occurs as medium- to fine-grained crystals in intimate association with K-feldspar, plagioclase, biotite, chlorite, quartz, carbonate, rutile and pyrite. Results of electron-microprobe analyses of fresh white mica are shown in Table 3.2 and Appendix 3b, and the results of XRF analyses of samples of white mica used for Ar–Ar dating are shown in Table 3.3. Based on the classification diagram of Deer *et al.* (1992) shown in Figure 3.6, the chemical composition of white mica is intermediate between muscovite and phengite. Correlation between  $(\text{Al}^{\text{iv}} + \text{Al}^{\text{vi}})$  and  $(\text{Si} + \text{Mg}^{2+} + \text{Fe}^{2+})$

## CHAPTER 3: HYDROTHERMAL ALTERATION

yields a negative linear trend as shown in Figure 3.7. Al<sup>vi</sup> occupies 75–95 % of the octahedral site, and in addition to Fe<sup>2+</sup> and Mg<sup>2+</sup>, Ti (up to 0.06 ions per formula unit, apfu) is also present. The other elements present in white mica is Na: 0.03-0.08 apfu.

Drill core samples provided insufficient fresh-rock white mica for Ar-Ar dating of the hydrothermal event. Instead, saprolite white mica was used. The saprolite white mica is weathered (Table 3.3), trending towards ‘eastonite’ composition (Figure 3.6). It is hydrated (~11 wt % LOI), and intergrowth of white mica with other minerals (e.g. goethite and Mn oxides from the supergene zone) should be taken into account in Table 3.3.

### CHAPTER 3: HYDROTHERMAL ALTERATION

**Table 3.2:** Representative electron-microprobe analyses of white mica from altered wall-rock at Batouri. Cl and F were sought for, but were below the detection limit of 0.03 and 0.05 wt %, respectively. FeO represents total iron content. The general formula for mica =  $X_2 Y_{4-6} [Z_8 O_{20}] (OH, F)_4$ , where X is K, Na, or Ca, but could also be Ba, Rb, Cs etc. Y is Al, Mg or Fe, but also Mn, Cr, Ti, Li etc. Z is mainly Si or Al, but could also be  $Fe^{3+}$  and Ti.

	MS_1	MS_2	MS_3	MS_4	MS_5	MS_6	MS_7	MS_8	MS_9	MS_10	MS_11
SiO <sub>2</sub> (wt %)	51.64	50.82	51.05	50.98	50.74	51.05	51.06	50.53	51.74	51.48	52.33
TiO <sub>2</sub> (wt %)	<0.03	<0.03	0.14	0.09	<0.03	<0.03	0.05	0.03	0.04	0.06	<0.03
Al <sub>2</sub> O <sub>3</sub> (wt %)	34.11	34.26	34.05	33.22	33.92	35.54	34.46	33.98	33.48	33.05	33.81
FeO (wt %)	1.93	1.80	3.22	3.59	1.89	1.33	1.91	2.17	2.28	2.34	2.17
MnO (wt %)	<0.05	<0.05	<0.05	<0.05	<0.05	<0.05	<0.05	<0.05	<0.05	<0.05	<0.05
MgO (wt %)	1.30	1.11	1.39	1.51	1.25	0.87	1.27	1.30	1.44	1.58	1.40
CaO (wt %)	<0.03	<0.03	<0.03	<0.03	<0.03	<0.03	<0.03	<0.03	<0.03	<0.03	<0.03
Na <sub>2</sub> O (wt %)	0.19	0.14	0.17	0.22	0.16	0.15	0.16	0.16	0.15	0.21	0.16
K <sub>2</sub> O (wt %)	7.74	8.49	7.29	7.89	7.19	8.30	7.56	7.59	7.52	7.78	6.70
Cl (wt %)	<0.03	<0.03	<0.03	<0.03	<0.03	<0.03	<0.03	<0.03	<0.03	<0.03	<0.03
F (wt %)	<0.05	<0.05	<0.05	<0.05	<0.05	<0.05	<0.05	<0.05	<0.05	<0.05	<0.05
<b>TOTAL (wt %)</b>	<b>96.26</b>	<b>96.01</b>	<b>96.67</b>	<b>96.92</b>	<b>94.56</b>	<b>96.61</b>	<b>95.82</b>	<b>95.12</b>	<b>96.03</b>	<b>95.86</b>	<b>95.93</b>
O=F, Cl	-	-	-	-	-	-	-	-	-	-	-
<b>TOTAL</b>	<b>96.26</b>	<b>96.01</b>	<b>96.67</b>	<b>96.92</b>	<b>94.56</b>	<b>96.61</b>	<b>95.82</b>	<b>95.12</b>	<b>96.03</b>	<b>95.86</b>	<b>95.93</b>
<b>Formula based on 22 oxygens</b>											
Si	6.60	6.54	6.53	6.54	6.58	6.50	6.55	6.54	6.63	6.62	6.66
Al <sup>IV</sup>	1.40	1.46	1.47	1.46	1.42	1.50	1.45	1.46	1.37	1.38	1.34
<b>Sum (Z)</b>	<b>8.00</b>										
Al <sup>VI</sup>	3.73	3.74	3.66	3.57	3.76	3.83	3.75	3.73	3.68	3.64	3.74
Ti	-	-	0.01	0.01	-	-	-	-	-	0.01	-
Fe <sup>2+</sup>	0.21	0.19	0.34	0.39	0.21	0.14	0.20	0.24	0.24	0.25	0.23
Mg	0.25	0.21	0.26	0.29	0.24	0.16	0.24	0.25	0.27	0.30	0.27
<b>Sum (Y)</b>	<b>4.18</b>	<b>4.14</b>	<b>4.28</b>	<b>4.26</b>	<b>4.21</b>	<b>4.14</b>	<b>4.21</b>	<b>4.22</b>	<b>4.20</b>	<b>4.20</b>	<b>4.24</b>
Na	0.05	0.03	0.04	0.05	0.04	0.04	0.04	0.04	0.04	0.05	0.04
K	1.26	1.39	1.19	1.29	1.19	1.35	1.24	1.25	1.23	1.28	1.09
<b>Sum (X)</b>	<b>1.31</b>	<b>1.43</b>	<b>1.23</b>	<b>1.34</b>	<b>1.23</b>	<b>1.39</b>	<b>1.28</b>	<b>1.29</b>	<b>1.27</b>	<b>1.33</b>	<b>1.13</b>
<b>Cations</b>	<b>13.49</b>	<b>13.57</b>	<b>13.51</b>	<b>13.60</b>	<b>13.44</b>	<b>13.52</b>	<b>13.48</b>	<b>13.51</b>	<b>13.47</b>	<b>13.53</b>	<b>13.36</b>
Anions	22.00	22.00	22.00	22.00	22.00	22.00	22.00	22.00	22.00	22.00	22.00
T2	7.67	7.73	7.68	7.71	7.79	7.65	7.70	7.78	7.70	7.73	7.65
Al (tot)	5.13	5.20	5.13	5.03	5.18	5.33	5.21	5.19	5.05	5.01	5.07
Fe+Mg	0.45	0.41	0.61	0.67	0.45	0.31	0.45	0.49	0.52	0.55	0.50

## CHAPTER 3: HYDROTHERMAL ALTERATION

**Table 3.3:** XRF chemical analyses of weathered hydrothermal white mica used for Ar–Ar dating

	MNC1 (Wt%)	Formula		MNC2 (Wt%)	Formula	
SiO <sub>2</sub>	39.89	Si:	6.01	<b>Z=8.0</b>	Si:	5.97
TiO <sub>2</sub>	1.78	Al <sup>IV</sup> :	1.99		Al <sup>IV</sup> :	2.03
Al <sub>2</sub> O <sub>3</sub>	24.55					26.22
FeO	12.31	Al <sup>VI</sup> :	2.37		Al <sup>VI</sup> :	2.60
MnO	0.10	Ti:	0.20		Ti:	0.18
MgO	4.75	Fe:	1.55	<b>Y=5.2</b>	Fe:	1.53
CaO	0.08	Mn:	0.01		Mn:	0.01
Na <sub>2</sub> O	0.03	Mg:	1.07		Mg:	0.88
K <sub>2</sub> O	4.05					3.36
P <sub>2</sub> O <sub>5</sub>	0.07	Ca:	0.01	<b>X=0.80</b>	Ca:	0.01
SO <sub>3</sub>	0.02	Na:	0.01		Na:	0.01
Cl	0.01	K:	0.78		K:	0.64
F	<0.05					<0.05
LOI	10.63					10.98
<b>Total</b>	<b>98.19</b>					<b>98.25</b>

- P<sub>2</sub>O<sub>5</sub>, SO<sub>3</sub>, and Cl are considered as impurities and are ignored in the stoichiometric calculations.
- LOI cannot be used in stoichiometric calculations, hence the formulae were calculated anhydrous.
- Fe originally expressed as ΣFe<sub>2</sub>O<sub>3</sub> is recalculated to FeO by multiplying measured wt % of Fe<sub>2</sub>O<sub>3</sub> by the factor 0.8998.

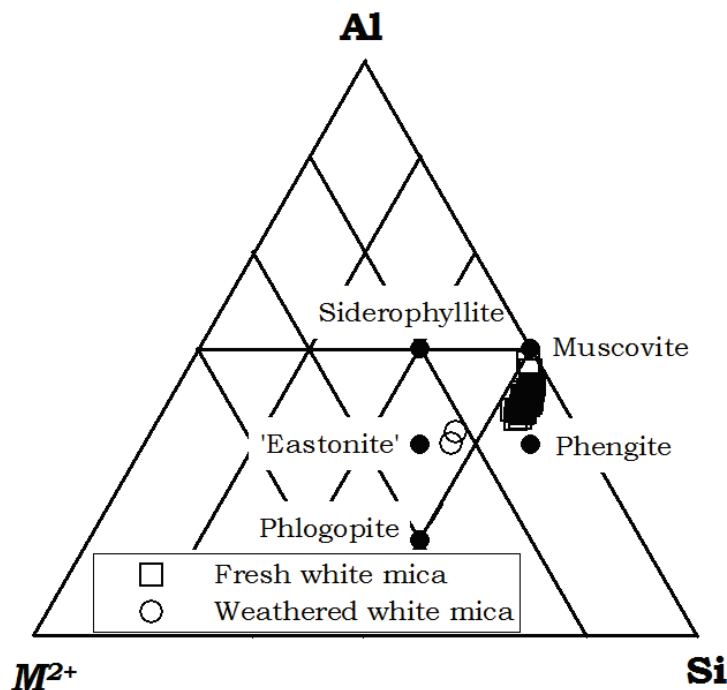


**Figure 3.6:** Composition of white mica from the hydrothermal alteration zones at the Batouri gold prospect. M<sup>2+</sup> is the sum of Fe<sup>2+</sup> and Mg<sup>2+</sup>.

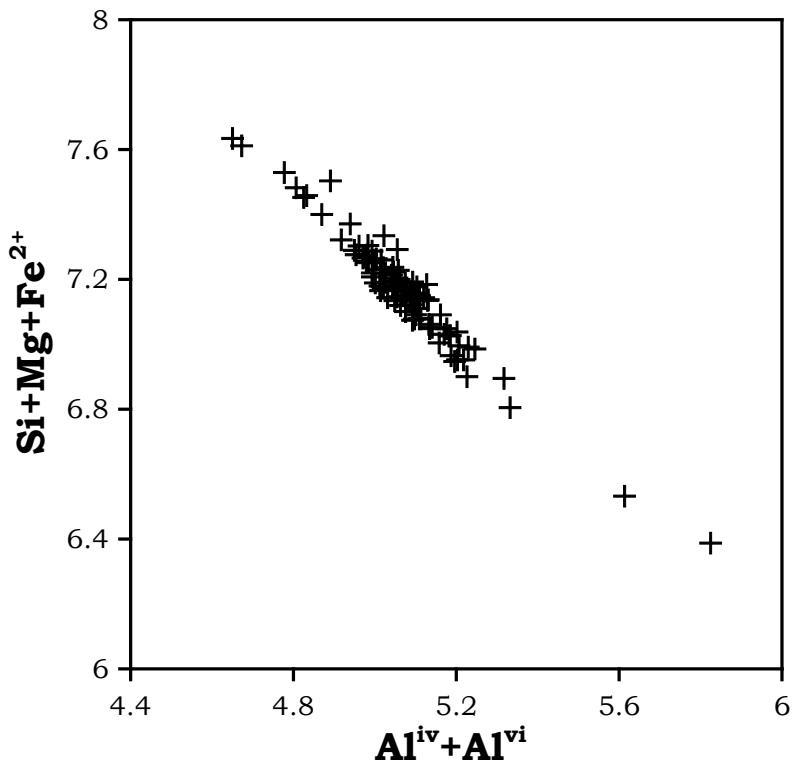


**Figure 3.7:** Correlation plot of  $(\text{Al}^{\text{iv}} + \text{Al}^{\text{vi}})$  and  $(\text{Si} + \text{Mg}^{2+} + \text{Fe}^{2+})$  for hydrothermal white mica (muscovite–phengite) from Batouri.

### 3.3.4 Carbonate mineral chemistry

Carbonate occurs as veins (Figure 3.8), and disseminations in the wall-rock, where it is intimately associated with chlorite, white mica, fluorapatite, rutile, quartz and Fe sulfides. Electron-microprobe analyses of carbonate (Table 3.4; Appendix 3c) reveal two main compositional groups, namely calcite, and Fe–Mg-carbonates (Figure 3.9a). On the ternary diagram of Trdlička and Hoffman (1976), the Fe–Mg-carbonates show a compositional variation from ferroan dolomite to magnesian ankerite (Figure 3.9b). According to Deer *et al.* (1992), ferroan dolomite is carbonate of the Fe–Mg-carbonate series with up to 20 percent of its Mg position filled by  $\text{Fe}^{2+}$ . If the carbonate is richer in ferrous iron and manganese, it is ankerite. Going by this classification, the Fe–Mg-carbonate from Batouri is ankerite. Rhodochrosite ( $\text{MnCO}_3$ ) content of these carbonates does not exceed 2.5 mole percent (Table 3.4; Appendix 3c), with the highest content occurring in calcite.

## CHAPTER 3: HYDROTHERMAL ALTERATION

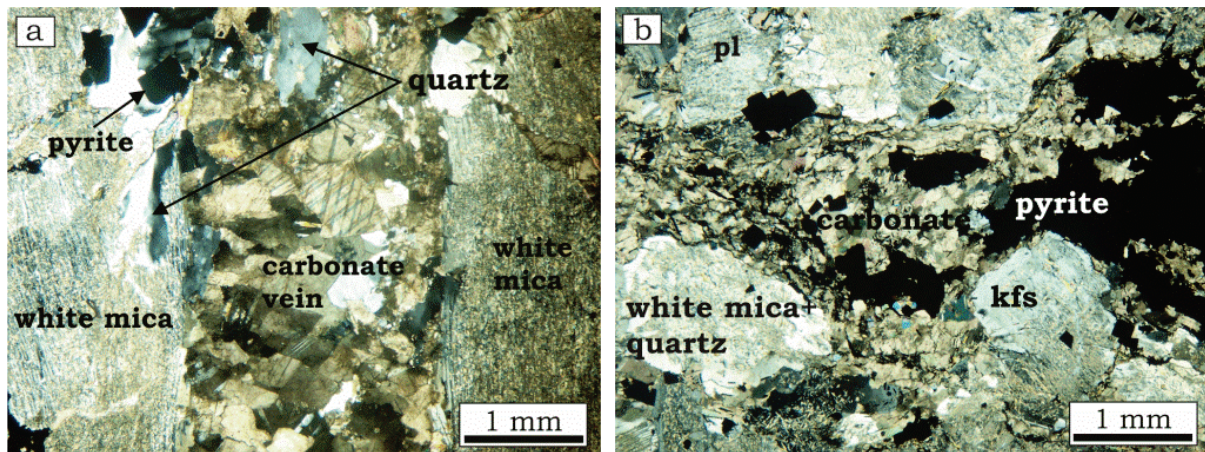


**Figure 3.8:** Transmitted-light photomicrographs (crossed nicols), showing carbonate veins with pyrite and associated hydrothermal quartz and white mica. The carbonate is predominantly ankerite.

**Table 3.4:** Representative electron microprobe analyses of carbonate from quartz-carbonate veins and altered wallrock at Kambélé.

	1 / 1	2 / 1	3 / 1	4 / 1	5 / 1	6 / 1	37 / 1	38 / 1	39 / 1	40 / 1
CaO (wt %)	62.06	59.71	56.01	46.76	58.70	55.38	28.16	28.56	28.48	28.74
MgO (wt %)	0.24	0.26	0.51	1.03	0.51	0.93	10.45	10.26	10.26	10.29
$\Sigma Fe_2O_3$ (wt %)	0.82	0.90	1.67	2.24	1.22	2.19	16.76	17.01	17.27	17.06
MnO (wt %)	1.02	0.95	1.02	0.78	1.12	1.02	0.39	0.34	0.36	0.38
TiO <sub>2</sub> (wt %)	0.09	0.61	<0.04	0.09	0.06	0.13	<0.04	<0.04	<0.04	<0.04
<b>sum (wt %)</b>	<b>64.23</b>	<b>62.43</b>	<b>59.24</b>	<b>50.89</b>	<b>61.60</b>	<b>59.66</b>	<b>55.75</b>	<b>56.19</b>	<b>56.38</b>	<b>56.48</b>
<b>Structural formulae basised on 1 cation per 2 oxygen atoms.</b>										
Ca	0.97	0.96	0.95	0.92	0.95	0.93	0.52	0.51	0.51	0.51
Mg	0.00	0.00	0.01	0.02	0.01	0.02	0.23	0.19	0.18	0.18
Fe	0.01	0.01	0.03	0.04	0.02	0.04	0.24	0.30	0.30	0.31
Mn	0.02	0.02	0.02	0.02	0.02	0.02	0.01	0.01	0.01	0.01
Ti	-	0.01	-	-	-	-	-	-	-	-
CaCO <sub>3</sub>	96.62	95.64	94.55	91.88	95.30	92.84	52.37	50.50	50.82	50.52
MgCO <sub>3</sub>	0.37	0.42	0.86	2.01	0.82	1.56	22.93	18.73	18.25	18.20
FeCO <sub>3</sub>	1.27	1.45	2.82	4.41	1.98	3.67	23.62	30.06	30.27	30.63
MnCO <sub>3</sub>	1.59	1.52	1.72	1.53	1.81	1.71	1.09	0.70	0.60	0.65
<b>Sum</b>	<b>99.85</b>	<b>99.03</b>	<b>99.95</b>	<b>99.83</b>	<b>99.91</b>	<b>99.78</b>	<b>100</b>	<b>100.0</b>	<b>99.94</b>	<b>100.0</b>

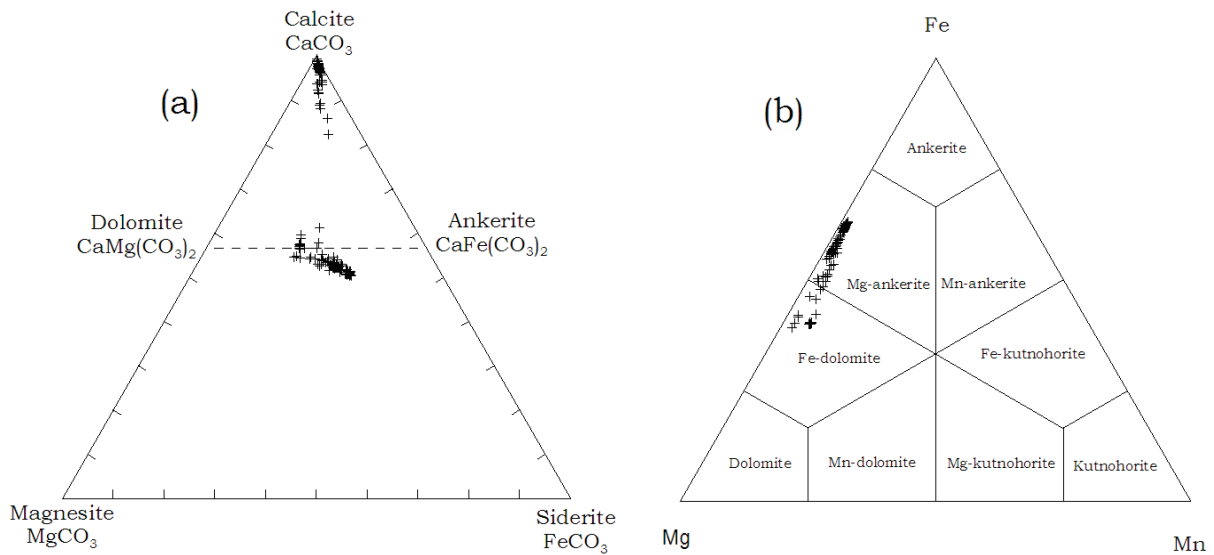


**Figure 3.9:** Classification of carbonates from Batouri. **(a)** Ternary plots of carbonate composition calculated from electron-microprobe analytical data. **(b)**  $\text{MnCO}_3\text{-FeCO}_3\text{-MgCO}_3$  triangular classification diagram of the dolomite group (Trdlicka and Hoffman, 1976).

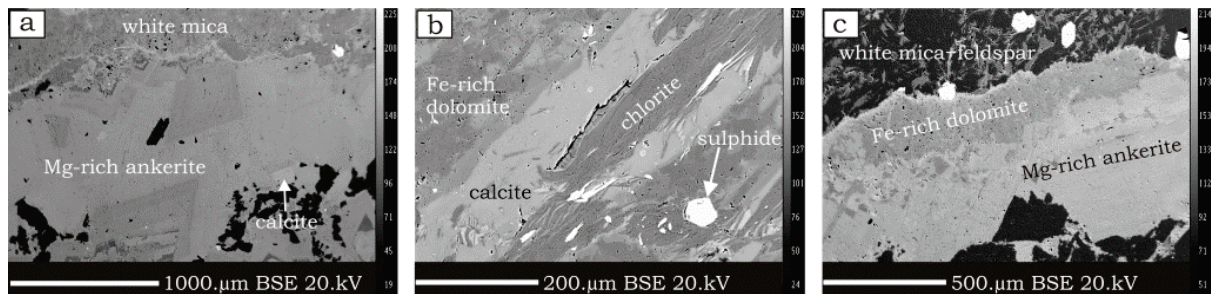


**Figure 3.10:** Back-scattered electron images showing microtextures in carbonates **(a)** Mg-rich ankerite vein with inclusions of subhedral calcite crystals. **(b)** Calcite and Fe-rich dolomite disseminated in wall rock. **(c)** Mg-rich ankerite replaces Fe-rich dolomite.

### 3.3.3 Apatite mineral chemistry

Apatite is a common accessory mineral in the Batouri granitoids, occurring as colourless needles (<50 µm in length) associated with biotite and zircon. It increases in abundance with increasing mafic mineral content of the rocks (observe the negative correlation between  $\text{SiO}_2$  and Zr in Figure 2.10). Hydrothermal apatite occurs abundantly in the distal zone of the altered wall-rock. It occurs as a coarse-grained (up to 1mm) prismatic crystals (Figure 3.11) intergrown with chlorite, sericite, sulfides and carbonate. Electron-microprobe analyses of the apatite (Table 3.5; Appendix 3d) indicates F contents between 2.01 and 2.41 wt % and negligible values of Cl,

## CHAPTER 3: HYDROTHERMAL ALTERATION

which are close to the detection limit of 0.03 wt %. In the ternary diagram (Figure 3.12) the analysed apatite plots in the fluorapatite field.

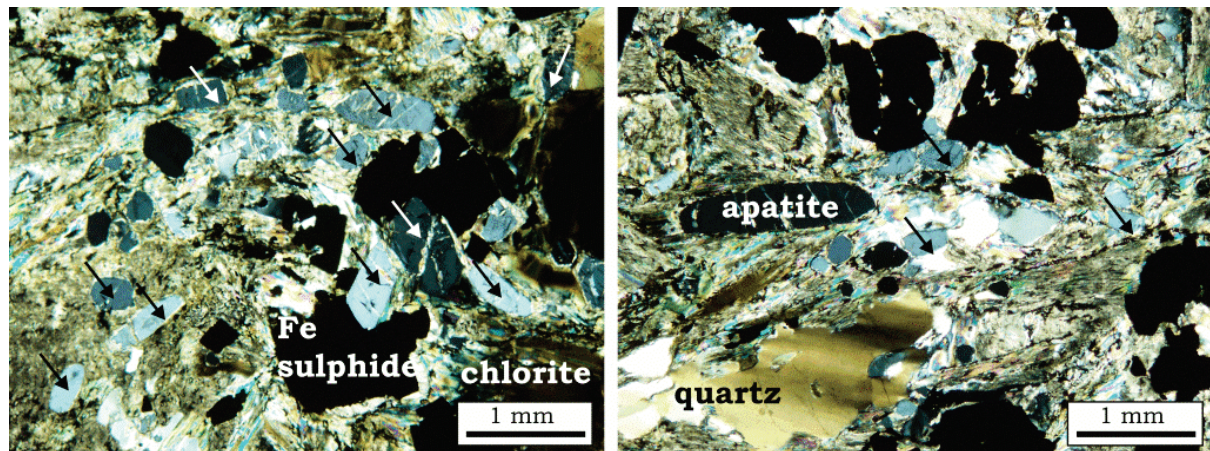


**Figure 3.11:** Transmitted-light photomicrographs (crossed nicols), showing hydrothermal apatite (grey crystals, arrowed) intergrown with carbonate, white mica, chlorite (matrix) and sulfides (opaque minerals).

**Table 3.5:** Representative electron microprobe analyses of hydrothermal apatite from altered wall-rock at Batouri. The formula of the admixture of the most common end-members of fluorite is  $\text{Ca}_{10}(\text{PO}_4)_6(\text{F},\text{OH},\text{Cl},\text{Br})_2$ .

	1/1	2/1	3/1	4/1	5/1	6/1	7/1	8/1	9/1	10/1	11/1
CaO (wt %)	56.77	56.33	56.92	56.00	56.28	56.21	56.13	56.39	56.26	56.20	56.13
MgO (wt %)	<0.03	<0.03	<0.03	<0.03	<0.03	<0.03	<0.03	<0.03	<0.03	<0.03	<0.03
P <sub>2</sub> O <sub>5</sub> (wt %)	41.75	41.65	41.77	41.82	41.47	42.27	42.23	41.63	40.28	40.83	42.49
Cl (wt %)	0.03	<0.03	<0.03	0.03	0.04	0.04	<0.03	0.06	0.06	<0.03	<0.03
F (wt %)	2.20	2.13	2.28	2.23	2.23	2.16	2.35	2.15	2.11	2.12	2.24
<b>TOTAL (wt %)</b>	<b>100.8</b>	<b>100.1</b>	<b>100.9</b>	<b>100.1</b>	<b>100.0</b>	<b>100.7</b>	<b>100.8</b>	<b>100.2</b>	<b>98.71</b>	<b>99.17</b>	<b>100.9</b>
O=F, Cl	0.93	0.90	0.96	0.95	0.95	0.92	0.99	0.92	0.90	0.89	0.94
<b>TOTAL</b>	<b>99.83</b>	<b>99.23</b>	<b>100.0</b>	<b>99.14</b>	<b>99.07</b>	<b>99.78</b>	<b>99.76</b>	<b>99.31</b>	<b>97.81</b>	<b>98.28</b>	<b>99.94</b>
<b>Structural formulae based on 25 O, OH, Cl, F</b>											
Ca	9.96	9.93	9.96	9.86	9.94	9.83	9.81	9.94	10.12	10.04	9.99
P	5.79	5.80	5.78	5.82	5.79	5.84	5.83	5.80	5.72	5.76	5.77
Cl	0.01	-	-	0.01	0.01	0.01	-	0.02	0.02	-	-
F	1.14	1.11	1.18	1.16	1.16	1.12	1.21	1.12	1.12	1.12	1.15
OH	0.85	0.89	0.82	0.83	0.83	0.87	0.78	0.87	0.86	0.88	0.85
<b><math>\Sigma</math></b>	<b>17.74</b>	<b>17.74</b>	<b>17.74</b>	<b>17.68</b>	<b>17.73</b>	<b>17.67</b>	<b>17.62</b>	<b>17.74</b>	<b>17.85</b>	<b>17.79</b>	<b>17.76</b>

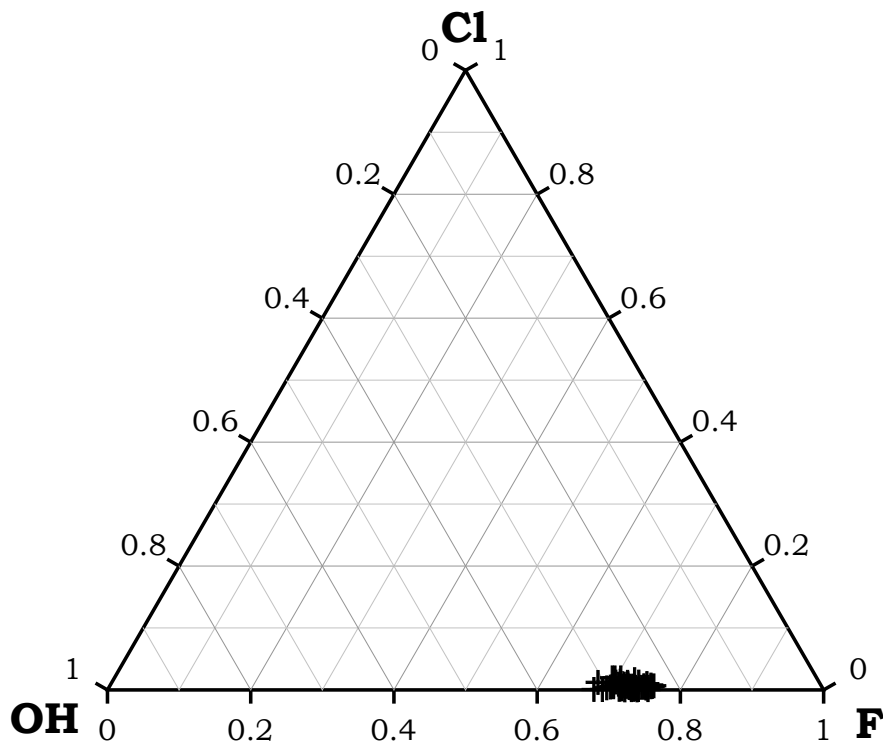


**Figure 3.12:** Ternary plot of the atomic proportions of F, Cl and OH of hydrothermal apatite from the Batouri gold deposit.

### 3.3.5 Iron sulfide minerals

Iron sulfides such as pyrite, chalcopyrite and pyrrhotite are disseminated in the wall-rock. Pyrite is more abundant than chalcopyrite and pyrrhotite, and the abundance of these sulfides diminishes in the distal zone. The sulfides occur in intimate association with magnetite, titano-magnetite, biotite (Figure 3.13a to d), ilmenite, haematite, chlorite and carbonate, and have partially replaced them. In places where pyrite replaced titano-magnetite or ilmenite, aggregates of rutile occur (Figure 3.13d). In the supergene zone, the rutile aggregates occur together with haematite and goethite (Figure 3.13e and f). Bulk chemical analyses of wall-rock samples yield gold contents ranging from 0.4 to 18 ppm (Appendix 2b).

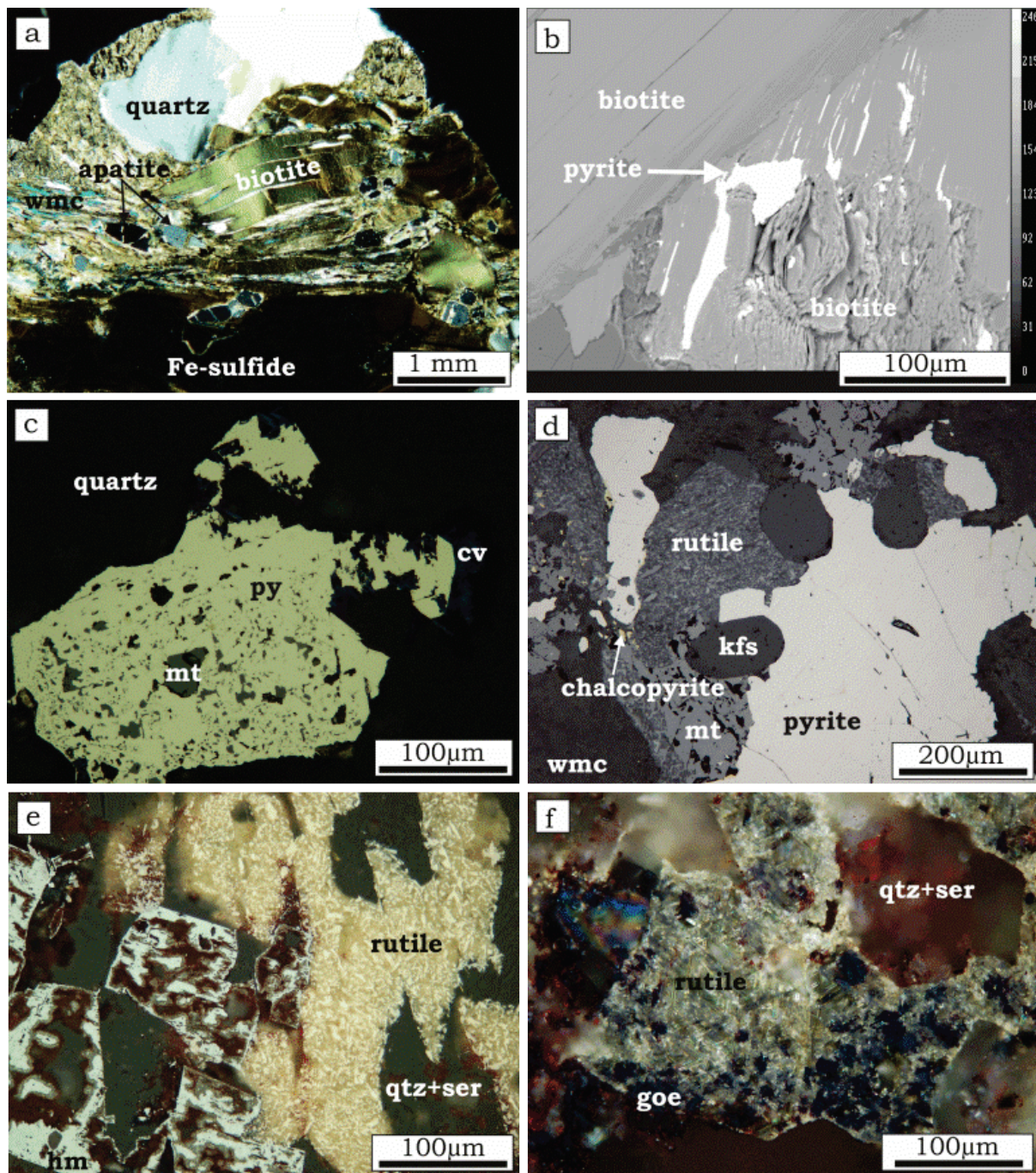


**Figure 3.13:** Transmitted-light photomicrograph (crossed-nicols) (a), back-scattered electron image (b) and reflected-light photomicrographs (plane-polarized) (c to f), showing the replacement of biotite, magnetite and titano-magnetite by iron sulfides. **(a)** Replacement of biotite by Fe-sulfide. **(b)** Replacement of biotite by pyrite. Pyrite replacement proceeds along the cleavage planes. **(c)** Replacement of magnetite (mt) by pyrite (py). **(d)** Replacement of titano-magnetite by pyrite. Rutile (rt) is the by-product of this replacement reaction. The rutile occurs as **(e)** a whitish mass of fine-grained crystals or **(f)** an aggregate of coarse-grained idiomorphic needles, which have assumed the crystal directions of the replaced mineral. Goethite (goe) is formed from the weathering of pyrite. Mineral abbreviations: qtz=quartz, cv=covellite, kfs=K-feldspar, wmc: white mica.

### 3.4 Interpretation and discussion

Quartz, white mica and pyrite dominate the wall-rock alteration mineralogy in the zone proximal to the auriferous quartz veins. This mineral assemblage represents phyllitic (or sericitic) alteration as defined by Meyer and Hemley (1967). In the distal zone, the dominant mineral is chlorite, which is characteristic of propylitic alteration, together with other minerals such as epidote, carbonate and white mica.

#### *Mineral alterations*

In the distal zone, relics of biotite and hornblende within chlorite and epidote indicate that latter minerals formed after the former through hydrolysis or  $H^+$  metasomatism. Chloritisation is also given by the pseudomorphic replacement of titanite-like crystals, which was replaced by fine-grained chlorite and rutile (Figure 3.2c; cf. Morad *et al.*, 2009). Replacements of hornblende by carbonate; biotite by carbonate, white mica and sulfides (Figure 3.13); and plagioclase by white mica and carbonate in the distal zone are indicative of a series reactions, which likely occurred alongside the main chlorite-forming process.

The white mica content increases towards the vein and is abundant in the proximal zone. In this zone, relics of K-feldspar, plagioclase, chlorite and biotite occur within masses of the white mica, indicating that white mica replaced these minerals. The abundance of white mica implies that  $K^+$  metasomatism was the dominant alteration process. The composition of white mica varies between muscovite and phengite (Figure 3.6). This compositional variation can be attributed to substitution of octahedral Al by  $Fe^{2+}$  and  $Mg^{2+}$  (Table 3.2; Appendix 3b). The negative correlation between  $Al^{iv}+Al^{vi}$  and  $Si+Mg^{2+}+Fe^{2+}$  (Figure 3.7), suggests that charge deficiencies resulting from such substitutions are balanced by excess Si in the tetrahedral site (Parry *et al.*, 1984).

Calcite and Mg–Fe-carbonates seem to be in equilibrium in Figure 3.10a. Two types of apatite were identified in the Batouri granitoids: magmatic and hydrothermal apatite. Magmatic apatite occurs as a colourless, fine-grained, euhedral crystal, whereas hydrothermal apatite is grey, coarse-grained and subhedral to euhedral. Experiments conducted by Ayers and Watson (1991) showed that apatite is only soluble in acid solutions. This implies that precipitation of apatite in the proximal zone occurred as a result of increase in solution pH, probably brought about by the buffering effect of wall-rock and carbonate. Fluorine may have been a primary component of the hydrothermal fluid, whereas phosphorus was probably remobilised from the wall-rock by the dissolution of magmatic apatite.

Sulfide minerals are omnipresent in variable amounts in the proximal and distal zones to auriferous quartz veins at Batouri. The presence of gold in the wall-rock at Batouri (0.4–18.5 ppm; Appendix 2b) suggests that wall-rock sulfidation (or desulfidation of the hydrothermal solution) was an important gold-depositing mechanism. This process has been suggested to have played an important role in other lode gold deposits (e.g. Philips 1986 and Dubé *et al.*, 2004).

Another alteration mineral that is closely related to sulfides is rutile (Figure 3.13d), which occurs in various forms ranging from very fine-grained whitish aggregates (Figure 3.13e) to coarse-grained idiomorphic needles (Figure 3.13f), oriented parallel along the crystallographic form of the former mineral (e.g. ilmenite). In the case of rutile, it seems to be a by-product of sulfidation of Fe–Ti oxides.

In conclusion, propylitic alteration (chloritisation) marks the distal wall-rock alteration in Batouri, and was dominated by H<sup>+</sup> metasomatism. The proximal wall-rock alteration is phyllitic (sericitic), where K<sup>+</sup> metasomatism, carbonatization and sulfidation gave rise to white mica, carbonate and sulfide minerals. The sulfide assemblage in the wall-rock has

pyrite, chalcopyrite (Figure 3.13d) and pyrrhotite, with disseminated gold mineralisation in the wall-rock. A schematic of the wall-rock alteration process at Batouri is shown in Figure 3.14.

#### *Chlorite thermometry*

According to Foster (1962), the compositional uniformity of chlorite, the low total alkali ( $\text{Na}_2\text{O}+\text{K}_2\text{O}+\text{CaO}$ ) contents (<0.5 wt %) and the lack of correlation between  $\text{Fe}/(\text{Fe}+\text{Mg})$  and  $\text{Al}^{\text{iv}}$ ,  $\text{Fe}/(\text{Fe}+\text{Mg})$  and  $\text{Al}^{\text{vi}}/\text{Al}_{\text{tot}}$ ,  $\text{Fe}/(\text{Fe}+\text{Mg})$  and  $\text{Si}/\text{Al}$ , and  $\text{Na}+\text{K}+2\text{Ca}$  and  $\text{T2}$  (octahedral valency) (Figure 3.3), all suggest the absence of smectite and/or illite intergrowths within chlorite flakes.

The narrow compositional range of the Batouri chlorite, with  $\text{Fe}/(\text{Fe}+\text{Mg})$  between 0.45 and 0.58 and  $\text{Al}^{\text{iv}}$  in the range of 2.05–2.57 a.p.f.u, suggests that the chlorite is suitable for use in thermometric determinations (e.g. Klein *et al.*, 2007). Based on the chlorite thermometry of Kranidiotis and MacLean (1987), the chlorite shows increasing temperatures of formation from the distal zone (273–308°C) towards the proximal zone (312–333°C; Figure 3.5). However, the reliability of chlorite thermometry based on chlorite composition may be problematic, as the chemistry of chlorite is also influenced by the fluid-to-rock ratio, oxygen and sulfur fugacities, pH, and the compositions of host rock and hydrothermal fluid. All these parameters differ from one hydrothermal system to another (De Caritat *et al.*, 1993; Klein *et al.*, 2007).

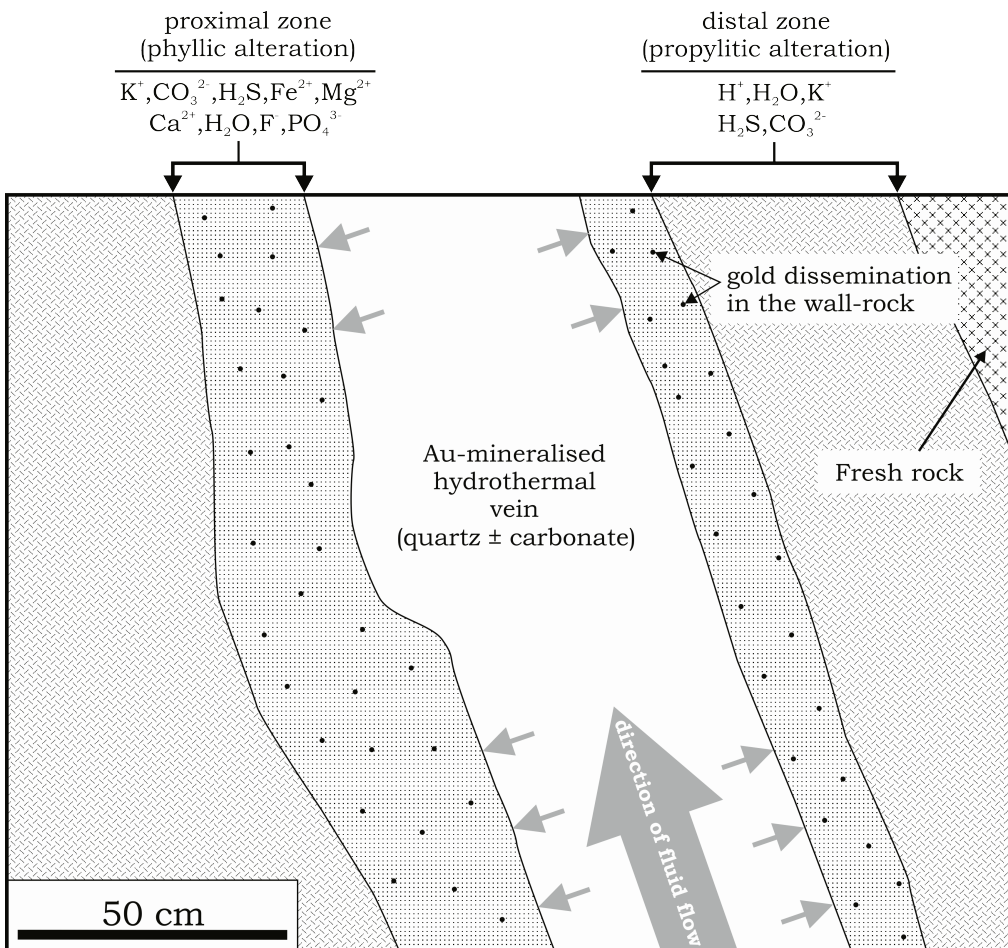


**Figure 3.14:** Schematic of the wall-rock alteration processes at Batouri, showing alteration zones and the ionic inputs that characterise each alteration type. The alteration zones are wider in the footwall than in the hanging wall.

### 3.5 Summary

The two main wall-rock alteration types that define zoning in the alteration halo around gold-mineralised veins at Batouri are phyllitic and propylitic alterations. Propylitic alteration, with the assemblage chlorite–quartz–white mica–epidote–carbonate–sulfide, characterises the distal zone. In the proximal zone of phyllitic alteration, the assemblage white mica–quartz–carbonate–pyrite is typical. The gold in the wall-rock is spatially related to sulphide minerals. Chlorite thermometry indicates that chlorite formed at temperatures ranging from 273 to 333°C.

## **CHAPTER 4: MINERALOGICAL AND PHYSICO-CHEMICAL ASPECTS OF GOLD MINERALISATION**

### **4.1 General description of gold-mineralised veins**

Gold-bearing veins and veinlets occur in a complex network of faults and fractures along regional-scale NE-trending ( $N35^\circ$ ) shear zones, which cut through large granitoid bodies. The spatial relationship between the shear zones and gold mineralisation at Batouri is illustrated in Figure 2.14. Quartz is the dominant vein-forming mineral, with or without carbonate veins. Sulfides make up just about 1–5 % of the veins.

In addition to hydrothermal ore minerals, pre-hydrothermal stage minerals from the wall-rock, such as magnetite, titanomagnetite and ilmenite are also present in the veins. The modes of occurrence of ore minerals in the veins vary from single-grain disseminations to randomly distributed clusters, and concentrations along fractures in laminated quartz.

Laminations in quartz veins are defined by sulfide-bearing or barren foliations along which quartz was fragmented. The foliations are conspicuous in the larger veins at Dimako (~70 cm thick), where they run parallel to the strike direction of the veins and are restricted to the peripheral regions of the veins. Most of the quartz vein samples in this study were collected from veins exposed in pits and trenches at Dem, Bote, Kambélé, Mboscoro, Mongonam and Dimako. Some of these samples are shown in Figure 4.1. A few drill cores from depths between 30 and 100 metres below surface were also studied.

In hand specimen, the quartz veins are massive, laminated or brecciated, and contain small amounts of sulfides and variable sizes of wall-rock fragments. On a microscopic scale, typical microstructures are serrated quartz grains mantled by tiny recrystallised grains (Figure 4.2a and b), bent quartz ribbons (Figure 4.2c) and fluid inclusion trails (Figure 4.2d). Open-space filling texture is absent in these gold-bearing veins.

## CHAPTER 4: GOLD MINERALISATION

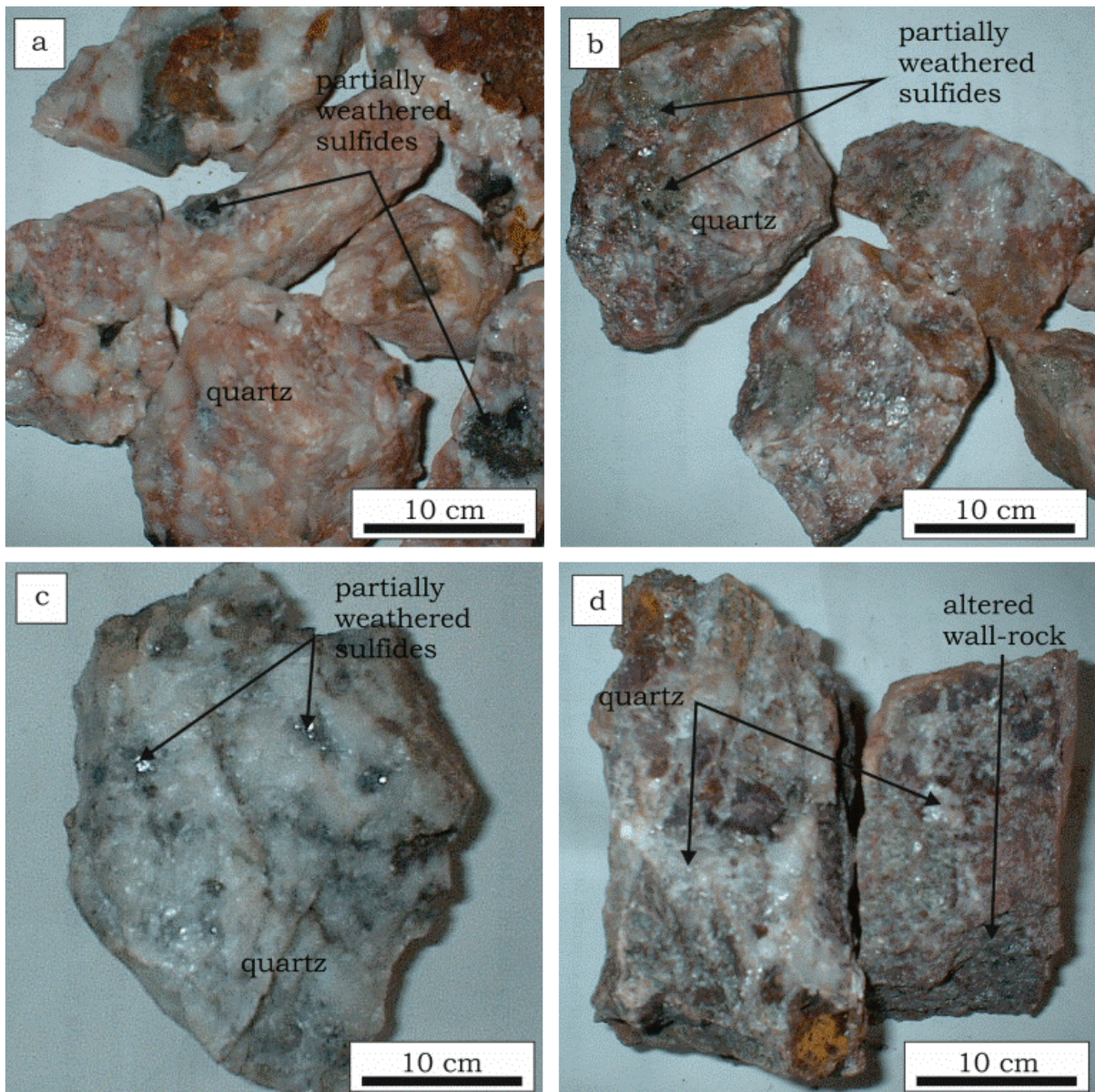


**Figure 4.1:** Quartz samples from gold-bearing veins at Batouri. The dominant sulfide in **(a)** and **(b)** is pyrite, while sphalerite dominates the sulfides in **(c)**. **(d)** Densely veined wall-rock from a proximal zone to a major vein.

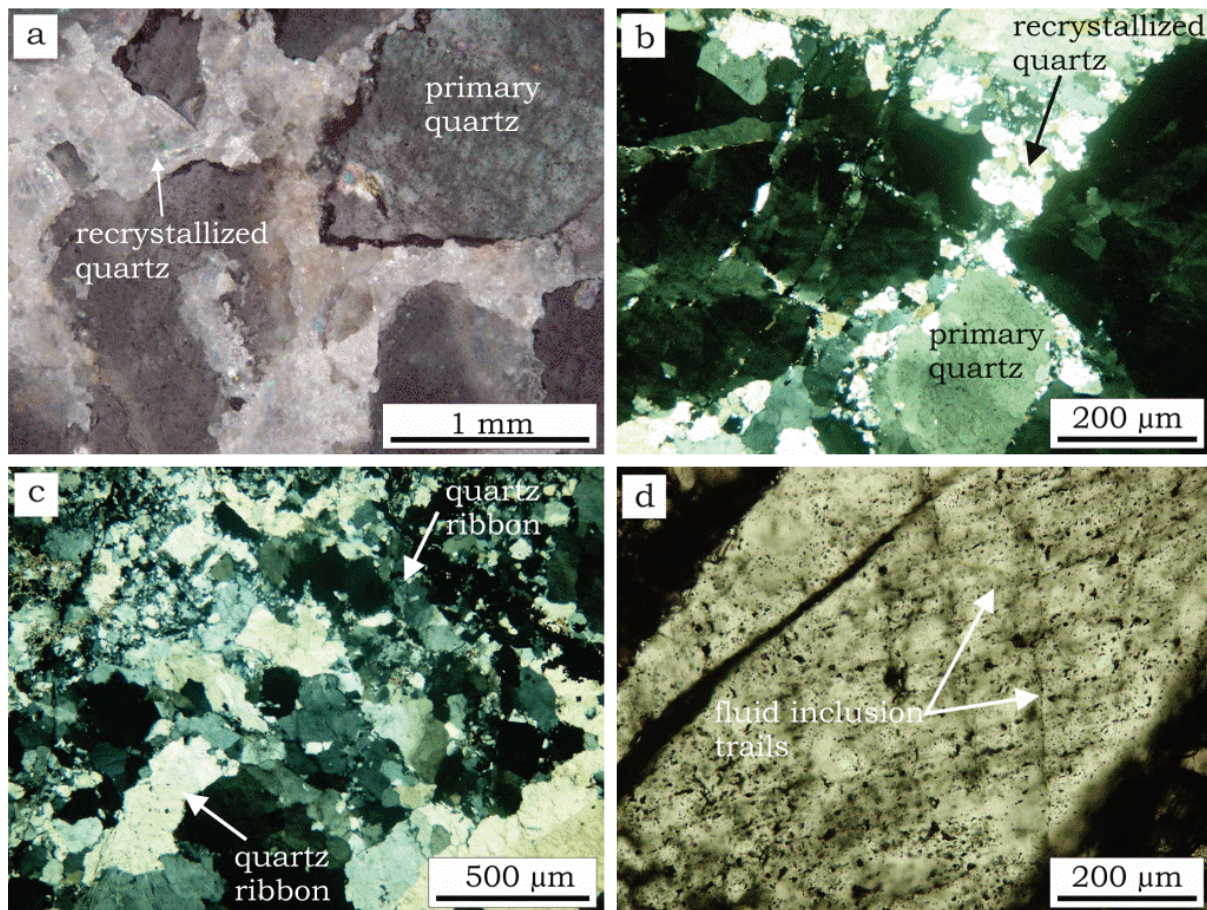


**Figure 4.2:** Reflected- and transmitted-light photomicrographs showing microstructures in quartz from gold-bearing veins. **(a)** Reflected-light photomicrograph (crossed nicols), showing primary and recrystallised quartz, observed in doubly polished thick section. **(b)** Transmitted-light photomicrograph (crossed nicols), showing serrated and recrystallised quartz, observed in thin section. **(c)** Transmitted-light photomicrograph (crossed nicols), showing serrated quartz, sub-grains and quartz ribbons in strongly deformed domain, observed in thin section. **(d)** Transmitted-light photomicrograph (plane-polarized light), showing secondary fluid inclusion trails in quartz, observed in doubly polished thick section.

## 4.2 Ore mineralogy and sulfide chemistry

### 4.2.1 Ore mineralogy

The hydrothermal ore minerals are essentially sulfides, viz: pyrite, sphalerite, arsenopyrite, pyrrhotite, chalcopyrite, galena and tetrahedrite. Besides the sulfides, rutile is the only other hydrothermal ore mineral encountered. Microscopic studies reveal that pyrite, arsenopyrite, sphalerite, and galena are the ore minerals associated with visible gold. Unassociated gold occurs along quartz fractures, as well as quartz grain boundaries. In

weathered samples gold is intergrown with secondary minerals, notably goethite and covellite. Other secondary minerals encountered include bornite, covellite, marcasite, greenockite, psilomelane, and pyrolusite.

Pyrite is the most abundant sulfide mineral at Batouri, and displays textural zoning consisting of a porous core (Figure 4.3a and b). For the purpose of this study, the porous core will be referred to as pyrite I and the overgrowth will be pyrite II (Figure 4.3a to e). In places, pyrite occurs as aggregates of predominantly very tiny regularly-shaped crystals (Figure 4.3f), assumed here to be a separate pyrite phase and designated as pyrite III.

Pyrite I is highly fractured and occurs as inclusions in Pyrite II, or as isolated subhedral grains, sometimes with numerous cavities (Figure 4.3a, b and c). In places, these cavities are occupied by chalcopyrite, pyrrhotite, galena, gold, and covellite. Pyrite II occurs as subhedral to euhedral crystals (Figure 4.3d), varying in size from a few micrometres to ~1 cm. It also contains cavities but these cavities are not as abundant as in pyrite I. The cavities are also occupied by chalcopyrite, pyrrhotite, covellite (Figure 4.3e), galena and Au. Pyrite II co-exists with arsenopyrite (Figure 4.4a and b). Arsenopyrite has no inclusions and occurs as subhedral crystals, varying in size from 20 µm to 1 mm. Also in close association with pyrite II are chalcopyrite and pyrrhotite.

In many places, chalcopyrite and pyrrhotite cross-cut pyrite II, partly replacing it along fractures and cavities (Figures 4.3e and 4.4c). Chalcopyrite also occurs as an inclusion in sphalerite (Figure 4.5a). Pyrrhotite has the tendency to form large euhedral grains that reach sizes of up to 1 cm. These grains of pyrrhotite enclose pyrite II and chalcopyrite (Figure 4.4d). Pyrrhotite co-exists with chalcopyrite in pyrite II cavities (Figure 4.3e). It also occurs as an inclusion in sphalerite. The pyrrhotite content increases with depth.

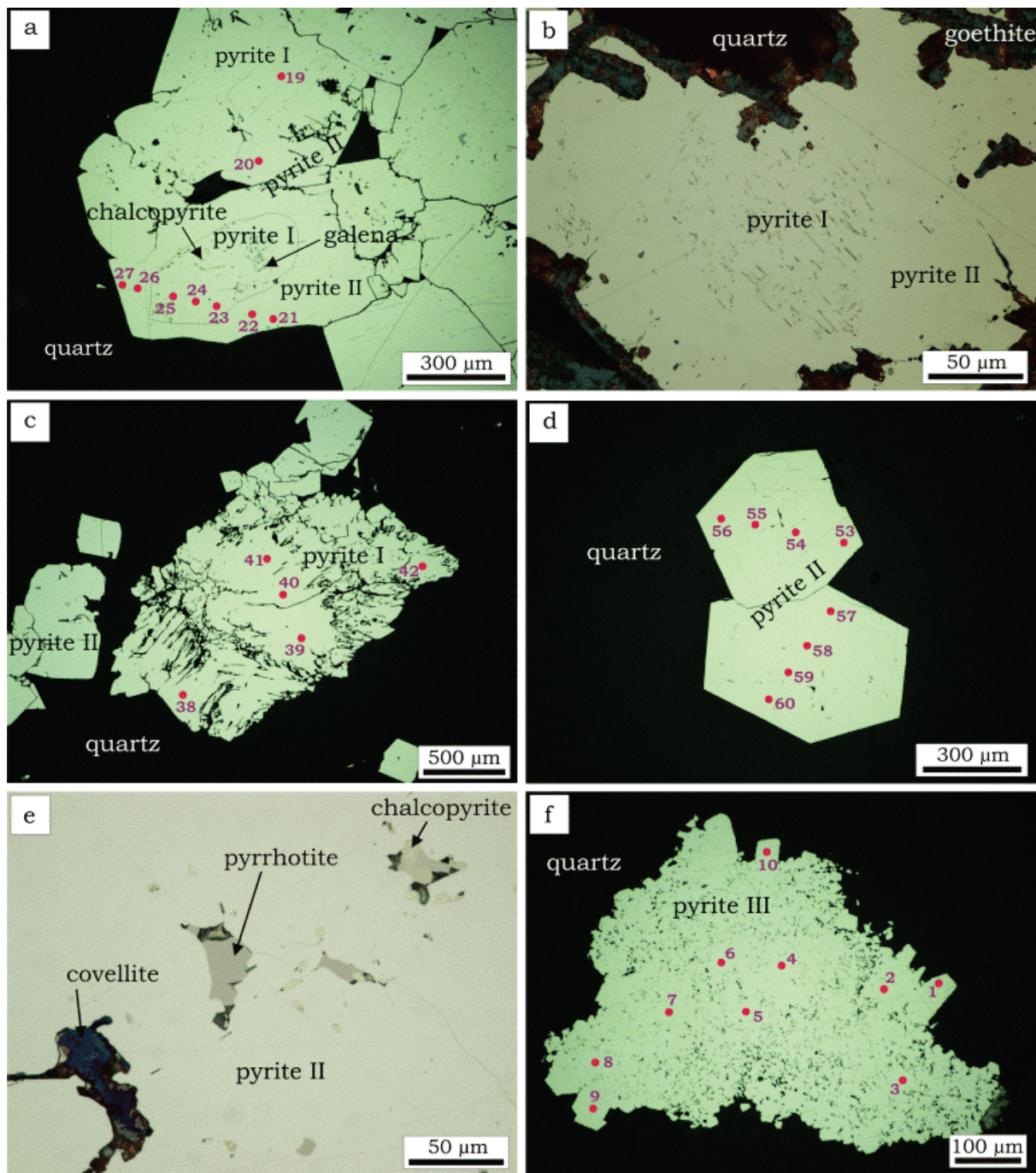


**Figure 4.3:** Reflected-light photomicrographs (plane-polarized light), showing modes of occurrence of pyrite associated with gold mineralisation at Batouri. **(a)** and **(b)** Textural zoning in pyrite, with pyrite II overgrowths on pyrite I. **(c)** A grain of highly fractured pyrite I. **(d)** Euhedral crystals of pyrite II. **(e)** Cavities in pyrite II occupied by younger chalcopyrite, pyrrhotite and covellite. **(f)** Aggregate of predominantly very fine-grained pyrite, here termed pyrite III. Red dots are locations of LA-ICP-MS analyses; the number labels correspond to the LA-ICP-MS data in Appendix 5.

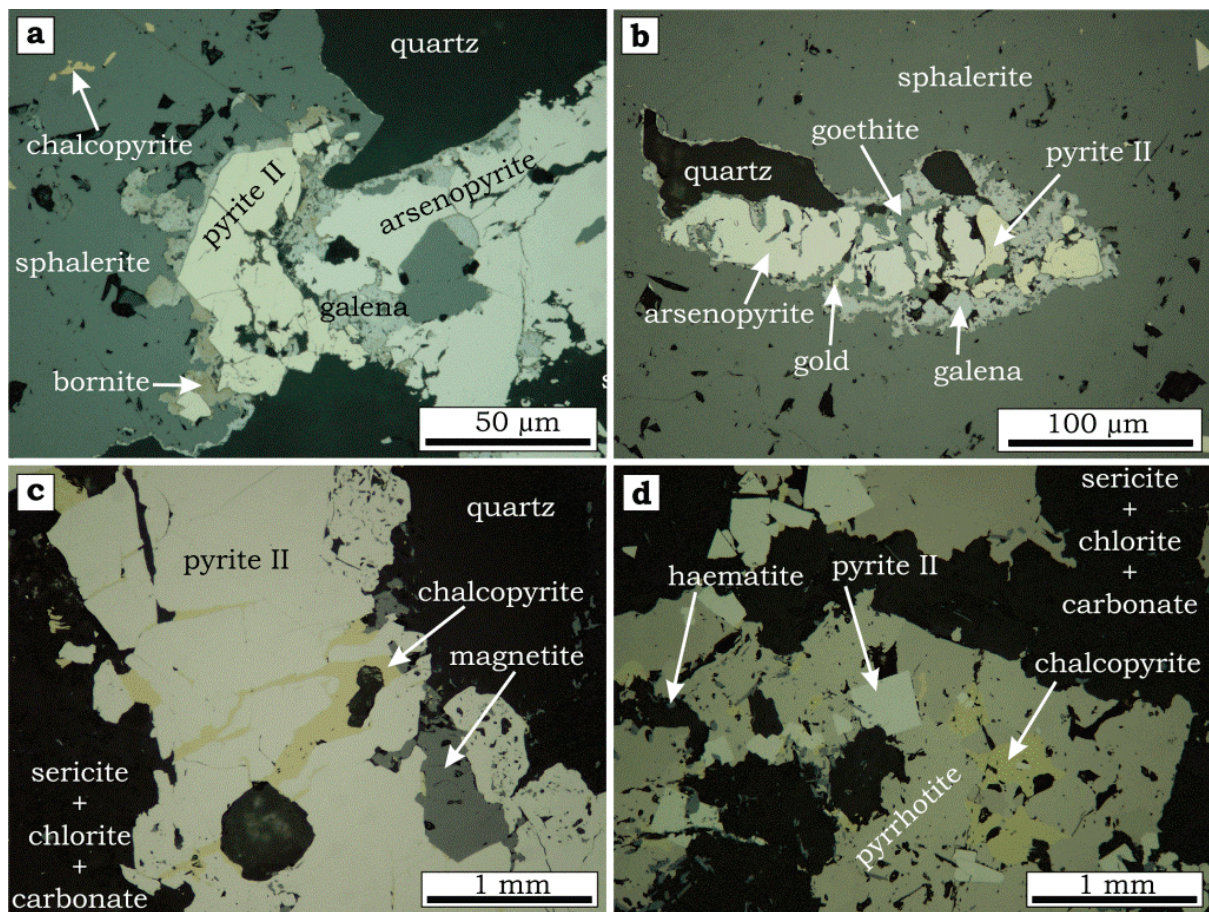


**Figure 4.4:** Reflected-light photomicrographs (plane-polarized light), showing textures in second-generation sulfides. **(a and b)** Intergrowth between arsenopyrite and pyrite II. The nature of the association between arsenopyrite and pyrite II does not indicate the order of deposition. **(c)** Fractures in pyrite II are healed by chalcopyrite. Pyrite II in this sample is secondary after magnetite. **(d)** Pyrrhotite overgrowths on pyrite II and chalcopyrite.

Pyrite III belongs to the last recognisable generation of hydrothermal ore minerals, which is dominated by base-metal sulfides such as sphalerite, galena, chalcopyrite and tetrahedrite. Sphalerite is the next abundant sulfide after pyrite in these veins. Sphalerite is subhedral, with a grain size that reaches ~1cm. It contains inclusions of arsenopyrite, pyrite II, chalcopyrite, pyrrhotite (Figure 4.5a), tetrahedrite, haematite (Figure 4.5b) and gold (Figure 4.5c). Gold occurs preferably along contacts of sphalerite with pyrite II or arsenopyrite inclusions. Sphalerite is replaced by galena (Figure 4.5d). Galena occupies cavities in pyrite I and pyrite II, and co-exists with gold along quartz fractures. A network of very tiny intergranular veinlets of galena occurs in fine-grained chlorite.

Goethite is the most abundant supergene mineral, and commonly replaces minerals such as pyrite, arsenopyrite and pyrrhotite. Greenockite ( $\text{CdS}$ ) occurs along fractures in sphalerite (Figure 4.5a) and along the edges of sphalerite crystals. Bornite and covellite are common replacement minerals of chalcopyrite. Manganese oxides, notably pyrolusite and psilomelane, occur in association with goethite.

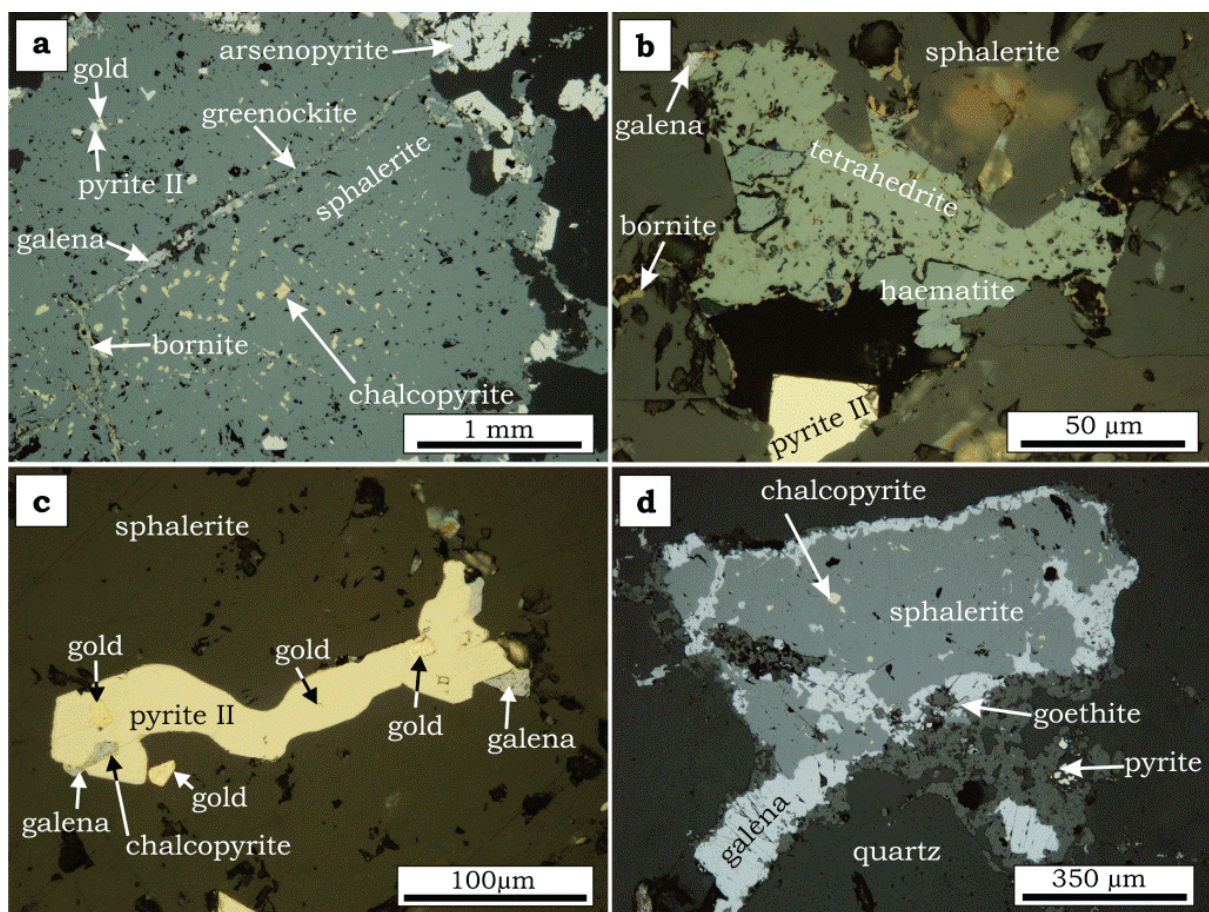


**Figure 4.5:** Reflected-light photomicrographs (plane-polarized light), showing microtextures in third generation sulfides. **(a)** Sphalerite with inclusions of chalcopyrite, pyrite I, arsenopyrite, and gold. Galena as well as greenockite and bornite occupy fractures in sphalerite. **(b)** Tetrahedrite and haematite inclusions in sphalerite. **(c)** Inclusions of Au in pyrite II and along pyrite II-sphalerite contact. **(d)** Peripheral replacement of sphalerite by galena.

#### 4.2.2 Sulfide chemistry

Electron-microprobe analyses were performed on sulfide minerals in order to precisely determine the mineralogy and quantify any chemical zoning, as well as to measure for Au within the ore minerals. The results of

these analyses are shown in Tables 4.1 and 4.2, and Appendix 4a. Figure 4.6 illustrates the compositions of the Fe-sulfides.

These results show that pyrite is composed of 45–47 wt % Fe, 51–54 wt % S, <0.006–1.2 wt % As, <0.01–0.31 wt % Cu, and trace amounts of Ni, Zn, Ag and Au. Based on the electron-microprobe data, the different phases of pyrite (pyrite I, II and III) are apparently chemically uniform. Eventhough the As content of pyrite is relatively high (up to 1.2 wt %), Au is barely detectable ( $\leq 0.01$  wt %). Arsenopyrite has 34–35 wt % Fe, 42–44 wt % As, 20–21 wt % S, and <0.03–1.19 wt % Zn; clearly exhibiting a uniform chemistry, with the same trace-element assemblage found in pyrite and very low Au contents ( $\leq 0.01$  wt %). A single spot analysis was performed on pyrrhotite, which gave the following composition: 58 wt % Fe, 39 wt % S, 0.21 wt % As, and 0.03 wt % Ag.

Sphalerite has 61–62 wt % Zn, 32–33 wt % S, 2.6–3.5 wt % Fe, 1.2–1.4 wt % Cd, <0.006–0.090 wt % As, and <0.01–0.90 wt % Cu, while chalcopyrite exhibits a composition consisting of 21–29 wt % Fe, 34–35 wt % S, 24–34 wt % Cu, <0.03–18 wt % Zn, <0.006–0.13 wt % As, and <0.006–0.04 wt % Ag. All chalcopyrite analysed in this study occurred as inclusions in sphalerite, and they display high Zn content. The composition of galena is 84–86 wt % Pb, 13–19 wt % S, 0.5–1.4 wt % Zn, and <0.006–0.09 wt %.

Two secondary sulfide minerals were also analysed: greenockite and covellite. The surface of bornite was too rough to analyse. The composition of greenockite is 73–75 wt % Cd, 21–22 wt % S, 1.8–2.2 wt % Zn, 0.10–0.15 wt % As, 0.02–0.06 wt % Cu, 0.03–0.04 wt % Ag, and covellite contains 64–69 wt % Cu, 23–33 wt % S, 0.3–4.3 wt % Fe, 0.04–0.06 wt % Zn, and 0.01–0.19 wt % Ag.

Due to the high detection limit of the electron-microprobe technique for most trace elements, the results barely indicate the presence of Au and other trace elements in pyrite and arsenopyrite. This, therefore, necessitated further micro-analyses of pyrite and arsenopyrite using the LA-ICP-MS

## CHAPTER 4: GOLD MINERALISATION

technique, which has much lower detection limits for Au and other trace elements. The complete results of these analyses are shown in Table 4.3 and Appendix 5. The absolute concentration values for Co, Cu, As, Ag and Sb were not determined as there were no reference materials of these elements in the laboratory. Hence they are expressed as counts per second (cps).

**Table 4.1:** Partial results of electron microprobe analyses of pyrite, arsenopyrite, chalcopyrite and pyrrhotite (Po).

	Pyrite				Arsenopyrite				Chalcopyrite			Po 106
	27	28	29	30	85	86	87	88	103	104	105	
Weight %												
Fe	47.31	47.13	47.06	47.12	35.11	35.01	34.71	34.96	28.91	29.14	21.73	58.60
S	53.21	53.48	53.50	53.43	20.88	20.59	20.29	20.94	34.88	34.75	35.23	39.05
As	0.31	0.12	0.00	0.02	43.40	44.13	44.18	43.15	<0.006	0.13	0.11	0.21
Ni	<0.02	<0.02	<0.02	<0.02	<0.02	<0.02	<0.02	<0.02	<0.02	<0.02	<0.02	<0.02
Cu	0.01	0.07	0.05	0.03	0.01	<0.01	0.01	0.01	33.61	34.59	24.27	<0.01
Zn	<0.03	<0.03	<0.03	<0.03	0.05	0.25	<0.03	<0.03	1.63	<0.03	18.80	<0.03
Ag	0.04	0.05	0.05	0.04	0.03	0.02	0.02	0.02	0.02	0.02	0.04	0.03
Au	0.01	0.01	0.01	0.01	<0.004	<0.004	0.01	0.01	<0.004	<0.004	<0.004	<0.004
<b>Sum</b>	<b>100.9</b>	<b>100.9</b>	<b>100.7</b>	<b>100.7</b>	<b>99.5</b>	<b>100.0</b>	<b>99.2</b>	<b>99.1</b>	<b>99.1</b>	<b>98.7</b>	<b>100.2</b>	<b>97.9</b>
Atomic %												
Fe	33.7	33.6	33.5	33.6	33.8	33.7	33.7	33.74	24.0	24.2	18.0	46.2
S	66.1	66.3	66.4	66.4	35.0	34.5	34.3	35.21	50.4	50.4	50.9	53.6
As	0.17	0.07	0.00	0.01	31.1	31.6	32.0	31.04	-	0.08	0.07	0.13
Cu	0.01	0.04	0.03	0.02	0.01	-	0.01	-	24.5	25.3	17.7	-
Zn	-	-	-	-	0.04	0.20	-	-	1.16	0.02	13.3	-
Ag	0.02	0.02	0.02	0.02	0.01	0.01	0.01	0.01	0.01	0.01	0.02	0.01
<b>Sum</b>	<b>100</b>	<b>100</b>	<b>100</b>	<b>100</b>	<b>100</b>	<b>100</b>	<b>100</b>	<b>100</b>	<b>100</b>	<b>100</b>	<b>100</b>	<b>100</b>
Formula												
Fe	1.01	1.01	1.01	1.01	1.01	1.01	1.01	1.01	0.72	0.73	0.54	1.39
S	1.98	1.99	1.99	1.99	1.05	1.03	1.03	1.06	1.51	1.51	1.53	1.61
As	-	-	-	-	0.93	0.95	0.96	0.93	-	-	-	-
Cu	-	-	-	-	-	-	-	-	0.73	0.76	0.53	-
Zn	-	-	-	-	-	0.01	-	-	0.03	0.00	0.40	-
<b>Sum apfu</b>	<b>3.00</b>	<b>3.00</b>	<b>3.00</b>	<b>3.00</b>	<b>3.00</b>	<b>3.00</b>	<b>3.00</b>	<b>3.00</b>	<b>3.00</b>	<b>3.00</b>	<b>3.00</b>	<b>3.00</b>
As/S	-	-	-	-	0.89	0.92	0.93	0.88	-	-	-	-
Au/As	-	0.01	-	0.05	-	-	-	-	-	-	-	-

## CHAPTER 4: GOLD MINERALISATION

**Table 4.2:** Partial results of electron microprobe analyses of sphalerite, galena, covellite and greenockite.

	Sphalerite				Galena				Covellite		Greenockite	
	108	109	110	111	117	118	119	120	130	131	133	134
Weight %												
Fe	2.88	2.89	2.83	3.51	0.00	0.00	<0.03	<0.03	0.30	4.30	0.02	<0.03
S	32.71	32.78	32.49	32.52	<0.03	<0.03	13.52	13.44	33.20	23.80	21.79	21.99
As	<0.006	<0.006	<0.006	0.09	13.85	13.54	<0.006	<0.006	<0.006	<0.006	0.10	0.15
Pb	<0.4	<0.4	<0.4	<0.4	<0.006	0.04	85.95	86.42	<0.4	<0.4	<0.4	<0.4
Cu	0.01	0.01	<0.01	0.90	85.20	85.71	<0.01	<0.01	64.47	69.82	0.02	0.06
Zn	62.84	62.17	62.80	61.14	<0.01	<0.01	0.03	0.17	0.05	0.05	1.87	2.24
Ag	<0.006	<0.006	<0.006	<0.006	0.79	0.04	<0.006	<0.006	0.18	0.09	0.03	0.04
Cd	1.27	1.36	1.27	1.34	<0.006	<0.006	<0.9	<0.9	<0.9	<0.9	75.30	73.22
<b>Sum</b>	<b>99.7</b>	<b>99.2</b>	<b>99.4</b>	<b>99.5</b>	<b>&lt;0.9</b>	<b>&lt;0.9</b>	<b>99.5</b>	<b>100.0</b>	<b>98.3</b>	<b>98.2</b>	<b>99.1</b>	<b>97.7</b>
Atomic %												
Fe	2.52	2.54	2.49	3.08	-	-	-	-	0.26	4.01	0.03	-
S	49.9	50.2	49.8	49.7	50.5	50.5	50.4	50.0	50.3	38.7	49.2	49.9
As	-	-	-	0.06	-	0.06	-	-	-	-	0.10	0.15
Pb	-	-	-	-	48.1	49.4	49.6	49.7	-	-	-	-
Cu	-	-	-	0.69	-	-	-	-	49.3	57.2	0.02	0.07
Zn	47.0	46.7	47.2	45.9	1.41	0.07	0.06	0.31	0.04	0.04	2.07	2.49
Ag	-	-	-	-	-	-	-	-	0.08	0.04	0.02	0.03
Cd	0.55	0.59	0.55	0.58	-	-	-	-	-	-	48.5	47.4
<b>Sum</b>	<b>100</b>	<b>100</b>	<b>100</b>	<b>100</b>	<b>100</b>	<b>100</b>	<b>100</b>	<b>100</b>	<b>100</b>	<b>100</b>	<b>100</b>	<b>100</b>
Formula												
Fe	0.08	0.08	0.07	0.09	0.00	0.00	0.00	0.00	0.01	0.12	0.00	0.00
S	1.50	1.51	1.49	1.49	1.52	1.51	1.51	1.50	1.51	1.16	1.48	1.50
Pb	-	-	-	-	1.44	1.48	1.49	1.49	-	-	-	-
Cu	-	-	-	0.02	-	-	-	-	1.48	1.72	-	-
Zn	1.41	1.40	1.42	1.38	0.04	-	-	0.01	-	-	0.06	0.07
Cd	0.02	0.02	0.02	0.02	-	-	-	-	-	-	1.46	1.42
<b>Sum apfu</b>	<b>3.00</b>	<b>3.00</b>	<b>3.00</b>	<b>3.00</b>	<b>3.00</b>	<b>3.00</b>	<b>3.00</b>	<b>3.00</b>	<b>3.00</b>	<b>3.00</b>	<b>3.00</b>	<b>3.00</b>
As/S	0.08	0.08	0.07	0.09	0.00	0.00	0.00	0.00	0.01	0.12	0.00	0.00

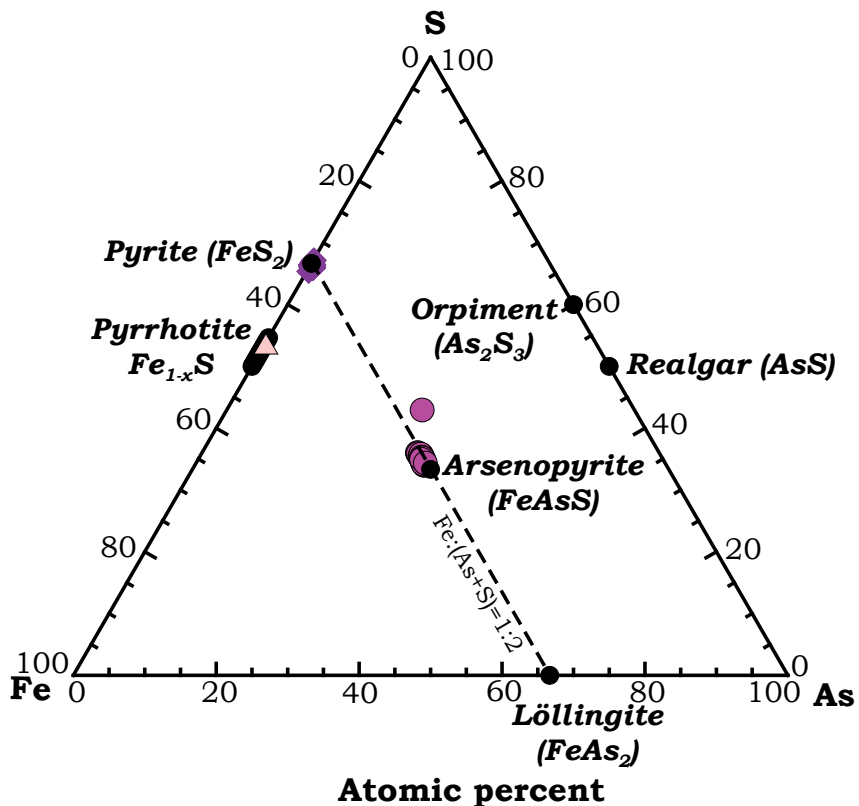


**Figure 4.6:** The composition of pyrite, arsenopyrite and pyrrhotite from Batouri lodes, as given by electron-microprobe analyses.

**Table 4.3:** Partial results of LA-ICP-MS analyses of pyrite and arsenopyrite from Batouri lodes.

	Pyrite I			Pyrite II			Pyrite III			Arsenopyrite	
	23	24	25	20	21	22	2	3	4	16	17
ppm											
Ni	55.5	27.6	101	<0.301	<0.252	42.8	19.9	31.9	74.1	10.7	5.48
Ru	<0.033	0.034	<0.029	<0.026	<0.029	<0.036	<0.031	<0.046	<0.052	0.082	<0.116
Rh	0.037	<0.005	0.057	<0.005	<0.005	<0.005	0.200	<0.008	0.015	<0.012	0.270
Pd	<0.031	0.032	0.081	<0.023	<0.025	<0.019	0.404	<0.029	<0.027	<0.049	<0.058
Re	<0.025	<0.016	<0.018	<0.013	<0.018	<0.021	<0.018	<0.021	<0.024	<0.041	<0.41
Os	<0.062	<0.041	<0.055	<0.044	<0.037	<0.049	<0.064	<0.043	<0.051	<0.095	<0.129
Ir	<0.014	0.014	<0.011	<0.011	<0.013	<0.011	0.013	0.014	<0.016	<0.028	<0.037
Pt	<0.026	<0.026	<0.029	<0.029	<0.021	<0.028	<0.031	<0.031	<0.024	<0.057	<0.077
Au	0.044	0.041	0.306	2.29	0.764	3.08	1.70	1.52	2.52	0.830	2.11
cps	<b>Background subtracted</b>										
Co	35810	20455	11548	387	4	76388	99118	213619	99143	5119	3156
Cu	106847	4739	102909	25	66	876	769674	7359	3489	4	379
As	311	82	6709	201183	137975	158752	24525	20115	13248	$5.9 \times 10^6$	$4.0 \times 10^6$
Ag	795	129	982	0	4	289	6330	1543	1439	9	997
Sb	574	93	1294	0	0	669	4771	3465	3393	9182	6150
Te	5	1	0	1	1	2	17	14	8	0	0
Bi	445	41	1025	0	18	862	5113	6489	4471	16	82

The LA-ICP-MS analyses show low concentrations of Au, As and Bi in the pyrite phases and in arsenopyrite. Despite the low concentrations, these elements, nevertheless, appear to show distinct patterns in the different pyrite phases (Figure 4.7). Gold concentration is very low in Pyrite I (<0.02–0.31 ppm), and higher in Pyrite II (<0.02–38.9 ppm) and pyrite III (0.3–2.5 ppm). The maximum concentrations of Au are encountered in pyrite II (Figure 4.7a). High Au broadly coincides with high As contents in pyrite (Figure 4.7a). Bi, however, shows a different concentration pattern. The highest counts for Bi were registered in pyrite I and III, while pyrite II show the lowest counts. Correlation between Au and As varies from positive in pyrite I, to weakly negative, if any, in pyrite III (Figure 4.7b). Apparently, Au does not correlate with As in pyrite II and arsenopyrite.

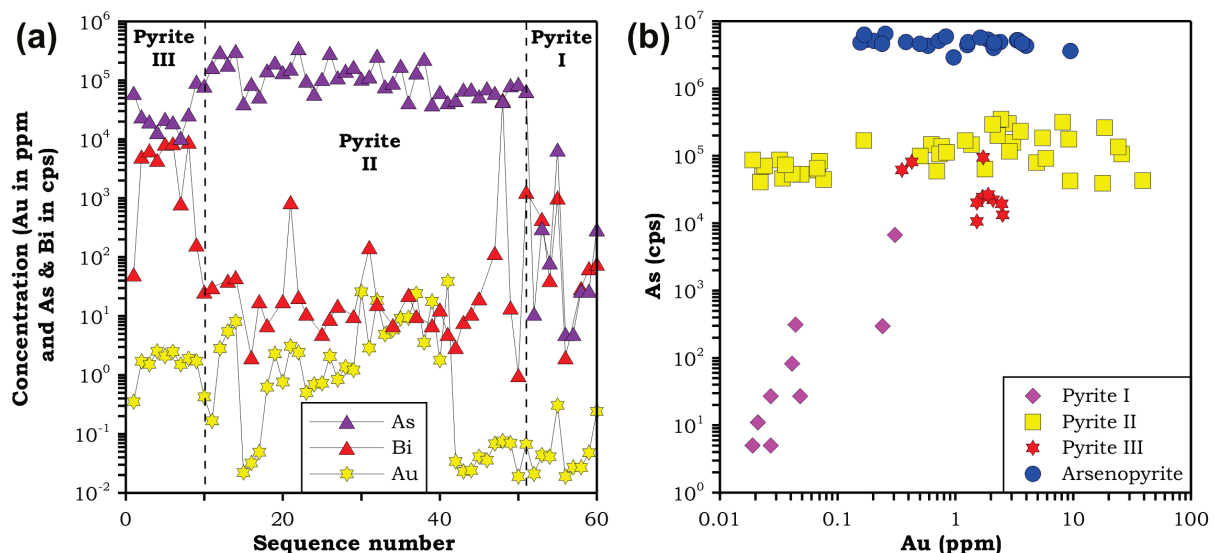


**Figure 4.7:** The distribution of As, Bi and Au in the pyrite phases and arsenopyrite from Batouri. **(a)** Variations of Au, Bi and As in the different pyrite phases. **(b)** Correlation between Au and As in the pyrite phases and in arsenopyrite.

### 4.3 Gold textures and chemistry

Gold occurs mainly as inclusions in pyrite I and II (Figure 4.5c), and arsenopyrite (Figure 4.4b), or as veinlets in pyrite II (Figure 4.8a). It is also associated with sphalerite and galena. In sphalerite, gold preferentially occurs at contacts between sphalerite and pyrite II inclusions (Figures 4.8b and c). It occurs in quartz along fractures (Figure 4.8d), where it is, in

## CHAPTER 4: GOLD MINERALISATION

places, intergrown with galena (Figure 4.8e). The occurrence of free gold along quartz fractures and grain boundaries (Figure 4.8d) characterises bonanza ore at Batouri. In the weathering zone, gold co-exists with goethite along quartz fractures (Figure 4.8f). It is also spatially associated with goethite and covellite (Figure 4.9). Intergrowths between gold and goethite is common (Figure 4.9a, b, c, d, and f). Very fine-grained particles of residual gold and goethite occur in quartz in spaces once occupied by another mineral, now leached (Figure 4.9a). In places, the gold appears to have been mixed with goethite (Figure 4.9b). Goethite and covellite manifest themselves as coatings on isolated gold grains (Figures 4.9d and e). Nevertheless, gold also occurs as a coatings on goethite (Figure 4.9f). Grain sizes of the Au associated with goethite range from <1  $\mu\text{m}$  to 2 mm.

## CHAPTER 4: GOLD MINERALISATION

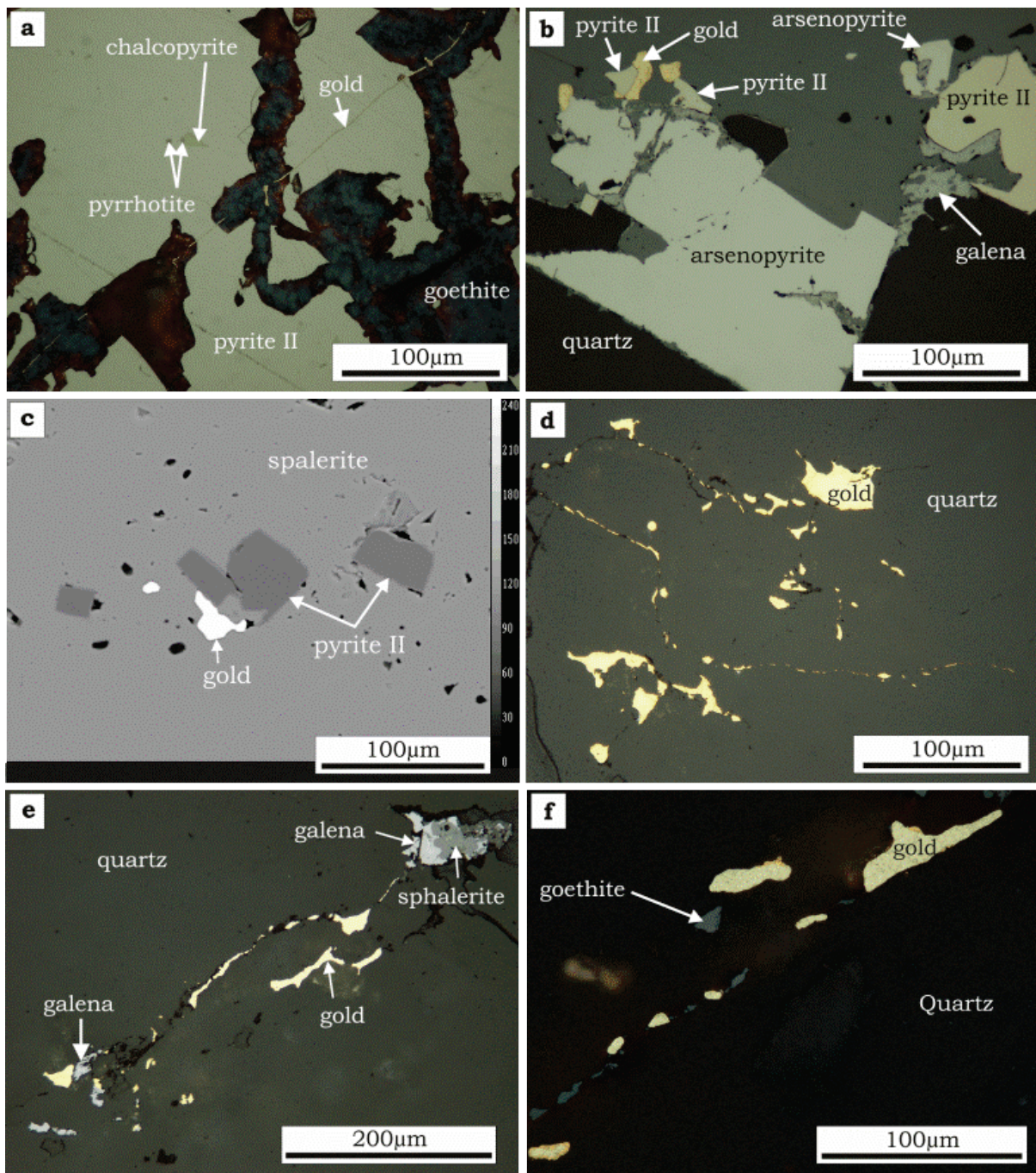


**Figure 4.8:** Reflected-light photomicrographs (plane-polarized light) and back-scattered electron image showing modes of occurrence of gold in primary quartz veins at Batouri. **(a)** Gold veinlet cross-cutting pyrite II. **(b)** Gold deposited along pyrite II-sphalerite and arsenopyrite-sphalerite contacts. **(c)** Backscatter-electron image showing free gold deposited in pore spaces along pyrite II-sphalerite contact. **(d)** Bonanza-type gold mineralisation, showing free gold deposited along microfractures in quartz. **(e)** Gold, galena and sphalerite occurring along microfractures un quartz. **(f)** Gold and goethite occurring together along microfractures in quartz.

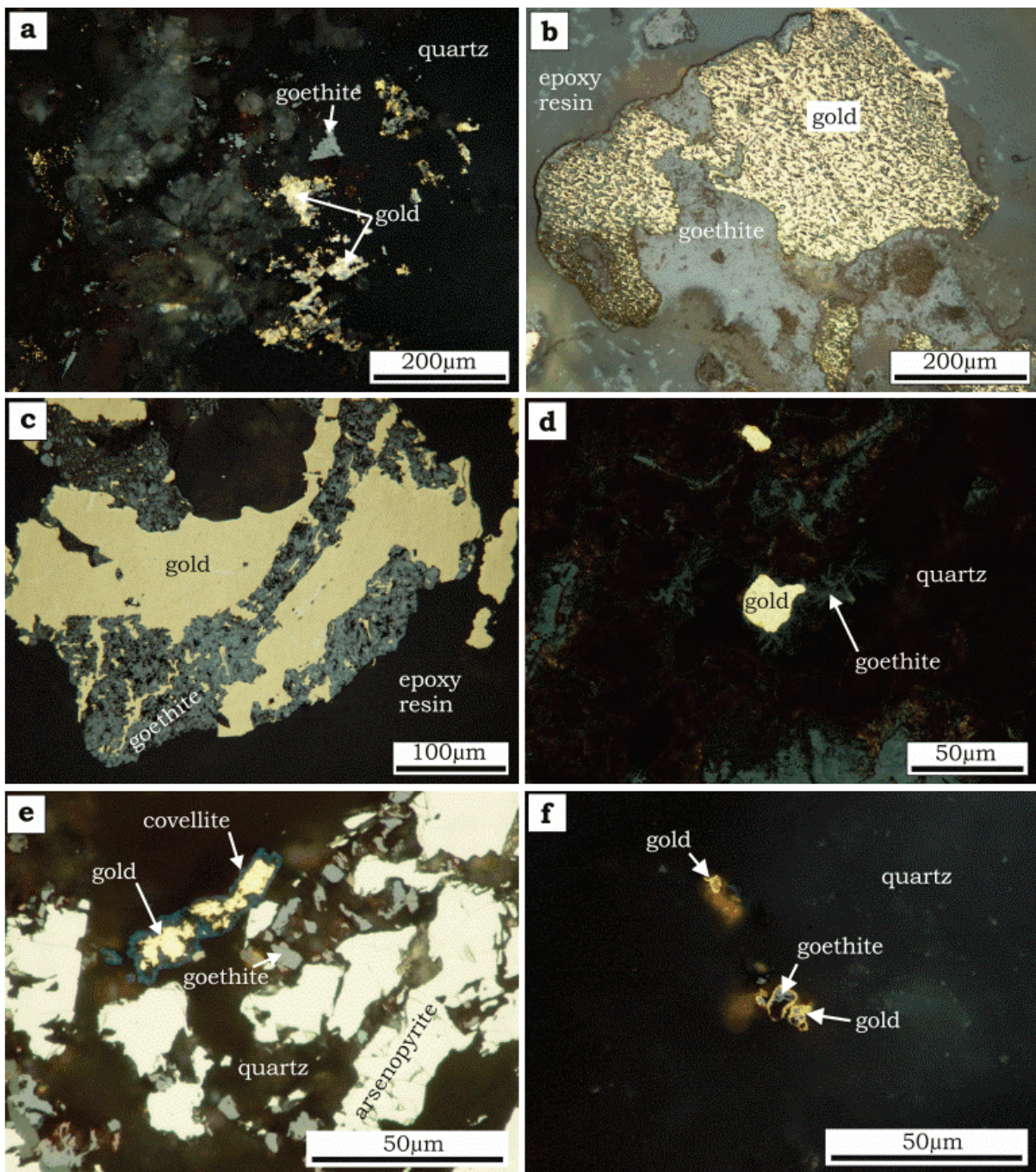


**Figure 4.9:** Reflected-light photomicrographs (plane-polarized light), showing modes of occurrence of gold in quartz strongly affected by supergene fluids. **(a)** Residual aggregates of fine-grained occupying the space previously occupied by another mineral that now been leached away by supergene fluids. **(b)** Mixture of gold and goethite in supergene zone. **(c)** Gold intergrown with goethite in primary quartz vein within the supergene zone. **(d)** Tiny elongated crystals of goethite overgrowths on gold grain. **(e)** Covellite overgrowths on gold grains. **(f)** Gold overgrowths on goethite grains.

In order to compare the chemical compositions of vein gold and alluvial gold, gold concentrates prepared from gold-bearing quartz sampled

from a vein outcrop, and from stream sediments, were micro-analysed. Both lode and placer gold display a core-and-rim zonation pattern, where the rim has a bright-yellow colour and the core, whitish yellow (e.g. red-arrowed grain in Figure 4.10a). Also common in both gold types is the occurrence of an electrum band at the boundary between the core and the rim of zoned gold (e.g. inset of enlarged gold grain in Figure 4.10b). Both gold types display a very wide compositional range, from Ag-poor gold rims (99 wt % Au, 0.04 wt % Ag) to the electrum zone (51 wt % Au, 49 wt % Ag). These compositions correspond to fineness of 508 to 999 (Table 4.4; Appendix 4b).

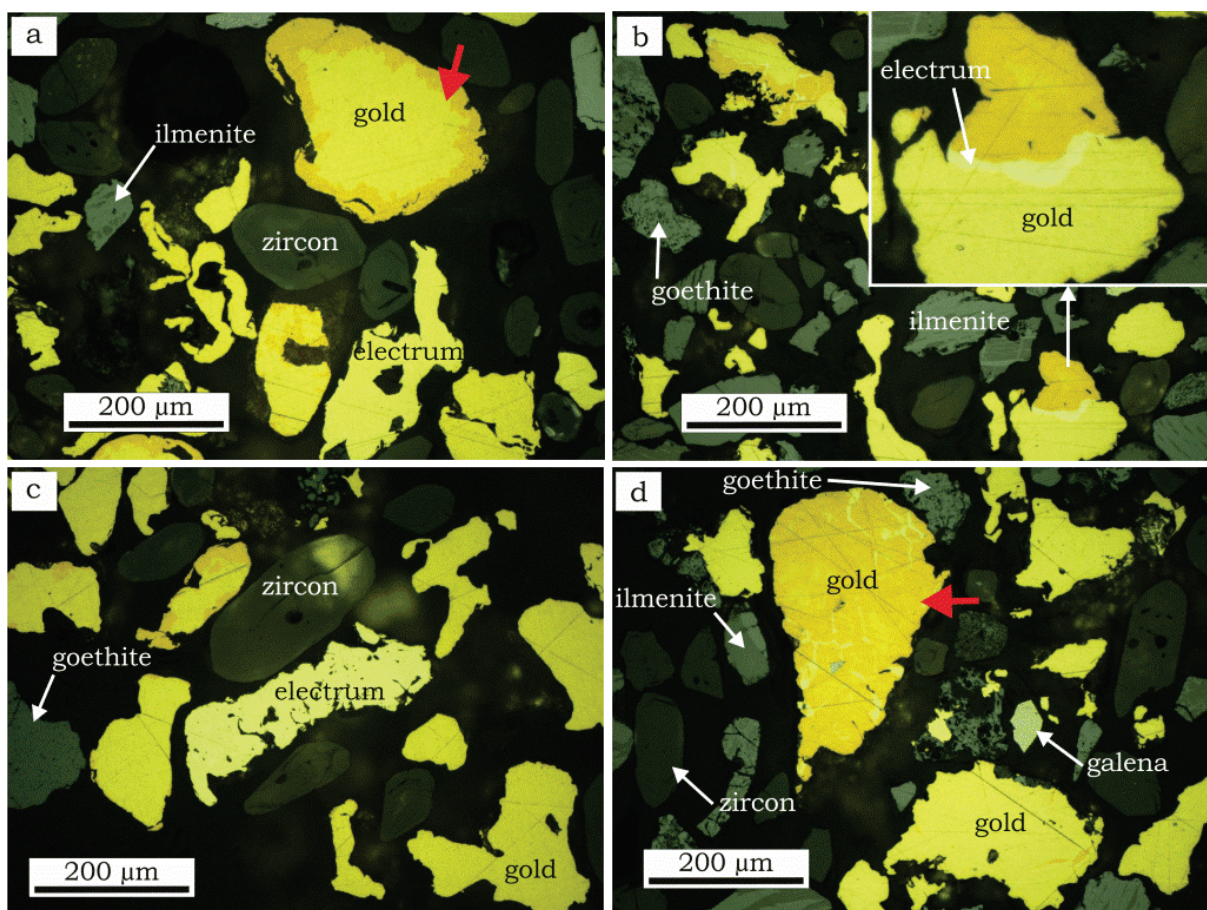


**Figure 4.10:** Reflected-light photomicrographs (plane-polarized light), of placer- (a and b) and vein-derived (c and d) gold from Batouri. **(a)** Gold and electrum from stream sediments at Kambélé. Zoned gold (red-arrowed) is characterised by a core-and-rim pattern, where the rim is Ag-poor and the core, Ag-rich. **(b)** Electrum occurring at the boundary between the core and the rim of zoned gold. Inset is the enlargement of gold grain described. **(c)** Electrum containing numerous cavities, a feature not common in gold. **(d)** Silver-poor gold (red-arrowed) with silver-rich internal discontinuities, from mineralised vein. The samples shown are gold concentrates containing other heavy minerals, mounted in epoxy resin and polished.

## CHAPTER 4: GOLD MINERALISATION

**Table 4.4:** Summary of electron-microprobe analyses of vein and placer gold from Batouri.

Gold type	Zone	Composition (wt %)			Fineness
Vein gold	Rims and Ag-poor gold grains	Au:	92–99		918–1000
		Ag:	0.04–8.20		
		Hg:	0.06–0.11		
Vein gold	Core and Ag-rich homogeneous grains	Au:	80–84		805–835
		Ag:	17–20		
		Hg:	0.07–0.10		
Vein gold	Electrum	Au:	56–78		531–757
		Ag:	24–47		
		Hg:	0.27–0.60		
Placer gold	Rims and Ag-poor gold grains	Au:	95–99		964–999
		Ag:	0.10–3.60		
		Hg:	0.07–0.12		
Placer gold	Core and Ag-rich homogeneous grains	Au:	81–88		803–875
		Ag:	13–20		
		Hg:	0.12–0.38		
Placer gold	Electrum	Au:	51–80		508–800
		Ag:	20–49		
		Hg:	0.15–0.99		

The summary of the electron-microprobe analyses of Batouri gold, given in Table 4.4, indicates that vein gold and placer gold have similar chemistry. Because of this chemical similarity, both gold types are treated together (Figure 4.11). The bulk of the gold grains are homogeneous. However, the rims of the zoned gold grains are poor in silver and range in composition from 0.04–8.20 wt % Ag and 92–99 wt % Au (918–1000 fineness; Table 4.4). This composition corresponds to group A of Figure 4.11. The composition of the cores ranges from 13–20 wt % Ag and 80–88 wt % Au (803–875 fineness), corresponding to group B of Figure 4.11. The composition of electrum ranges from 20–49 wt % Ag and 51–80 wt % Au (508–799 fineness), which corresponds to group C in Figure 4.11. Few gold grains display overall low silver contents (e.g. red-arrowed grain in Figure 4.10d). Electrum does not only occur as bands at contacts between rim and core of some zoned gold grains, but also occurs as discrete homogeneous grains e.g. Figure 4.10a and c. Some crystals of electrum

contain numerous cavities (Figure 4.10c). Noteworthy is the presence of Mercury in the Batouri gold (0.06–0.99 wt % Hg; Table 4.4). The bivariate plot in Figure 4.11b shows a positive correlation between mercury and silver. About 70% by volume of gold grains analysed have group B composition in Figure 4.11.

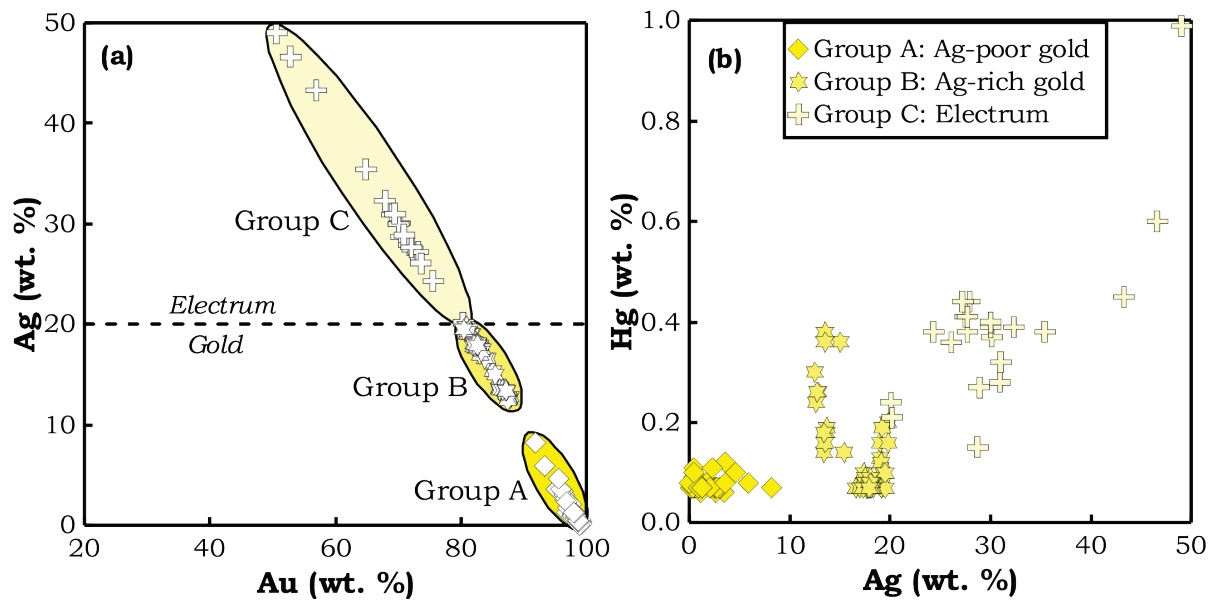


**Figure 4.11:** Scatter diagrams showing the compositional variations in gold and electrum from Batouri. **(a)** Gold displays good negative correlation with Ag. Group A represents the composition of Ag-poor gold, e. g. rims of zoned gold crystals. Group B represents the composition of Ag-rich gold, e. g. core of zoned gold grains. Group C represents electrum composition. **(b)** Silver correlates positively with Hg. Electrum, therefore, has the highest Hg contents.

#### 4.4 Interpretation of ore chemistry and paragenesis

Based on microscopic and chemical studies pyrite (i.e. pyrite I, II and III) and arsenopyrite from Batouri host both visible and invisible gold. Invisible gold in pyrite could be lattice-bound or occur in these minerals as nanoparticles of native gold. Reich *et al.* (2005) proposed that the Au/As molar ratio in pyrite depends on the mode of Au occurrence in these minerals. So when invisible gold in pyrite is lattice-bound, the Au/As molar ratio is less than 0.02. If this value is exceeded, then gold exists in pyrite as nanoparticles of the native metal. In the case of pyrite from Batouri, the Au/As molar ratio is below 0.02, except for analysis 30 (Table 4.1; Appendix

4a), which has a Au/As molar ratio of 0.05. The low As/Au molar ratio, therefore, implies that invisible gold in pyrite from Batouri is lattice-bound.

The concentration of gold is lower in pyrite I, than in pyrite II and pyrite III. A possible explanation for the low gold content of pyrite I is that, the hydrothermal fluid was poor in As and Au at the time pyrite I was precipitated. However, the positive correlation between Au and As in pyrite I (Figure 4.7b) suggests that As may have played a role in Au fixation in pyrite I. This phenomenon is reflected in the coincidence of high Au and As in pyrite in many Au deposits around the world, e.g. the Ashanti in Ghana (Oberthür *et al.*, 1997). The positive correlation between Au and As is absent in pyrite II and III, as well as in arsenopyrite (Figure 4.7b).

The occurrence of invisible Au in arsenopyrite (Table 4.3, Appendix 5) is also a common feature that has been described in many gold deposits (e.g. Cepedal *et al.*, 2008; Morey *et al.*, 2008; Sung *et al.*, 2009). In an earlier investigation of invisible Au in synthetic arsenopyrite and natural samples from the Carlin Trend gold mine in Nevada, USA, Fleet and Mumin (1997) found that Au enrichment in arsenopyrite coincided with Fe-deficiency and As-enrichment. They interpreted this trend to imply that, Au was removed from hydrothermal fluids by chemisorption at As-rich, Fe-deficient sites. In a separate study, Cabri *et al.* (2000) identified the species of this structurally-bound gold in arsenopyrite from mines in Siberia, Russia and São Bento, Brazil, as  $\text{Au}^+$ .

Microscopic intergrowths between pyrite II and arsenopyrite provide no clue as to the order of precipitation between the two minerals (e.g. Figure 4.4a and b), indicating that they are coeval. The close similarity in the scatter patterns of their Au and As contents (Figure 4.7b) suggests that both pyrite II and arsenopyrite incorporated Au at roughly constant As values.

Based on intergrowth and cross-cutting relationships between the sulfides, (Figures 4.4), chalcopyrite and pyrrhotite are interpreted as belonging to the same depositional phase as pyrite II and arsenopyrite.

Sphalerite is the most abundant mineral post-dating pyrite II. It probably belongs to the last paragenetic phase, which also consists of chalcopyrite, galena, pyrite III and subordinate tetrahedrite. The exsolution blebs of chalcopyrite occurring in sphalerite were likely formed by the reaction of Cu-bearing fluids with the iron content of sphalerite ("chalcopyrite disease"; Ramdohr, 1969). Whereas tetrahedrite appears to be cogenetic with sphalerite, the latter is cross-cut by galena. Galena is in turn cross-cut by pyrite III. The intergrowth of galena and native gold along quartz fractures (Figure 4.8e) suggests that both minerals are coeval.

However, native gold occurs more often along fracture surfaces and cavities in pyrite II than intergrown with galena. This tendency to associate with pyrite can be explained by electrochemical accumulation of Au on the surface of pyrite II, which was facilitated by the presence of As, which enhances P-type conductivity in the pyrite (Möller and Kersten, 1994). Intuitively, an electrochemical accretion of Au would result in increasing Au contents at constant As content, which is the pattern of pyrite II and arsenopyrite in Figure 4.7b.

The core-and-rim pattern of gold zoning observed at Batouri has previously been described by Suh and Lehmann (2003). This zoning pattern has also been described worldwide from weathering profiles over hypogene gold deposits and alluvial deposits (e.g. Mann, 1984; Grimm and Friedrich, 1990; Colin and Vieillard, 1991; Larizzatti *et al.*, 2008). The Au-rich, Ag-depleted rimming around Au-Ag cores has been considered a diagnostic feature of weathering, caused by selective leaching of Ag by supergene solutions.

The occurrence of a thin layer of electrum at the contact between the Ag-rich gold core and Ag-depleted gold rim (e.g. Figure 4.10b) is described for the first time in gold from Batouri. A similar feature has also been observed in weathered gold from the Gentio du Ouro (Grimm and Friedrich, 1990) and Fazenda Pison (Larizzatti *et al.*, 2008) deposits in Brazil. Grimm

and Friedrich (1990) attributed the origin, of the electrum layer in weathered gold from Gentio du Ouro, to rapid re-deposition of Ag re-mobilised as a thiosulfate complex from the core of the gold grain by supergene solutions. This, however, is not likely to have been the scenario at Batouri, especially as the cores of the zoned gold grains do not show signs of silver depletion.

The occurrence of homogeneous grains of electrum in the vein and placer samples (Figure 4.10), suggests that silver enrichment may have been a primary process. This is further corroborated by the presence of trace amounts of silver in all the sulfides (Table 4.1 and 4.2, and Appendix 4a). Gold cores and electrum rims were probably precipitated from progressively Ag-rich hydrothermal fluids, at different phases of ore formation. Preferential leaching of silver from the electrum rims under supergene conditions (Figure 4.12), may have produced the observed zonation pattern.

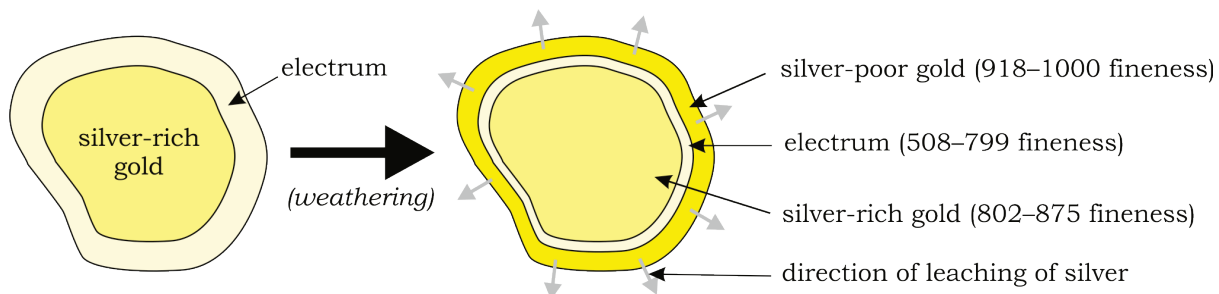


**Figure 4.12:** Schematic showing the selective leaching of silver from the electrum rim of a gold grain.

The similarity in zonation patterns and chemistry of gold and electrum from vein and placer (Table 4.4), is probably due to the fact vein gold was sampled from the outcrop, where it interacted with supergene solutions and was subjected to weathering. However, the composition of homogeneous gold and electrum grains, as well as cores and electrum bands in zoned gold, seem to represent the primary composition of the gold-silver alloys at Batouri (508–875 fineness).

Morrison *et al.* (1991) investigated the occurrence, within the same deposit, of gold with a wide range of fineness values. They reviewed

previously published thermodynamic and chemical analytical data from a wide range of gold deposits, and noted that gold and silver form the same complex species in hydrothermal solutions with near-neutral pH (i.e. ~5.5). In these solutions, the dominant species for Au is the bisulfide complex ( $\text{Au}(\text{HS})_2^-$ ), while the chloride complex ( $\text{AgCl}_2^-$ ) dominates for Ag. When ore deposition is controlled by wall-rock sulfidation, the bisulfide complex is destabilised and more gold is deposited than silver, hence the high fineness of the precipitated gold. However, when the ore deposition process is controlled by a diversity of mechanisms such as cooling, boiling and/or mixing, both chloro- and bisulfide- complexes of gold and silver are destabilised and the metals are co-precipitated, resulting in gold with high Ag content and low fineness.

Morrison *et al.* (1991) concluded that the composition of gold precipitated from a hydrothermal solution rich in Ag depends on the ore deposition mechanism. Based on the primary zonation patterns observed at Batouri gold and the wide difference in the chemical composition of the gold core and the electrum rim, it is suggested that the precipitation of gold at Batouri was initially controlled by wall-rock sulfidation processes, which accounted for the bulk of the gold deposited; and subsequently by processes such as cooling, boiling and mixing, which acted alone or in combinations, leading to the deposition of electrum. Based on their chemical association with gold, Ag and As are important path-finder elements for gold at Batouri.

Low-temperature minerals such as marcasite, bornite, covellite, greenockite, goethite and manganese oxides, such as psilomelane and pyrolusite, are found to overprint all generations of pyrite and the base metal sulfides at Batouri. Because the overprinting mineral assemblage occurs in the weathering zone, and has not been observed at depth, its origin is attributed to supergene process. In this context, marcasite should represent the early stage of supergene alteration of pyrite (Ramdohr, 1969). Likewise, greenockite formed after sphalerite, and bornite and covellite after chalcopyrite. Being the end-product of the weathering of minerals such as

pyrite, arsenopyrite and pyrrhotite, goethite is the most abundant supergene mineral.

Gold displays various modes of association with secondary minerals, including goethite and covellite (Figure 4.9). In places, the gold occurs as clouds of very fine particles deposited on goethite (Figure 4.9a and f). The apparent nano-scale particle sizes, and their accumulation on the surfaces of goethite clearly indicates reprecipitation from supergene solutions. A number of ligands, including chloride, thiosulfate, hydroxyl and chloro-hydroxyl ions, as well as humic acids, have been implicated in gold remobilisation in the supergene environment under various climatic conditions (Krauskopf, 1951; Mann, 1984; Webster and Mann, 1984; Webster, 1986; Benedetti and Boulègue, 1991; Colin and Vieillard, 1991; Colin *et al.*, 1993). In tropical humid rain-forest conditions, such as prevails at Batouri, the groundwater is slightly to moderately acid and very diluted (Colin *et al.*, 1993). Under such conditions, gold is more likely to form complexes with organic ligands, hydroxyl and chloro-hydroxyl ions, and is redeposited over short distances (Colin and Vieillard, 1991; Colin *et al.*, 1993).

Supergene remobilisation of gold is considered a gold purification process, such that remobilised gold rarely contains more than 1 wt % Ag (Seeley and Senden, 1994; Hough *et al.*, 2007). At Batouri, fine- to coarse-grained nuggets of placer gold (10 µm–2 mm) occurring in association with goethite (e.g. Figure 4.9c) also contain high silver (>10 wt %; Table 4.4, Appendix 4b), and are interpreted here as hypogene gold that was mechanically released from the veins. The Batouri ore mineral paragenesis is systematically shown in Figure 4.13.

## CHAPTER 4: GOLD MINERALISATION

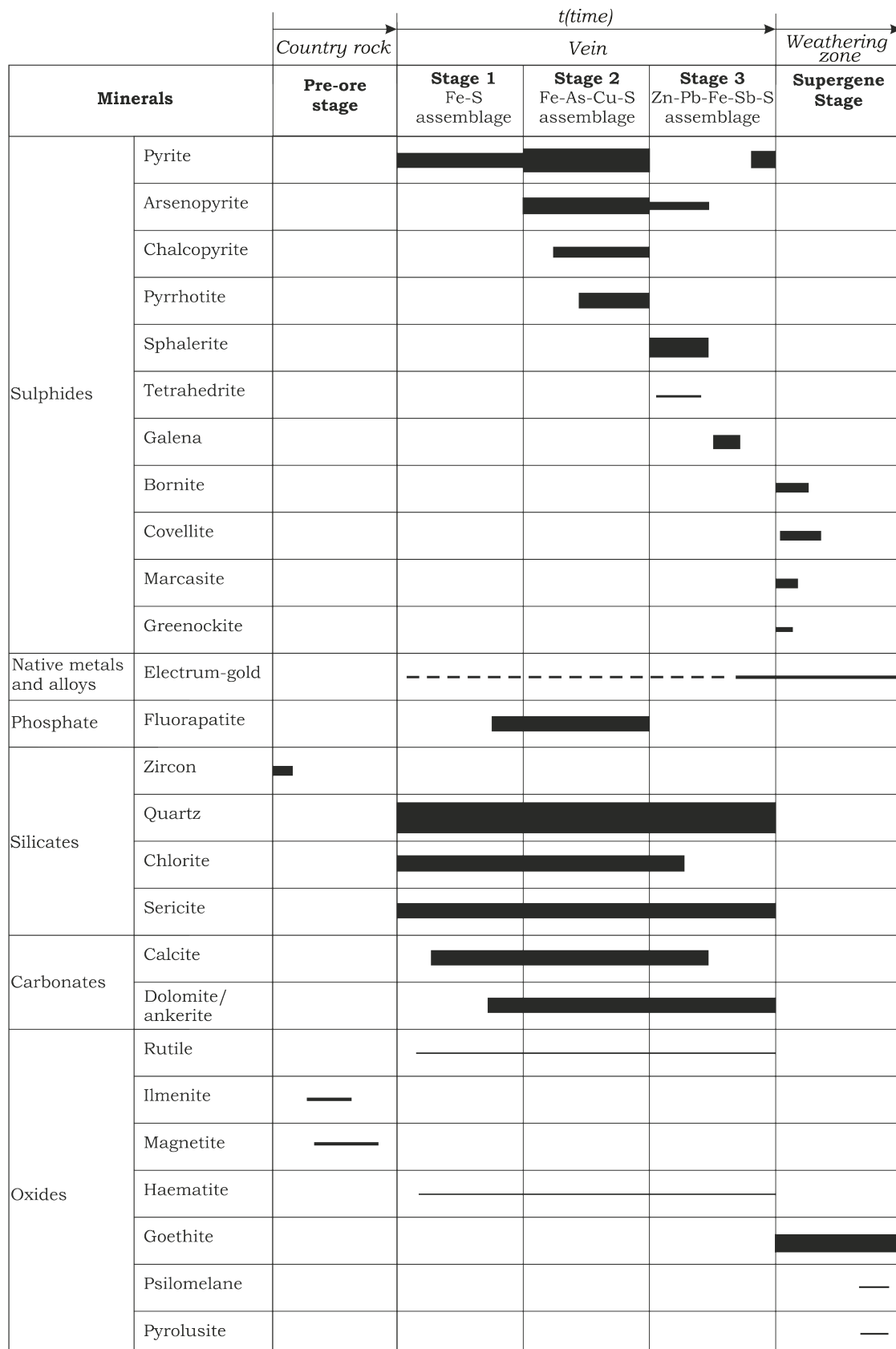


**Figure 4.13:** Paragenetic assemblages of minerals associated with Au-bearing veins at Batouri.

## 4.5 Constraints on temperature and sulfur fugacity

Based on research conducted by Barton Jr. (1969) and Kretschmar and Scott (1976), the composition of arsenopyrite (FeAsS) is a function of sulfur fugacity, temperature and, to a minor extent pressure, assuming arsenopyrite and either pyrite or pyrrhotite coexisted in equilibrium. It is therefore possible to determine the prevailing temperature and sulfur fugacity at the time of deposition of an Fe-As-S assemblage from the chemical composition of arsenopyrite (Figure 4.14). The refractory behaviour of arsenopyrite to textural and compositional changes makes it suitable for geothermometry (Choi and Youm, 2000).

At the Batouri deposit, arsenopyrite often occurs in association with pyrite and sphalerite, but not with pyrrhotite. Petrographical observations indicate that arsenopyrite and pyrite were cogenetic, whereas chalcopyrite and sphalerite were precipitated later than pyrite (Figures 4.4). Based on this, it is likely that arsenopyrite co-existed in equilibrium with pyrite. The composition of arsenopyrite (Table 4.1, Appendix 4a) is relatively homogeneous within the range between ~30 and ~32 at % As. This compositional range implies temperatures between 310 and 420°C, with corresponding sulfur fugacities  $\log f(S_2)$  varying from -6 to -10 (Figure 4.14).

## 4.6 Reconnaissance fluid inclusion studies

### 4.6.1 Introduction

The study of fluid inclusions can provide important clues to the physico-chemical conditions under which minerals were formed (Roedder, 1984). For the purpose of the present study, three doubly polished thick sections of quartz samples from the Batouri auriferous veins were subjected to fluid inclusion petrographic and microthermometric examination in order to elucidate the physico-chemical conditions under which gold was likely deposited.

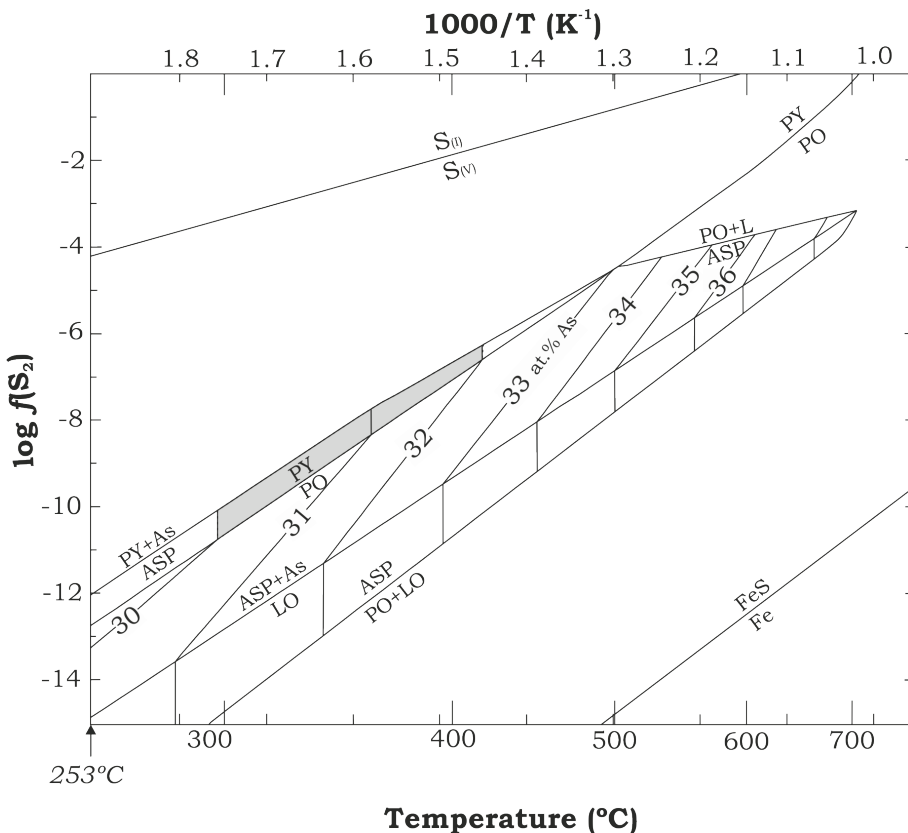


**Figure 4.14:** Temperature and sulfur fugacity estimation based on sulfide assemblage and the composition of arsenopyrite (shaded) from the Batouri deposit. Diagram after Kretschmar and Scott (1976), as modified by Sharp *et al.* (1985). PY: pyrite, ASP: arsenopyrite, PO: pyrrhotite, LO: löllingite, As: arsenic, S: sulfur, Fe: iron, FeS: iron sulfide, L: liquid.

#### 4.6.2 Fluid inclusion petrography

Fluid inclusions occurring in auriferous quartz from major veins are: 1) randomly distributed, 2) aligned along intragranular and trans-granular fractures, and 3) aligned along grain boundaries (intergranular). The fluid inclusions mostly exist in two phases, liquid and vapour, at room temperature.

The randomly distributed fluid inclusions occur either isolated or in clusters in undeformed domains of the host quartz. They vary from <1 to 13 µm in length, exhibiting shapes that range from regular (negative crystals) to irregular. Tiny elongated fluid inclusion trails arranged along fractures within quartz crystals or cutting across grain boundaries are abundant. Associated with these inclusions are vapour-dominant inclusions.

Recrystallised domains in quartz contain a few relics of leaked fluid inclusions.

Another generation of fluid inclusions is located in quartz veinlets that cross-cut major quartz veins. The veinlet quartz-hosted fluid inclusions are less than 8 µm in diameter and consists of vapour and liquid at room temperature. An overview of the common fluid inclusion textures in auriferous quartz from Batouri are shown in Figure 4.15.

#### **4.6.3 Microthermometry**

*Aqueous-carbonic inclusions: [H<sub>2</sub>O-CO<sub>2</sub>(±CH<sub>4</sub>±N<sub>2</sub>)]*

Most of the data reported here were obtained from measurements of inclusions in quartz from the major veins (referred to as vein quartz), as these were sufficiently large for phase changes to be accurately observed. The inclusions exhibit two phases at room temperature: liquid H<sub>2</sub>O and CO<sub>2</sub> gas. The aqueous phase surrounds the carbonic phase and occupies 0.5 to 0.7 volume fraction. Upon cooling, CO<sub>2</sub> underwent phase separation below 8°C and a CO<sub>2</sub> liquid phase appeared. Total freezing of these inclusions was achieved below -110°C. Upon heating, the CO<sub>2</sub> fraction melted at -57.4 to -58.6°C. Homogenisation of the carbon dioxide into the gas phase (T<sub>h</sub> CO<sub>2</sub>) was achieved at 8.7 to 11.1°C. These homogenisation temperatures correspond to CO<sub>2</sub> densities of 0.85 to 0.87 g/cm<sup>3</sup> (Duschek *et al.*, 1990, calculated using Bakker, 2003). The fluid inclusions in veinlet quartz were too tiny for changes in carbon dioxide phases to be accurately observed. However, one inclusion was sufficiently large and carbon dioxide was observed to homogenise into the gaseous phase at 17°C, corresponding to a density of 0.80 g/cm<sup>3</sup>. Total homogenisation temperatures (T<sub>h</sub>) of the aqueous-carbonic inclusions is in the range from 291 to 355°C for vein quartz, and 245 to 270°C for veinlet quartz (Figure 4.16).

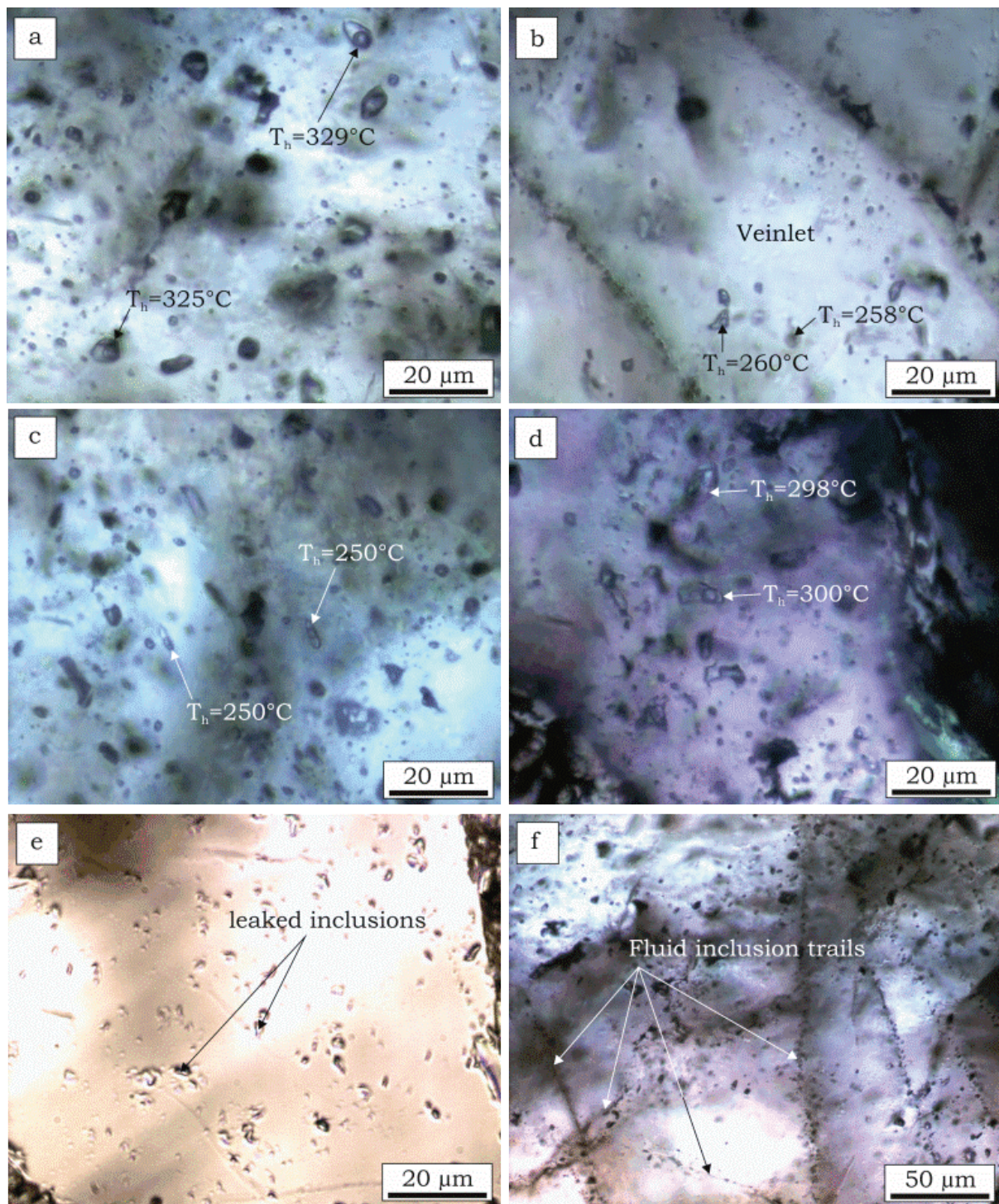


**Figure 4.15:** Transmitted-light photomicrographs (plane-polarized), showing fluid inclusion textures in quartz from gold-bearing veins at Batouri. Homogenisation temperatures,  $T_h$ , of some fluid inclusions are also indicated. **(a)** Primary aqueous-carbonic inclusions in quartz. **(b)** Vein quartz cross-cut by a quartz veinlet. The veinlets also contains aqueous-carbonic inclusions. **(c)** Elongate aqueous-carbonic inclusions in veinlet quartz. **(d)** Randomly distributed aqueous-carbonic inclusions in vein quartz. **(e)** Remnants of leaked fluid inclusions in recrystallised quartz. **(f)** Multidirectional trails of secondary fluid inclusions.

*Nitrogen ± carbonic inclusions: [N<sub>2</sub>±CO<sub>2</sub>]*

Several low-density, ~9 to ~13 µm-sized, gas inclusions, sometimes containing aqueous films, occur in vein quartz. The inclusions homogenise into the liquid or vapour phases at temperatures of about -150.2°C, which point to the presence of nitrogen. A two-phase inclusion of nitrogen and carbon dioxide was observed, with carbon dioxide surrounding nitrogen. This inclusion gave a melting temperature of carbon dioxide (T<sub>m</sub> CO<sub>2</sub>) of -60.3°C, with nitrogen homogenised (T<sub>h</sub> N<sub>2</sub>) at -148°C.

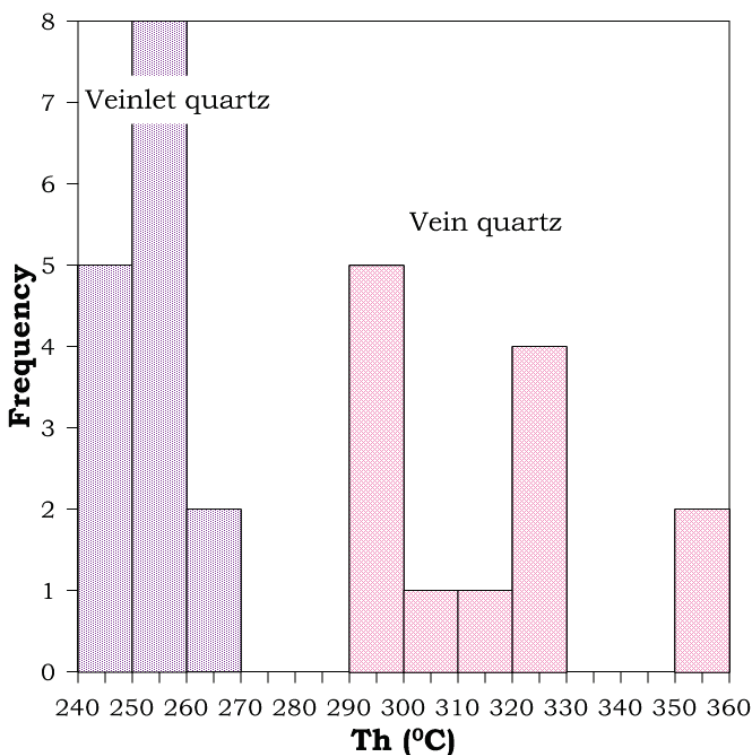


**Figure 4.16:** Histogram showing homogenisation temperatures of aqueous-carbonic (H<sub>2</sub>O-CO<sub>2</sub>) inclusions in quartz samples from gold-mineralised veins at Batouri. Inclusions in vein quartz homogenises between 291 and 355°C, while those in veinlet quartz that cross-cuts vein quartz, gave T<sub>h</sub> between 245 and 270°C.

#### 4.6.4 Interpretation and discussion of fluid inclusion data

The dominant occurrence of aqueous-carbonic fluid inclusions in quartz from gold-bearing veins at Batouri invokes a genetic relationship in that mixed aqueous-carbonic hydrothermal fluids are responsible for gold transport in hydrothermal systems (Brown, 1998; Groves *et al.*, 1998; Ridley and Diamond, 2000; Wilkinson, 2001). The T<sub>m</sub> CO<sub>2</sub>, between -57.4 and -

58.6°C, indicates depression below the CO<sub>2</sub> triple point of -56.6°C (Rosso and Bodnar, 1995). The depressed T<sub>m</sub> CO<sub>2</sub> may be due to the presence of small quantities of lighter gases such as N<sub>2</sub> and/or CH<sub>4</sub> (Van den Kerkhof and Thiéry, 2001).

The T<sub>h</sub> N<sub>2</sub> is about -150°C, which is slightly below the critical point of nitrogen (-147°C). The depression from the critical point of nitrogen may be related to density fluctuations at the time of entrapment (Touret, 1982). While carbon dioxide in these inclusions probably came from the hypogene fluid, nitrogen was most likely derived from the alteration of wall-rock minerals such as feldspars and micas, which usually contain traces of ammonium (Van den Kerkhof and Thiéry, 2001).

In the absence of geobarometric data for estimating trapping temperatures, the T<sub>h</sub> of 355 to 291°C (Figure 4.16) of the aqueous-carbonic inclusions in the vein quartz, represent the lowest possible trapping temperatures of these fluid inclusions, and correspond to the formation temperatures of chlorite (i.e. 333 to 312°C; Figure 3.5) in the proximal zone of the wall-rock. This temperature range is overlapped by the formation temperature calculated for arsenopyrite (420 to 310°C; Figure 4.14). This gives a temperature of at least ~300°C during the major vein emplacement. However, ore fabric suggest that arsenopyrite precipitated together with stage 2 ore mineral assemblage (Figure 4.13). If the vein quartz-hosted fluid inclusions record the major quartz vein emplacement, with which stage 1 ore mineral assemblage is associated, stage 2 arsenopyrite could have followed at more or less the same temperature as stage 1, but at lower sulphur fugacity. The aqueous-carbonic fluid inclusions in veinlet quartz homogenised between 245 and 270°C, indicating entrapment temperatures of >250°C. This late hydrothermal overprint could correspond to stage 3 ore mineral assemblage.

## 4.7 Gold transport and deposition mechanism

In solution, gold occurs either as Au(I) or Au(III), and can form stable complexes with such ligands as bisulfide ( $\text{HS}^-$ ) or chloride ( $\text{Cl}^-$ ) depending on the prevailing physico-chemical conditions of the solution (e.g. Seward, 1984; Romberger, 1988). Only Au(I) is known to form bisulfide and chloride complexes important for the transport of Au in most hydrothermal fluids (Fyfe and Kerrich, 1984; Seward, 1984; Romberger, 1988; Hayashi and Ohmoto, 1991; Wood and Samson, 1998; Loucks and Mavrogenes, 1999). The dominant complex species responsible for Au transport in any hydrothermal system depends on the redox state, the pH and the temperature conditions of the system. Several experimental studies have led to the conclusion that, in terms of stability and concentration, Au(I) bisulfide complexes predominate in mildly oxidising to reducing hydrothermal fluids over a wide range of temperature and pH. On the other hand, Au(I) chloride complexes are more important in hydrothermal fluids with high chlorine activity, under moderately to highly oxidising acid conditions (Romberger, 1988; Wood and Samson, 1998).

The physico-chemical conditions of the hydrothermal fluids during Au deposition at Batouri can be deciphered from features of the deposit such as: the dominantly sulfide hydrothermal ore mineralogy; highly sericitised wall-rock; and mineralisation temperatures of  $>250^\circ\text{C}$ . These features match those of reducing mesothermal fluids at near-neutral pH (Romberger, 1988; Groves *et al.*, 1998, Ridley and Diamond, 2000), in which Au is likely transported mainly as a bisulfide complex (Romberger, 1988; Hayashi and Ohmoto, 1991; Wood and Samson, 1998).

The identity of the stoichiometry of the major Au(I) bisulfide complex species responsible for Au transport in hydrothermal deposits is still a contentious issue. Disagreement has largely been over the stoichiometry of the dominant Au(I) bisulfide species in acidic hydrothermal fluids. Proposed species include  $\text{Au}(\text{HS})^\circ$  (Seward, 1973; Benning and Seward, 1996),

$\text{HAu}(\text{HS})_2^\circ$  (Hayashi and Ohmoto, 1991), and  $\text{AuHS}(\text{H}_2\text{S})_3^\circ$  (Loucks and Mavrogenes, 1999).

The experiments of Loucks and Mavrogenes (1999), which were conducted under high temperatures (550–725°C) and variable pressures (100–400 kbar), were aimed at identifying the stoichiometry of the stable complex species in strongly acidic hydrothermal fluids. The results of the measurements are presented in a bivariate plot of temperature versus Au concentration (Figure 4.17). The plotted contours were extrapolated to the lower limit temperatures expected for mesothermal systems. In this experiment  $\text{AuHS}(\text{H}_2\text{S})_3^\circ$  was considered to be the dominant species at all temperatures under high pressures (>300 MPa). However, the concentration of  $\text{Au}(\text{HS})^\circ$  increased with decrease in temperature and pressure. In a recent review of the available thermodynamic data, Pokrovski *et al.* (2009) suggested that  $\text{HAu}(\text{HS})_2^\circ$ , proposed by Hayashi and Ohmoto (1991), is the most thermodynamically stable Au(I) bisulfide complex species in strongly acidic hydrothermal fluids.

On the other side of the spectrum are the strongly alkaline hydrothermal solutions in which, Au is likely to be transported in the form  $\text{Au}_2(\text{HS})_2\text{S}^{2-}$  (Seward, 1973; Romberger, 1988).

Between the acid and alkaline fluid compositions are the near-neutral hydrothermal fluids, which are characteristic of mesothermal (or orogenic) deposits (Groves *et al.*, 1998; Ridley and Diamond, 2000). Seward (1973) identified the stoichiometry of the most stable Au complex species in these fluids to be  $\text{Au}(\text{HS})_2^-$ . Results of subsequent investigations (Shenberger and Barnes, 1989; Hayashi and Ohmoto, 1991; Benning and Seward, 1996; Stefánsson and Seward, 2004; Tagirov *et al.*, 2005; Tagirov *et al.*, 2006) have not diverged from this formula, and the solubility of Au in the near-neutral fluids is expressed by:

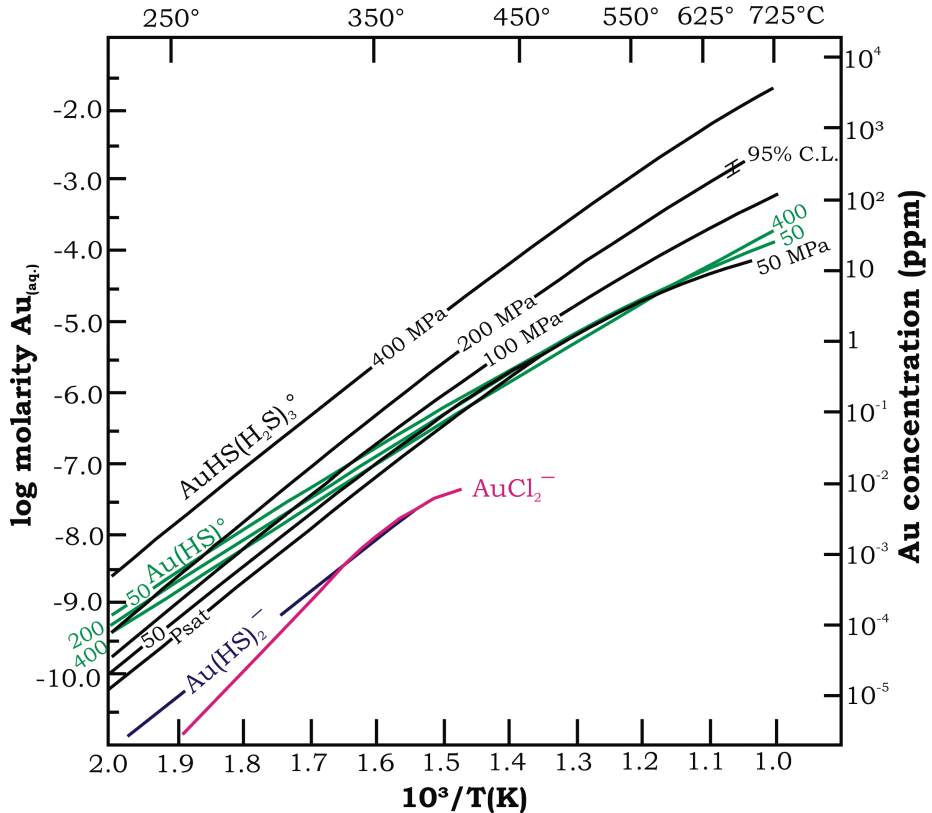
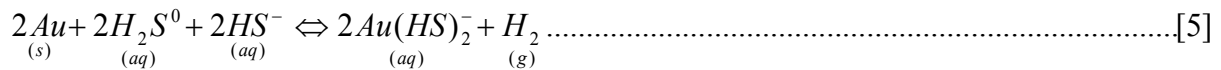


**Figure 4.17:** Solubility of the major Au complexes in acid (or <5.5 pH) hydrothermal fluids at variable pressures. C.L. stands for confidence limit of measurements. The diagram shows that  $\text{AuHS}(\text{H}_2\text{S})_3^\circ$  is the dominant complex responsible for Au transport in a wide temperature and pressure regime for low pH systems. Another important Au-carrying complex under these conditions is  $\text{Au}(\text{HS})^\circ$ . The pyrrhotite-magnetite-pyrite (PMP) buffer was used to fix the redox state of the fluid. Diagram has been adapted from Loucks and Mavrogenes (1999).

The stability of the species  $\text{Au}(\text{HS})_2^-$  in near-neutral fluids is illustrated by the pH versus solubility plot of Pokrovski *et al.* (2009) shown in Figure 4.18. This diagram shows the increasing compositional dominance of  $\text{Au}(\text{HS})_2^-$  over acid-stable  $\text{AuHS}^\circ$  as the pH tends more towards neutrality. Due to the near-neutral pH deduced for hydrothermal fluids associated with Au mineralisation at Batouri, it is probable that  $\text{Au}(\text{HS})_2^-$  was the dominant Au complex responsible for Au transport.

The chemistry of gold and other ore minerals from Batouri shows the significant presence of Ag in these minerals, indicating that it was an

important component of the hydrothermal fluid. Contrary to Au, the dominant aqueous species for Ag in near-neutral and reducing solutions is a chloride complex (Morrison *et al.*, 1991).

Several physico-chemical changes take place in hydrothermal fluids as they rise along flow pathways. These changes can destabilise Au complexes, resulting in their breakdown and eventual precipitation of Au-bearing sulfides and native gold. Sulfidation of the wall-rock by hydrothermal fluids is as one of the processes that can trigger gold deposition from hydrothermal fluids. This process was, evidently, widespread in the wall-rock at Batouri and appears to have played an important role in gold deposition.

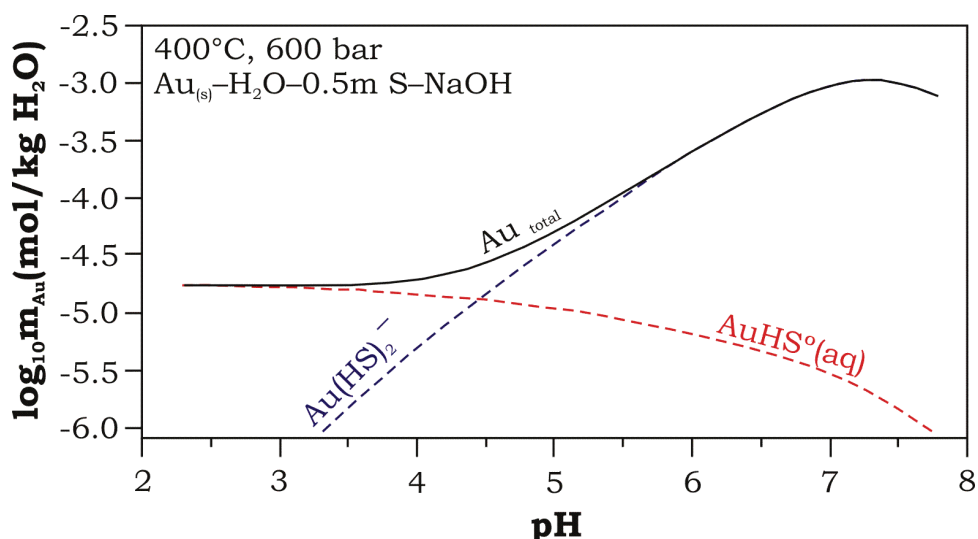


**Figure 4.18:** The solubility of Au(I) bisulfide complex species in aqueous solution as a function of pH at 400 °C and 600 bars.  $\text{AuHS}^\circ(\text{aq})$  is more soluble at acidic pH, but its peak solubility is still much less than the solubility of  $\text{Au}(\text{HS})_2^-$  attained at pH ~7.5. The diagram has been taken from Pokrovski *et al.* (2009).

However, it is unlikely that wall-rock sulfidation was the only mechanism that influenced gold deposition at Batouri. Unmixing of parent Au-bearing homogeneous aqueous-carbonic fluids, implicated by Robert and Kelly (1987) for triggering gold deposition at the Sigma Mine Quebec in Canada, has been noted by Goldfarb *et al.* (2005) as one of the important ore-forming processes in quartz vein-hosted gold deposits. This process, with or without metal-precipitating mechanisms such as temperature

decrease and mixing of hypogene fluids with infiltrating water from external sources, may have contributed to gold deposition during the late stages of hydrothermal activity.

#### **4.8 Summary**

Hydrothermal minerals were deposited from reducing aqueous–carbonic fluids, in three main phases at temperatures between 250 and 420°C. The dominant hydrothermal minerals are pyrite and sphalerite. Gold was transported predominantly as a bisulfide complex. Desulfidation of hydrothermal fluids by Fe-bearing minerals in the wall-rock triggered the main gold precipitation phase. However, late deposition of electrum on gold indicates another gold deposition mechanism during the late stages, which favoured the deposition of both gold and silver.

## **CHAPTER 5: GEOCHRONOLOGY**

### **5.1 Introduction**

The ages of the Batouri granites reported in the literature have been speculative, as no geochronological studies have been conducted in the area in the past. Suh *et al.* (2006) proposed a genetic link between gold mineralisation in the Batouri granites, and the greenstone belts of the Congo Craton outcropping in the Ntem complex. They cited a gold mineralisation age of  $2374 \pm 188$  Ma, inferred from the whole-rock Rb–Sr dating of host granite at the Dondo Mobi gold deposit in Gabon, reported by Prian *et al.* (1988). Milési *et al.* (2006), in their review paper on the geology and ore deposits of central Africa, situated Batouri within the Pan-African (Neoproterozoic) mobile belt, albeit without geochronological evidence. In this chapter, U–Pb ages of zircon and Ar–Ar ages of K-feldspar from the Batouri granites, as well as Ar–Ar ages of hydrothermal muscovite related to the gold mineralisation, are presented.

### **5.2 U–Pb dating of granites at Kambélé mines**

U–Pb isotope analyses were performed on zircon grains obtained from stream sediments (sample GC) and wall-rock (sample HR) sampled at an active gold mining site at Kambélé III. The analyses were done at the Geological Survey of Denmark and Greenland (GEUS) in Copenhagen, Denmark, by laser ablation-magnetic sectorfield-inductively coupled plasma-mass spectrometry (LA-SF-ICP-MS) technique, following the procedure described in Frei and Gerdes (2009). The zircon grains analysed were mostly euhedral, exhibited bipyramidal habits and attained lengths of up to 400  $\mu\text{m}$ . They displayed magmatic textures, with no evidence for inherited zircons (See Figures 5.1 and 5.2). Growth zones revealed equant habits at the centre of some zircon grains (e.g. HR-01 in Figure 5.1). Grains were clear and generally colourless, with a few brown-tinted crystals.

## CHAPTER 5: GEOCHRONOLOGY

Thirty spot analyses were performed on 22 zircon crystals from sample GC and 25 analyses on 20 crystals from sample HR. The results are shown in Tables 5.1 and 5.2, respectively. Wetherill Concordia plots (Figures 5.3 and 5.4) were constructed from these results using the Isoplot 3.0 software in Microsoft Excel. The plots yielded good concordant ages of  $624 \pm 2$  Ma for sample GC and  $619 \pm 2$  Ma for sample HR.

## CHAPTER 5: GEOCHRONOLOGY

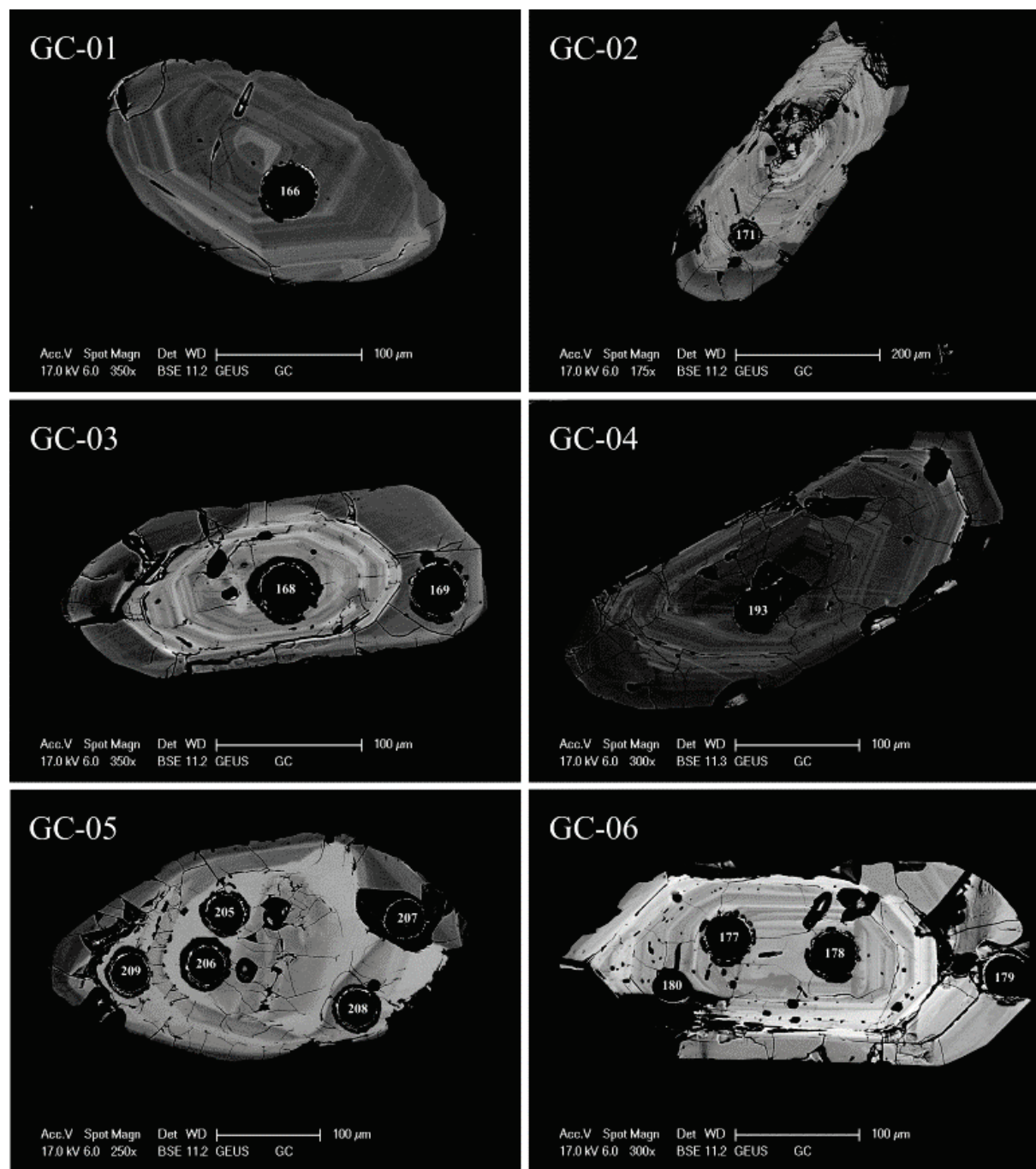


**Figure 5.1:** Back-scattered images of selected analysed GC zircon grains. Laser pits are about 40 µm in diameter. Numbers in pits refer to corresponding annotation in Tables 5.1

## CHAPTER 5: GEOCHRONOLOGY

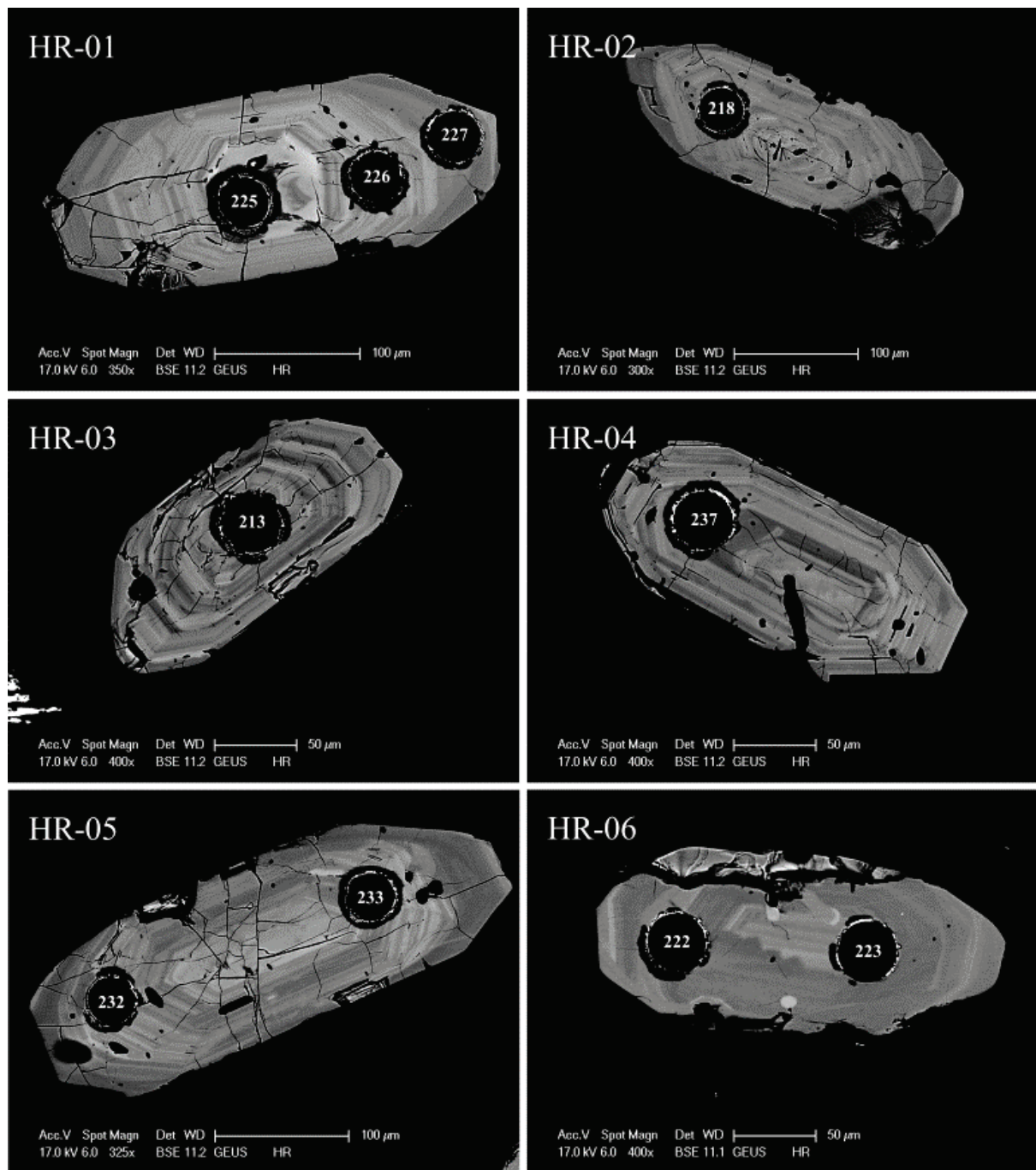


**Figure 5.2:** Back-scattered images of selected analysed HR zircon grains. Laser pits are about 40 µm in diameter. Numbers in pits refer to corresponding annotation in Tables 5.2.

**Table 5.1:** LA-SF-ICP-MS U-Pb zircon analytical data for GC samples from Kambélé in Batouri, Cameroon.

Analyses Number	$^{207}\text{Pb}^a$ [cps]	$U^b$ [ppm]	$\text{Pb}^b$ [ppm]	$^{206}\text{Pb}/^{204}\text{Pb}$	$\text{Th}/\text{U}$	Atomic Ratios						Ages [Ma]						Conc. [%] <sup>e</sup>	BSE	Remark	
						$^{207}\text{Pb}/^{235}\text{U}^c$	2 s [%] <sup>e</sup>	$^{206}\text{Pb}/^{238}\text{U}^c$	2 s [%] <sup>e</sup>	$\text{rho}^d$	$^{207}\text{Pb}/^{206}\text{Pb}^f$	2 s [%] <sup>e</sup>	$^{207}\text{Pb}/^{235}\text{U}$	2 s	$^{206}\text{Pb}/^{238}\text{U}$	2 s	$^{207}\text{Pb}/^{206}\text{Pb}$	2 s			
GC-163	14680	295	32	2400	0.33	0.8493	4.4	0.1014	2.4	0.56	0.0608	3.6	624	27	622	15	631	39	100		
GC-164	4894	103	12	1869	0.77	0.8414	3.3	0.1018	2.3	0.70	0.0600	2.3	620	20	625	14	602	25	101		
GC-165	7074	140	17	2344	1.09	0.8407	7.2	0.1006	3.6	0.50	0.0606	6.2	620	44	618	22	626	67	100		
GC-166	10387	168	22	842	1.33	0.8586	4.8	0.1024	2.7	0.56	0.0608	4.0	629	30	628	17	633	43	100	GC-01	
GC-167	43057	567	65	315	0.61	0.8427	3.6	0.1021	2.3	0.64	0.0599	2.7	621	22	627	14	599	30	101		
GC-168	28991	561	63	1896	0.76	0.8295	3.0	0.0998	2.3	0.76	0.0603	1.9	613	18	613	14	614	21	100	GC-03	core
GC-169	6504	141	14	2297	0.56	0.8453	6.0	0.1012	2.9	0.48	0.0606	5.3	622	38	622	18	623	57	100	GC-03	rim
GC-170	66378	348	53	89	0.92	0.8462	8.1	0.1013	2.7	0.34	0.0606	7.7	623	51	622	17	624	83	100		
GC-171	8298	138	16	1300	0.73	0.8834	4.3	0.1050	2.9	0.68	0.0610	3.2	643	28	644	19	640	34	100	GC-02	
GC-172	21504	395	44	1163	0.56	0.8589	4.4	0.1029	3.1	0.71	0.0605	3.1	630	28	631	20	623	33	100		
GC-177	19012	385	42	4599	0.62	0.8440	3.3	0.1011	2.7	0.81	0.0605	1.9	621	20	621	17	623	21	100	GC-06	core left
GC-178	15594	246	27	525	1.32	0.8267	5.4	0.0990	2.7	0.49	0.0606	4.7	612	33	609	16	623	51	99	GC-06	core right
GC-179	20263	411	46	3090	0.71	0.8610	3.2	0.1024	2.4	0.73	0.0610	2.2	631	20	628	15	639	24	100	GC-06	core right
GC-180	7141	144	17	2908	0.91	0.8592	3.3	0.1031	2.4	0.73	0.0604	2.3	630	21	633	15	619	24	100	GC-06	core left
GC-181	20964	404	45	2024	0.80	0.8359	3.7	0.0997	2.4	0.64	0.0608	2.9	617	23	613	15	632	31	99		
GC-182	14003	277	34	3104	1.16	0.8382	3.2	0.1006	2.3	0.71	0.0604	2.3	618	20	618	14	618	25	100		
GC-183	13582	99	14	162	1.24	0.8686	5.7	0.1032	2.2	0.38	0.0610	5.2	635	36	633	14	640	56	100		
GC-184	35681	271	42	160	1.36	0.8716	4.9	0.1037	3.2	0.65	0.0610	3.7	636	31	636	20	638	40	100		
GC-185	27020	417	48	623	0.76	0.8353	3.9	0.1002	2.3	0.58	0.0605	3.2	617	24	615	14	620	35	100		
GC-193	6760	142	19	8240	1.24	0.8604	3.3	0.1026	2.8	0.84	0.0608	1.8	630	21	630	18	633	19	100	GC-04	
GC-194	21094	385	42	817	0.53	0.8387	3.8	0.1005	2.6	0.69	0.0605	2.7	618	24	617	16	622	30	100		
GC-198	4942	97	11	9124	0.65	0.8835	3.3	0.1036	2.6	0.79	0.0619	2.0	643	21	635	17	669	22	99		
GC-199	9837	198	21	5664	0.48	0.8473	2.8	0.1009	2.2	0.78	0.0609	1.8	623	18	619	14	637	19	99		
GC-200	10279	192	22	2606	0.53	0.8691	3.0	0.1041	2.3	0.76	0.0605	2.0	635	19	638	15	623	21	101		
GC-201	11033	198	21	1053	0.54	0.8581	3.7	0.1030	2.3	0.62	0.0604	2.9	629	23	632	14	619	31	100		
GCS1-205	43326	994	102	9302	0.32	0.8418	1.8	0.1007	1.6	0.86	0.0606	0.9	620	11	619	10	625	10	100	GC-05	core
GCS2-206	46360	1067	110	32200	0.32	0.8416	1.7	0.1018	1.6	0.91	0.0600	0.7	620	11	625	10	603	8	101	GC-05	core
GCS3-207	6135	129	13	3695	0.39	0.8496	4.3	0.1016	2.6	0.62	0.0607	3.3	624	27	624	16	627	36	100	GC-05	rim
GCS4-208	16721	381	37	9537	0.16	0.8556	2.0	0.1022	1.5	0.76	0.0607	1.3	628	13	627	10	630	14	100	GC-05	rim
GCS5-209	37586	797	79	2569	0.28	0.8472	1.9	0.1015	1.5	0.80	0.0605	1.1	623	12	623	9	623	12	100	GC-05	rim

**Table 5.2:** LA-SF-ICP-MS U-Pb zircon analytical data for HR samples from Kambélé in Batouri, Cameroon.

Analyses Number	$^{207}\text{Pb}^a$ [cps]	$U^b$ [ppm]	$\text{Pb}^b$ [ppm]	$^{206}\text{Pb}/^{204}\text{Pb}$	Th/U	Atomic Ratios						Ages [Ma]						Conc [%] <sup>e</sup>	BSE	Remark	
						$^{207}\text{Pb}/^{235}\text{U}^c$	2 s [%] <sup>e</sup>	$^{206}\text{Pb}/^{238}\text{U}^c$	2 s [%] <sup>e</sup>	$\text{rho}^d$	$^{207}\text{Pb}/^{206}\text{Pb}^f$	2 s [%] <sup>e</sup>	$^{207}\text{Pb}/^{235}\text{U}$	2 s [Ma]	$^{206}\text{Pb}/^{238}\text{U}$	2 s	$^{207}\text{Pb}/^{206}\text{Pb}$	2 s			
HR 210	17995	733	82	2207	0.64	0.8426	2.3	0.1007	1.8	0.78	0.0607	1.5	621	14	619	11	628	16	100		
HR 211	5922	248	28	10516	0.66	0.8598	2.7	0.1031	2.0	0.74	0.0605	1.8	630	17	633	13	620	20	100		
HR 212	4002	174	21	3536	0.92	0.8421	3.3	0.1006	2.5	0.75	0.0607	2.2	620	21	618	15	629	24	100		
HR 213	6118	267	28	4412	0.39	0.8431	2.4	0.1008	1.6	0.65	0.0607	1.8	621	15	619	10	627	20	100	HR-03	
HR 214	4198	180	21	3047	0.94	0.8349	4.6	0.1001	1.7	0.37	0.0605	4.2	616	28	615	10	621	46	100		
HR 218	5914	257	29	48908	0.71	0.8395	2.9	0.1006	1.8	0.62	0.0605	2.2	619	18	618	11	623	24	100	HR-02	
HR 219	13348	598	62	42985	0.39	0.8380	2.8	0.1006	1.8	0.66	0.0604	2.1	618	17	618	11	618	22	100		
HR 221	9381	393	43	1813	0.60	0.8447	4.3	0.1013	2.9	0.68	0.0605	3.2	622	27	622	18	620	34	100		
HR 222	18055	766	84	4450	0.54	0.8677	4.0	0.1033	3.5	0.86	0.0609	2.0	634	25	634	22	637	22	100	HR-06	left
HR 223	12986	505	55	1589	0.64	0.8499	2.9	0.1013	1.7	0.60	0.0609	2.3	625	18	622	11	635	25	100	HR-06	right
HR 224	37532	1427	156	1757	0.53	0.8593	2.8	0.1025	2.3	0.80	0.0608	1.7	630	18	629	14	632	18	100		
HR 225	56281	2507	274	3434	0.32	0.8361	2.5	0.1007	2.0	0.80	0.0602	1.5	617	15	619	12	611	16	100	HR-01	Core
HR 226	22802	885	100	1627	0.73	0.8479	3.6	0.1011	2.3	0.63	0.0608	2.8	624	22	621	14	634	30	100	HR-01	Middle
HR 227	7394	315	34	18222	0.55	0.8411	2.8	0.1005	2.0	0.73	0.0607	1.9	620	17	617	13	628	21	100	HR-01	Rim
HR 231	12902	532	49	3083	0.07	0.8190	2.1	0.0986	1.6	0.79	0.0602	1.3	608	13	606	10	613	14	100		
HR 232	56495	2278	322	2826	0.25	0.8417	2.5	0.1016	2.1	0.81	0.0601	1.5	620	16	624	13	606	16	101	HR-05	Middle left
HR 233	17595	725	78	3868	0.59	0.8339	3.2	0.0994	2.6	0.80	0.0609	1.9	616	20	611	16	634	21	99	HR-05	Middle right
HR 234	23347	979	106	2635	0.70	0.8351	2.5	0.1000	1.6	0.64	0.0606	2.0	616	16	614	10	625	21	100		
HR 235	21160	665	82	730	1.14	0.8486	3.7	0.1016	3.3	0.90	0.0606	1.6	624	23	624	21	625	18	100		
HR 236	11514	430	46	1250	0.96	0.8283	3.2	0.0994	2.4	0.74	0.0604	2.2	613	20	611	15	619	23	100		
HR 237	14499	583	63	2935	0.60	0.8417	3.0	0.1007	2.2	0.71	0.0606	2.1	620	19	618	13	626	23	100	HR-04	
HR 238	9555	411	42	3171	0.43	0.8322	4.1	0.1000	1.8	0.44	0.0604	3.7	615	25	614	11	617	39	100		
HR 239	15578	657	75	3710	0.69	0.8571	2.8	0.1026	2.0	0.70	0.0606	2.0	629	18	629	12	625	22	100		
HR 240	14587	628	68	25267	0.61	0.8394	3.1	0.1005	2.0	0.65	0.0606	2.4	619	19	617	12	625	25	100		

## CHAPTER 5: GEOCHRONOLOGY

Parameters used during calculations:

<sup>a</sup> Within-run background-corrected mean  $^{207}\text{Pb}$  signal in counts per second [cps]

<sup>b</sup> U and Pb concentrations and Th/U ratios are calculated relative to GJ-1 reference zircon

<sup>c</sup> Corrected for background and within-run Pb/U fractionation and normalised to reference zircon GJ-1 (ID-TIMS values/measured value);  $^{207}\text{Pb}/^{235}\text{U}$  calculated using  $(^{207}\text{Pb}/^{206}\text{Pb})/(^{238}\text{U}/^{206}\text{Pb} * 1/137.88)$

<sup>d</sup> Rho is the error correlation defined as the quotient of the propagated errors of the  $^{206}\text{Pb}/^{238}\text{U}$  and the  $^{207}\text{Pb}/^{235}\text{U}$  ratio

<sup>e</sup> Quadratic addition of within-run errors (2 SD) and daily reproducibility of GJ-1 (2SD)

<sup>f</sup> Corrected for mass-bias by normalising to GJ-1 reference zircon (~0.6 per atomic mass unit) and common Pb using the model Pb composition of Stacey & Kramers (1975)

<sup>g</sup> Degree of concordance =  $(^{206}\text{Pb}/^{238}\text{U} \text{ age} * 100)/(^{207}\text{Pb}/^{235}\text{U} \text{ age})$

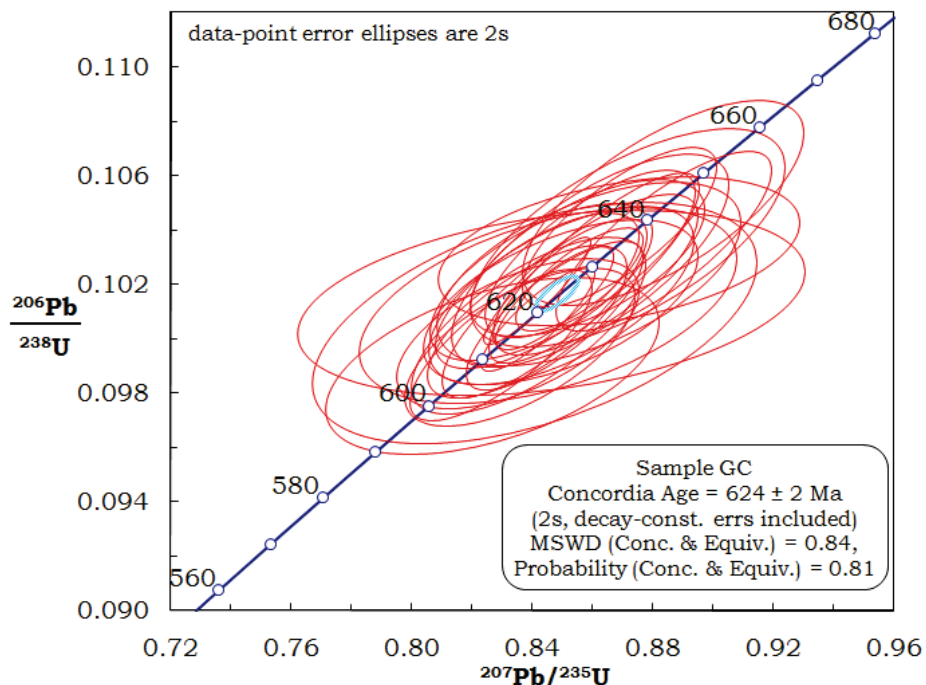


**Figure 5.3:** Wetherill concordia diagram depicting results for 30 U-Pb spot measurements of zircon grains obtained from stream sediments in the mining area by LA-SF-ICP-MS. The blue ellipse in the centre of the group represents the weighted mean error ellipse.

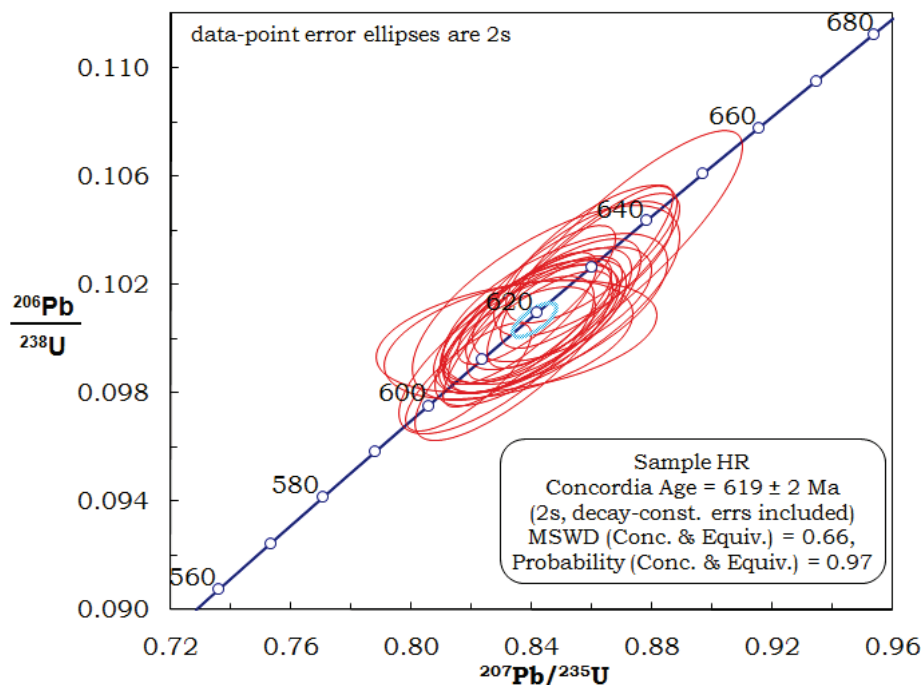


**Figure 5.4:** Wetherill concordia diagram depicting results for 24 U-Pb spot measurements of zircon grains obtained from host rock (monzogranite) by LA-SF-ICP-MS. The blue ellipse in the centre of the group represents the weighted mean error ellipse.

### 5.2.1 Interpretation of U-Pb geochronology

The spot analyses from each sample are normally distributed, indicating the absence of inherited zircon cores. Also, the results from both samples show that their  $^{207}\text{Pb}/^{235}\text{U}$ ,  $^{206}\text{Pb}/^{238}\text{U}$  and  $^{207}\text{Pb}/^{206}\text{Pb}$  ages are in agreement. These ages serve as an internal check for consistency (Richards and Noble, 1998), and agreement between them shows that the U-Pb system has remained closed since the crystallisation of zircon (Faure, 1986; Dickin, 1995; Richards and Noble, 1998). Sample GC, having been collected from stream sediments, represents a wider area than sample HR, which was collected from wall-rock at Kambélé III. The results show good concordant ages of  $624 \pm 2$  Ma for sample GC and  $619 \pm 2$  Ma for sample HR, as shown on Figures 5.3 and 5.4. The age difference between the two samples is not geologically significant and probably represents the same granite emplacement event.

These early mid-Neoproterozoic ages confirm that the Batouri granites were emplaced during the Pan-African orogeny in southeastern Cameroon.

The study area is replete with enclaves of older biotite gneiss, so the apparent absence of inherited zircon in the studied samples may be due to limited sampling. The stability of the U–Pb system in the zircon shows that hydrothermal activity did not affect zircon.

### **5.3 Ar–Ar dating of Bougogo granites and hydrothermal muscovite from the Dimako mining sites**

Argon–argon dating is a variant of the K–Ar geochronological technique described in detail by Faure (1986). Samples for Ar–Ar dating were obtained from the Bougogo granite outcrop (BAT-1: K-feldspar separate, and BAT-2: K-feldspar granite whole-rock), and from the Dimako mines (MNC-1: white mica from sapropelite, and MNC-2: white mica from weathered wall-rock). These samples were analysed by the Ar–Ar stepped-heating technique at the School of Earth, Atmospheric and Environmental Sciences of the University of Manchester, United Kingdom. The analyses were done according to the procedure described in Hennig *et al.* (2008).

The analytical results for BAT-1, BAT-2, MNC-1 and MNC-2 are shown in Table 5.3 and 5.4. The essential feature of the data is the absence of a plateau, as no three or more consecutive steps carry more than 50% of the total  $^{39}\text{Ar}$  released (see Baksi, 2006). The K-feldspar (BAT-1) gives a relatively flat age spectrum at about 630–640 Ma, while the whole-rock (BAT-2) gives a more complex spectrum of rising ages reaching a peak at 590 Ma (Figure 5.5).

The white mica samples (MNC-1 and MNC-2) were obtained from the regolith, due to the unavailability of fresh rock samples with sufficient white mica. Chemical analyses of these samples reveal significant loss of potassium due to weathering (Table 3.3), implying a significant loss of Ar as well. The results of the  $^{40}\text{Ar}$ – $^{39}\text{Ar}$  analyses of the mica, shown in Table 5.5 and Figure 5.6 depict similar age spectral trends for the samples, with peak ages of 480 Ma. Isochron plots for these data displayed very high scatter, recording mean square of weighted deviates (MSWD) of 20 and more, and were discarded.

### 5.3.1 Interpretation of Ar–Ar geochronology

BAT-1 and BAT-2 were sampled at the surface of the Bougogo K-feldspar granite outcrop, and the open system behaviour they exhibit is probably due to the effects of weathering. However, BAT-1 gives a more defined age spectrum for this granite (630–640 Ma). Even though the Ar–Ar system is clearly disturbed, the derived age roughly corresponds to the U–Pb concordant ages (620–624 Ma) for the Kambélé granite.

White mica also exhibits open system behaviour as can be expected. However, its  $^{40}\text{Ar}$ – $^{39}\text{Ar}$  ages would not have been affected if argon loss did not exceed 20% (see Mitchell and Taka, 1984). This does not seem to be the case with MNC-1 and MNC-2, which display significant disturbance of the Ar–Ar system. Due to the open-system behaviour displayed by the muscovite, the 480 Ma it yields is interpreted here as the minimum possible age for hydrothermal vein formation and gold mineralisation. It is not possible with these samples to determine accurate ages of the hydrothermal events, but the minimum age of 480 Ma suggests that gold mineralisation occurred earlier, probably during Neoproterozoic times, coincidental with the final stages of the Pan-African orogeny.

**Table 5.3:**  $^{40}\text{Ar}$ - $^{39}\text{Ar}$  stepped heating data for K-feldspar from Batouri.

Temperature (°C)	$^{36}\text{Ar}$ (cc)	$\pm^{36}\text{Ar}$ cc)	$^{39}\text{Ar}$ (cc)	$\pm^{39}\text{Ar}$ (cc)	$^{40}\text{Ar}$ (cc)	$\pm^{40}\text{Ar}$ (cc)	$^{40}\text{Ar}^*$ (moles)	$\pm^{40}\text{Ar}^*$ (moles)	Cl (moles)	$\pm\text{Cl}$ (moles)	K (moles)	$\pm\text{K}$ (moles)	Age (Ma)	$\pm\text{Age}$ (Ma)
<b>J value = 0.01010135 +/- 0.000027</b>														
<b>BAT-1 (K-Feldspar) / mass = 0.0144 g</b>														
600	9.61E-11	8.60E-13	7.39E-10	5.52E-13	3.32E-08	2.06E-11	2.14E-13	9.99E-16	6.86E-09	4.76E-11	2.66E-07	7.36E-10	114.66	5.89
700	6.91E-12	7.20E-13	6.62E-12	1.69E-13	6.39E-10	9.75E-12	-6.27E-14	1.84E-15	-9.27E-12	1.03E-11	2.38E-09	6.13E-11	nd	
800	2.95E-12	7.00E-13	1.16E-11	2.25E-13	1.15E-09	1.48E-12	1.24E-14	9.10E-16	1.29E-10	1.05E-11	4.17E-09	8.16E-11	393.40	262.71
900	8.39E-12	7.87E-13	4.39E-10	4.88E-13	1.96E-08	2.49E-11	7.66E-13	1.26E-15	3.67E-09	3.01E-11	1.58E-07	4.56E-10	601.90	6.96
940	1.50E-11	1.11E-12	1.57E-09	1.72E-12	6.74E-08	1.17E-10	2.81E-12	3.27E-15	1.17E-08	7.16E-11	5.65E-07	1.63E-09	615.81	2.84
965	4.59E-12	7.60E-13	1.68E-09	1.65E-12	6.98E-08	8.14E-11	3.05E-12	3.15E-15	1.23E-08	6.96E-11	6.04E-07	1.72E-09	623.69	1.77
980	7.67E-13	9.58E-13	2.28E-09	2.33E-12	9.46E-08	1.26E-10	4.21E-12	4.42E-15	1.67E-08	9.31E-11	8.21E-07	2.34E-09	631.67	1.68
990	2.22E-12	1.02E-12	2.09E-09	2.33E-12	8.67E-08	1.60E-10	3.84E-12	4.41E-15	1.53E-08	8.60E-11	7.52E-07	2.17E-09	628.83	2.06
1000	2.89E-12	6.77E-13	2.15E-09	2.14E-12	8.91E-08	1.02E-10	3.94E-12	4.01E-15	1.57E-08	8.93E-11	7.72E-07	2.20E-09	628.48	1.25
1015	2.65E-12	1.11E-12	2.46E-09	3.12E-12	1.02E-07	1.15E-10	4.53E-12	5.85E-15	1.81E-08	1.03E-10	8.86E-07	2.61E-09	630.11	1.80
1030	2.43E-12	1.02E-12	2.88E-09	3.08E-12	1.19E-07	1.49E-10	5.29E-12	5.77E-15	2.11E-08	1.17E-10	1.03E-06	2.97E-09	629.66	1.44
1040	3.26E-12	9.03E-13	2.78E-09	2.99E-12	1.15E-07	1.41E-10	5.10E-12	5.58E-15	2.04E-08	1.15E-10	1.00E-06	2.87E-09	629.06	1.33
1055	3.89E-12	9.32E-13	2.09E-09	2.19E-12	8.72E-08	9.98E-11	3.84E-12	4.14E-15	1.53E-08	8.78E-11	7.53E-07	2.16E-09	628.54	1.74
1070	4.65E-12	1.01E-12	1.74E-09	1.89E-12	7.27E-08	7.27E-11	3.18E-12	3.61E-15	1.28E-08	7.50E-11	6.28E-07	1.81E-09	625.53	2.23
1100	3.71E-12	1.11E-12	1.57E-09	1.60E-12	6.61E-08	7.30E-11	2.90E-12	3.15E-15	1.16E-08	6.53E-11	5.66E-07	1.61E-09	630.54	2.70
1140	3.89E-12	7.55E-13	2.04E-09	2.14E-12	8.61E-08	1.03E-10	3.79E-12	4.09E-15	1.58E-08	8.77E-11	7.35E-07	2.10E-09	634.50	1.48
1175	4.72E-12	8.18E-13	3.06E-09	1.89E-12	1.30E-07	8.08E-11	5.73E-12	3.66E-15	3.28E-08	1.79E-10	1.10E-06	3.02E-09	638.41	1.06
1200	3.21E-12	8.01E-13	3.81E-09	2.89E-12	1.61E-07	7.51E-11	7.13E-12	5.49E-15	4.41E-08	2.42E-10	1.37E-06	3.80E-09	639.08	0.87
1250	1.24E-11	1.64E-12	6.41E-09	4.35E-12	2.70E-07	1.34E-10	1.19E-11	8.16E-15	7.04E-08	3.89E-10	2.31E-06	6.34E-09	633.43	1.02
1300	5.37E-12	6.50E-13	2.88E-09	1.35E-12	1.21E-07	6.72E-11	5.33E-12	2.63E-15	2.43E-08	1.37E-10	1.04E-06	2.80E-09	633.04	0.88
1400	1.99E-11	7.16E-13	2.03E-09	1.22E-12	8.65E-08	6.07E-11	3.60E-12	2.33E-15	1.15E-08	6.75E-11	7.31E-07	2.00E-09	610.09	1.41
1500	7.76E-11	7.54E-13	3.14E-10	2.52E-13	1.64E-08	8.61E-12	-2.93E-13	9.13E-16	8.79E-10	2.43E-11	1.13E-07	3.15E-10	nd	
<i>Total</i>										8.08E-11	1.90E-14	3.81E-07	6.05E-10	1.62E-05
<i>No plateau</i>												1.17E-08	616.74	0.38

**Table 5.4:**  $^{40}\text{Ar}$ - $^{39}\text{Ar}$  stepped heating data for granite (whole rock) from Batouri.

## CHAPTER 5: GEOCHRONOLOGY

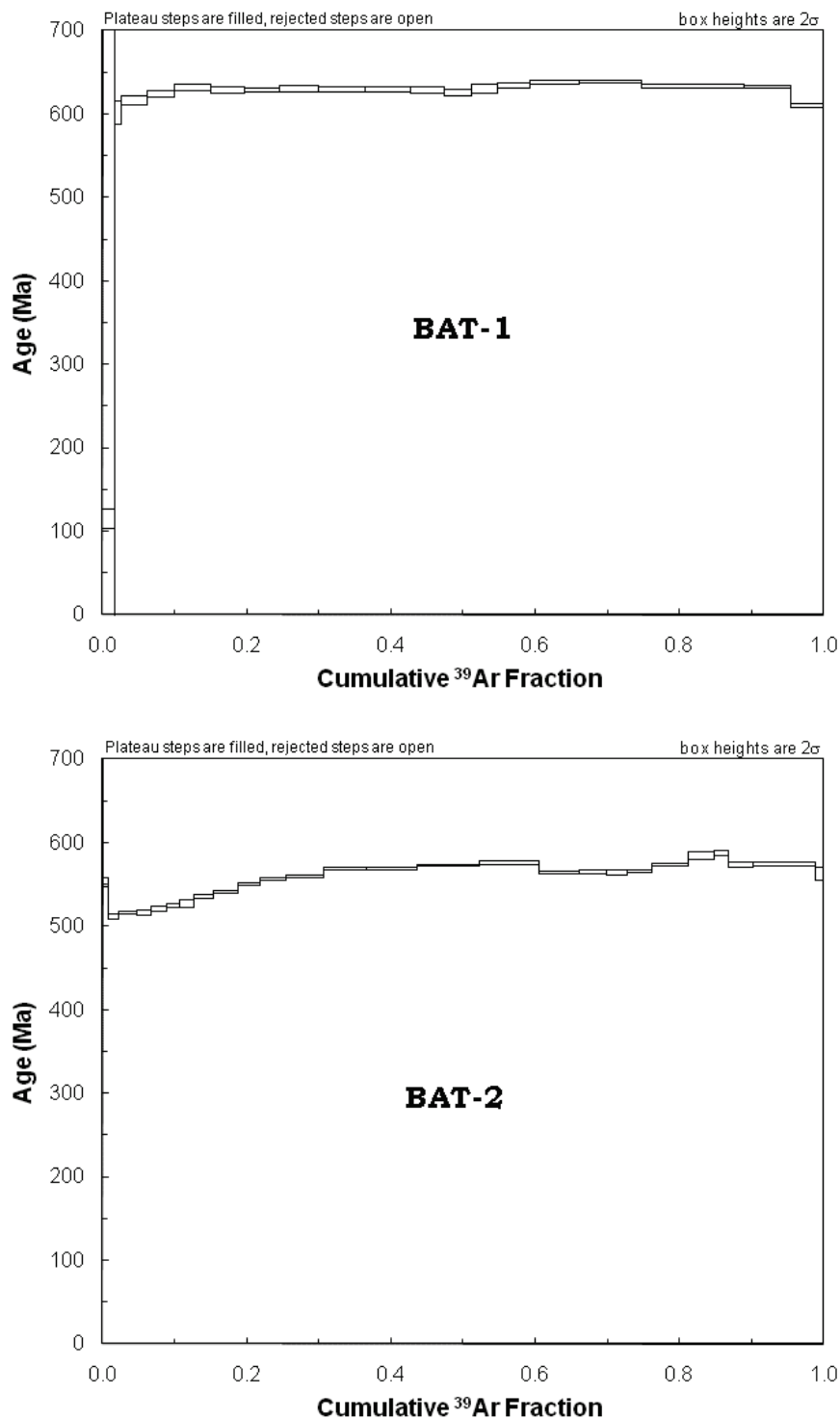


**Figure 5.5:** Ar-Ar age spectra for K-feldspar (BAT-1) and alkali-feldspar granite (BAT-2) sampled at the Bougogo outcrop located in northern Batouri. Error boxes are shown at the  $2\sigma$  level of uncertainty.

**Table 5.5:**  $^{40}\text{Ar}$ - $^{39}\text{Ar}$  stepped heating data for weathered hydrothermal white mica from Batouri.

Temperature (°C)	$^{36}\text{Ar}$ (cc)	$\pm^{36}\text{Ar}$ cc)	$^{39}\text{Ar}$ (cc)	$\pm^{39}\text{Ar}$ (cc)	$^{40}\text{Ar}$ (cc)	$\pm^{40}\text{Ar}$ (cc)	$^{40}\text{Ar}^*$ (moles)	$\pm^{40}\text{Ar}^*$ (moles)	Cl (moles)	$\pm\text{Cl}$ (moles)	K (moles)	$\pm\text{K}$ (moles)	Age (Ma)	$\pm\text{Age}$ (Ma)
<b>J value = 0.01010135 +/- 0.000027</b>														
<b>MNC1 (weathered hydrothermal muscovite) / Mass = 0.00584 g</b>														
500	1.09E-11	9.61E-13	5.20E-12	4.38E-13	3.00E-09	2.60E-12	-1.01E-14	1.31E-15	1.64E-10	2.14E-11	1.87E-09	1.58E-10	nd	nd
600	8.03E-12	5.08E-13	1.92E-11	3.35E-13	2.15E-09	4.46E-12	-9.97E-15	7.78E-16	2.85E-10	2.63E-11	6.89E-09	1.22E-10	nd	nd
700	1.26E-11	7.36E-13	1.41E-10	8.78E-13	4.75E-09	6.33E-12	4.57E-14	9.43E-16	1.08E-09	2.11E-11	5.06E-08	3.44E-10	128.40	26.37
800	4.53E-11	7.33E-13	8.63E-10	9.23E-13	2.57E-08	2.88E-11	5.50E-13	1.06E-15	3.03E-09	2.57E-11	3.10E-07	8.91E-10	244.09	4.01
850	4.61E-11	8.37E-13	2.32E-09	2.44E-12	5.42E-08	7.03E-11	1.81E-12	2.13E-15	6.53E-09	4.32E-11	8.36E-07	2.40E-09	293.65	1.69
875	3.77E-11	7.60E-13	2.86E-09	2.84E-12	7.50E-08	7.79E-11	2.85E-12	2.97E-15	8.05E-09	4.68E-11	1.03E-06	2.92E-09	368.47	1.18
900	1.19E-11	9.49E-13	1.57E-09	1.70E-12	4.34E-08	4.25E-11	1.78E-12	2.12E-15	4.35E-09	3.13E-11	5.64E-07	1.62E-09	413.71	2.61
925	1.48E-11	1.06E-12	1.33E-09	1.35E-12	4.13E-08	5.16E-11	1.65E-12	1.99E-15	3.84E-09	3.27E-11	4.78E-07	1.36E-09	448.34	3.40
950	9.80E-12	6.91E-13	8.19E-10	1.11E-12	2.64E-08	2.78E-11	1.05E-12	1.62E-15	2.52E-09	2.19E-11	2.95E-07	8.80E-10	461.18	3.56
1000	1.15E-11	9.40E-13	1.80E-09	1.87E-12	5.78E-08	7.52E-11	2.43E-12	2.70E-15	5.36E-09	3.11E-11	6.48E-07	1.85E-09	481.40	2.20
1025	4.85E-12	1.02E-12	6.24E-10	8.16E-13	1.98E-08	1.99E-11	8.19E-13	1.49E-15	1.68E-09	2.46E-11	2.24E-07	6.66E-10	470.84	6.83
1075	1.60E-11	5.69E-13	5.58E-10	8.72E-13	1.96E-08	1.96E-11	6.65E-13	1.30E-15	1.38E-09	1.31E-11	2.01E-07	6.20E-10	432.12	4.37
1150	1.19E-11	9.16E-13	5.67E-10	7.96E-13	1.87E-08	1.94E-11	6.79E-13	1.34E-15	1.47E-09	2.36E-11	2.04E-07	6.14E-10	434.31	6.88
1250	6.91E-12	6.32E-13	5.94E-10	6.70E-13	1.76E-08	1.99E-11	6.95E-13	1.13E-15	1.70E-09	2.22E-11	2.14E-07	6.19E-10	424.89	4.55
1400	6.40E-12	7.60E-13	1.48E-10	4.91E-13	6.23E-09	8.19E-12	1.93E-13	1.08E-15	3.43E-10	1.69E-11	5.33E-08	2.26E-10	468.90	21.45
<i>Total</i>							1.52E-11	6.65E-15	4.18E-08	1.09E-10	5.11E-06	5.06E-09	392.05	0.98
<b>No plateau</b>														
<b>MNC2 (weathered hydrothermal muscovite) / Mass = 0.0078 g</b>														
600	2.26E-11	8.55E-13	6.26E-11	4.15E-13	6.61E-09	2.13E-11	-2.35E-15	9.85E-16	9.76E-10	1.53E-11	2.25E-08	1.61E-10	nd	nd
700	8.37E-12	1.17E-12	1.76E-10	6.14E-13	4.69E-09	3.61E-12	9.88E-14	1.20E-15	1.80E-09	2.03E-11	6.32E-08	2.78E-10	216.82	31.79
800	2.90E-11	7.32E-13	1.74E-09	1.35E-12	3.87E-08	3.42E-11	1.35E-12	1.39E-15	7.24E-09	4.39E-11	6.25E-07	1.74E-09	292.45	1.96
850	5.75E-11	9.58E-13	3.74E-09	4.89E-12	8.42E-08	1.46E-10	3.00E-12	4.07E-15	1.25E-08	8.08E-11	1.35E-06	3.99E-09	301.93	1.35
875	1.47E-11	6.02E-13	2.28E-09	1.94E-12	5.63E-08	3.78E-11	2.32E-12	2.13E-15	7.69E-09	4.79E-11	8.21E-07	2.30E-09	374.79	1.19
900	8.81E-12	8.64E-13	1.47E-09	1.27E-12	3.97E-08	2.78E-11	1.65E-12	1.74E-15	4.84E-09	2.87E-11	5.28E-07	1.48E-09	411.43	2.55
950	1.15E-11	9.55E-13	1.94E-09	2.13E-12	5.77E-08	5.19E-11	2.42E-12	2.85E-15	6.90E-09	4.26E-11	6.99E-07	2.01E-09	450.28	2.13
1000	1.10E-11	1.09E-12	1.93E-09	1.61E-12	6.11E-08	3.32E-11	2.58E-12	2.39E-15	6.73E-09	5.11E-11	6.95E-07	1.94E-09	478.24	2.36
1050	6.72E-12	1.07E-12	9.68E-10	9.91E-13	2.91E-08	1.70E-11	1.21E-12	1.65E-15	3.10E-09	2.27E-11	3.48E-07	9.94E-10	450.47	4.67
1100	9.11E-12	9.16E-13	5.17E-10	7.88E-13	1.59E-08	8.95E-12	5.88E-13	1.35E-15	1.67E-09	2.26E-11	1.86E-07	5.71E-10	414.24	7.62
1200	6.32E-12	7.08E-13	4.81E-10	7.10E-13	1.41E-08	9.97E-12	5.48E-13	1.20E-15	1.52E-09	2.73E-11	1.73E-07	5.27E-10	415.37	6.34
1400	4.03E-12	7.91E-13	1.81E-10	8.88E-13	5.72E-09	3.56E-12	2.02E-13	1.36E-15	5.79E-10	4.99E-11	6.50E-08	3.64E-10	408.37	18.95
<i>Total</i>							1.60E-11	7.08E-15	5.55E-08	1.45E-10	5.57E-06	6.00E-09	377.94	0.91
<b>No plateau</b>														

## CHAPTER 5: GEOCHRONOLOGY

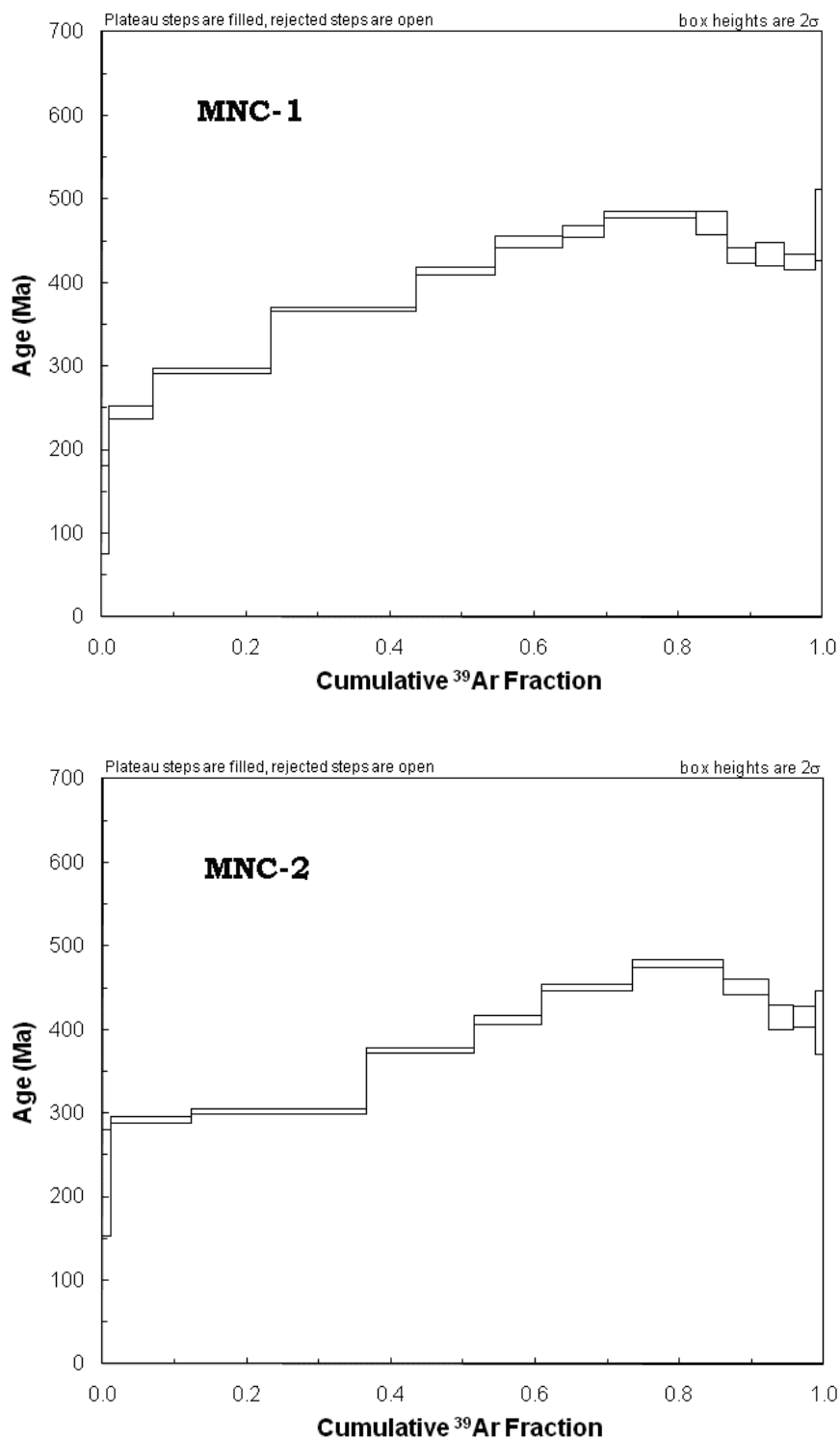


**Figure 5.6:** Ar-Ar age spectra for muscovite from saprolite (mine dump) (MNC-1) and weathered wall-rock (MNC-2) at the Dimako mine. Error boxes are shown at the  $2\sigma$  level of uncertainty.

## 5.4 Discussion of U-Pb and Ar-Ar geochronology

An overview of the geodynamic setting of Batouri is necessary in the discussion of the geochronological data. Batouri is situated in the Adamawa-Yadé domain (AY; Figure 1.4) of the Central African Fold Belt (CAFB; Figure 1.4) in Cameroon. This belt is understood to be a juxtaposition of recycled and juvenile lithologies extending north of the Congo Craton (Milési *et al.*, 2006), and related to a subduction zone that evolved from the collision of West African Craton with the Congo Craton (Toteu *et al.*, 2004). This collision induced crustal thickening, high-grade metamorphism of the intervening volcano-sedimentary sequences, and calc-alkaline magmatism between 640–610 Ma (Toteu *et al.*, 2004). The Adamawa-Yadé domain is dominated by the 640–610 Ma plutons, which are syn- to late-collisional high-K calc-alkaline granitoids intruding high-grade gneisses (Toteu *et al.*, 2004; Tanko Njiosseu *et al.*, 2005; Van Schmus *et al.*, 2008). These granites make up the main lithological unit at Batouri, and the high-grade gneiss they intruded occurs as biotite gneiss enclaves of variable sizes in the plutons. The 640–620 Ma ages obtained from these granites place Batouri at the centre stage of collisional magmatism in eastern Cameroon.

Granitoids of similar age as the Batouri granitoids have been reported at other locations in the Adamawa-Yadé domain, e.g. the 639±20 Ma Landou granite in Tchollire (Pinna *et al.*, 1994); the Yaoundé domain (Y; Figure 1.4), e.g. the 639±16 Ma monzogranite at Tina (Toteu *et al.*, 2006c); and the North-West Cameroon domain (NWC; Figure 1.4), e.g. the 638±1 Ma granitoid at Lere (Penaye *et al.*, 2006). Reported ages of inherited zircon (Toteu *et al.*, 2006b) from 600 Ma granitoids in the Yaoundé domain (e.g. Elon, Ngaa Mbappe and Tina granitoids) indicate that magmas generated during the nappe tectonics incorporated 635–620 Ma zircons derived from similarly aged granitoids assimilated by the magma (Toteu *et al.*, 2006b, 2006c). Samarium-neodymium ( $T_{\text{DM}}$ ) model ages of 2.2 to 1.4 Ga have been recorded at multiple locations in the AY domain (Figure 1.5; Toteu *et al.*, 2001, 2006c). However, due to the occurrence of 2.8 Ga and 2.0 Ga detrital

zircon in metasedimentary sequences at Bangbei and Betare Oya, these apparent Palaeo- and Mesoproterozoic model ages are probably the result of the mixture of Archaean to late-Mesoproterozoic crustal material with Neoproterozoic juvenile material.

In the Borborema Province, which is the Brazilian equivalent for the CAFB, there is no equivalent for the AY domain (Van Schmus *et al.*, 2008). However, granitoids in the 620–640 Ma age range are significantly present in the Sergipano, Transverse, and Pernambuco-Alagoas domains (Galindo *et al.*, 1995; Van Schmus *et al.*, 2008).

Goldfarb (2001) noted that significant gold-forming events occurred in the late Neoproterozoic (beginning at 600 Ma) as part of the Pan-African–Braziliano orogeny. Shear zone controlled lode gold deposited during this period, occurs at several locations along the Pan-African orogenic belt. Examples include:

1. the N-trending Ouzzal shear zone-hosted Amesmesssa and Tirek gold deposits in Algeria, formed at 611 and 575 Ma, respectively (Ferkous and Monie, 2002);
2. the 545 Ma Lega Dembi gold deposit in Ethiopia, hosted by N-trending D<sub>2</sub> shear zones (Ghebreab *et al.*, 1992; Billay *et al.*, 1997); and
3. the NNE-trending shear zone-hosted São Francisco gold deposit in the Seridó, Belt northeastern Brazil, formed at 580±30 Ma (Araújo *et al.*, 2002).

These deposits were all formed in multiple stages, during the final phase of the Pan-African–Braziliano orogeny, by the intrusion of gold-bearing quartz veins along N- to NE-trending D<sub>2</sub> deformation structures similar to the Batouri shear zone. Gold mineralisation at Batouri occurred before 480 Ma, and may have coincided with final stages of the Pan-African orogeny.

## 5.5 Summary

Uranium–lead dating of zircon from the monzogranite at Kambélé and Ar–Ar dating of K-feldspar and whole-rock K-feldspar granite from Bougogo yield crystallisation ages of 620 to 640 Ma for the Batouri granitoids. These ages confirm that the rocks were formed during the Pan-African orogeny. Argon–Argon dating of white mica from the hydrothermal gold system are inconclusive, but sets a minimum age of 480 Ma.

## **CHAPTER 6: CONCLUSIONS AND RECOMMENDATIONS**

### **6.1 Conclusions**

Gold mineralisation at Batouri occurs within felsic to intermediate granitoid rocks, rich in ferromagnesian minerals and iron-bearing oxides. These rocks consist of hornblende- and biotite-bearing syeno-monzogranites and granodiorite. The mineralisation is confined, as quartz veins and disseminations in the wall-rock, along N35°-trending, steeply dipping shear zones and secondary structures. The main quartz veins are discontinuous, with individual segments having thicknesses of up to 70 cm and attaining lengths of ~15 m. The mineralisation corridor extends for 13 km from Dem to Dimako, and ranges in width from about 100 metres to 1 kilometre.

The gold content of veins exceeds 30 g/t in places, while the wall-rock contain up to ~19 g/t gold. Primary gold is present in pyrite and arsenopyrite, either as invisible gold (refractory ore), or as visible gold. Free gold occurs along microfractures in quartz. Visible gold is the dominant mode of gold occurrence at Batouri and contains significant amounts of silver, with some mercury. It displays concentric zoning of primary and supergene origins. About 70% by volume of the Batouri gold has fineness values between 803 and 875.

The gold-bearing veins are composed predominantly of quartz, with subordinate carbonate and sulphides. The proximal and distal wall-rock alterations are characterised by dominant white mica and chlorite compositions, respectively. Vein ore mineralogy and microthermometry of vein quartz-hosted fluid inclusions, further suggest that reduced aqueous-carbonic fluids were the main gold-mineralising fluid at Batouri. Dissemination of gold in the wall-rock implies that wall-rock alteration was important in triggering gold precipitation. In this sense, sulfidation is likely the wall-rock alteration process that triggered gold precipitation. Other processes such unmixing of the parent hydrothermal fluid, decrease in

temperature, and/or mixing of hypogene fluids with water from external sources, could have contributed to gold deposition at late stages of hydrothermal activity. Ore deposition occurred at temperatures  $>300^{\circ}\text{C}$ , with visible gold deposited at lower temperatures. Based on sulfide chemistry and wall-rock alteration, important path finder elements for gold at Batouri would include silver, arsenic and sulfur.

The granitic host rocks at Batouri have geochemical characteristics of continental arc magmatism. The 640–620 Ma ages obtained from the rocks place Batouri at the centre of granitic magmatism associated with the Pan-African orogeny. On a regional scale, the magmatic rocks are thought to be juxtaposed with recycled crust (Milési *et al.*, 2006), derived from Archean to late-Mesoproterozoic sources (Toteu *et al.*, 2006c). The Batouri gold mineralisation was post-620 Ma and pre-480 Ma. It probably coincided with the major ore-forming events that occurred towards the end of the Pan-African orogeny (~600 Ma), cf. Goldfarb *et al.* (2001). A proposed genetic model of gold mineralisation at Batouri is illustrated in Figure 6.1.

The geotectonic setting, structural controls, hydrothermal alteration mineralogy, ore mineralogy and fluid inclusion characteristics, all indicate that the gold mineralisation at Batouri corresponds to the orogenic (or mesothermal) gold-type deposit spectrum (Groves *et al.*, 1998; Bierlein and Crowe, 2000; Hagemann and Cassidy, 2000; Partington and Williams, 2000; Ridley and Diamond, 2000; Groves *et al.*, 2003; Goldfarb *et al.*, 2005).

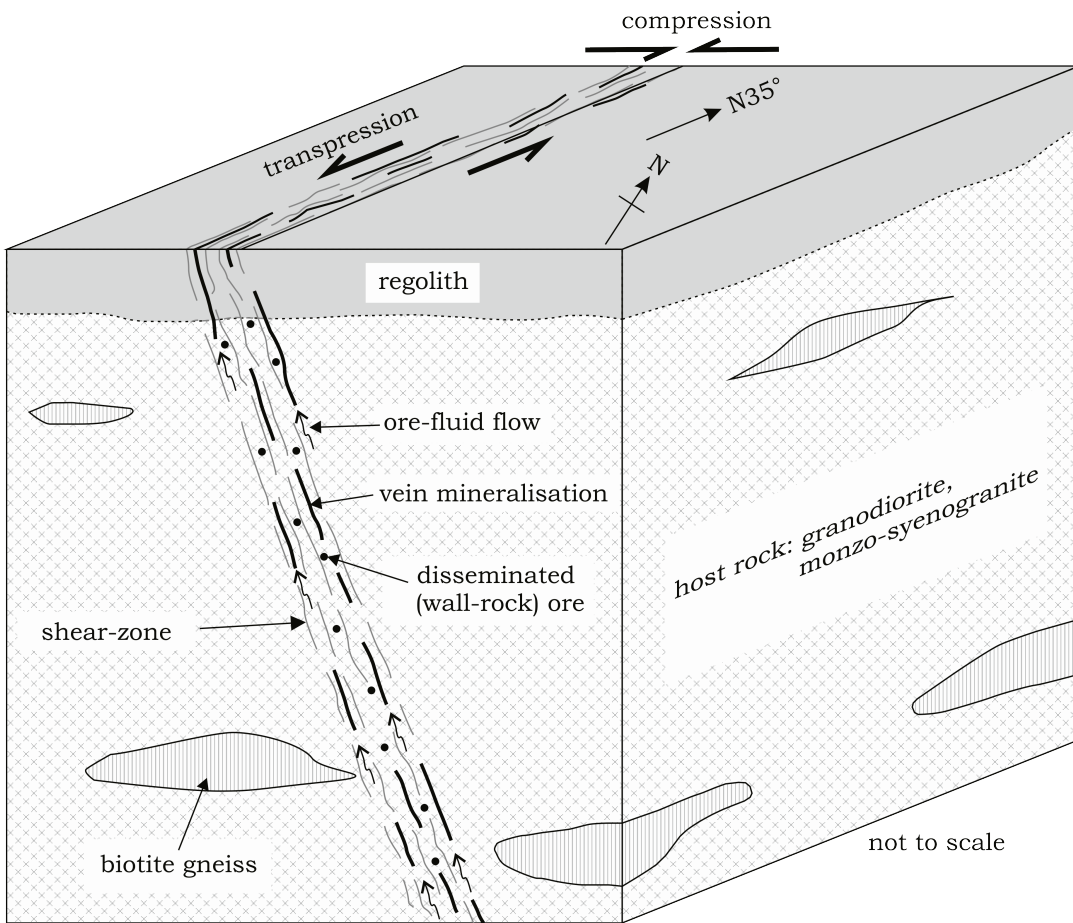


**Figure 6.1:** Block diagram illustrating the genetic model for gold mineralisation proposed for Batouri. Ore-fluid sources are not defined in the diagram.

## 6.1 Recommendations

No detailed geological mapping has been conducted in the area, so the geology and detailed structural configuration of the area are largely unknown. The lack of a well-defined geological context necessarily limits the understanding of the geology of the gold mineralisation at Batouri. It is, therefore, strongly recommended that detailed geological mapping of the Batouri area be conducted. Such a study would form the basis for more detailed characterisation of primary gold mineralisation, and would also facilitate ore reserve estimation. In view of the wall-rock alteration, quartz-carbonate veins and associated alteration haloes could serve as important guides to gold exploration at Batouri and the surrounding areas. Key path finder elements include S, As and Ag.

## REFERENCES

- Abdelsalam M. G., Liégeois J.-P., and Stern R. J. (2002) The Saharan Metacraton. *Journal of African Earth Sciences* **34**(3-4), 119-136.
- Achoundong G. (2007) Vegetation. In *Atlas of Cameroon* (eds. N. Houstin and C. Seignobos), pp. 64-65. Les Éditions Jeune Afrique, Paris.
- African Aura Mining (2009) *Batouri gold project, Cameroon*. African Aura Resources (UK) Ltd., London. <http://www.african-aura.com/s/Batouri.asp> Accessed on March 7, 2009.
- Araújo M. N. C., Alves da Silva F. C., Jardim de Sá E. F., and Holcombe R. J. (2002) Geometry and structural control of gold vein mineralizations in the Seridó Belt, northeastern Brazil. *Journal of South American Earth Sciences* **15**(3), 337-348.
- Ayers J. C. and Watson E. B. (1991) Solubility of apatite, monazite, zircon, and rutile in supercritical aqueous fluids with implications for subduction zone geochemistry. *Philosophical Transactions of the Royal Society of London. Series A: Physical and Engineering Sciences* **335**(1638), 365-375.
- Ayonghe S. N., Ntasin E. B., Samalang P., and Suh C. E. (2004) The June 27, 2001 landslide on volcanic cones in Limbe, Mount Cameroon, West Africa. *Journal of African Earth Sciences* **39**(3-5), 435-439.
- Bailey S. W. (1980) Summary of recommendations of AIPSA Nomenclature Committee on clay minerals. *American Mineralogist* **65**(1-2), 1-7.
- Bakker R. J. (2003) Package FLUIDS 1. Computer programs for analysis of fluid inclusion data and for modelling bulk fluid properties. *Chemical Geology* **194**(1-3), 3-23.
- Baksi A. K. (2006) *Guidelines for assessing the reliability of <sup>40</sup>Ar/<sup>39</sup>Ar plateau ages: Application to ages relevant to hotspot tracks*. Mantle Plumes. <http://www.mantleplumes.org/ArAr.html> Accessed on September 7, 2009.
- Barbarin B. (1996) Genesis of the two main types of peraluminous granitoids, pp. 295-298.
- Barton Jr P. B. (1969) Thermochemical study of the system Fe-As-S. *Geochimica et Cosmochimica Acta* **33**(7), 841-857.
- Bayliss P. (1975) Nomenclature of the trioctahedral chlorites. *Canadian Mineralogist* **13**(2), 178-180.
- Benedetti M. and Boulègue J. (1991) Mechanism of gold transfer and deposition in a supergene environment. *Geochimica et Cosmochimica Acta* **55**(6), 1539-1547.
- Benning L. G. and Seward T. M. (1996) Hydrosulphide complexing of Au (I) in hydrothermal solutions from 150-400°C and 500-1500 bar. *Geochimica et Cosmochimica Acta* **60**(11), 1849-1871.
- Bierlein F. P. and Crowe D. E. (2000) Phanerozoic orogenic lode gold deposits. In *Gold in 2000* (eds. S. G. Hagemann and P. E. Brown), pp. 103-139. Society of Economic Geologists, Inc., Littleton.
- Billay A. Y., Kisters A. F. M., Meyer F. M., and Schneider J. (1997) The geology of the Lega Dembi gold deposit, southern Ethiopia:

## REFERENCES

- implications for Pan-African gold exploration. *Mineralium Deposita* **32**(5), 491-504.
- Brown P. E. (1998) Fluid inclusion modeling for hydrothermal systems. In *Techniques in hydrothermal ore deposits geology* (ed. J. P. R. a. P. B. Larson), pp. 151-171. Society of Economic Geologists, Inc, Littleton.
- Brownfield M. E. and Charpentier R. R. (2006) *Geology and total petroleum systems of the West-Central Coastal Province (7203), West Africa*. U.S. Geological Survey (U.S. Department of the Interior), Reston. <http://www.usgs.gov/bul/2207/B/> Accessed on 17th October, 2009.
- Burgess R., Kiviet G. B., and Harris J. W. (2004) Ar-Ar age determinations of eclogitic clinopyroxene and garnet inclusions in diamonds from the Venetia and Orapa kimberlites. *Lithos* **77**(1-4), 113-124.
- Burrows D. R. and Spooner E. T. C. (1987) Generation of a magmatic H<sub>2</sub>O-CO<sub>2</sub> fluid enriched in Au, Mo, and W within an Archean sodic granodiorite stock, Mink Lake, northwestern Ontario. *Economic Geology* **82**(7), 1931-1957.
- Cabri L. J., Newville M., Gordon R. A., Crozier E. D., Sutton S. R., McMahon G., and Jiang D.-T. (2000) Chemical speciation of gold in arsenopyrite. *Canadian Mineralogist* **38**(5), 1265-1281.
- Cathelineau M. (1988) Cation site occupancy in chlorites and illites as a function of temperature. *Clay Minerals* **23**(December), 471-485.
- Cathelineau M. and Nieva D. (1985) A chlorite solid solution geothermometer the Los Azufres (Mexico) geothermal system. *Contributions to Mineralogy and Petrology* **91**(3), 235-244.
- Cawthorn R. G. and Brown P. A. (1976) A Model for the formation and crystallization of corundum-normative calc-alkaline magmas through amphibole fractionation. *The Journal of Geology* **84**(4), 467-476.
- Cepedal A., Fuertes-Fuente M., Martin-Izard A., Gonzalez-Nistal S., and Barrero M. (2008) Gold-bearing As-rich pyrite and arsenopyrite from the El Valle gold deposit, Asturias, northwestern Spain. *Canadian Mineralogist* **46**, 233-247.
- Choi S.-G. and Youm S.-J. (2000): Compositional variation of arsenopyrite and fluid evolution at the Ulsan Deposit, southeastern Korea: A low-sulfidation porphyry system. *Can Mineral* **38**(3), 567-583.
- CIA (2009) *World Factbook*. CIA, Washington, D.C. <https://www.cia.gov/library/publications/the-world-factbook/geos/cm.html> Accessed on 29th October, 2009.
- Colin F. and Vieillard P. (1991) Behavior of gold in the lateritic equatorial environment: weathering and surface dispersion of residual gold particles, at Dondo Mobi, Gabon. *Applied Geochemistry* **6**(3), 279-290.
- Colin F., Vieillard P., and Ambrosi J. P. (1993) Quantitative approach to physical and chemical gold mobility in equatorial rainforest lateritic environment. *Earth and Planetary Science Letters* **114**(2-3), 269-285.
- Cooke D. R. and Simmons S. F. (2000) Characteristics and genesis of epithermal gold deposits. In *Gold in 2000* (eds. S. G. Hagemann and P. E. Brown), pp. 221-244. Society of Economic Geologists Inc., Littleton.

## REFERENCES

- Coté A. J. (1999) A trigger mechanism for the Lake Nyos disaster. *Journal of Volcanology and Geothermal Research* **88**(4), 343-347.
- De Caritat P., Hutcheon I., and Walshe J. L. (1993) Chlorite geothermometry; a review. *Clays and Clay Minerals* **41**(2), 219-239.
- De Souza Z. S., Martin H., Peucat J.-J., Jardim De Sa E. F., and Macedo M. H. D. F. (2007) Calc-alkaline magmatism at the Archean Proterozoic Transition: the Caico Complex Basement (NE Brazil), pp. 2149-2185.
- de Wit M. J., de Brito Neves B. B., Trouw R. A. J., and Pankhurst R. J. (2008) Pre-Cenozoic correlations across the South Atlantic region: (the ties that bind). *Geological Society, London, Special Publications* **294**(1), 1-8.
- Deer W. A., Howie R. A., and Zussman J. (1992) *An Introduction to the rock forming minerals*. Pearson Education Limited, Essex. pp. 696.
- Dickin A. P. (1995) *Radiogenic isotope geology*. Cambridge University Press, Cambridge. pp. 452.
- Dubé B., Williamson K., Mcnicoll V., Malo M., Skulski T., Twomey T., and Sanborn-Barrie M. (2004) Timing of gold mineralization at Red Lake, northwestern Ontario, Canada: new constraints from U-Pb geochronology at the Goldcorp high-grade zone, Red Lake Mine, and the Madsen Mine. *Economic Geology* **99**(8), 1611-1641.
- Duschek W., Kleinrahm R., and Wagner W. (1990) Measurement and correlation of the (pressure, density, temperature) relation of carbon dioxide II. Saturated-liquid and saturated-vapour densities and the vapour pressure along the entire coexistence curve. *The Journal of Chemical Thermodynamics* **22**(9), 841-864.
- Edwards A. D. and Bignell R. (1988) Nine major play types recognised in salt basin. *Oil and Gas Journal* **86**(51), 55-58.
- Eseme E., Agyingi C. M., and Foba-Tendo J. (2002) Geochemistry and genesis of brine emanations from Cretaceous strata of the Mamfe Basin, Cameroon. *Journal of African Earth Sciences* **35**(4), 467-476.
- Faure G. (1986) *Principles of isotope geology*. John Wiley & Sons. pp. 608.
- Ferkous K. and Monie P. (2002) Neoproterozoic shearing and auriferous hydrothermalism along the lithospheric N-S East In Ouzzal shear zone (Western Hoggar, Algeria, North Africa). *Journal of African Earth Sciences* **35**(3), 399-415.
- Feybesse J. L., Johan V., Maurizot P., and Abessolo A. (1986) Mise en évidence d'une nappe syn-métamorphe d'âge Eburnéen dans le partie Nord-Ouest du craton Zaïrois, Sud-Ouest Cameroun. In *Les formations birrimiennes en Afrique de l'Ouest, journée scientifique, compte rendu de conférence*, pp. 105-111. Occasional Publications-CIFEG.
- Feybesse J. L., Johan V., Triboulet C., Guerrot C., Mayaga-Mikolo F., Bouchot V., and Eko N'dong J. (1998) The West Central African belt: a model of 2.5-2.0 Ga accretion and two-phase orogenic evolution. *Precambrian Research* **87**(3-4), 161-216.

## REFERENCES

- Fitton J. G. (1980) The Benue trough and cameroon line -- A migrating rift system in West Africa. *Earth and Planetary Science Letters* **51**(1), 132-138.
- Fitton J. G. (1987) The Cameroon line, West Africa: a comparison between oceanic and continental alkaline volcanism. *Geological Society, London, Special Publications* **30**(1), 273-291.
- Fitton J. G. and Dunlop H. M. (1985) The Cameroon line, West Africa, and its bearing on the origin of oceanic and continental alkali basalt. *Earth and Planetary Science Letters* **72**(1), 23-38.
- Fitton J. G. and Underhill J. R. (2009) *Controls on the development of and evolution of the Cameroon Line, West Africa*. Grant Institute of Earth Science, School of Geosciences, The University of Edinburgh, Edinburgh.  
<http://www.geos.ed.ac.uk/postgraduate/PhD/getDocument?SerialNo=459> Accessed on 22nd October, 2009.
- Fleet M. E. and Mumin A. H. (1997) Gold-bearing arsenian pyrite and marcasite and arsenopyrite from Carlin Trend gold deposits and laboratory synthesis. *American Mineralogist* **82**(1-2), 182-193.
- Foster M. D. (1962) Interpretation of the composition and a classification of the chlorites. *Professional Paper* **414-A**, A1-A33.
- Frei D. and Gerdes A. (2009) Precise and accurate in situ U-Pb dating of zircon with high sample throughput by automated LA-SF-ICP-MS. *Chemical Geology* **261**(3-4), 261-270.
- Fyfe W. S. and Kerrich R. (1984) Gold: Natural concentration processes. In *Gold '82: The geology, geochemistry and genesis of gold deposits* (ed. R. P. Foster), pp. 99-127. A. A. Balkema, Rotterdam.
- Galindo A. C., Dall'Agnol R., McReath I., Lafon J. M., and Teixeira N. (1995) Evolution of Brasiliano-age granitoid types in a shear-zone environment, Umarizal-Caraubas region, Rio Grande do Norte, northeast Brazil. *Journal of South American Earth Sciences* **8**(1), 79-95.
- Gazel J. and Gérard G. (1954) Carte géologique de reconnaissance du Cameroun au 1/500 000, feuille Batouri-Est avec notice explicative., pp. Memoir. Direction Mines Géologie, Yaoundé, Cameroon.
- Gentry C. F. (2009) Cameroon a new destination for mining investment in Africa, pp. 28, Yaounde.
- George M. W. (2009) USGS Minerals yearbook 2007: Gold, pp. 31.1-31.14. U.S. Department of the Interior, US Geological Survey, Washington D.C.
- Ghebreab W., Yohannes E., and Giorgis L. W. (1992) The Lega Dembi gold mine: an example of shear zone-hosted mineralization in the Adola greenstone belt, Southern Ethiopia. *Journal of African Earth Sciences* **15**(3-4), 489-500.
- Ghogomu R., Moreau C., Brown W. L., and Rocc G. (1989) The Ntumbaw Complex, NW Cameroon: An atypicalanorogenic ring complex of intermediate composition. *Journal of African Earth Sciences* **8**(1), 1-9.

## REFERENCES

- Giere R. (1996) Formation of rare earth minerals in hydrothermal systems. In *Rare Earth Minerals, Chemistry, Origin and Ore Deposits* (eds. A. P. Jones, F. Wall, and C. T. Williams), pp. 105-150. Chapman and Hall, London.
- Goldfarb R. J., Baker T., Dubé B., Groves D. I., Hart C. J. R., and Gosselin P. (2005) Distribution, character, and genesis of gold deposits in metamorphic terranes. In *Economic Geology: One Hundreth Anniversary Volume* (eds. J. W. Hedenquist, J. F. H. Thompson, R. J. Goldfarb, and J. P. Richards), pp. 407 - 450. Society of Economic Geologists, Inc., Littleton, Colorado.
- Goldfarb R. J., Groves D. I., and Gardoll S. (2001) Orogenic gold and geologic time: a global synthesis. *Ore Geology Reviews* **18**(1-2), 1-75.
- Gosselin P. and Dubé B. (2005) Gold deposits of the world: distribution, geological parameters and gold content. Geological Survey of Canada, Open File 4895, 1 CD-ROM
- Green T. H. and Pearson N. J. (1986) Ti-rich accessory phase saturation in hydrous mafic-felsic compositions at high P,T. *Chemical Geology* **54**(3-4), 185-201.
- Grimm B. and Friedrich G. (1990) Weathering effects on supergene gold in soils of a semiarid environment, Gentio do Ouro, Brazil. *Chemical Geology* **84**(1-4), 70-73.
- Groves D. I., Goldfarb R. J., Gebre-Mariam M., Hagemann S. G., and Robert F. (1998) Orogenic gold deposits: A proposed classification in the context of their crustal distribution and relationship to other gold deposit types. *Ore Geology Reviews* **13**(1-5), 7-27.
- Groves D. I., Goldfarb R. J., Robert F., and Hart C. J. R. (2003) Gold deposits in metamorphic belts: overview of current understanding, outstanding problems, future research, and exploration significance. *Economic Geology* **98**(1), 1-29.
- Hagemann S. G. and Cassidy K. F. (2000) Archean orogenic lode gold deposits. In *Gold in 2000* (eds. S. G. Hagemann and P. E. Brown), pp. 9-68. Society of Economic Geologists, Inc, Littleton, Co.
- Halliday A. N., Dickin A. P., Fallick A. E., and Fitton J. G. (1988) Mantle dynamics: A Nd, Sr, Pb and O isotopic study of the Cameroon Line volcanic chain. *J. Petrology* **29**(1), 181-211.
- Hayashi K.-i. and Ohmoto H. (1991) Solubility of gold in NaCl-and H<sub>2</sub>S-bearing aqueous solutions at 250-350°C. *Geochimica et Cosmochimica Acta* **55**(8), 2111-2126.
- Heinhorst J., Lehmann B., and Seltmann S. (1996) New geochemical data on granitic rocks of central Kazakhstan. In *Granite-related ore deposits of central Kazakhstan and adjacent areas* (eds. V. Shatov, R. Seltmann, A. Kremenetsky, B. Lehmann, V. Popov, and P. Ermolov). Glagol Publishing House, St. Petersburg.
- Hennig D., Lehmann B., Burgess R., and Nekouvaght Tak M. A. (2008) Geology, geochemistry and <sup>40</sup>Ar/<sup>39</sup>Ar ages of the Cerro Millo

## REFERENCES

- epithermal high-sulfidation gold prospect, southern Peru. *Ore Geology Reviews* **34**(3), 304-316.
- Hey M. H. (1954) A new review of the chlorites. *Mineralogical Magazine* **30**, 277-292.
- Hough R. M., Butt C. R. M., Reddy S. M., and Verrall M. (2007) Gold nuggets: supergene or hypogene? *Australian Journal of Earth Sciences* **54**(7), 959-964.
- Hronsky J. M. A. and Groves D. I. (2009) Towards a unified model for magmatic-hydrothermal gold metallogeny with implications for orogenic gold. In *smart science for exploration and mining* (ed. P. J. Williams), pp. 102-104. Economic Geology Research Unit, James Cook University, Townsville, Australia.
- Irvine T. N. and Baragar W. R. A. (1971) A Guide to the chemical classification of the common volcanic rocks *Canadian Journal of Earth Sciences* **8**(5), 523-548.
- Ishihara S. (1977) The magnetite-series and ilmenite-series granitic rocks. *Mining Geology* **27**, 293-305.
- Ishihara S. (2004) The redox state of granitoids relative to tectonic setting and earth history: The magnetite-ilmenite series 30 years later. *Geological Society of America Special Papers* **389**, 23-33.
- Jensen E. P. and Barton M. D. (2000) Gold deposits related to alkaline magmatism. In *Gold in 2000* (eds. S. G. Hagemann and P. E. Brown), pp. 279-314. Society of Economic Geologists Inc., Littleton.
- Jourdan F., Verati C., and Féraud G. (2006) Intercalibration of the Hb3gr 40Ar/39Ar dating standard. *Chemical Geology* **231**(3), 177-189.
- Kamguia J., Manguelle-Dicoum A. E., Tabod A. C. T., and Tadjou A. J. M. (2005) Geological models deduced from gravity data in the Garoua basin, Cameroon. *Journal of Geophysics and Engineering* **2**(2), 147-152.
- Kinnaird J. (2008) Exploration reviews: Africa-Cameroon. In *SEG Newsletter*, pp. 24. Society of Economic Geologists, Inc., Littleton.
- Kishida A. and Kerrich R. (1987) Hydrothermal alteration zoning and gold concentration at the Kerr-Addison Archean lode gold deposit, Kirkland Lake, Ontario. *Economic Geology* **82**(3), 649-690.
- Klein E. L., Harris C., Giret A., and Moura C. A. V. (2007) The Cipóeiro gold deposit, Gurupi Belt, Brazil: Geology, chlorite geochemistry, and stable isotope study. *Journal of South American Earth Sciences* **23**(2-3), 242-255.
- Kornprobst J., Lasserre M., Rollet M., and Soba D. (1976) Existence au Cameroun d'un magmatisme alcalin Pan-Africain ou plus ancien: la syénite néphélinique de Nkonglong. Comparaison avec les roches alcalines connues dans la même région. *Bulletin Société Géologique de France* **18**(5), 1295-1305.
- Kranidiotis P. and MacLean W. H. (1987) Systematics of chlorite alteration at the Phelps Dodge massive sulfide deposit, Matagami, Quebec. *Economic Geology* **82**(7), 1898-1911.

## REFERENCES

- Krauskopf K. B. (1951) The solubility of gold. *Economic Geology* **46**(8), 858-870.
- Kretschmar U. and Scott S. D. (1976) Phase relations involving arsenopyrite in the system Fe-As-S and their application. *Can Mineral* **14**(3), 364-386.
- Kusakabe M., Ohsumi T., and Aramaki S. (1989) The Lake Nyos gas disaster: chemical and isotopic evidence in waters and dissolved gases from three Cameroonian crater lakes, Nyos, Monoun and Wum. *Journal of Volcanology and Geothermal Research* **39**(2-3), 167-185.
- Larizzatti J. H., Oliveira S. M. B., and Butt C. R. M. (2008) Morphology and composition of gold in a lateritic profile, Fazenda Pison "Garimpo", Amazon, Brazil. *Journal of South American Earth Sciences* **25**(3), 359-376.
- Lasserre M. and Soba D. (1976) Age libérien des granodiorites et des gneiss à pyroxènes du Cameroun méridional. *Bulletin Bureau National Recherches Minières* **2**, 17-32.
- Lee D.-C., Halliday A. N., Davies G. R., Essene E. J., Fitton J. G., and Temdjam R. (1996) Melt enrichment of shallow depleted mantle: a detailed petrological, trace element and isotopic study of mantle-derived xenoliths and megacrysts from the Cameroon Line. *J. Petrology* **37**(2), 415-441.
- Lerouge C., Cocherie A., Toteu S. F., Penaye J., Milesi J.-P., Tchameni R., Nsifa E. N., Mark Fanning C., and Deloule E. (2006) Shrimp U-Pb zircon age evidence for Paleoproterozoic sedimentation and 2.05 Ga syntectonic plutonism in the Nyong Group, South-Western Cameroon: consequences for the Eburnean-Transamazonian belt of NE Brazil and Central Africa. *Journal of African Earth Sciences* **44**(4-5), 413-427.
- Loucks R. R. and Mavrogenes J. A. (1999) Gold solubility in supercritical hydrothermal brines measured in synthetic fluid inclusions. *Science* **284**(5423), 2159-2163.
- Ludwig K. (2003) *Isoplot/Ex Version 3: A geochronological toolkit for Microsoft Excel*. Geochronology Center, Berkeley, USA.
- Luzzi-Arbouille T., Schmid E., and Piperi T. (2009) Recent discoveries offshore Douala Basin. *Search and Discovery* #**10185**.
- MacDonald G. A. and Katsura T. (1964) Chemical composition of Hawaiian lavas. *J. Petrology* **5**(1), 82-133.
- Maniar P. D. and Piccoli P. M. (1989) Tectonic discrimination of granitoids. *Geological Society of America Bulletin* **101**(5), 635-643.
- Mann A. W. (1984) Mobility of gold and silver in lateritic weathering profiles; some observations from Western Australia. *Economic Geology* **79**(1), 38-49.
- Marzoli A., Piccirillo E. M., Renne P. R., Bellieni G., Iacumin M., Nyobe J. B., and Tongwa A. T. (2000) The Cameroon Volcanic Line Revisited: Petrogenesis of continental basaltic magmas from lithospheric and asthenospheric mantle sources. *J. Petrology* **41**(1), 87-109.
- Mateer N. J., Wycisk P., Jacobs L. L., Brunet M., Luger P., Arush M. A., Hendriks F., Weissbrod T., Gvirtzman G., Mbede E., Dina A., Moody R.

## REFERENCES

- T. J., Weigelt G., El-Nakhal H. A., Hell J., and Stets J. (1992) Correlation of nonmarine Cretaceous strata of Africa and the Middle East. *Cretaceous Research* **13**(3), 273-318.
- Maurin J. C. and Guiraud R. (1990) Relationships between tectonics and sedimentation in the Barremo-Aptian intracontinental basins of Northern Cameroon. *Journal of African Earth Sciences* **10**(1-2), 331-340.
- McDowell S. D. and Elders W. A. (1980) Authigenic layer silicate minerals in borehole Elmore 1, Salton Sea Geothermal Field, California, USA. *Contributions to Mineralogy and Petrology* **74**(3), 293-310.
- Meinert L. D. (2000) Gold in skarns related to epizonal intrusions. In *Gold in 2000* (eds. S. G. Hagemann and P. E. Brown), pp. 347-375. Society of Economic Geologists Inc., Littleton.
- Mega Uranium (2009). The official website of Mega Uranium. <http://www.megauranium.com/main/index.php?cameroon> Accessed on 25th October, 2009.
- Meyer C. and Hemley J. J. (1967) Wall rock alteration. In *Geochemistry of hydrothermal ore deposits* (ed. H. L. Barnes), pp. 166-235. Holt, Rinehart and Winston, Inc., New York.
- Meyers J. B., Rosendahl B. R., Groschel-Becker H., Austin J. A., and Rona P. A. (1996) Deep penetrating MCS imaging of the rift-to-drift transition, offshore Douala and North Gabon basins, West Africa. *Marine and Petroleum Geology* **13**(7), 791-835.
- Milési J. P., Toteu S. F., Deschamps Y., Feybesse J. L., Lerouge C., Cocherie A., Penaye J., Tchameni R., Moloto-A-Kenguemba G., Kampunzu H. A. B., Nicol N., Duguey E., Leistel J. M., Saint-Martin M., Ralay F., Heinry C., Bouchot V., Doumnang Mbaiagne J. C., Kanda Kula V., Chene F., Monthel J., Boutin P., and Cailteux J. (2006) An overview of the geology and major ore deposits of Central Africa: Explanatory note for the 1:4,000,000 map "Geology and major ore deposits of Central Africa". *Journal of African Earth Sciences* **44**(4-5), 571-595.
- Milési J. P., Toteu S. F., Deschamps Y., Feybesse J. L., Lerouge C., Cocherie A., Tchameni R., Moloto-A-Kenguemba G., Kampunzu H. A. B., Nicol N., Duguey E., Leistel J. M., Saint-Martin M., Ralay F., Heinry C., Doumnang Mbaiagne J. C., Chêne F., Monthel J., Boutin P., and Rolin P. (2004) Geology and major ore deposits of Central Africa (ed. BRGM). BRGM, Orléans Cedex.
- Mitchell J. G. and Taka A. S. (1984) Potassium and argon loss patterns in weathered micas: implications for detrital mineral studies, with particular reference to the triassic palaeogeography of the British Isles. *Sedimentary Geology* **39**(1-2), 27-52.
- Möller P. and Kersten G. (1994) Electrochemical accumulation of visible gold on pyrite and arsenopyrite surfaces. *Mineralium Deposita* **29**(5), 404-413.
- Morad S., El-Ghali M. A. K., Caja M. A., Al-Ramadan K., and Mansurbeg H. (2009) Hydrothermal alteration of magmatic titanite: evidence from

## REFERENCES

- Proterozoic granitic rocks, southeastern Sweden. *Canadian Mineralogist* **47**(4), 801-811.
- Moreau C., Regnoult J. M., Déruelle B., and Robineau B. (1987) A new tectonic model for the Cameroon Line, Central Africa. *Tectonophysics* **141**(4), 317-334.
- Morey A. A., Tomkins A. G., Bierlein F. P., Weinberg R. F., and Davidson G. J. (2008) Bimodal distribution of gold in pyrite and arsenopyrite: examples from the Archean Boorara and Bardoc shear systems, Yilgarn craton, Western Australia. *Economic Geology* **103**(3), 599-614.
- Morrison G. W., Rose W. J., and Jaireth S. (1991) Geological and geochemical controls on the silver content (fineness) of gold in gold-silver deposits. *Ore Geology Reviews* **6**(4), 333-364.
- Moundi A., Wandji P., Bardintzeff J.-M., Ménard J.-J., Okomo Atouba L. C., Mouncherou O. F., Reusser É., Bellon H., and Tchoua F. M. (2007) Les basaltes éocènes à affinité transitionnelle du plateau Bamoun, témoins d'un réservoir mantellique enrichi sous la ligne volcanique du Cameroun. *Comptes Rendus Geosciences* **339**(6), 396-406.
- Ndougsa-Mbarga T., Manguelle-Dicoum E., Campos-Enriquez J.-O., and Atangana Q. Y. (2007) Gravity anomalies, sub-surface structure and oil and gas migration in the Mamfe, Cameroon-Nigeria, sedimentary basin. *Geofísica Internacional* **46**(2), 129-139.
- Nédélec A., Nsifa E. N., and Martin H. (1990) Major and trace element geochemistry of the Archaean Ntem plutonic complex (south Cameroon): petrogenesis and crustal evolution. *Precambrian Research* **47**(1-2), 35-50.
- Newman H. R. (2008) The mineral industries of Cameroon and Cape Verde. In *USGS 2007 Minerals Yearbook - Area Reports: International*, pp. 7.1-7.3. U.S. Department of the Interior, Washington D.C.
- Ngako V. (2007) Geology and mineral resources. In *Atlas of Cameroon* (eds. N. Houstin and C. Seignobos), pp. 60-61. Les Éditions Jeune Afrique, Paris.
- Ngwa J. A. (1978) *A new geography of Cameroon*. Longman Group Limited, Harlow. pp. 147.
- Njanko T., Nédélec A., and Affaton P. (2006) Synkinematic high-K calc-alkaline plutons associated with the Pan-African Central Cameroon shear zone (W-Tibati area): petrology and geodynamic significance. *Journal of African Earth Sciences* **44**(4-5), 494-510.
- Nkouathio D., Kagou Dongmo A., Bardintzeff J., Wandji P., Bellon H., and Pouclet A. (2008) Evolution of volcanism in graben and horst structures along the Cenozoic Cameroon Line (Africa): implications for tectonic evolution and mantle source composition. *Mineralogy and Petrology* **94**(3), 287-303.
- Nsifa E. N. and Riou R. (1990) Post-Archaean migmatization in the charnockitic series of the Ntem Complex, Congo Craton, southern Cameroon. In *15th Colloquium on African Geology*, pp. 33-36. Publications Occasionnelle, CIFEG, University of Nancy I.

## REFERENCES

- Ntamak-Nida M.-J., Baudin F., Schnyder J., Makong J.-C., Komguem P. B., and Abolo G. M. (2008) Depositional environments and characterisation of the organic matter of the Lower Mundek Formation (Barremian ?-Aptian) of the Kribi-Campo sub-basin (South Cameroon): Implications for petroleum exploration. *Journal of African Earth Sciences* **51**(4), 207-219.
- Nzenti J. P., Barbey P., Macaudiere J., and Soba D. (1988) Origin and evolution of the late precambrian high-grade Yaounde gneisses (Cameroon). *Precambrian Research* **38**(2), 91-109.
- O'Connor J. T. (1965) A classification of quartz-rich igneous rocks based on feldspar ratios. *US Geological Survey Professorial Paper* **525B**, B79-B84.
- Oba A. O. (2001) *Stratigraphy of the Sergipe-Alagoas (Brazil), Douala, Rio Muni, and Gabon (West Africa) sedimentary basins (Aptian-Albian intervals)*. Department of Geological Sciences, University of South Carolina, Columbia, S.C.  
<http://rainier.seis.sc.edu/alfredo/OvonoOba.htm> Accessed on 17th October, 2009.
- Oberthür T., Weiser T., Amanor J. A., and Chryssoulis S. L. (1997) Mineralogical siting and distribution of gold in quartz veins and sulfide ores of the Ashanti mine and other deposits in the Ashanti belt of Ghana: genetic implications. *Mineralium Deposita* **32**(1), 2-15.
- Parry W. T., Ballantyne J. M., and Jacobs D. C. (1984) Geochemistry of hydrothermal sericite from Roosevelt Hot Springs and the Tintic and Santa Rita porphyry copper systems. *Economic Geology* **79**(1), 72-86.
- Partington G. A. and Williams P. J. (2000) Proterozoic Lode Gold and (Iron)-Copper-Gold Deposits: A comparison of Australian and global examples. In *Gold in 2000* (eds. S. G. Hagemann and P. E. Brown), pp. 69-101. Society of Economic Geologists, Inc., Littleton.
- Pauken R. J. and Thompson J. M. (1991) Geology of the Douala Basin, offshore Cameroon, West Africa. *AAPG Bulletin* **75**.
- Pearce J. A., Harris N. B. W., and Tindle A. G. (1984) Trace element discrimination diagrams for the tectonic interpretation of granitic rocks. *J. Petrology* **25**(4), 956-983.
- Peccerillo A. and Taylor S. R. (1976) Geochemistry of eocene calc-alkaline volcanic rocks from the Kastamonu area, Northern Turkey. *Contributions to Mineralogy and Petrology* **58**(1), 63-81.
- Peive A. (2007) Linear volcanic chains in oceans: possible formation mechanisms. *Geotectonics* **41**(4), 281-295.
- Penaye J., Kroner A., Toteu S. F., Van Schmus W. R., and Douumnang J.-C. (2006) Evolution of the Mayo Kebbi region as revealed by zircon dating: An early (ca. 740 Ma) Pan-African magmatic arc in southwestern Chad. *Journal of African Earth Sciences* **44**(4-5), 530-542.
- Penaye J., Toteu S. F., Tchameni R., Van Schmus W. R., Tchakounte J., Ganwa A., Minyem D., and Nsifa E. N. (2004) The 2.1 Ga West Central

## REFERENCES

- African Belt in Cameroon: extension and evolution. *Journal of African Earth Sciences* **39**(3-5), 159-164.
- Phillips G. N. (1986) Geology and alteration in the Golden Mile, Kalgoorlie. *Economic Geology* **81**(4), 779-808.
- Pinna P., Calvez J. Y., Abessolo A., Angel J. M., Mekoulou-Mekoulou T., Mananga G., and Vernhet Y. (1994) Neoproterozoic events in the Tcholliré area: Pan-African crustal growth and geodynamics in central-northern Cameroon (Adamawa and North Provinces). *Journal of African Earth Sciences* **18**(4), 347-353.
- Pirajno F. and Jacob R. E. (1988) Gold mineralisation in the intracontinental branch of the Damara Orogen, Nambia. In *Bicentennial Gold '88*, pp. 168-171. Geological Society of Australia Abstract Series 23, Melbourne.
- Pokrovski G. S., Tagirov B. R., Schott J., Hazemann J.-L., and Proux O. (2009) A new view on gold speciation in sulfur-bearing hydrothermal fluids from in situ X-ray absorption spectroscopy and quantum-chemical modeling. *Geochimica et Cosmochimica Acta* **73**(18), 5406-5427.
- Prian J. P., Simeon Y., Johan V., Ledru P., Plantone P., Coste B., and Eko N'dong J. (1988) Valorisation géologique de l'inventaire minier de l'Archéen et du Protérozoïque inférieur des feuilles Mitzic, Booué et Mouila, à 1/20000 (Gabon Central). *Chronique de la Recherche Minière* **56**(491), 67-104.
- Ramdohr P. (1969) *The ore minerals and their intergrowths*. Pergamon Press, Braunschweig. pp. 1174.
- Reich M., Kesler S. E., Utsunomiya S., Palenik C. S., Chryssoulis S. L., and Ewing R. C. (2005) Solubility of gold in arsenian pyrite. *Geochimica et Cosmochimica Acta* **69**(11), 2781-2796.
- Rice A. (2000) Rollover in volcanic crater lakes: a possible cause for Lake Nyos type disasters. *Journal of Volcanology and Geothermal Research* **97**(1-4), 233-239.
- Richards J. P. and Noble S. R. (1998) Application of radiogenic isotope systems to the timing of origin of hydrothermal processes. In *Techniques in hydrothermal ore deposits geology* (eds. J. P. Richards and P. B. Larson), pp. 195-233. Society of Economic Geologists, Littleton.
- Rickwood P. C. (1989) Boundary lines within petrologic diagrams which use oxides of major and minor elements. *Lithos* **22**(4), 247-263.
- Ridley J. R. and Diamond L. W. (2000) Fluid chemistry of orogenic lode gold deposits and implications for genetic models. In *Gold in 2000* (eds. S. G. Hagemann and P. E. Brown), pp. 141-162. Society of Economic Geologists, Inc., Littleton, Co.
- Robert F. and Kelly W. C. (1987) Ore-forming fluids in Archean gold-bearing quartz veins at the Sigma Mine, Abitibi greenstone belt, Quebec, Canada. *Economic Geology* **82**(6), 1464-1482.
- Roberts M. P. and Clemens J. D. (1993) Origin of high-potassium, talc-alkaline, I-type granitoids. *Geology* **21**(9), 825-828.

## REFERENCES

- Roedder E. (1984) *Fluid inclusions*. Mineralogical Society of America, Michigan. pp. 646.
- Rollingon H. R. (1993) *Using geochemical data: evaluation, presentation, interpretation*. Pearson Education Limited, Essex. pp. 352.
- Romberger S. B. (1988) Geochemistry of gold in hydrothermal deposits. In *US Geological Survey Bulletin 1857-A*, pp. A9-A25. US Government Printing Office, Washington, DC.
- Rose A. W. and Burt D. M. (1979) Hydrothermal alteration. In *Geochemistry of hydrothermal ore deposits* (ed. H. L. Barnes), 2<sup>nd</sup> edition, pp. 798. John Wiley & Sons, New York.
- Rosso K. M. and Bodnar R. J. (1995) Microthermometric and Raman spectroscopic detection limits of CO<sub>2</sub> in fluid inclusions and the Raman spectroscopic characterization of CO<sub>2</sub>. *Geochimica et Cosmochimica Acta* **59**(19), 3961-3975.
- Rudnick R. L. and Gao S. (2005) Composition of the continental crust. In *Treatise on Geochemistry: The Crust* (ed. R. L. Rudnick), pp. 683. Elsevier Ltd., Oxford.
- Sato K., Kovalenko S. V., Romanovsky N. P., Nedachi M., Berdnikov N. V., and Ishihara T. (2004) Crustal control on the redox state of granitoid magmas: tectonic implications from the granitoid and metallogenic provinces in the circum-Japan Sea Region. *Geological Society of America Special Papers* **389**, 319-337.
- Schlüter T. (2006) *Geological atlas of Africa*. Springer, Heidelberg. pp. 261.
- Schmid M., Lorke A., Dinkel C., Tanyileke G., and Wüst A. (2004) Double-diffusive convection in Lake Nyos, Cameroon. *Deep Sea Research Part I: Oceanographic Research Papers* **51**(8), 1097-1111.
- Seeley J. B. and Senden T. J. (1994) Alluvial gold in Kalimantan, Indonesia: A colloidal origin? *Journal of Geochemical Exploration* **50**(1-3), 457-478.
- Seward T. M. (1973) Thio complexes of gold and the transport of gold in hydrothermal ore solutions. *Geochimica et Cosmochimica Acta* **37**(3), 379-399.
- Seward T. M. (1984) The transport and deposition of gold in hydrothermal systems. In *Gold '82: The Geology, Geochemistry and Genesis of Gold Deposits* (ed. R. P. Foster), pp. 165-181. A. A. Balkema, Rotterdam.
- Shang C., Satir M., Nsifa E., Liégeois J.-P., Siebel W., and Taubald H. (2007) Archaean high-K granitoids produced by remelting of earlier tonalite-trondhjemite-granodiorite (TTG) in the Sangmelima region of the Ntem complex of the Congo craton, southern Cameroon. *International Journal of Earth Sciences* **96**(5), 817-841.
- Shang C. K., Satir M., Siebel W., Nsifa E. N., Taubald H., Liégeois J. P., and Tchoua F. M. (2004a) TTG magmatism in the Congo craton; a view from major and trace element geochemistry, Rb-Sr and Sm-Nd systematics: case of the Sangmelima region, Ntem complex, southern Cameroon. *Journal of African Earth Sciences* **40**(1-2), 61-79.
- Shang C. K., Siebel W., Satir M., Chen F., and Mvondo J. O. (2004b) Zircon Pb-Pb and U-Pb systematics of TTG rocks in the Congo Craton:

## REFERENCES

- Constraints on crust formation, magmatism, and Pan-African lead loss. *Bulletin of Geosciences* **79**(4), 205-219.
- Shanklin E. (1989) Exploding lakes and maleficent water in Grassfields legends and myth. *Journal of Volcanology and Geothermal Research* **39**(2-3), 233-246.
- Sharp Z. D., Essene E. J., and Kelly W. C. (1985) A re-examination of the arsenopyrite geothermometer; pressure considerations and applications to natural assemblages. *Can Mineral* **23**(4), 517-534.
- Shenberger D. M. and Barnes H. L. (1989) Solubility of gold in aqueous sulfide solutions from 150 to 350°C. *Geochimica et Cosmochimica Acta* **53**(2), 269-278.
- Sigurdsson H., Devine J. D., Tchua F. M., Presser F. M., Pringle M. K. W., and Evans W. C. (1987) Origin of the lethal gas burst from Lake Monoun, Cameroun. *Journal of Volcanology and Geothermal Research* **31**(1-2), 1-16.
- Sillitoe R. H. (2000) Gold-rich porphyry deposits: descriptive and genetic models and their role in exploration and discovery. In *Gold in 2000* (eds. S. G. Hagemann and P. E. Brown), pp. 315-345. Society of Economic Geologists Inc., Littleton.
- Stefánsson A. and Seward T. M. (2004) Gold(I) complexing in aqueous sulphide solutions to 500°C at 500 bar. *Geochimica et Cosmochimica Acta* **68**(20), 4121-4143.
- Streckeisen A. (1974) Classification and nomenclature of plutonic rocks recommendations of the IUGS subcommission on the systematics of Igneous Rocks. *International Journal of Earth Sciences* **63**(2), 773-786.
- Suh C., Ayonghe S., Sparks R., Annen C., Fitton J., Nana R., and Luckman A. (2003) The 1999 and 2000 eruptions of Mount Cameroon: eruption behaviour and petrochemistry of lava. *Bulletin of Volcanology* **65**(4), 267-281.
- Suh C. E. and Lehmann B. (2003) Morphology and electron-probe microanalysis of residual gold-grains at Dimako, Southeast Cameroun. *Neues Jahrbuch für Mineralogie - Monatshefte* **2003**, 255-275.
- Suh C. E., Lehmann B., and Mafany G. T. (2006) Geology and geochemical aspects of lode gold mineralization at Dimako-Mboscorro, SE Cameroon. *Geochemistry: Exploration, Environment, Analysis* **6**(4), 295-309.
- Sung Y. H., Brugger J., Ciobanu C. L., Pring A., Skinner W., and Nugus M. (2009) Invisible gold in arsenian pyrite and arsenopyrite from a multistage Archaean gold deposit: Sunrise Dam, Eastern Goldfields Province, Western Australia. *Mineralium Deposita* **44**(7), 765-791.
- Tabod C. T., Fairhead J. D., Stuart G. W., Ateba B., and Ntepe N. (1992) Seismicity of the Cameroon Volcanic Line, 1982-1990. *Tectonophysics* **212**(3-4), 303-320.
- Tagirov B. R., Baranova N. N., Zotov A. V., Schott J., and Bannykh L. N. (2006) Experimental determination of the stabilities of Au<sub>2</sub>S(cr) at

## REFERENCES

- 25 °C and at 25-250 °C. *Geochimica et Cosmochimica Acta* **70**(14), 3689-3701.
- Tagirov B. R., Salvi S., Schott J., and Baranova N. N. (2005) Experimental study of gold-hydrosulphide complexing in aqueous solutions at 350-500°C, 500 and 1000 bars using mineral buffers. *Geochimica et Cosmochimica Acta* **69**(8), 2119-2132.
- Tamfu S. F., Batupe M., Pauken R. J., and Boatwright D. C. (1995) Geological setting, stratigraphy and hydrocarbon habitat of the Douala Basin, Cameroon. *AAPG Bulletin* **79**(13), 95.
- Tanko Njisseu E. L., Nzenti J.-P., Njanko T., Kapajika B., and Nédélec A. (2005) New UPb zircon ages from Tonga (Cameroon): coexisting Eburnean-Transamazonian (2.1 Ga) and Pan-African (0.6 Ga) imprints. *Comptes Rendus Geosciences* **337**(6), 551-562.
- Tchameni R., Mezger K., Nsifa N. E., and Pouclet A. (2000) Neoarchaean crustal evolution in the Congo Craton: evidence from K rich granitoids of the Ntem Complex, southern Cameroon. *Journal of African Earth Sciences* **30**(1), 133-147.
- Tchameni R., Mezger K., Nsifa N. E., and Pouclet A. (2001) Crustal origin of Early Proterozoic syenites in the Congo Craton (Ntem Complex), South Cameroon. *Lithos* **57**(1), 23-42.
- Tchameni R., Pouclet A., Penaye J., Ganwa A. A., and Toteu S. F. (2006) Petrography and geochemistry of the Ngaoundere Pan-African granitoids in Central North Cameroon: Implications for their sources and geological setting. *Journal of African Earth Sciences* **44**(4-5), 511-529.
- Tchawa P. (2007) Relief and hydrography. In *Atlas of Cameroon* (eds. N. Houstin and C. Seignobos), pp. 58-59. Les Éditions Jeune Afrique, Paris.
- Thirlwall M. F., Smith T. E., Graham A. M., Theodorou N., Hollings P., Davidson J. P., and Arculus R. J. (1994) High field strength element anomalies in arc lavas: source or process? *J. Petrology* **35**(3), 819-838.
- Thompson J. F. H. and Newberry R. J. (2000) Gold deposits related to reduced granitic intrusions. In *Gold in 2000* (eds. S. G. Hagemann and P. E. Brown), pp. 377-400. Society of Economic Geologists Inc., Littleton.
- Toteu S. F., Schmus W. R. v., and Penaye J. (2006a) The Precambrian of Central Africa: Summary and perspectives. *Journal of African Earth Sciences* **44**(4-5), vii-x.
- Toteu S. F., Fouateu R. Y., Penaye J., Tchakounte J., Mouangue A. C. S., Van Schmus W. R., Deloule E., and Stendal H. (2006b) U-Pb dating of plutonic rocks involved in the nappe tectonic in southern Cameroon: consequence for the Pan-African orogenic evolution of the central African fold belt. *Journal of African Earth Sciences* **44**(4-5), 479-493.
- Toteu S. F., Penaye J., Deloule E., Van Schmus W. R., and Tchameni R. (2006c) Diachronous evolution of volcano-sedimentary basins north of the Congo craton: Insights from U-Pb ion microprobe dating of zircons

## REFERENCES

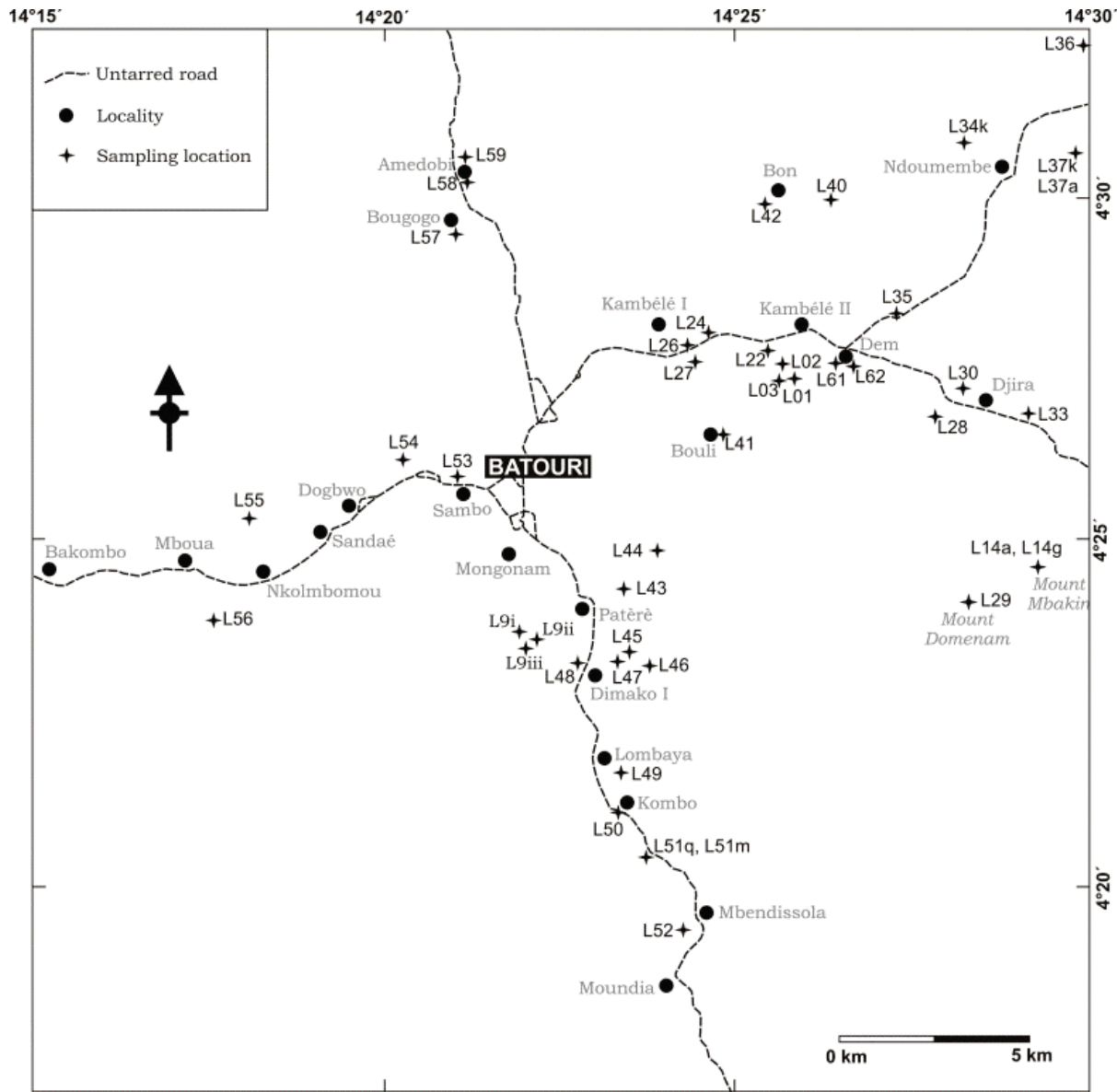
- from the Poli, Lom and Yaoundé Groups (Cameroon). *Journal of African Earth Sciences* **44**(4-5), 428-442.
- Toteu S. F., Penaye J., and Djomani Y. P. (2004) Geodynamic evolution of the Pan-African belt in central Africa with special reference to Cameroon. *Canadian Journal of Earth Science* **41**, 73-85.
- Toteu S. F., Van Schmus W. R., Penaye J., and Michard A. (2001) New U-Pb and Sm-Nd data from north-central Cameroon and its bearing on the pre-Pan African history of central Africa. *Precambrian Research* **108**(1-2), 45-73.
- Toteu S. F., Van Schmus W. R., Penaye J., and Nyobe J. B. (1994) U---Pb and Sm---N evidence for Eburnian and Pan-African high-grade metamorphism in cratonic rocks of southern Cameroon. *Precambrian Research* **67**(3-4), 321-347.
- Touret J. (1982) An empirical phase diagram for a part of the N<sub>2</sub>---CO<sub>2</sub> system at low temperature. *Chemical Geology* **37**(1-2), 49-58.
- Trdlička Z. and Hoffman V. (1976) Untersuchungen der chemischen Zusammensetzung der Gangkarbonate von Kutná Hora (ČSSR). *Freiberger Forschungshefte* **C321**, 29-81.
- Tsaléfac M. (2007) Climate. In *Atlas of Cameroon* (eds. N. Houstin and C. Seignobos), pp. 62-63. Les Éditions Jeune Afrique, Paris.
- Van den Kerkhof A. and Thiéry R. (2001) Carbonic inclusions. *Lithos* **55**(1-4), 49-68.
- Van Schmus W. R., de Brito Neves B. B., Hackspacher P., and Babinski M. (1995) U/Pb and Sm/Nd geochronologic studies of the eastern Borborema Province, Northeastern Brazil: initial conclusions. *Journal of South American Earth Sciences* **8**(3-4), 267-288.
- Van Schmus W. R., Oliveira E. P., da Silva Filho A. F., Toteu S. F., Penaye J., and Guimaraes I. P. (2008) Proterozoic links between the Borborema Province, NE Brazil, and the Central African Fold Belt. *Geological Society, London, Special Publications* **294**(1), 69-99.
- Wandji P., Tsafack J., Bardintzeff J., Nkouathio D., Kagou Dongmo A., Bellon H., and Guillou H. (2009) Xenoliths of dunites, wehrlites and clinopyroxenites in the basanites from Batoke volcanic cone (Mount Cameroon, Central Africa): petrogenetic implications. *Mineralogy and Petrology* **96**(1), 81-98.
- Webster J. G. (1986) The solubility of gold and silver in the system Au---Ag---S---O<sub>2</sub>---H<sub>2</sub>O at 25°C and 1 atm. *Geochimica et Cosmochimica Acta* **50**(9), 1837-1845.
- Webster J. G. and Mann A. W. (1984) The influence of climate, geomorphology and primary geology on the supergene migration of gold and silver. *Journal of Geochemical Exploration* **22**(1-3), 21-42.
- Wilkinson J. J. (2001) Fluid inclusions in hydrothermal ore deposits. *Lithos* **55**(1-4), 229-272.
- Wilson M. (1989) *Igneous Petrogenesis*. Unwin Hyman, London. pp. 450.
- Wood S. A. and Samson I. M. (1998) Solubility of ore minerals and complexation of ore metals in hydrothermal solutions. In *Techniques*

## REFERENCES

- in hydrothermal ore deposits geology* (eds. J. P. Richards and P. B. Larson), pp. 33-80. Society of Economic Geologists, Inc., Littleton.
- Woolley A. R. (2001) *Alkaline rocks and carbonatites of the world - Part 3: Africa*. The Geological Society, London. pp. 372.
- Yerima B. P. K. and Ranst E. V. (2005) *Major soil classification systems used in the Tropics: Soils of Cameroon*. Trafford Publishing, Victoria.
- Zang W. and Fyfe W. S. (1995) Chloritization of the hydrothermally altered bedrock at the Igarapé Bahia gold deposit, Carajás, Brazil. *Mineralium Deposita* **30**(1), 30-38.
- Zaraisky G., Aksyuk A., Devyatova V., Udrovatina O., and Chevychelov V. (2009) The Zr/Hf ratio as a fractionation indicator of rare-metal granites. *Petrology* **17**(1), 25-45.
- Zen E. (2003) Phase relations of peraluminous granitic rocks and their petrogenetic implications. *Annual Review of Earth and Planetary Sciences* **16**(1), 21-51.
- Zhu D., Mo X., Wang L., Zhao Z., Niu Y., Zhou C., and Yang Y. (2009) Petrogenesis of highly fractionated I-type granites in the Zayu area of eastern Gangdese, Tibet: Constraints from zircon U-Pb geochronology, geochemistry and Sr-Nd-Hf isotopes. *Science in China Series D: Earth Sciences* **52**(9), 1223-1239.
- Zogning A., Ngouanet C., and Tiafack O. (2007) The catastrophic geomorphological processes in humid tropical Africa: A case study of the recent landslide disasters in Cameroon. *Sedimentary Geology* **199**(1-2), 13-27.
- Zoheir B. A. (2004) Gold mineralization in the Um El Tuyor area, South Eastern Desert, Egypt: geologic context, characteristics and genesis. Ph.D thesis. University of Munich, Munich.
- Zoheir B. A., Mehanna A. M., and Qaoud N. N. (2008) Geochemistry and geothermobarometry of the Um Eleiga Neoproterozoic island arc intrusive complex, SE Egypt: genesis of a potential gold-hosting intrusion. *Applied Earth Science : IMM Transactions section B* **117**(3), 89-111.

## APPENDIX

**Appendix 1:** Sample map of Batouri.



## APPENDIX

**Appendix 2a:** Major- (wt %) and trace-element (ppm) analytical data for granitoids in the Batouri area. Shaded rows indicate analyses by INAA.

Sample N°	Alkali-feldspar granite										
	L14a	L34a	L37a	L14g	L28	L29	L30	L33	L34k	L36	L37k
Analytical method	XRF	XRF	XRF	XRF	XRF	XRF	XRF	XRF	XRF	XRF	XRF
	INAA	INAA	INAA	INAA	INAA	INAA	INAA	INAA	INAA	INAA	INAA
SiO <sub>2</sub>	77.12	77.07	77.73	75.31	78.11	76.87	76.43	75.70	74.05	76.41	75.95
TiO <sub>2</sub>	0.04	0.09	0.08	0.25	0.10	0.15	0.19	0.14	0.27	0.18	0.24
Al <sub>2</sub> O <sub>3</sub>	12.72	12.31	12.25	13.21	12.13	12.56	12.72	13.28	13.61	12.70	12.71
Fe <sub>2</sub> O <sub>3</sub>	0.63	0.95	0.66	1.55	0.77	1.09	1.22	1.03	1.77	1.02	1.42
MnO	0.01	0.02	0.01	0.04	0.04	0.05	0.05	0.02	0.05	0.01	0.03
MgO	<0.01	0.06	0.05	0.46	0.06	0.16	0.23	0.21	0.44	0.12	0.28
CaO	0.67	0.53	0.54	1.60	0.44	0.63	0.81	1.01	1.34	0.58	1.01
Na <sub>2</sub> O	2.66	2.53	2.84	3.17	3.40	3.50	3.50	3.10	3.50	2.52	3.20
K <sub>2</sub> O	5.74	6.02	5.38	3.80	4.44	4.47	4.37	4.88	4.32	5.78	4.58
P <sub>2</sub> O <sub>5</sub>	0.01	0.02	0.01	0.06	0.01	0.03	0.04	0.03	0.06	0.02	0.04
(SO <sub>3</sub> )	<0.01	<0.01	<0.01	<0.01	<0.01	<0.01	<0.01	<0.01	<0.01	<0.01	<0.01
(Cl)	0.01	0.02	0.01	0.02	0.01	0.01	0.01	0.02	0.01	0.02	0.01
(F)	<0.05	<0.05	<0.05	<0.05	<0.05	<0.05	<0.05	<0.05	<0.05	<0.05	<0.05
LOI	0.24	0.20	0.29	0.28	0.33	0.33	0.25	0.35	0.36	0.39	0.31
<b>Sum</b>	<b>99.85</b>	<b>99.81</b>	<b>99.86</b>	<b>99.76</b>	<b>99.86</b>	<b>99.83</b>	<b>99.83</b>	<b>99.80</b>	<b>99.76</b>	<b>99.73</b>	<b>99.77</b>
Rb	142	161	123	110	182	207	176	103	123	138	117
Ba	182	535	205	747	113	245	392	734	678	1018	457
Th	39	30	31	10	30	36	25	20	23	14	33
U	<3	<3	<3	<3	<3	<3	<3	<3	<3	<3	<3
Nb	<3	3	<2	6	10	12	13	3	9	4	3
La	5.40	10.10	20.50	27.60	31.50	30.90	23.60	39.40	29.80	38.60	40.80
Ce	7	14	28	42	46	45	42	56	44	65	61
Sr	63	108	47	211	32	49	71	170	151	141	95
Nd	25	<16	20	<16	27	21	<16	18	32	30	34
Zr	192	156	76	113	85	97	120	67	125	152	117
Hf	7	7	2	3	4	2	3	<1	3	3	2
Sm	0.20	0.40	0.80	1.60	1.00	2.00	2.20	1.80	2.60	2.80	3.30
Eu	0.50	0.70	<0.2	0.70	<0.2	<0.2	<0.2	0.70	0.60	0.80	0.60
Y	4	<3	<3	6	8	21	18	<3	17	6	13
Yb	0.90	0.70	<0.2	0.80	1.50	2.30	1.50	0.30	1.40	<0.2	1.20
Lu	0.17	0.13	0.10	0.18	0.23	0.40	0.28	<0.05	0.26	0.13	0.21
V	<5	<5	<5	17	5	<5	7	11	14	7	11
Ta	<0.50	<0.50	<0.50	<0.50	<0.50	<0.50	2.5	<0.50	<0.50	<0.50	<0.50
Rb/Sr	2.25	1.49	2.62	0.52	5.69	4.22	2.48	0.61	0.81	0.98	1.23
Rb/Ba	0.78	0.30	0.60	0.15	1.61	0.84	0.45	0.14	0.18	0.14	0.26
Zr/Hf	27.43	22.29	38.00	37.67	21.25	48.50	40.00	-	41.67	50.67	58.50
Na <sub>2</sub> O+K <sub>2</sub> O	8.40	8.55	8.22	6.97	7.84	7.97	7.87	7.98	7.82	8.30	7.78
FeO <sub>(total)</sub>	0.57	0.85	0.59	1.39	0.69	0.98	1.10	0.93	1.59	0.92	1.28
A/CNK	1.08	1.06	1.07	1.08	1.08	1.07	1.06	1.09	1.06	1.11	1.05
A/NK	1.20	1.15	1.17	1.42	1.17	1.18	1.21	1.28	1.30	1.22	1.24
Or	55.54	58.51	53.06	38.40	44.55	43.46	42.32	46.89	40.38	57.37	44.69
An	5.34	4.11	4.36	12.91	3.60	4.82	6.16	7.83	9.90	4.62	7.85
Ab	39.12	37.37	42.57	48.69	51.85	51.72	51.52	45.27	49.72	38.01	47.46

## APPENDIX

### Appendix 2a Continued.

Sample N°	Syeno-monzo-granite							Granodiorite			
	L44	L45	L46	L57	L59	L40	L52	L27	L41m	L42	L43
Analytical method	XRF	XRF	XRF	XRF	XRF	XRF	XRF	XRF	XRF	XRF	XRF
	INAA	INAA	INAA	INAA	INAA	INAA	INAA	INAA	INAA	INAA	INAA
SiO <sub>2</sub>	72.56	71.14	72.18	72.03	73.42	69.79	69.02	66.76	65.55	65.75	65.37
TiO <sub>2</sub>	0.26	0.44	0.38	0.28	0.26	0.49	0.50	0.61	0.73	0.77	0.79
Al <sub>2</sub> O <sub>3</sub>	14.25	14.30	14.03	14.15	13.57	15.01	15.27	15.32	15.42	15.55	16.52
Fe <sub>2</sub> O <sub>3</sub>	2.12	2.86	2.89	2.45	2.29	3.27	3.13	3.94	5.90	4.33	3.88
MnO	0.04	0.04	0.07	0.04	0.05	0.04	0.04	0.07	0.05	0.07	0.05
MgO	0.29	0.98	0.67	0.28	0.25	1.10	1.14	1.62	1.37	1.97	1.47
CaO	1.21	1.78	1.48	1.34	1.19	2.63	2.73	3.38	3.23	3.59	3.73
Na <sub>2</sub> O	3.39	2.53	3.80	3.47	3.29	3.34	3.52	3.50	3.96	3.57	4.10
K <sub>2</sub> O	5.15	4.80	3.54	5.15	5.08	3.37	3.50	3.65	2.71	3.19	2.71
P <sub>2</sub> O <sub>5</sub>	0.05	0.12	0.10	0.07	0.06	0.12	0.16	0.18	0.20	0.24	0.26
(SO <sub>3</sub> )	<0.01	<0.01	<0.01	<0.01	<0.01	0.01	<0.01	0.11	0.03	0.01	0.03
(Cl)	0.01	0.02	0.01	0.02	0.02	0.02	0.02	0.02	0.02	0.02	0.02
(F)	<0.05	<0.05	<0.05	<0.05	<0.05	<0.05	0.05	<0.05	0.07	0.05	0.06
LOI	0.43	0.54	0.58	0.41	0.27	0.52	0.42	0.47	0.46	0.55	0.62
<b>Sum</b>	<b>99.78</b>	<b>99.57</b>	<b>99.76</b>	<b>99.71</b>	<b>99.75</b>	<b>99.72</b>	<b>99.52</b>	<b>99.64</b>	<b>99.70</b>	<b>99.66</b>	<b>99.59</b>
Rb	141	121	140	134	142	96	91	91	104	113	83
Ba	607	1816	708	843	753	863	2290	1113	676	936	1472
Th	22	30	14	18	19	11	6	8	17	8	5
U	<3	<3	<3	<3	<3	<3	<3	<3	<3	<3	<3
Nb	10	9	13	10	10	6	6	10	8	10	8
La	57.60	44.10	30.50	n.d	n.d	43.80	22.90	17.30	53.70	28.20	n.d
Ce	99	77	59	n.d	n.d	69	36	44	88	49	n.d
Sr	106	370	182	108	100	261	732	480	403	523	707
Nd	45	56	36	79	64	33	32	46	63	35	31
Zr	238	448	161	280	269	186	144	161	295	198	229
Hf	5	8	5	n.d	n.d	2	3	4	3	4	n.d
Sm	5.80	4.40	3.50	n.d	n.d	3.10	2.80	4.00	5.50	3.90	n.d
Eu	0.70	1.40	0.80	n.d	n.d	0.80	1.00	1.20	<0.2	1.00	n.d
Y	28	17	21	31	43	12	12	22	24	16	13
Yb	2.80	1.80	2.70	n.d	n.d	<0.2	0.90	2.40	1.20	1.50	n.d
Lu	0.46	0.28	0.50	n.d	n.d	0.13	0.19	0.37	0.18	0.23	n.d
V	10	44	26	8	7	39	47	67	86	70	59
Ta	2.9	<0.50	<0.50	n.d	n.d	<0.50	<0.50	<0.50	<0.50	<0.50	n.d
Rb/Sr	1.33	0.33	0.77	n.d	n.d	0.37	0.12	0.19	0.26	0.22	n.d
Rb/Ba	0.23	0.07	0.20	n.d	n.d	0.11	0.04	0.08	0.15	0.12	n.d
Zr/Hf	47.60	56.00	32.20	-	-	93.00	48.00	40.25	98.33	49.50	-
Na <sub>2</sub> O+K <sub>2</sub> O	8.54	7.33	7.34	8.62	8.37	6.71	7.02	7.15	6.67	6.76	6.81
FeO <sub>(total)</sub>	1.91	2.57	2.60	2.20	2.06	2.94	2.82	3.55	5.31	3.90	3.49
A/CNK	1.07	1.14	1.10	1.03	1.04	1.08	1.05	0.97	1.01	0.98	1.00
A/NK	1.28	1.53	1.39	1.25	1.24	1.64	1.59	1.58	1.63	1.67	1.71
Or	45.72	47.97	33.88	44.89	46.13	32.03	31.92	31.57	24.15	28.07	22.99
An	8.53	13.61	10.84	9.14	8.47	19.73	19.30	22.42	22.21	24.19	24.14
Ab	45.74	38.42	55.28	45.97	45.40	48.24	48.79	46.01	53.64	47.74	52.87

## APPENDIX

**Appendix 2a continued.**

Sample N°	Granodiorite		Tonalite			
	L54	L56	L49	L50	L51m	L51q
Analytical method	XRF	XRF	XRF	XRF	XRF	XRF
	INAA	INAA	INAA	INAA	INAA	INAA
SiO <sub>2</sub>	66.41	67.53	61.73	59.69	61.68	62.20
TiO <sub>2</sub>	0.67	0.62	0.94	1.01	1.00	1.10
Al <sub>2</sub> O <sub>3</sub>	16.23	15.99	16.82	16.95	16.22	16.50
Fe <sub>2</sub> O <sub>3</sub>	3.65	3.40	5.89	6.29	5.77	5.97
MnO	0.05	0.04	0.07	0.10	0.09	0.07
MgO	1.32	1.07	2.62	3.13	2.70	2.68
CaO	3.20	2.71	4.08	4.90	4.48	3.83
Na <sub>2</sub> O	3.97	3.80	4.06	4.01	3.60	3.59
K <sub>2</sub> O	3.34	3.64	2.36	2.45	3.05	2.67
P <sub>2</sub> O <sub>5</sub>	0.22	0.20	0.33	0.34	0.30	0.36
(SO <sub>3</sub> )	0.03	0.02	0.01	0.01	0.02	0.02
(Cl)	0.02	0.01	0.02	0.02	0.02	0.03
(F)	0.07	0.05	0.05	0.07	<0.05	0.10
LOI	0.36	0.45	0.58	0.55	0.55	0.52
<b>Sum</b>	<b>99.54</b>	<b>99.53</b>	<b>99.56</b>	<b>99.54</b>	<b>99.54</b>	<b>99.65</b>
Rb	68	78	86	70	92	128
Ba	1847	1863	1069	1490	1463	1009
Th	11	12	11	15	13	16
U	<3	<3	<3	<3	<3	<3
Nb	8	8	8	9	8	12
La	42.00	52.00	33.10	35.90	41.80	25.80
Ce	72	91	65	66	67	43
Sr	688	570	793	932	750	616
Nd	57	51	37	53	46	29
Zr	254	229	239	245	245	219
Hf	4	5	4	4	4	4
Sm	4.20	3.60	4.90	4.30	4.20	3.10
Eu	1.20	1.50	0.90	1.40	1.10	1.00
Y	13	9	22	18	18	16
Yb	0.90	0.80	1.20	0.90	1.40	1.20
Lu	0.17	0.17	0.25	0.26	0.16	0.22
V	54	37	94	117	111	120
Ta	<0.50	<0.50	<0.50	<0.50	<0.50	<0.50
Rb/Sr	0.10	0.14	0.11	0.08	0.12	0.21
Rb/Ba	0.04	0.04	0.08	0.05	0.06	0.13
Zr/Hf	63.50	45.80	59.75	61.25	61.25	54.75
Na <sub>2</sub> O+K <sub>2</sub> O	7.31	7.44	6.42	6.46	6.65	6.26
FeO <sub>(total)</sub>	3.28	3.06	5.30	5.66	5.19	5.37
A/CNK	1.02	1.06	1.01	0.93	0.93	1.05
A/NK	1.60	1.57	1.82	1.83	1.76	1.88
Or	28.26	31.74	20.36	20.25	25.95	24.40
An	20.68	17.91	26.41	29.40	27.50	25.75
Ab	51.06	50.35	53.23	50.36	46.55	49.85

## APPENDIX

**Appendix 2b:** INNA, Hg-FIMS and AR-MS analyses of gold-bearing vein and wall-rock samples from Batouri.

	Au ppb	Hg ppb	Zn ppm	Pb ppm	Fe %	As ppm	S %	Cu ppm	Mo ppm	Ag ppm	Sb ppm
	INNA	Hg-FIMS	AR-MS	AR-MS	AR-ICP	AR-MS	AR-ICP	AR-MS	AR-MS	AR-MS	AR-MS
<b>Quartz Vein</b>											
L1	36	< 5	7.1	8.37	0.42	4.4	0.002	< 0.01	0.41	0.068	0.26
L8i	6850	4520	> 5000	416	0.51	0.7	0.923	33.2	0.12	1.48	0.35
L8ii	14600	21	4.1	11.6	0.12	0.5	0.002	1.05	0.07	3.05	0.07
L8iii	12100	< 5	1.9	746	0.26	20.7	0.233	1.89	0.15	3.53	0.17
L9iii	> 30000	5620	> 5000	4850	0.84	3420	0.766	202	1.12	53.4	13.2
L9iv	3490	1980	> 5000	1630	0.21	831	0.386	21.3	0.13	2.84	2.94
L9viii	27500	53	16.9	55.4	0.34	50.7	0.086	1.83	0.19	31.8	0.55
L9xi	91	< 5	5.1	35.6	0.16	10.9	0.006	0.99	0.12	0.237	0.24
<b>Wall-rock</b>											
L7	1310	24	29.7	151	2.05	5.7	1.013	83.4	2.96	1.04	0.21
L9i	3910	6	27.2	69.1	1.43	106	0.001	1.86	1.13	1.36	5.7
L9v	542	< 5	10.5	52.7	1.91	51.4	0.007	3.21	0.75	0.179	1.21
L9vi	18500	222	1270	8600	4.15	17.7	0.197	98.9	0.24	18.5	7.25
L9vii	512	7	22.1	118	2.11	59	0.001	26.9	1.12	0.107	1.13
L9ix	431	< 5	10.4	67.7	2.31	52.9	0.004	2.53	0.68	0.145	2.18

## APPENDIX

**Appendix 3a:** Electron microprobe analyses of chlorite from altered wall rock at Batouri. Chlorine and F were sought for, but were below the detection limit of 0.03 wt %. Shaded columns show analyses of chlorite from the distal zone of the wall-rock. FeO represents total iron content.

	1/1	2/1	3/1	4/1	5/1	6/1	7/1	8/1	9/1	10/1
SiO <sub>2</sub> (wt %)	26.64	26.78	28.38	26.44	26.02	25.72	26.98	26.95	26.28	27.06
TiO <sub>2</sub> (wt %)	0.09	0.12	0.17	0.14	0.28	0.21	0.06	0.08	0.09	0.06
Al <sub>2</sub> O <sub>3</sub> (wt %)	20.45	19.68	18.22	19.65	19.71	20.53	20.49	20.18	20.04	20.71
FeO (wt %)	24.62	26.36	26.64	28.16	28.35	27.93	25.09	24.27	26.55	24.03
MnO (wt %)	0.37	0.24	0.24	0.19	0.11	0.16	0.18	0.37	0.29	0.37
MgO (wt %)	15.96	14.93	14.52	13.82	13.91	13.83	14.55	15.77	14.83	16.38
CaO (wt %)	<0.03	0.05	0.14	0.06	0.06	0.05	0.18	0.06	0.04	<0.03
Na <sub>2</sub> O (wt %)	<0.04	0.06	0.06	<0.04	0.07	0.04	0.04	0.05	0.06	<0.04
K <sub>2</sub> O (wt %)	0.08	0.18	0.11	0.11	0.07	0.18	0.21	0.27	0.15	0.05
Cl (wt %)	<0.03	0.03	<0.03	<0.03	<0.03	<0.03	<0.03	<0.03	<0.03	<0.03
F (wt %)	<0.03	<0.03	<0.03	<0.03	<0.03	<0.03	<0.03	<0.03	<0.03	<0.03
<b>TOTAL (wt %)</b>	<b>87.58</b>	<b>87.77</b>	<b>87.84</b>	<b>87.95</b>	<b>87.95</b>	<b>88.03</b>	<b>87.14</b>	<b>87.36</b>	<b>87.70</b>	<b>88.07</b>
O=F, Cl	-	0.01	-	-	-	-	-	-	-	-
<b>TOTAL</b>	<b>87.57</b>	<b>87.76</b>	<b>87.84</b>	<b>87.94</b>	<b>87.95</b>	<b>88.03</b>	<b>87.14</b>	<b>87.36</b>	<b>87.69</b>	<b>88.06</b>
T2	12.52	12.62	12.59	12.72	12.74	12.71	12.60	12.54	12.66	12.39
No Anions	28.00	28.00	28.00	28.00	28.00	28.00	28.00	28.00	28.00	28.00
<b>Formula based on 28 oxygens</b>										
Si	5.55	5.63	5.95	5.60	5.52	5.44	5.66	5.63	5.54	5.58
Ti	0.01	0.02	0.03	0.02	0.04	0.03	0.01	0.01	0.01	0.01
Al <sup>iv</sup>	2.45	2.37	2.05	2.40	2.48	2.56	2.34	2.37	2.46	2.42
Al <sup>vi</sup>	2.58	2.50	2.45	2.50	2.44	2.56	2.73	2.59	2.51	2.62
Altot	5.02	4.87	4.50	4.90	4.93	5.12	5.07	4.97	4.98	5.03
Fe <sup>2+</sup>	4.29	4.63	4.67	4.98	5.03	4.94	4.40	4.24	4.68	4.15
Mn	0.06	0.04	0.04	0.03	0.02	0.03	0.03	0.07	0.05	0.06
Mg	4.96	4.68	4.54	4.36	4.40	4.36	4.55	4.91	4.66	5.04
Ca	-	0.01	0.03	0.01	0.01	0.01	0.04	0.01	0.01	-
Na	-	0.02	0.02	-	0.03	0.02	0.02	0.02	0.03	-
K	0.02	0.05	0.03	0.03	0.02	0.05	0.06	0.07	0.04	0.01
Cl	-	0.01	-	-	-	-	-	-	-	-
<b>TOTAL</b>	<b>19.93</b>	<b>19.95</b>	<b>19.80</b>	<b>19.93</b>	<b>19.98</b>	<b>19.98</b>	<b>19.83</b>	<b>19.91</b>	<b>19.98</b>	<b>19.88</b>
Al <sup>iv</sup> <sub>c1</sub>	2.77	2.72	2.41	2.78	2.85	2.93	2.68	2.70	2.81	2.73
Al <sup>iv</sup> <sub>c2</sub>	2.34	2.24	1.91	2.23	2.31	2.39	2.21	2.26	2.32	2.32
*T°C <sub>Cath</sub>	363	351	300	356	369	381	346	351	366	358
**T°C <sub>K&amp;M</sub>	312	307	273	312	321	329	302	304	316	308
***T°C <sub>Z&amp;F</sub>	266	255	220	255	263	272	252	258	264	264
Fe/(Fe+Mg)	0.46	0.50	0.51	0.53	0.53	0.53	0.49	0.46	0.50	0.45
Al <sup>iv</sup> /Al <sub>tot</sub>	0.49	0.49	0.46	0.49	0.50	0.50	0.46	0.48	0.49	0.48
Si/Al <sub>tot</sub>	1.11	1.15	1.32	1.14	1.12	1.06	1.12	1.13	1.11	1.11
Na+K+2Ca	0.02	0.09	0.12	0.06	0.07	0.09	0.15	0.12	0.09	0.03

\*Cathelineau (1988); \*\*Kranidiotis and MacLean (1987); \*\*\* Zang and Fyfe (1995).

## APPENDIX

**Appendix 3a** continued.

	11/1	12/1	13/1	14/1	15/1	16/1	17/1	18/1	19/1	20/1
SiO <sub>2</sub> (wt %)	26.92	25.60	26.99	27.58	27.85	28.15	27.65	27.09	27.10	26.66
TiO <sub>2</sub> (wt %)	0.09	0.11	0.22	0.08	0.09	0.08	0.15	0.10	0.06	0.23
Al <sub>2</sub> O <sub>3</sub> (wt %)	19.70	21.85	20.88	19.71	19.38	19.21	20.21	19.72	19.96	20.80
FeO (wt %)	25.56	29.03	28.21	26.79	27.00	26.78	26.61	26.39	25.60	27.56
MnO (wt %)	0.23	0.16	0.18	0.18	0.18	0.18	0.15	0.35	0.39	0.19
MgO (wt %)	14.64	11.74	13.10	14.44	14.58	14.31	14.18	15.39	15.68	12.99
CaO (wt %)	0.09	<0.03	<0.03	<0.03	0.03	0.07	0.08	<0.03	0.03	<0.03
Na <sub>2</sub> O (wt %)	<0.04	0.04	<0.04	<0.04	<0.04	0.04	<0.04	<0.04	<0.04	<0.04
K <sub>2</sub> O (wt %)	0.06	0.06	0.40	0.09	0.15	0.15	0.34	0.06	0.07	0.44
Cl (wt %)	<0.03	<0.03	<0.03	<0.03	<0.03	<0.03	<0.03	<0.03	<0.03	<0.03
F (wt %)	<0.03	<0.03	<0.03	<0.03	<0.03	<0.03	<0.03	<0.03	<0.03	<0.03
<b>TOTAL (wt %)</b>	<b>86.66</b>	<b>87.95</b>	<b>89.38</b>	88.23	88.64	88.31	88.74	<b>88.48</b>	<b>88.24</b>	<b>88.26</b>
O=F, Cl	-	-	-	-	-	-	-	-	-	-
<b>TOTAL</b>	<b>86.66</b>	<b>87.95</b>	<b>89.38</b>	88.23	88.64	88.31	88.74	<b>88.48</b>	<b>88.24</b>	<b>88.26</b>
T2	12.71	12.75	12.48	12.53	12.49	12.51	12.45	12.50	12.48	12.62
No Anions	28.00	28.00	28.00	28.00	28.00	28.00	28.00	28.00	28.00	28.00
<b>Formula based on 28 oxygens</b>										
Si	5.70	5.43	5.61	5.75	5.79	5.86	5.73	5.64	5.63	5.60
Ti	0.01	0.02	0.03	0.01	0.01	0.01	0.02	0.02	0.01	0.04
Al <sup>iv</sup>	2.30	2.57	2.39	2.25	2.21	2.14	2.27	2.36	2.37	2.40
Al <sup>vi</sup>	2.61	2.89	2.72	2.59	2.54	2.58	2.67	2.47	2.52	2.75
Al <sub>tot</sub>	4.91	5.46	5.11	4.84	4.75	4.71	4.94	4.84	4.89	5.15
Fe <sup>2+</sup>	4.52	5.15	4.90	4.67	4.69	4.66	4.61	4.59	4.45	4.84
Mn	0.04	0.03	0.03	0.03	0.03	0.03	0.03	0.06	0.07	0.03
Mg	4.62	3.71	4.06	4.49	4.52	4.44	4.38	4.77	4.86	4.07
Ca	0.02	-	-	-	0.01	0.02	0.02	-	0.01	-
Na	-	0.01	-	-	-	0.01	-	-	-	-
K	0.02	0.02	0.11	0.02	0.04	0.04	0.09	0.02	0.02	0.12
<b>TOTAL</b>	<b>19.84</b>	<b>19.83</b>	<b>19.85</b>	19.82	19.84	19.79	19.82	<b>19.93</b>	<b>19.92</b>	<b>19.86</b>
Al <sup>iv</sup> <sub>c1</sub>	2.65	2.98	2.78	2.61	2.57	2.50	2.63	2.71	2.70	2.78
Al <sup>iv</sup> <sub>c2</sub>	2.17	2.36	2.21	2.10	2.06	1.99	2.12	2.23	2.25	2.22
*T°C <sub>Cath</sub>	340	383	354	331	325	313	334	350	350	356
**T°C <sub>K&amp;M</sub>	<b>299</b>	<b>333</b>	<b>312</b>	294	290	283	297	<b>305</b>	<b>305</b>	<b>313</b>
***T°C <sub>Z&amp;F</sub>	248	268	252	241	237	228	242	255	256	254
Fe/(Fe+Mg)	0.49	0.58	0.55	0.51	0.51	0.51	0.51	0.49	0.48	0.54
Al <sup>iv</sup> /Al <sub>tot</sub>	0.47	0.47	0.47	0.46	0.47	0.45	0.46	0.49	0.48	0.47
Si/Al <sub>tot</sub>	1.16	0.99	1.10	1.19	1.22	1.24	1.16	1.17	1.15	1.09
Na+K+2Ca	0.06	0.04	0.13	0.03	0.07	0.08	0.13	0.03	0.03	0.13

## APPENDIX

**Appendix 3b:** Electron microprobe analyses of white mica from altered wall rock at Batouri. Cl and F were sought for, but were below the detection limit of 0.03 and 0.05 wt %, respectively. FeO represents total iron content.

	<b>MS_1</b>	<b>MS_2</b>	<b>MS_3</b>	<b>MS_4</b>	<b>MS_5</b>	<b>MS_6</b>	<b>MS_7</b>	<b>MS_8</b>	<b>MS_9</b>	<b>MS_10</b>	<b>MS_11</b>
SiO <sub>2</sub> (wt %)	51.64	50.82	51.05	50.98	50.74	51.05	51.06	50.53	51.74	51.48	52.33
TiO <sub>2</sub> (wt %)	<0.03	<0.03	0.14	0.09	<0.03	<0.03	0.05	0.03	0.04	0.06	<0.03
Al <sub>2</sub> O <sub>3</sub> (wt %)	34.11	34.26	34.05	33.22	33.92	35.54	34.46	33.98	33.48	33.05	33.81
FeO (wt %)	1.93	1.80	3.22	3.59	1.89	1.33	1.91	2.17	2.28	2.34	2.17
MnO (wt %)	<0.05	<0.05	<0.05	<0.05	<0.05	<0.05	<0.05	<0.05	<0.05	<0.05	<0.05
MgO (wt %)	1.30	1.11	1.39	1.51	1.25	0.87	1.27	1.30	1.44	1.58	1.40
CaO (wt %)	<0.03	<0.03	<0.03	<0.03	<0.03	<0.03	<0.03	<0.03	<0.03	<0.03	<0.03
Na <sub>2</sub> O (wt %)	0.19	0.14	0.17	0.22	0.16	0.15	0.16	0.16	0.15	0.21	0.16
K <sub>2</sub> O (wt %)	7.74	8.49	7.29	7.89	7.19	8.30	7.56	7.59	7.52	7.78	6.70
Cl (wt %)	<0.03	<0.03	<0.03	<0.03	<0.03	<0.03	<0.03	<0.03	<0.03	<0.03	<0.03
F (wt %)	<0.05	<0.05	<0.05	<0.05	<0.05	<0.05	<0.05	<0.05	<0.05	<0.05	<0.05
<b>TOTAL (wt %)</b>	<b>96.26</b>	<b>96.01</b>	<b>96.67</b>	<b>96.92</b>	<b>94.56</b>	<b>96.61</b>	<b>95.82</b>	<b>95.12</b>	<b>96.03</b>	<b>95.86</b>	<b>95.93</b>
O=F, Cl	-	-	-	-	-	-	-	-	-	-	-
<b>TOTAL</b>	<b>96.26</b>	<b>96.01</b>	<b>96.67</b>	<b>96.92</b>	<b>94.56</b>	<b>96.61</b>	<b>95.82</b>	<b>95.12</b>	<b>96.03</b>	<b>95.86</b>	<b>95.93</b>
<b>Formula based on 22 oxygens</b>											
Si	6.60	6.54	6.53	6.54	6.58	6.50	6.55	6.54	6.63	6.62	6.66
Al <sup>iv</sup>	1.40	1.46	1.47	1.46	1.42	1.50	1.45	1.46	1.37	1.38	1.34
<b>Sum (Z)</b>	<b>8.00</b>										
Al <sup>vi</sup>	3.73	3.74	3.66	3.57	3.76	3.83	3.75	3.73	3.68	3.64	3.74
Ti	-	-	0.01	0.01	-	-	-	-	-	0.01	-
Fe <sup>2+</sup>	0.21	0.19	0.34	0.39	0.21	0.14	0.20	0.24	0.24	0.25	0.23
Mg	0.25	0.21	0.26	0.29	0.24	0.16	0.24	0.25	0.27	0.30	0.27
<b>Sum (Y)</b>	<b>4.18</b>	<b>4.14</b>	<b>4.28</b>	<b>4.26</b>	<b>4.21</b>	<b>4.14</b>	<b>4.21</b>	<b>4.22</b>	<b>4.20</b>	<b>4.20</b>	<b>4.24</b>
Na	0.05	0.03	0.04	0.05	0.04	0.04	0.04	0.04	0.04	0.05	0.04
K	1.26	1.39	1.19	1.29	1.19	1.35	1.24	1.25	1.23	1.28	1.09
<b>Sum (X)</b>	<b>1.31</b>	<b>1.43</b>	<b>1.23</b>	<b>1.34</b>	<b>1.23</b>	<b>1.39</b>	<b>1.28</b>	<b>1.29</b>	<b>1.27</b>	<b>1.33</b>	<b>1.13</b>
<b>Cations</b>	<b>13.49</b>	<b>13.57</b>	<b>13.51</b>	<b>13.60</b>	<b>13.44</b>	<b>13.52</b>	<b>13.48</b>	<b>13.51</b>	<b>13.47</b>	<b>13.53</b>	<b>13.36</b>
Anions	22.00	22.00	22.00	22.00	22.00	22.00	22.00	22.00	22.00	22.00	22.00
T2	7.67	7.73	7.68	7.71	7.79	7.65	7.70	7.78	7.70	7.73	7.65
Al (tot)	5.13	5.20	5.13	5.03	5.18	5.33	5.21	5.19	5.05	5.01	5.07
Fe+Mg	0.45	0.41	0.61	0.67	0.45	0.31	0.45	0.49	0.52	0.55	0.50

## APPENDIX

**Appendix 3b** continued.

	<b>MS_12</b>	<b>MS_13</b>	<b>MS_14</b>	<b>MS_15</b>	<b>MS_16</b>	<b>MS_17</b>	<b>MS_18</b>	<b>MS_19</b>	<b>MS_20</b>	<b>MS_21</b>
SiO <sub>2</sub> (wt %)	49.78	51.28	50.78	48.60	48.48	51.11	50.95	51.88	52.11	51.91
TiO <sub>2</sub> (wt %)	0.36	0.03	<0.03	0.04	0.06	<0.03	<0.03	<0.03	<0.03	<0.03
Al <sub>2</sub> O <sub>3</sub> (wt %)	31.14	33.10	33.56	38.77	36.63	33.49	33.34	33.20	34.01	33.68
FeO (wt %)	5.17	2.72	2.26	1.56	0.99	2.12	2.17	2.60	2.20	2.18
MnO (wt %)	<0.05	<0.05	<0.05	<0.05	<0.05	<0.05	<0.05	<0.05	<0.05	<0.05
MgO (wt %)	1.73	1.45	1.52	0.13	0.62	1.56	1.42	1.62	1.60	1.39
CaO (wt %)	<0.03	<0.03	<0.03	0.06	<0.03	0.00	0.06	<0.03	<0.03	<0.03
Na <sub>2</sub> O (wt %)	0.18	0.14	0.16	0.26	0.30	0.12	0.17	0.15	0.15	0.14
K <sub>2</sub> O (wt %)	7.97	8.19	8.75	7.77	8.35	8.51	6.63	8.04	7.21	7.89
Cl (wt %)	<0.03	<0.03	<0.03	<0.03	<0.03	<0.03	<0.03	<0.03	<0.03	<0.03
F (wt %)	<0.05	<0.05	<0.05	<0.05	<0.05	<0.05	<0.05	<0.05	<0.05	<0.05
<b>TOTAL</b> (wt %)	<b>95.70</b>	<b>96.27</b>	<b>96.45</b>	<b>96.54</b>	<b>94.79</b>	<b>96.26</b>	<b>94.11</b>	<b>96.88</b>	<b>96.65</b>	<b>96.57</b>
O=F, Cl	-	-	-	-	-	-	-	-	-	-
<b>TOTAL</b>	<b>95.70</b>	<b>96.27</b>	<b>96.45</b>	<b>96.54</b>	<b>94.79</b>	<b>96.26</b>	<b>94.11</b>	<b>96.88</b>	<b>96.65</b>	<b>96.57</b>
<b>Formula based on 22 oxygens</b>										
Si	6.54	6.60	6.54	6.20	6.30	6.57	6.62	6.62	6.61	6.62
Al <sup>IV</sup>	1.46	1.40	1.46	1.80	1.70	1.43	1.38	1.38	1.39	1.38
<b>Sum (Z)</b>	<b>8.00</b>									
Al <sup>VI</sup>	3.37	3.62	3.63	4.02	3.92	3.65	3.73	3.62	3.70	3.69
Ti	0.04	-	-	-	0.01	-	-	-	-	-
Fe <sup>2+</sup>	0.57	0.29	0.24	0.17	0.11	0.23	0.24	0.28	0.23	0.23
Mg	0.34	0.28	0.29	0.03	0.12	0.30	0.27	0.31	0.30	0.27
<b>Sum (Y)</b>	<b>4.32</b>	<b>4.20</b>	<b>4.17</b>	<b>4.22</b>	<b>4.15</b>	<b>4.18</b>	<b>4.24</b>	<b>4.20</b>	<b>4.24</b>	<b>4.19</b>
Ca	-	-	-	0.01	-	-	0.01	-	-	-
Na	0.04	0.03	0.04	0.06	0.08	0.03	0.04	0.04	0.04	0.03
K	1.34	1.34	1.44	1.26	1.38	1.40	1.10	1.31	1.17	1.28
<b>Sum (X)</b>	<b>1.38</b>	<b>1.38</b>	<b>1.49</b>	<b>1.34</b>	<b>1.46</b>	<b>1.43</b>	<b>1.15</b>	<b>1.35</b>	<b>1.20</b>	<b>1.32</b>
<b>Cations</b>	<b>13.70</b>	<b>13.58</b>	<b>13.65</b>	<b>13.55</b>	<b>13.61</b>	<b>13.60</b>	<b>13.39</b>	<b>13.55</b>	<b>13.44</b>	<b>13.50</b>
Anions	22.00	22.00	22.00	22.00	22.00	22.00	22.00	22.00	22.00	22.00
T2	7.90	7.73	7.74	7.66	7.81	7.73	7.81	7.67	7.63	7.66
Al (tot)	4.83	5.02	5.09	5.82	5.61	5.08	5.11	4.99	5.09	5.06
Fe+Mg	0.91	0.57	0.53	0.19	0.23	0.53	0.51	0.58	0.54	0.50

## APPENDIX

**Appendix 3b** continued.

	MS_22	MS_23	MS_24	MS_25	MS_26	MS_27	MS_28	MS_29	MS_30	MS_31
SiO <sub>2</sub> (wt %)	51.40	52.09	52.01	50.92	51.49	48.03	51.87	50.52	51.44	50.98
TiO <sub>2</sub> (wt %)	<0.03	0.03	0.34	0.54	<0.03	<0.03	0.06	0.10	0.07	0.22
Al <sub>2</sub> O <sub>3</sub> (wt %)	32.93	33.37	30.86	30.40	33.78	32.86	31.58	34.56	33.35	32.93
FeO (wt %)	2.55	2.32	3.32	4.13	2.05	3.11	3.39	2.01	3.19	3.05
MnO (wt %)	<0.05	<0.05	<0.05	<0.05	<0.05	<0.05	<0.05	<0.05	<0.05	<0.05
MgO (wt %)	1.50	1.46	2.99	2.98	1.53	1.31	2.16	1.06	1.73	1.88
CaO (wt %)	<0.03	<0.03	<0.03	<0.03	<0.03	<0.03	<0.03	<0.03	<0.03	<0.03
Na <sub>2</sub> O (wt %)	0.14	0.18	0.12	0.13	0.14	0.15	0.11	0.18	0.16	0.14
K <sub>2</sub> O (wt %)	8.08	7.87	7.51	7.93	7.49	9.79	7.06	9.00	5.80	7.21
Cl (wt %)	<0.03	<0.03	<0.03	<0.03	<0.03	<0.03	<0.03	<0.03	<0.03	<0.03
F (wt %)	<0.05	<0.05	<0.05	<0.05	<0.05	<0.05	<0.05	<0.05	<0.05	<0.05
<b>TOTAL</b> (wt %)	<b>95.98</b>	<b>96.69</b>	<b>96.51</b>	<b>96.40</b>	<b>95.88</b>	<b>94.68</b>	<b>95.60</b>	<b>96.79</b>	<b>95.10</b>	<b>95.81</b>
O=F, Cl	-	-	-	-	-	-	-	-	-	-
<b>TOTAL</b>	<b>95.98</b>	<b>96.69</b>	<b>96.51</b>	<b>96.40</b>	<b>95.88</b>	<b>94.68</b>	<b>95.60</b>	<b>96.79</b>	<b>95.10</b>	<b>95.81</b>
<b>Formula based on 22 oxygens</b>										
Si	6.62	6.64	6.68	6.61	6.60	6.40	6.70	6.48	6.62	6.57
Al <sup>IV</sup>	1.38	1.36	1.32	1.39	1.40	1.60	1.30	1.52	1.38	1.43
<b>Sum (Z)</b>	<b>8.00</b>									
Al <sup>VI</sup>	3.63	3.66	3.36	3.26	3.70	3.56	3.51	3.71	3.67	3.58
Ti	-	-	0.03	0.05	-	-	0.01	0.01	0.01	0.02
Fe <sup>2+</sup>	0.28	0.25	0.36	0.45	0.22	0.35	0.37	0.22	0.34	0.33
Mg	0.29	0.28	0.57	0.58	0.29	0.26	0.42	0.20	0.33	0.36
<b>Sum (Y)</b>	<b>4.19</b>	<b>4.18</b>	<b>4.32</b>	<b>4.34</b>	<b>4.21</b>	<b>4.17</b>	<b>4.29</b>	<b>4.14</b>	<b>4.35</b>	<b>4.29</b>
Na	0.04	0.05	0.03	0.03	0.03	0.04	0.03	0.05	0.04	0.03
K	1.33	1.28	1.23	1.31	1.22	1.66	1.16	1.47	0.95	1.19
<b>Sum (X)</b>	<b>1.37</b>	<b>1.33</b>	<b>1.26</b>	<b>1.35</b>	<b>1.26</b>	<b>1.70</b>	<b>1.19</b>	<b>1.52</b>	<b>0.99</b>	<b>1.22</b>
<b>Cations</b>	<b>13.56</b>	<b>13.51</b>	<b>13.58</b>	<b>13.68</b>	<b>13.48</b>	<b>13.87</b>	<b>13.49</b>	<b>13.65</b>	<b>13.35</b>	<b>13.51</b>
Anions	22.00	22.00	22.00	22.00	22.00	22.00	22.00	22.00	22.00	22.00
T2	7.74	7.66	7.72	7.80	7.70	8.00	7.76	7.71	7.73	7.75
Al (tot)	5.00	5.01	4.67	4.65	5.10	5.16	4.81	5.23	5.05	5.00
Fe+Mg	0.56	0.52	0.93	1.02	0.51	0.61	0.78	0.42	0.68	0.69

## APPENDIX

**Appendix 3b** continued.

	<b>MS_32</b>	<b>MS_33</b>	<b>MS_34</b>	<b>MS_35</b>	<b>MS_36</b>	<b>MS_37</b>	<b>MS_38</b>	<b>MS_39</b>	<b>MS_40</b>	<b>MS_41</b>
SiO <sub>2</sub> (wt %)	51.81	51.76	51.68	51.41	51.87	51.39	51.41	52.10	51.81	51.45
TiO (wt %) <sub>2</sub>	0.04	0.04	0.04	0.03	0.03	0.54	<0.03	0.05	0.15	0.06
Al <sub>2</sub> O <sub>3</sub> (wt %)	32.66	33.55	33.47	34.57	33.84	32.68	34.13	33.87	33.20	33.85
FeO (wt %)	2.47	2.25	2.30	1.84	2.13	2.61	2.36	2.45	2.81	2.31
MnO (wt %)	<0.05	<0.05	<0.05	<0.05	<0.05	<0.05	<0.05	<0.05	<0.05	<0.05
MgO (wt %)	1.60	1.47	1.43	1.18	1.42	1.81	1.31	1.45	1.61	1.39
CaO (wt %)	0.03	<0.03	<0.03	<0.03	<0.03	<0.03	<0.03	<0.03	<0.03	<0.03
Na <sub>2</sub> O (wt %)	0.17	0.11	0.17	0.20	0.14	0.13	0.18	0.16	0.12	0.13
K <sub>2</sub> O (wt %)	6.72	5.84	7.92	8.29	7.26	6.21	8.05	7.45	7.75	8.00
Cl (wt %)	<0.03	<0.03	<0.03	<0.03	<0.03	<0.03	<0.03	<0.03	<0.03	<0.03
F (wt %)	<0.05	<0.05	<0.05	<0.05	<0.05	<0.05	<0.05	<0.05	<0.05	<0.05
<b>TOTAL</b> (wt %)	<b>94.87</b>	<b>94.38</b>	<b>96.36</b>	<b>96.90</b>	<b>96.06</b>	<b>94.71</b>	<b>96.80</b>	<b>96.90</b>	<b>96.83</b>	<b>96.55</b>
O=F, Cl	-	-	-	-	-	-	-	-	-	-
<b>TOTAL</b>	94.87	94.38	96.36	96.90	96.06	94.71	96.80	96.90	96.83	96.55
<b>Formula based on 22 oxygens</b>										
Si	6.69	6.67	6.62	6.55	6.62	6.64	6.56	6.61	6.61	6.58
Al <sup>IV</sup>	1.31	1.33	1.38	1.45	1.38	1.36	1.44	1.39	1.39	1.42
<b>Sum (Z)</b>	<b>8.00</b>									
Al <sup>VI</sup>	3.66	3.76	3.66	3.73	3.72	3.61	3.69	3.68	3.61	3.68
Ti	-	-	-	-	-	0.05	-	0.01	0.01	0.01
Fe <sup>2+</sup>	0.27	0.24	0.25	0.20	0.23	0.28	0.25	0.26	0.30	0.25
Mg	0.31	0.28	0.27	0.22	0.27	0.35	0.25	0.28	0.31	0.27
<b>Sum (Y)</b>	<b>4.24</b>	<b>4.29</b>	<b>4.19</b>	<b>4.16</b>	<b>4.22</b>	<b>4.30</b>	<b>4.20</b>	<b>4.22</b>	<b>4.23</b>	<b>4.20</b>
Na	0.04	0.03	0.04	0.05	0.03	0.03	0.04	0.04	0.03	0.03
K	1.11	0.96	1.29	1.35	1.18	1.02	1.31	1.21	1.26	1.30
<b>Sum (X)</b>	<b>1.16</b>	<b>0.99</b>	<b>1.33</b>	<b>1.40</b>	<b>1.22</b>	<b>1.05</b>	<b>1.35</b>	<b>1.25</b>	<b>1.30</b>	<b>1.34</b>
<b>Cations</b>	<b>13.39</b>	<b>13.28</b>	<b>13.52</b>	<b>13.55</b>	<b>13.43</b>	<b>13.35</b>	<b>13.55</b>	<b>13.47</b>	<b>13.52</b>	<b>13.53</b>
Anions	22.00	22.00	22.00	22.00	22.00	22.00	22.00	22.00	22.00	22.00
T2	7.76	7.74	7.69	7.65	7.67	7.76	7.67	7.63	7.67	7.68
Al (tot)	4.97	5.09	5.05	5.19	5.09	4.97	5.13	5.07	4.99	5.10
Fe+Mg	0.57	0.52	0.52	0.42	0.50	0.63	0.50	0.53	0.61	0.51

**Appendix 3c:** Representative electron microprobe analyses of carbonate from quartz-carbonate veins within altered wall-rock at Batouri

	1 / 1	2 / 1	3 / 1	4 / 1	5 / 1	6 / 1	7 / 1	8 / 1	9 / 1	10 / 1	11 / 1	12 / 1	13 / 1	14 / 1	15 / 1	16 / 1	17 / 1	18 / 1	19 / 1
CaO (wt %)	62.06	59.71	56.01	46.76	58.70	55.38	58.60	57.19	59.76	60.23	58.15	58.52	59.60	56.76	47.60	54.98	58.51	59.19	62.40
MgO (wt %)	0.24	0.26	0.51	1.03	0.51	0.93	0.51	0.57	0.56	0.57	0.53	0.51	0.48	0.40	0.35	0.48	0.38	0.44	0.12
FeO (wt %)	0.82	0.90	1.67	2.24	1.22	2.19	1.17	1.30	1.14	1.13	1.18	1.03	0.95	0.96	0.88	1.09	1.01	0.86	0.23
MnO (wt %)	1.02	0.95	1.02	0.78	1.12	1.02	1.27	1.38	1.38	1.41	1.44	1.28	1.27	1.23	1.05	1.26	1.14	1.26	0.40
TiO <sub>2</sub> (wt %)	0.09	0.61	<0.04	0.09	0.06	0.13	<0.04	0.21	<0.04	<0.04	<0.04	0.05	0.08	0.08	0.04	<0.04	0.04	0.15	<0.04
<b>sum (wt %)</b>	<b>64.23</b>	<b>62.43</b>	<b>59.24</b>	<b>50.89</b>	<b>61.60</b>	<b>59.66</b>	<b>61.55</b>	<b>60.65</b>	<b>62.85</b>	<b>63.33</b>	<b>61.33</b>	<b>61.38</b>	<b>62.37</b>	<b>59.43</b>	<b>49.91</b>	<b>57.84</b>	<b>61.08</b>	<b>61.89</b>	<b>63.17</b>
<b>Structural formulae basis on cation per 2 oxygen atoms</b>																			
Ca	0.97	0.96	0.95	0.92	0.95	0.93	0.95	0.94	0.95	0.95	0.95	0.95	0.96	0.96	0.95	0.95	0.96	0.96	0.99
Mg	-	-	0.01	0.02	0.01	0.02	0.01	0.01	0.01	0.01	0.01	0.01	0.01	0.01	0.01	0.01	0.01	0.01	-
Fe	0.01	0.01	0.03	0.04	0.02	0.04	0.02	0.02	0.02	0.02	0.02	0.02	0.02	0.02	0.02	0.02	0.02	0.01	-
Mn	0.02	0.02	0.02	0.02	0.02	0.02	0.02	0.02	0.02	0.02	0.02	0.02	0.02	0.02	0.02	0.02	0.02	0.02	0.01
Ti	-	0.01	-	-	-	-	-	-	-	-	-	-	-	-	-	-	-	-	
CaCO <sub>3</sub>	96.62	95.64	94.55	91.88	95.30	92.84	95.20	94.31	95.08	95.10	94.81	95.33	95.55	95.51	95.37	95.06	95.79	95.63	98.79
MgCO <sub>3</sub>	0.37	0.42	0.86	2.01	0.82	1.56	0.83	0.94	0.89	0.91	0.87	0.82	0.76	0.68	0.70	0.82	0.63	0.71	0.19
FeCO <sub>3</sub>	1.27	1.45	2.82	4.41	1.98	3.67	1.91	2.14	1.82	1.78	1.92	1.68	1.52	1.62	1.77	1.88	1.66	1.39	0.36
MnCO <sub>3</sub>	1.59	1.52	1.72	1.53	1.81	1.71	2.06	2.27	2.20	2.22	2.35	2.09	2.04	2.07	2.10	2.18	1.87	2.03	0.63
<b>Sum</b>	<b>99.85</b>	<b>99.03</b>	<b>99.95</b>	<b>99.83</b>	<b>99.91</b>	<b>99.78</b>	<b>100.0</b>	<b>99.65</b>	<b>100.0</b>	<b>100.0</b>	<b>99.95</b>	<b>99.92</b>	<b>99.88</b>	<b>99.87</b>	<b>99.93</b>	<b>99.95</b>	<b>99.94</b>	<b>99.76</b>	<b>99.97</b>

**Appendix 3c** continued.

	<b>20/ 1</b>	<b>21/ 1</b>	<b>22/ 1</b>	<b>23/ 1</b>	<b>24/ 1</b>	<b>25/ 1</b>	<b>26/ 1</b>	<b>27/ 1</b>	<b>28/ 1</b>	<b>29/ 1</b>	<b>30/ 1</b>	<b>31/ 1</b>	<b>32/ 1</b>	<b>33/ 1</b>	<b>34/ 1</b>	<b>35/ 1</b>	<b>36/ 1</b>
CaO (wt %)	56.91	59.99	62.91	61.58	61.82	59.35	30.29	59.01	57.79	28.91	30.16	30.31	50.12	30.05	53.48	56.99	28.82
MgO (wt %)	0.44	0.58	0.12	0.22	0.32	0.36	13.44	0.68	0.68	12.66	13.43	12.87	2.51	13.31	1.69	0.32	11.62
FeO (wt %)	1.07	1.36	0.29	0.51	0.68	0.88	10.01	1.62	1.85	13.04	9.95	10.41	3.48	9.76	1.89	0.65	13.62
MnO (wt %)	1.17	1.40	0.45	0.69	0.75	0.96	1.37	0.44	0.31	0.60	1.27	1.34	0.57	1.27	0.64	0.66	0.80
TiO <sub>2</sub> (wt %)	<0.04	<0.04	<0.04	<0.04	<0.04	<0.04	<0.04	<0.04	<0.04	<0.04	<0.04	<0.04	<0.04	<0.04	<0.04	<0.04	<0.04
<b>sum (wt %)</b>	<b>59.60</b>	<b>63.35</b>	<b>63.76</b>	<b>63.01</b>	<b>63.57</b>	<b>61.54</b>	<b>55.11</b>	<b>61.76</b>	<b>60.63</b>	<b>55.20</b>	<b>54.80</b>	<b>54.94</b>	<b>56.69</b>	<b>54.38</b>	<b>57.71</b>	<b>58.65</b>	<b>54.87</b>
<b>Structural formulae basis on cation per 2 oxygen atoms</b>																	
Ca	0.95	0.95	0.99	0.98	0.97	0.96	0.55	0.96	0.95	0.52	0.55	0.55	0.88	0.55	0.93	0.97	0.53
Mg	0.01	0.01	-	-	0.01	0.01	0.24	0.01	0.01	0.23	0.25	0.23	0.04	0.24	0.03	0.01	0.21
Fe	0.02	0.02	-	0.01	0.01	0.01	0.18	0.03	0.03	0.24	0.18	0.19	0.06	0.18	0.03	0.01	0.25
Mn	0.02	0.02	0.01	0.01	0.01	0.02	0.02	0.01	0.01	0.01	0.02	0.02	0.01	0.02	0.01	0.01	0.01
CaCO <sub>3</sub>	95.48	94.69	98.66	97.74	97.26	96.44	54.96	95.55	95.31	52.37	55.03	55.17	88.42	55.25	92.67	97.18	52.53
MgCO <sub>3</sub>	0.74	0.91	0.19	0.35	0.50	0.58	24.39	1.09	1.13	22.93	24.50	23.43	4.42	24.47	2.93	0.55	21.18
FeCO <sub>3</sub>	1.79	2.15	0.45	0.81	1.07	1.43	18.16	2.63	3.04	23.62	18.15	18.95	6.14	17.94	3.27	1.11	24.81
MnCO <sub>3</sub>	1.97	2.21	0.70	1.10	1.17	1.55	2.49	0.72	0.51	1.09	2.31	2.43	1.00	2.33	1.11	1.13	1.45
<b>Sum</b>	<b>99.98</b>	<b>99.95</b>	<b>100.0</b>	<b>100.0</b>	<b>100.0</b>	<b>100.0</b>	<b>100.0</b>	<b>100.0</b>	<b>99.99</b>	<b>100.0</b>	<b>99.99</b>	<b>99.99</b>	<b>99.98</b>	<b>100.0</b>	<b>99.98</b>	<b>99.97</b>	<b>99.97</b>

**Appendix 3c** continued.

	<b>37 /1</b>	<b>38 /1</b>	<b>39 /1</b>	<b>40 /1</b>	<b>41 /1</b>	<b>42 /1</b>	<b>43 /1</b>	<b>44 /1</b>	<b>45 /1</b>	<b>46 /1</b>	<b>47 /1</b>	<b>48 /1</b>	<b>49 /1</b>	<b>50 /1</b>	<b>51 /1</b>	<b>52 /1</b>	<b>53 /1</b>
CaO (wt %)	28.16	28.56	28.48	28.74	28.64	28.86	29.03	28.91	28.96	29.08	32.50	28.61	28.40	28.42	28.75	28.51	28.53
MgO (wt %)	10.45	10.26	10.26	10.29	10.04	10.80	11.16	11.18	11.42	10.77	12.65	10.09	10.33	10.48	9.94	10.25	10.16
FeO (wt %)	16.76	17.01	17.27	17.06	16.55	15.26	14.95	15.37	15.02	15.69	9.40	17.56	17.62	17.23	17.48	17.37	17.00
MnO (wt %)	0.39	0.34	0.36	0.38	0.39	0.45	0.44	0.43	0.41	0.45	0.51	0.36	0.33	0.28	0.38	0.35	0.37
TiO <sub>2</sub> (wt %)	<0.04	<0.04	<0.04	<0.04	<0.04	<0.04	<0.04	<0.04	<0.04	<0.04	<0.04	<0.04	<0.04	<0.04	<0.04	<0.04	<0.04
<b>sum</b> (wt %)	<b>55.75</b>	<b>56.19</b>	<b>56.38</b>	<b>56.48</b>	<b>55.63</b>	<b>55.38</b>	<b>55.58</b>	<b>55.89</b>	<b>55.82</b>	<b>55.99</b>	<b>55.07</b>	<b>56.63</b>	<b>56.68</b>	<b>56.41</b>	<b>56.57</b>	<b>56.47</b>	<b>56.06</b>
<b>Structural formulae basis on cation per 2 oxygen atoms</b>																	
Ca	0.51	0.51	0.51	0.51	0.51	0.52	0.52	0.52	0.52	0.52	0.59	0.51	0.50	0.50	0.51	0.50	0.51
Mg	0.19	0.18	0.18	0.18	0.18	0.19	0.20	0.20	0.20	0.20	0.19	0.23	0.18	0.18	0.19	0.18	0.18
Fe	0.30	0.30	0.31	0.30	0.30	0.28	0.27	0.28	0.27	0.28	0.17	0.31	0.31	0.31	0.31	0.31	0.30
Mn	0.01	0.01	0.01	0.01	0.01	0.01	0.01	0.01	0.01	0.01	0.01	0.01	0.01	0.00	0.01	0.01	0.01
CaCO <sub>3</sub>	50.50	50.82	50.52	50.88	51.49	52.12	52.24	51.73	51.88	51.94	59.02	50.52	50.11	50.39	50.82	50.48	50.89
MgCO <sub>3</sub>	18.73	18.25	18.20	18.22	18.04	19.49	20.08	20.00	20.47	19.24	22.98	17.82	18.22	18.57	17.58	18.14	18.11
FeCO <sub>3</sub>	30.06	30.27	30.63	30.21	29.75	27.56	26.90	27.50	26.91	28.02	17.06	31.01	31.09	30.54	30.89	30.76	30.32
MnCO <sub>3</sub>	0.70	0.60	0.65	0.68	0.70	0.82	0.78	0.76	0.74	0.80	0.93	0.63	0.59	0.50	0.67	0.62	0.66
<b>Sum</b>	<b>100.0</b>	<b>99.94</b>	<b>100.0</b>	<b>99.99</b>	<b>99.99</b>	<b>100.0</b>	<b>100.0</b>	<b>100.0</b>	<b>100.0</b>	<b>100.0</b>	<b>99.98</b>	<b>99.98</b>	<b>100.0</b>	<b>100.0</b>	<b>99.96</b>	<b>100.0</b>	<b>99.99</b>

**Appendix 3c** continued.

	<b>54/1</b>	<b>55/1</b>	<b>56/1</b>	<b>57/1</b>	<b>58/1</b>	<b>59/1</b>	<b>60/1</b>	<b>61/1</b>	<b>62/1</b>	<b>63/1</b>	<b>64/1</b>	<b>65/1</b>	<b>66/1</b>	<b>67/1</b>	<b>68/1</b>	<b>69/1</b>
CaO (wt %)	28.89	28.76	29.51	29.41	29.15	28.65	28.27	29.24	28.53	28.45	58.72	29.36	29.36	28.98	29.31	28.65
MgO (wt %)	11.36	12.02	11.28	11.17	11.31	9.94	10.10	11.56	10.12	10.35	0.59	10.24	10.58	10.18	11.25	10.11
FeO (wt %)	14.80	14.90	14.87	14.70	15.03	17.36	17.56	14.61	17.41	16.78	1.22	15.77	15.98	16.88	15.07	16.92
MnO (wt %)	0.45	0.38	0.40	0.41	0.57	0.35	0.31	0.45	0.37	0.38	0.46	0.39	0.45	0.36	0.43	0.37
TiO <sub>2</sub> (wt %)	<0.04	<0.04	<0.04	<0.04	<0.04	<0.04	<0.04	<0.04	<0.04	<0.04	<0.04	<0.04	<0.04	<0.04	<0.04	<0.04
<b>sum (wt %)</b>	<b>55.50</b>	<b>56.06</b>	<b>56.05</b>	<b>55.69</b>	<b>56.07</b>	<b>56.29</b>	<b>56.24</b>	<b>55.89</b>	<b>56.43</b>	<b>55.96</b>	<b>61.00</b>	<b>55.78</b>	<b>56.37</b>	<b>56.41</b>	<b>56.08</b>	<b>56.06</b>
<b>Structural formulae basis on cation per 2 oxygen atoms</b>																
Ca	0.52	0.51	0.53	0.53	0.52	0.51	0.50	0.52	0.51	0.51	0.96	0.53	0.52	0.51	0.52	0.51
Mg	0.20	0.21	0.20	0.20	0.20	0.18	0.18	0.21	0.18	0.18	0.01	0.18	0.19	0.18	0.20	0.18
Fe	0.27	0.27	0.27	0.26	0.27	0.31	0.31	0.26	0.31	0.30	0.02	0.28	0.28	0.30	0.27	0.30
Mn	0.01	0.01	0.01	0.01	0.01	0.01	0.01	0.01	0.01	0.01	0.01	0.01	0.01	0.01	0.01	0.01
CaCO <sub>3</sub>	52.06	51.31	52.64	52.81	51.99	50.90	50.26	52.32	50.57	50.84	96.26	52.63	52.08	51.38	52.26	51.11
MgCO <sub>3</sub>	20.46	21.43	20.12	20.06	20.18	17.65	17.97	20.68	17.93	18.49	0.97	18.36	18.77	18.04	20.06	18.03
FeCO <sub>3</sub>	26.67	26.58	26.53	26.39	26.80	30.83	31.22	26.14	30.85	29.99	1.99	28.27	28.35	29.93	26.86	30.19
MnCO <sub>3</sub>	0.81	0.67	0.71	0.73	1.02	0.62	0.55	0.80	0.65	0.69	0.75	0.69	0.80	0.64	0.77	0.67
<b>Sum</b>	<b>100.0</b>	<b>99.99</b>	<b>100.0</b>	<b>100.0</b>	<b>99.99</b>	<b>100.0</b>	<b>100.0</b>	<b>99.94</b>	<b>100.0</b>	<b>100.0</b>	<b>99.97</b>	<b>99.95</b>	<b>100.0</b>	<b>100.0</b>	<b>99.95</b>	<b>100.0</b>

## APPENDIX

**Appendix 3d:** Representative electron microprobe analyses of hydrothermal apatite from altered wall-rock at Batouri.

	1/1	2/1	3/1	4/1	5/1	6/1	7/1	8/1	9/1	10/1	11/1
CaO (wt %)	56.77	56.33	56.92	56.00	56.28	56.21	56.13	56.39	56.26	56.20	56.13
MgO (wt %)	<0.03	<0.03	<0.03	<0.03	<0.03	<0.03	<0.03	<0.03	<0.03	<0.03	<0.03
P <sub>2</sub> O <sub>5</sub> (wt %)	41.75	41.65	41.77	41.82	41.47	42.27	42.23	41.63	40.28	40.83	42.49
Cl (wt %)	0.03	<0.03	<0.03	0.03	0.04	0.04	<0.03	0.06	0.06	<0.03	<0.03
F (wt %)	2.20	2.13	2.28	2.23	2.23	2.16	2.35	2.15	2.11	2.12	2.24
<b>TOTAL (wt %)</b>	<b>101</b>	<b>100</b>	<b>101</b>	<b>100</b>	<b>100</b>	<b>101</b>	<b>101</b>	<b>100</b>	<b>98.71</b>	<b>99.17</b>	<b>101</b>
O=F, Cl	0.93	0.90	0.96	0.95	0.95	0.92	0.99	0.92	0.90	0.89	0.94
<b>TOTAL</b>	<b>99.83</b>	<b>99.23</b>	<b>100.0</b>	<b>99.14</b>	<b>99.07</b>	<b>99.78</b>	<b>99.76</b>	<b>99.31</b>	<b>97.81</b>	<b>98.28</b>	<b>99.94</b>
<b>Structural formulae based on 25 O, OH, Cl, F</b>											
Ca	9.96	9.93	9.96	9.86	9.94	9.83	9.81	9.94	10.12	10.04	9.99
P	5.79	5.80	5.78	5.82	5.79	5.84	5.83	5.80	5.72	5.76	5.77
Cl	0.01	-	-	0.01	0.01	0.01	-	0.02	0.02	-	-
F	1.14	1.11	1.18	1.16	1.16	1.12	1.21	1.12	1.12	1.12	1.15
OH	0.85	0.89	0.82	0.83	0.83	0.87	0.78	0.87	0.86	0.88	0.85
$\Sigma$	<b>17.74</b>	<b>17.74</b>	<b>17.74</b>	<b>17.68</b>	<b>17.73</b>	<b>17.67</b>	<b>17.62</b>	<b>17.74</b>	<b>17.85</b>	<b>17.79</b>	<b>17.76</b>
	12/1	13/1	14/1	15/1	16/1	17/1	18/1	19/1	20/1	21/1	22/1
CaO (wt %)	56.67	55.60	56.11	56.54	56.47	55.81	55.93	56.87	56.28	56.47	56.66
MgO (wt %)	<0.03	<0.03	<0.03	<0.03	<0.03	<0.03	<0.03	<0.03	0.03	0.03	<0.03
P <sub>2</sub> O <sub>5</sub> (wt %)	41.45	42.37	41.82	41.82	41.67	41.87	41.99	41.76	41.73	41.33	41.37
Cl (wt %)	<0.03	<0.03	<0.03	<0.03	<0.03	0.04	0.05	<0.03	<0.03	<0.03	<0.03
F (wt %)	2.21	2.28	2.14	2.12	2.21	2.18	2.28	2.07	2.27	2.01	2.27
<b>TOTAL (wt %)</b>	<b>100</b>	<b>100</b>	<b>100</b>	<b>101</b>	<b>100</b>	<b>99.9</b>	<b>100</b>	<b>101</b>	<b>100</b>	<b>99.84</b>	<b>100</b>
O=F, Cl	0.93	0.96	0.90	0.89	0.93	0.93	0.97	0.87	0.96	0.85	0.96
<b>TOTAL</b>	<b>99.42</b>	<b>99.30</b>	<b>99.20</b>	<b>99.62</b>	<b>99.46</b>	<b>98.99</b>	<b>99.28</b>	<b>99.84</b>	<b>99.35</b>	<b>98.99</b>	<b>99.35</b>
<b>Structural formulae based on 25 O, OH, Cl, F</b>											
Ca	9.99	9.74	9.88	9.93	9.94	9.84	9.83	9.98	9.90	10.00	9.99
Mg	-	-	-	-	-	-	-	-	0.01	0.01	-
P	5.77	5.87	5.82	5.81	5.79	5.83	5.83	5.79	5.80	5.79	5.77
Cl	-	-	-	-	-	0.01	0.01	-	-	-	-
F	1.15	1.18	1.11	1.10	1.15	1.14	1.18	1.07	1.18	1.05	1.18
OH	0.85	0.82	0.88	0.90	0.85	0.85	0.80	0.93	0.82	0.95	0.82
$\Sigma$	<b>17.76</b>	<b>17.61</b>	<b>17.71</b>	<b>17.74</b>	<b>17.71</b>	<b>17.68</b>	<b>17.66</b>	<b>17.78</b>	<b>17.71</b>	<b>17.80</b>	<b>17.76</b>

## APPENDIX

**Appendix 3d** continued.

	23/1	24/1	25/1	26/1	27/1	28/1	29/1	30/1	31/1	32/1	33/1
CaO (wt %)	56.55	56.30	55.87	55.83	56.17	56.35	56.43	56.10	56.53	56.11	56.53
MgO (wt %)	<0.03	<0.03	<0.03	0.03	<0.03	<0.03	<0.03	<0.03	<0.03	<0.03	0.03
P <sub>2</sub> O <sub>5</sub> (wt %)	41.49	41.32	41.21	42.39	41.91	41.54	41.70	41.66	41.21	41.70	41.67
Cl (wt %)	<0.03	<0.03	<0.03	<0.03	<0.03	<0.03	<0.03	<0.03	<0.03	<0.03	0.03
F (wt %)	2.24	2.38	2.16	2.27	2.10	2.27	2.24	2.40	2.23	2.41	2.40
<b>TOTAL (wt %)</b>	<b>100</b>	<b>100</b>	<b>99.27</b>	<b>101</b>	<b>100</b>	<b>100</b>	<b>100</b>	<b>99.98</b>	<b>100</b>	<b>100</b>	<b>101</b>
O=F, Cl	0.94	1.00	0.91	0.95	0.88	0.96	0.94	1.01	0.94	1.02	1.01
<b>TOTAL</b>	<b>99.35</b>	<b>99.02</b>	<b>98.36</b>	<b>99.56</b>	<b>99.31</b>	<b>99.22</b>	<b>99.46</b>	<b>99.17</b>	<b>99.04</b>	<b>99.22</b>	<b>99.63</b>
<b>Structural formulae based on 25 O, OH, Cl, F</b>											
Ca	9.97	9.95	9.94	9.76	9.88	9.94	9.92	9.88	10.01	9.88	9.92
Mg	-	-	-	0.01	-	-	-	-	-	-	0.01
P	5.78	5.77	5.79	5.86	5.83	5.79	5.80	5.80	5.76	5.80	5.78
Cl	-	-	-	-	-	-	-	-	-	-	0.01
F	1.16	1.24	1.14	1.17	1.09	1.18	1.16	1.25	1.17	1.25	1.24
OH	0.83	0.75	0.86	0.83	0.91	0.81	0.83	0.75	0.83	0.74	0.75
$\Sigma$	<b>17.75</b>	<b>17.72</b>	<b>17.73</b>	<b>17.63</b>	<b>17.71</b>	<b>17.72</b>	<b>17.71</b>	<b>17.68</b>	<b>17.77</b>	<b>17.66</b>	<b>17.71</b>
	34/1	35/1	36/1	37/1	38/1	39/1	40/1	41/1	42/1	43/1	44/1
CaO (wt %)	56.43	56.80	55.90	56.32	56.19	56.13	56.73	56.44	56.16	56.64	56.06
MgO (wt %)	0.03	0.03	<0.03	<0.03	<0.03	<0.03	<0.03	0.03	<0.03	<0.03	<0.03
P <sub>2</sub> O <sub>5</sub> (wt %)	41.50	41.52	41.99	41.56	41.29	41.56	41.68	41.14	41.11	41.46	41.44
Cl (wt %)	<0.03	0.03	<0.03	<0.03	<0.03	<0.03	<0.03	<0.03	<0.03	<0.03	0.03
F (wt %)	2.30	2.21	2.37	2.28	2.25	2.32	2.25	2.28	2.18	2.25	2.36
<b>TOTAL (wt %)</b>	<b>100</b>	<b>101</b>	<b>100</b>	<b>100</b>	<b>99.76</b>	<b>100</b>	<b>101</b>	<b>99.90</b>	<b>99.46</b>	<b>100</b>	<b>99.89</b>
O=F, Cl	0.97	0.94	1.00	0.96	0.95	0.98	0.95	0.96	0.92	0.95	1.00
<b>TOTAL</b>	<b>99.30</b>	<b>99.65</b>	<b>99.27</b>	<b>99.22</b>	<b>98.81</b>	<b>99.05</b>	<b>99.73</b>	<b>98.94</b>	<b>98.54</b>	<b>99.42</b>	<b>98.89</b>
<b>Structural formulae based on 25 O, OH, Cl, F</b>											
Ca	9.95	9.99	9.82	9.93	9.96	9.90	9.96	10.00	9.99	9.98	9.91
Mg	0.01	0.01	-	-	-	-	-	0.01	-	-	-
P	5.78	5.77	5.83	5.79	5.78	5.79	5.78	5.76	5.78	5.77	5.79
Cl	-	0.01	-	-	-	-	-	-	-	-	0.01
F	1.20	1.15	1.23	1.19	1.18	1.21	1.16	1.19	1.15	1.17	1.23
OH	0.80	0.84	0.77	0.81	0.82	0.79	0.83	0.81	0.85	0.83	0.76
$\Sigma$	<b>17.73</b>	<b>17.77</b>	<b>17.65</b>	<b>17.72</b>	<b>17.73</b>	<b>17.70</b>	<b>17.74</b>	<b>17.76</b>	<b>17.76</b>	<b>17.75</b>	<b>17.70</b>

## APPENDIX

**Appendix 3d** continued.

	45/1	46/1	47/1	48/1	49/1	50/1	51/1	52/1	53/1	54/1
CaO (wt %)	56.56	55.65	56.34	56.72	56.53	56.29	55.92	55.95	56.45	55.97
MgO (wt %)	<0.03	<0.03	<0.03	<0.03	<0.03	<0.03	<0.03	0.03	<0.03	<0.03
P <sub>2</sub> O <sub>5</sub> (wt %)	41.51	42.51	41.61	41.66	41.34	41.73	41.90	41.20	39.88	41.06
Cl (wt %)	0.03	0.04	<0.03	<0.03	<0.03	<0.03	<0.03	<0.03	0.04	0.06
F (wt %)	2.17	2.32	2.35	2.36	2.25	2.30	2.19	2.35	2.01	2.17
<b>TOTAL</b> (wt %)	<b>100</b>	<b>101</b>	<b>100</b>	<b>101</b>	<b>100</b>	<b>100</b>	<b>100</b>	<b>99.55</b>	<b>98.39</b>	<b>99.27</b>
O=F, Cl	0.92	0.99	0.99	0.99	0.95	0.97	0.92	0.99	0.86	0.93
<b>TOTAL</b>	<b>99.34</b>	<b>99.53</b>	<b>99.33</b>	<b>99.77</b>	<b>99.19</b>	<b>99.36</b>	<b>99.09</b>	<b>98.56</b>	<b>97.54</b>	<b>98.34</b>
<b>Structural formulae based on 25 O, OH, Cl, F</b>										
Ca	9.97	9.72	9.92	9.95	9.99	9.90	9.85	9.93	10.21	9.97
Mg	-	-	-	-	-	-	-	0.01	-	-
P	5.78	5.87	5.79	5.77	5.77	5.80	5.83	5.78	5.70	5.78
Cl	0.01	0.01	-	-	-	-	-	-	0.01	0.02
F	1.13	1.20	1.22	1.22	1.17	1.19	1.14	1.23	1.07	1.14
OH	0.86	0.79	0.78	0.78	0.83	0.81	0.86	0.76	0.92	0.84
$\Sigma$	<b>17.76</b>	<b>17.59</b>	<b>17.71</b>	<b>17.73</b>	<b>17.76</b>	<b>17.70</b>	<b>17.68</b>	<b>17.71</b>	<b>17.91</b>	<b>17.75</b>

**Appendix 4a:** Electron-microprobe analyses of pyrite, arsenopyrite, chalcopyrite, pyrrhotite, sphalerite, galena, covellite and greenockite from Batouri lodes.

**Appendix 4a** continued.

	Pyrite																	
	19	20	21	22	23	24	25	26	27	28	29	30	31	32	33	34	35	36
<b>Weight %</b>																		
Fe	47.16	47.06	47.15	47.09	47.10	46.89	46.95	47.58	47.31	47.13	47.06	47.12	46.74	46.67	47.05	47.12	46.57	45.73
S	53.21	53.51	53.36	52.94	53.56	52.91	52.80	51.90	53.21	53.48	53.50	53.43	52.97	53.02	53.37	53.15	52.53	52.86
As	0.55	0.15	0.16	0.49	0.24	0.95	0.82	0.48	0.31	0.12	0.00	0.02	0.12	0.55	0.29	0.35	0.57	0.13
Ni	<0.02	<0.02	<0.02	<0.02	<0.02	<0.02	<0.02	<0.02	<0.02	<0.02	<0.02	<0.02	<0.02	<0.02	<0.02	<0.02	<0.02	<0.02
Cu	<0.01	<0.01	<0.01	<0.01	<0.01	0.01	0.01	0.04	0.01	0.07	0.05	0.03	0.31	0.01	0.02	0.01	0.05	0.16
Zn	<0.03	<0.03	0.03	<0.03	<0.03	<0.03	0.03	<0.03	<0.03	<0.03	<0.03	0.04	<0.03	<0.03	0.03	0.03	0.03	<0.03
Ag	0.04	0.04	0.05	0.04	0.04	0.04	0.04	0.05	0.04	0.05	0.05	0.04	0.05	0.04	0.05	0.04	0.04	0.03
Au	<0.004	<0.004	0.01	<0.004	0.01	<0.004	0.01	<0.004	0.01	0.01	0.01	0.01	0.01	0.01	0.01	0.01	0.01	0.01
<b>Sum</b>	<b>101</b>	<b>100</b>	<b>101</b>	<b>101</b>	<b>101</b>	<b>101</b>	<b>100</b>	<b>100</b>	<b>101</b>	<b>101</b>	<b>99.8</b>	<b>99.0</b>						
<b>Atomic %</b>																		
Fe	33.6	33.5	33.6	33.7	33.5	33.5	33.6	34.4	33.7	33.6	33.5	33.6	33.5	33.5	33.5	33.7	33.6	33.1
S	66.1	66.4	66.3	66.0	66.4	65.9	65.9	65.3	66.1	66.3	66.4	66.4	66.2	66.2	66.3	66.1	66.0	66.7
As	0.29	0.08	0.09	0.26	0.12	0.51	0.44	0.26	0.17	0.07	0.00	0.01	0.07	0.29	0.16	0.18	0.31	0.07
Ni	-	-	-	-	-	-	-	-	-	-	-	-	-	-	0.02	-	-	-
Cu	-	-	-	-	-	-	-	0.01	0.03	0.01	0.04	0.03	0.02	0.20	0.01	0.01	0.03	0.10
Zn	-	0.01	0.02	-	-	-	0.02	0.01	-	-	-	-	0.02	-	-	0.02	0.02	-
Ag	0.02	0.02	0.02	0.02	0.02	0.02	0.02	0.02	0.02	0.02	0.02	0.02	0.02	0.02	0.02	0.02	0.02	0.01
Au	-	-	-	-	-	-	-	-	-	-	-	-	-	-	-	-	-	-
<b>Sum</b>	<b>100</b>																	
<b>Formula</b>																		
Fe	1.01	1.01	1.01	1.01	1.00	1.01	1.01	1.03	1.01	1.01	1.01	1.01	1.00	1.01	1.01	1.01	1.01	0.99
S	1.98	1.99	1.99	1.98	1.99	1.98	1.98	1.96	1.98	1.99	1.99	1.99	1.98	1.99	1.99	1.98	1.98	2.00
As	0.01	-	-	0.01	-	0.02	0.01	0.01	-	-	-	-	-	0.01	-	0.01	0.01	-
Cu	-	-	-	-	-	-	-	-	-	-	-	-	-	0.01	-	-	-	-
<b>Sum apfu</b>	<b>3.00</b>																	
As/S	-	-	-	-	-	0.01	0.01	-	-	-	-	-	-	-	-	-	-	
Au/As	-	-	0.01	-	-	-	-	-	-	0.01	-	0.05	0.01	-	-	-	-	0.01

## Appendix 4a continued.

	Pyrite																	
	37	38	39	40	41	42	43	44	45	46	47	48	49	50	51	52	53	54
Weight %																		
Fe	46.18	45.75	46.40	46.50	46.40	46.30	46.70	46.50	46.30	46.30	46.30	46.40	45.90	46.39	46.42	46.36	46.18	46.01
S	53.27	52.11	53.20	53.30	52.80	53.10	53.70	53.90	52.90	53.10	53.30	53.40	52.80	53.87	53.96	53.83	53.88	53.76
As	0.12	0.10	0.71	0.12	1.19	0.67	0.11	0.13	0.72	0.89	0.13	0.51	0.86	0.13	0.13	0.13	0.13	0.13
Ni	<0.02	<0.02	<0.02	<0.02	<0.02	<0.02	<0.02	<0.02	<0.02	<0.02	<0.02	<0.02	<0.02	<0.02	<0.02	<0.02	<0.02	<0.02
Cu	0.03	0.05	0.01	<0.01	<0.01	<0.01	<0.01	<0.01	0.01	0.01	0.18	0.06	0.03	0.02	0.02	0.02	0.02	0.02
Zn	<0.03	<0.03	<0.03	0.03	<0.03	<0.03	<0.03	<0.03	<0.03	<0.03	<0.03	<0.03	<0.03	<0.03	<0.03	<0.03	<0.03	<0.03
Ag	0.03	0.03	0.03	0.03	0.03	0.03	0.03	0.03	0.03	0.03	0.03	0.03	0.03	0.03	0.03	0.03	0.03	0.03
Au	0.01	0.01	<0.004	<0.004	<0.004	<0.004	<0.004	<0.004	<0.004	<0.004	<0.004	<0.004	<0.004	<0.004	0.01	0.01	<0.004	<0.004
<b>Sum</b>	<b>99.9</b>	<b>98.3</b>	<b>101</b>	<b>100</b>	<b>101</b>	<b>100</b>	<b>101</b>	<b>101</b>	<b>100</b>	<b>100</b>	<b>100</b>	<b>101</b>	<b>99.6</b>	<b>100</b>	<b>101</b>	<b>100</b>	<b>100</b>	<b>100</b>
Atomic %																		
Fe	33.2	33.4	33.2	33.3	33.3	33.2	33.3	33.1	33.3	33.2	33.2	33.2	33.1	33.1	33.0	33.1	33.0	32.9
S	66.7	66.4	66.4	66.6	66.0	66.4	66.7	66.8	66.3	66.3	66.6	66.5	66.4	66.9	66.9	66.9	67.0	67.0
As	0.06	0.05	0.38	0.07	0.64	0.36	0.06	0.07	0.38	0.47	0.07	0.27	0.46	0.07	0.07	0.07	0.07	0.07
Cu	0.02	0.03	-	-	-	-	-	-	-	-	0.12	0.04	0.02	0.01	0.01	0.01	0.01	0.01
Zn	-	-	-	0.02	-	-	-	-	-	-	-	-	-	-	-	-	-	-
Ag	0.01	0.01	0.01	0.01	0.01	0.01	0.01	0.01	0.01	0.01	0.01	0.01	0.01	0.01	0.01	0.01	0.01	0.01
<b>Sum</b>	<b>100</b>																	
Formula																		
Fe	0.99	1.00	1.00	1.00	1.00	1.00	1.00	0.99	1.00	1.00	1.00	1.00	0.99	0.99	0.99	0.99	0.99	0.99
S	2.00	1.99	1.99	2.00	1.98	1.99	2.00	2.00	1.99	1.99	2.00	2.00	1.99	2.01	2.01	2.01	2.01	2.01
As	-	-	0.01	-	0.02	0.01	-	-	0.01	0.01	-	0.01	0.01	-	-	-	-	-
<b>Sum apfu</b>	<b>3.00</b>																	
As/S	-	-	0.01	-	0.01	0.01	-	-	0.01	0.01	-	-	0.01	-	-	-	-	-
Au/As	0.01	0.01	-	-	-	-	-	-	-	-	-	-	-	0.01	0.01	0.01	-	-

### **Appendix 4a** continued.

**Appendix 4a** continued.

	Arsenopyrite																
	72	73	74	75	76	77	78	79	80	81	82	83	84	85	86	87	88
<b>Weight %</b>																	
Fe	27.46	34.87	34.98	35.44	35.52	35.37	35.08	35.33	35.09	35.14	35.11	35.02	35.19	35.11	35.01	34.71	34.96
S	22.78	20.73	20.70	21.61	21.72	21.54	20.78	21.27	21.48	20.50	20.63	20.22	20.63	20.88	20.59	20.29	20.94
As	33.91	43.48	43.80	42.82	42.48	42.58	43.77	43.18	43.57	44.18	43.75	44.43	44.07	43.40	44.13	44.18	43.15
Ni	<0.02	<0.02	<0.02	<0.02	<0.02	<0.02	<0.02	<0.02	<0.02	<0.02	<0.02	<0.02	<0.02	<0.02	<0.02	<0.02	<0.02
Cu	0.02	<0.01	<0.01	0.01	<0.01	0.01	<0.01	0.01	0.05	<0.01	<0.01	<0.01	0.01	0.01	<0.01	0.01	0.01
Zn	13.95	<0.03	0.04	0.03	0.03	0.04	<0.03	0.03	0.26	0.04	<0.03	0.05	0.08	0.05	0.25	<0.03	<0.03
Ag	0.02	0.02	0.02	0.02	0.02	0.02	0.02	0.02	0.02	0.02	0.02	0.02	0.03	0.02	0.02	0.02	0.02
Au	<0.004	<0.004	<0.004	<0.004	<0.004	<0.004	<0.004	<0.004	<0.004	<0.004	<0.004	<0.004	<0.004	<0.004	<0.004	0.01	0.01
<b>Sum</b>	<b>98.5</b>	<b>99.2</b>	<b>99.5</b>	<b>99.9</b>	<b>99.8</b>	<b>99.5</b>	<b>99.7</b>	<b>99.8</b>	<b>100.5</b>	<b>99.9</b>	<b>99.5</b>	<b>99.7</b>	<b>100</b>	<b>99.5</b>	<b>100</b>	<b>99.2</b>	<b>99.1</b>
<b>Atomic %</b>																	
Fe	26.3	33.7	33.7	33.7	33.8	33.8	33.8	33.8	33.3	33.8	33.9	33.9	33.8	33.8	33.7	33.7	33.74
S	38.0	35.0	34.8	35.8	36.0	35.8	34.9	35.4	35.6	34.4	34.7	34.1	34.5	35.0	34.5	34.3	35.21
As	24.2	31.3	31.5	30.4	30.1	30.3	31.4	30.8	30.9	31.7	31.5	32.0	31.6	31.1	31.6	32.0	31.04
Cu	0.01	-	-	0.01	0.00	0.01	-	0.01	0.04	-	-	-	0.01	0.01	-	0.01	-
Zn	11.4	-	0.04	0.02	0.02	0.03	-	0.02	0.21	0.03	-	0.04	0.07	0.04	0.20	-	-
Ag	0.01	0.01	0.01	0.01	0.01	0.01	0.01	0.01	0.01	0.01	0.01	0.01	0.01	0.01	0.01	0.01	0.01
<b>Sum</b>	<b>100</b>	<b>100</b>	<b>100</b>	<b>100</b>	<b>100</b>	<b>100</b>	<b>100</b>	<b>100</b>	<b>100</b>	<b>100</b>	<b>100</b>	<b>100</b>	<b>100</b>	<b>100</b>	<b>100</b>	<b>100</b>	<b>100</b>
<b>Formula</b>																	
Fe	0.79	1.01	1.01	1.01	1.01	1.01	1.01	1.01	1.00	1.02	1.02	1.02	1.01	1.01	1.01	1.01	1.01
S	1.14	1.05	1.04	1.08	1.08	1.08	1.04	1.06	1.07	1.03	1.04	1.02	1.04	1.05	1.03	1.03	1.06
As	0.73	0.94	0.94	0.91	0.90	0.91	0.94	0.92	0.93	0.95	0.94	0.96	0.95	0.93	0.95	0.96	0.93
Zn	0.34	-	-	-	-	-	-	-	0.01	-	-	-	-	-	0.01	-	-
<b>Sum apfu</b>	<b>3.00</b>	<b>3.00</b>	<b>3.00</b>	<b>3.00</b>	<b>3.00</b>	<b>3.00</b>	<b>3.00</b>	<b>3.00</b>	<b>3.00</b>	<b>3.00</b>	<b>3.00</b>	<b>3.00</b>	<b>3.00</b>	<b>3.00</b>	<b>3.00</b>	<b>3.00</b>	<b>3.00</b>
As/S	0.64	0.90	0.91	0.85	0.84	0.85	0.90	0.87	0.87	0.92	0.91	0.94	0.91	0.89	0.92	0.93	0.88

**Appendix 4a** continued.

	Arsenopyrite												
	89	90	91	92	93	94	95	96	97	98	99	100	101
<b>Weight %</b>													
Fe	34.61	35.02	34.85	34.78	35.00	34.92	34.94	35.10	34.81	35.10	35.13	35.19	34.71
S	20.88	21.25	20.75	20.90	20.91	20.83	21.44	21.16	20.98	20.66	20.32	20.92	20.40
As	43.37	43.07	43.84	43.92	43.87	43.79	42.99	43.51	43.53	44.10	44.18	43.66	44.52
Ni	<0.02	<0.02	<0.02	<0.02	<0.02	<0.02	<0.02	<0.02	<0.02	<0.02	<0.02	<0.02	<0.02
Cu	0.01	0.01	0.01	0.01	0.01	0.01	0.01	<0.01	<0.01	<0.01	<0.01	0.01	0.09
Zn	0.07	0.11	0.36	0.82	0.75	0.29	1.19	0.85	1.12	0.10	0.03	0.40	1.00
Ag	0.02	0.03	0.02	0.02	0.02	0.03	0.02	0.02	0.02	0.03	0.03	0.02	0.02
Au	<0.004	<0.004	<0.004	<0.004	<0.004	<0.004	<0.004	<0.004	<0.004	<0.004	<0.004	<0.004	<0.004
<b>Sum</b>	<b>99.0</b>	<b>99.5</b>	<b>99.8</b>	<b>100</b>	<b>101</b>	<b>99.9</b>	<b>101</b>	<b>101</b>	<b>101</b>	<b>100</b>	<b>99.7</b>	<b>100</b>	<b>101</b>
<b>Atomic %</b>													
Fe	33.5	33.6	33.5	33.2	33.4	33.5	33.2	33.4	33.2	33.7	34.0	33.7	33.3
S	35.2	35.5	34.8	34.8	34.8	34.9	35.5	35.1	34.9	34.6	34.2	34.9	34.0
As	31.3	30.8	31.4	31.3	31.2	31.4	30.4	30.9	31.0	31.6	31.8	31.1	31.8
Cu	0.01	0.01	0.01	0.01	0.01	0.01	0.01	-	-	-	-	0.01	0.08
Zn	0.06	0.09	0.30	0.67	0.61	0.24	0.96	0.69	0.91	0.08	0.02	0.32	0.82
Ag	0.01	0.01	0.01	0.01	0.01	0.01	0.01	0.01	0.01	0.01	0.01	0.01	0.01
<b>Sum</b>	<b>100</b>	<b>100</b>	<b>100</b>	<b>100</b>	<b>100</b>	<b>100</b>	<b>100</b>	<b>100</b>	<b>100</b>	<b>100</b>	<b>100</b>	<b>100</b>	<b>100</b>
<b>Formula</b>													
Fe	1.00	1.01	1.01	1.00	1.00	1.01	0.99	1.00	1.00	1.01	1.02	1.01	1.00
S	1.06	1.07	1.04	1.04	1.04	1.05	1.06	1.05	1.05	1.04	1.03	1.05	1.02
As	0.94	0.92	0.94	0.94	0.94	0.94	0.91	0.93	0.93	0.95	0.95	0.93	0.95
Zn	-	-	0.01	0.02	0.02	0.01	0.03	0.02	0.03	-	-	0.01	0.02
<b>Sum apfu</b>	<b>3.00</b>	<b>3.00</b>	<b>3.00</b>	<b>3.00</b>	<b>3.00</b>	<b>3.00</b>	<b>3.00</b>	<b>3.00</b>	<b>3.00</b>	<b>3.00</b>	<b>3.00</b>	<b>3.00</b>	<b>3.00</b>
As/S	0.89	0.87	0.90	0.90	0.90	0.90	0.86	0.88	0.89	0.91	0.93	0.89	0.93

**Appendix 4a** continued.

	Chalcopyrite				Po*	Sphalerite								Galena				
	102	103	104	105		106	107	108	109	110	111	112	113	114	115	116	117	118
<b>Weight %</b>																		
Fe	28.85	28.91	29.14	21.73	58.60	2.79	2.88	2.89	2.83	3.51	2.89	2.89	2.90	2.66	2.58	<0.03	<0.03	
S	34.53	34.88	34.75	35.23	39.05	32.96	32.71	32.78	32.49	32.52	32.34	32.31	32.20	33.36	33.11	13.85	13.54	
As	<0.006	<0.006	0.13	0.11	0.21	<0.006	<0.006	<0.006	<0.006	0.09	0.02	0.08	0.05	<0.006	<0.006	<0.006	0.04	
Pb	<0.4	<0.4	<0.4	<0.4	<0.4	<0.4	<0.4	<0.4	<0.4	<0.4	<0.4	<0.4	<0.4	<0.4	<0.4	85.20	85.71	
Cu	33.09	33.61	34.59	24.27	<0.01	0.01	0.01	0.01	<0.01	0.90	0.01	<0.01	0.01	0.01	0.02	<0.01	<0.01	
Zn	2.87	1.63	<0.03	18.80	<0.03	62.51	62.84	62.17	62.80	61.14	62.77	62.61	62.61	61.36	61.78	0.79	0.04	
Ag	0.03	0.02	0.02	0.04	0.03	<0.006	<0.006	<0.006	<0.006	<0.006	<0.006	<0.006	<0.006	<0.006	0.01	<0.006	<0.006	
Cd	<0.9	<0.9	<0.9	<0.9	<0.9	1.26	1.27	1.36	1.27	1.34	1.36	1.30	1.26	1.33	1.20	<0.9	<0.9	
<b>Sum</b>	<b>99.4</b>	<b>99.1</b>	<b>98.7</b>	<b>100</b>	<b>97.9</b>	<b>99.5</b>	<b>99.7</b>	<b>99.2</b>	<b>99.4</b>	<b>99.5</b>	<b>99.4</b>	<b>99.2</b>	<b>99.0</b>	<b>99.0</b>	<b>98.7</b>	<b>98.7</b>	<b>99.8</b>	<b>99.3</b>
<b>Atomic %</b>																		
Fe	23.9	24.0	24.2	18.0	46.2	2.44	2.52	2.54	2.49	3.08	2.54	2.55	2.57	2.33	2.27	-	-	
S	49.9	50.4	50.4	50.9	53.6	50.3	49.9	50.2	49.8	49.7	49.6	49.6	49.6	51.0	50.7	50.5	50.5	
As	-	-	0.08	0.07	0.13	-	-	-	-	0.06	0.01	0.05	0.03	-	-	-	0.06	
Pb	-	-	-	-	-	-	-	-	-	-	-	-	-	-	-	48.1	49.4	
Cu	24.1	24.5	25.3	17.7	-	0.01	-	-	-	0.69	0.01	-	0.01	0.01	0.02	-	-	
Zn	2.03	1.16	0.02	13.3	-	46.8	47.0	46.7	47.2	45.9	47.2	47.2	47.3	46.0	46.4	1.41	0.07	
Ag	0.01	0.01	0.01	0.02	0.01	-	-	-	-	-	-	-	-	-	-	-	-	
Cd	-	-	-	-	-	0.55	0.55	0.59	0.55	0.58	0.60	0.57	0.55	0.58	0.53	-	-	
<b>Sum</b>	<b>100</b>	<b>100</b>	<b>100</b>	<b>100</b>	<b>100</b>	<b>100</b>	<b>100</b>	<b>100</b>	<b>100</b>	<b>100</b>	<b>100</b>	<b>100</b>	<b>100</b>	<b>100</b>	<b>100</b>	<b>100</b>	<b>100</b>	
<b>Formula</b>																		
Fe	0.72	0.72	0.73	0.54	1.39	0.07	0.08	0.08	0.07	0.09	0.08	0.08	0.08	0.07	0.07	0.00	0.00	
S	1.50	1.51	1.51	1.53	1.61	1.51	1.50	1.51	1.49	1.49	1.49	1.49	1.49	1.53	1.52	1.52	1.51	
Pb	-	-	-	-	-	-	-	-	-	-	-	-	-	-	-	1.44	1.48	
Cu	0.72	0.73	0.76	0.53	-	-	-	-	-	0.02	-	-	-	-	-	-	-	
Zn	0.06	0.03	0.00	0.40	-	1.40	1.41	1.40	1.42	1.38	1.42	1.42	1.42	1.38	1.39	0.04	-	
Cd	-	-	-	-	-	0.02	0.02	0.02	0.02	0.02	0.02	0.02	0.02	0.02	0.02	-	-	
<b>Sum apfu</b>	<b>3.00</b>	<b>3.00</b>	<b>3.00</b>	<b>3.00</b>	<b>3.00</b>	<b>3.00</b>	<b>3.00</b>	<b>3.00</b>	<b>3.00</b>	<b>3.00</b>	<b>3.00</b>	<b>3.00</b>	<b>3.00</b>	<b>3.00</b>	<b>3.00</b>	<b>3.00</b>	<b>3.00</b>	

### **Appendix 4a** continued.

## APPENDIX

**Appendix 4b:** Electron-microprobe analyses of placer and vein gold from Batouri. (Bright yellow=rim; whitish yellow=core & unzoned gold; white=electrum)

	Placer gold													
	1	2	3	4	5	6	7	8	9	10	11	12	13	14
<b>Weight %</b>														
Hg	0.18	0.19	0.07	0.08	0.26	0.24	0.26	0.08	0.07	0.09	0.28	0.45	0.14	0.99
Ag	13.6	13.7	1.00	0.30	12.8	12.6	12.7	1.00	0.40	0.40	30.9	43.3	15.4	49.0
Au	86.0	86.2	98.0	98.7	87.9	87.7	87.5	98.3	99.2	99.1	68.9	56.9	85.1	50.6
<b>Sum</b>	<b>99.8</b>	<b>100</b>	<b>99.1</b>	<b>99.1</b>	<b>101</b>	<b>100</b>	<b>100</b>	<b>99.4</b>	<b>99.7</b>	<b>99.6</b>	<b>100</b>	<b>100</b>	<b>100</b>	<b>100</b>
<b>Atomic %</b>														
Hg	0.16	0.17	0.07	0.08	0.23	0.21	0.23	0.08	0.07	0.09	0.22	0.32	0.12	0.69
Ag	22.4	22.5	1.83	0.55	21.0	20.7	20.9	1.82	0.73	0.73	44.9	58.0	24.8	63.4
Au	77.5	77.4	98.1	99.4	78.8	79.1	78.9	98.1	99.2	99.2	54.9	41.7	75.1	35.9
<b>Sum</b>	<b>100</b>													
<b>Formula</b>														
Hg	-	0.01	-	-	0.01	0.01	0.01	-	-	-	0.01	0.01	-	0.02
Ag	0.67	0.67	0.05	0.02	0.63	0.62	0.63	0.05	0.02	0.02	1.35	1.74	0.74	1.90
Au	2.32	2.32	2.94	2.98	2.36	2.37	2.37	2.94	2.98	2.98	1.65	1.25	2.25	1.08
<b>Sum</b>	<b>3.00</b>													
<b>Fineness</b>	863	863	990	997	873	874	873	990	996	996	690	568	847	508
	Placer gold													
	15	16	17	18	19	20	21	22	23	24	25	26	27	28
<b>Weight %</b>														
Hg	0.20	0.24	0.21	0.15	0.30	0.08	0.07	0.36	0.12	0.07	0.38	0.36	0.13	0.16
Ag	19.8	20.1	20.2	28.7	12.5	1.20	0.40	15.0	3.60	1.30	13.5	13.5	19.0	19.0
Au	80.7	80.3	80.3	70.5	87.4	98.2	98.6	85.4	95.1	96.9	86.2	86.6	81.7	81.2
<b>Sum</b>	<b>100</b>	<b>100</b>	<b>100</b>	<b>99.4</b>	<b>100</b>	<b>99.5</b>	<b>99.0</b>	<b>100</b>	<b>98.8</b>	<b>98.2</b>	<b>100</b>	<b>100</b>	<b>100</b>	<b>100</b>
<b>Atomic %</b>														
Hg	0.17	0.20	0.18	0.12	0.27	0.08	0.07	0.31	0.12	0.07	0.34	0.32	0.11	0.14
Ag	30.9	31.3	31.4	42.6	20.7	2.18	0.73	24.2	6.46	2.39	22.2	22.1	29.8	29.9
Au	68.9	68.5	68.4	57.3	79.1	97.7	99.2	75.5	93.4	97.5	77.5	77.6	70.1	70.0
<b>Sum</b>	<b>100</b>													
<b>Formula</b>														
Hg	0.01	0.01	0.01	-	0.01	-	-	0.01	-	-	0.01	0.01	-	-
Ag	0.93	0.94	0.94	1.28	0.62	0.07	0.02	0.73	0.19	0.07	0.66	0.66	0.89	0.90
Au	2.07	2.05	2.05	1.72	2.37	2.93	2.98	2.26	2.80	2.93	2.33	2.33	2.10	2.10
<b>Sum</b>	<b>3.00</b>													
<b>Fineness</b>	803	800	799	711	875	988	996	851	964	987	865	865	811	810
	Placer gold													
	29	30	31	32	33	34	35	36	37	38	39	40	41	42
<b>Weight %</b>														
Hg	0.12	0.16	0.19	0.14	0.07	0.16	0.07	0.18	0.08	0.37	0.39	0.40	0.40	0.32
Ag	19.1	19.8	19.2	13.4	0.60	13.5	0.10	13.4	0.90	30.1	30.0	30.0	30.0	31.0
Au	81.3	80.9	80.7	87.3	99.0	87.1	99.0	87.2	97.9	70.2	70.0	70.0	70.0	69.4
<b>Sum</b>	<b>100</b>	<b>100</b>	<b>100</b>	<b>100</b>	<b>99.6</b>	<b>100</b>	<b>99.2</b>	<b>100</b>	<b>98.9</b>	<b>100</b>	<b>100</b>	<b>100</b>	<b>100</b>	<b>100</b>
<b>Atomic %</b>														
Hg	0.10	0.13	0.16	0.12	0.07	0.14	0.07	0.16	0.08	0.29	0.31	0.31	0.31	0.25
Ag	30.0	30.9	30.2	21.9	1.09	22.0	0.18	21.9	1.65	43.8	43.8	43.8	43.8	44.8
Au	69.9	69.0	69.6	78.0	98.8	77.8	99.8	78.0	98.3	55.9	55.9	55.9	55.9	54.9
<b>Sum</b>	<b>100</b>													
<b>Formula</b>														
Hg	-	-	-	-	-	-	-	-	-	0.01	0.01	0.01	0.01	0.01
Ag	0.90	0.93	0.91	0.66	0.03	0.66	0.01	0.66	0.05	1.31	1.31	1.31	1.31	1.34
Au	2.10	2.07	2.09	2.34	2.97	2.33	2.99	2.34	2.95	1.68	1.68	1.68	1.68	1.65
<b>Sum</b>	<b>3.00</b>													
<b>Fineness</b>	810	803	808	867	994	866	999	867	991	700	700	700	700	691

## APPENDIX

### Appendix 4b continued.

	Placer gold					Vein gold									
	43	44	45	46	47	48	49	50	51	52	53	54	55	56	
<b>Weight %</b>															
Hg	0.44	0.38	0.41	0.44	0.41	0.07	0.07	0.08	0.06	0.06	0.06	0.08	0.07	0.07	0.08
Ag	27.9	27.7	27.5	27.2	27.7	2.6	1.00	0.20	1.10	3.40	2.60	1.70	0.20	0.70	
Au	71.8	72.1	72.3	73.2	72.1	96.8	98.2	98.6	97.8	96.2	96.8	97.1	98.9	98.4	
<b>Sum</b>	<b>100</b>	<b>100</b>	<b>100</b>	<b>100</b>	<b>100</b>	<b>99.5</b>	<b>99.3</b>	<b>98.9</b>	<b>99.0</b>	<b>99.7</b>	<b>99.5</b>	<b>98.9</b>	<b>99.1</b>	<b>99.2</b>	
<b>Atomic %</b>															
Hg	0.35	0.30	0.33	0.35	0.33	0.07	0.07	0.08	0.06	0.06	0.06	0.08	0.07	0.07	0.08
Ag	41.4	41.1	40.9	40.3	41.1	4.67	1.82	0.37	2.01	6.06	4.67	3.10	0.37	1.28	
Au	58.3	58.6	58.8	59.4	58.6	95.3	98.1	99.6	97.9	93.9	95.3	96.8	99.6	98.6	
<b>Sum</b>	<b>100</b>	<b>100</b>	<b>100</b>	<b>100</b>	<b>100</b>	<b>100</b>	<b>100</b>	<b>100</b>	<b>100</b>	<b>100</b>	<b>100</b>	<b>100</b>	<b>100</b>	<b>100</b>	<b>100</b>
<b>Formula</b>															
Hg	0.01	0.01	0.01	0.01	0.01	-	-	-	-	-	-	-	-	-	-
Ag	1.24	1.23	1.23	1.21	1.23	0.14	0.05	0.01	0.06	0.18	0.14	0.09	0.01	0.04	
Au	1.75	1.76	1.76	1.78	1.76	2.86	2.94	2.99	2.94	2.82	2.86	2.90	2.99	2.96	
<b>Sum</b>	<b>3.00</b>	<b>3.00</b>	<b>3.00</b>	<b>3.00</b>	<b>3.00</b>	<b>3.00</b>	<b>3.00</b>	<b>3.00</b>	<b>3.00</b>	<b>3.00</b>	<b>3.00</b>	<b>3.00</b>	<b>3.00</b>	<b>3.00</b>	<b>3.00</b>
<b>Fineness</b>	720	722	724	729	722	974	990	998	989	966	974	983	998	993	
	Vein gold														
	64	65	66	67	68	69	70	71	72	73	74	75	76	77	
	<b>Weight %</b>														
Hg	0.07	0.07	0.07	0.07	0.07	0.07	0.09	0.07	0.08	0.07	0.08	0.07	0.08	0.38	
Ag	17.7	17.7	17.8	17.7	17.9	17.0	17.8	0.10	5.90	0.30	0.90	2.50	0.90	35.4	
Au	83.1	83.0	82.9	82.5	83.0	83.0	82.6	99.2	93.4	98.5	97.7	96.7	97.8	64.8	
<b>Sum</b>	<b>100</b>	<b>100</b>	<b>100</b>	<b>100</b>	<b>101</b>	<b>100</b>	<b>100</b>	<b>99.4</b>	<b>99.4</b>	<b>98.9</b>	<b>98.7</b>	<b>99.2</b>	<b>98.8</b>	<b>100</b>	
<b>Atomic %</b>															
Hg	0.06	0.06	0.06	0.06	0.06	0.06	0.08	0.07	0.08	0.07	0.08	0.07	0.08	0.29	
Ag	28.0	28.0	28.2	28.1	28.2	27.2	28.2	0.18	10.3	0.55	1.65	4.50	1.65	49.8	
Au	72.0	71.9	71.8	71.8	71.7	72.7	71.7	99.8	89.6	99.4	98.3	95.4	98.3	49.9	
<b>Sum</b>	<b>100</b>	<b>100</b>	<b>100</b>	<b>100</b>	<b>100</b>	<b>100</b>	<b>100</b>	<b>100</b>	<b>100</b>	<b>100</b>	<b>100</b>	<b>100</b>	<b>100</b>	<b>100</b>	
<b>Formula</b>															
Hg	-	-	-	-	-	-	-	-	-	-	-	-	-	-	0.01
Ag	0.84	0.84	0.84	0.84	0.85	0.82	0.85	0.01	0.31	0.02	0.05	0.14	0.05	1.49	
Au	2.16	2.16	2.15	2.15	2.15	2.18	2.15	2.99	2.69	2.98	2.95	2.86	2.95	1.50	
<b>Sum</b>	<b>3.00</b>	<b>3.00</b>	<b>3.00</b>	<b>3.00</b>	<b>3.00</b>	<b>3.00</b>	<b>3.00</b>	<b>3.00</b>	<b>3.00</b>	<b>3.00</b>	<b>3.00</b>	<b>3.00</b>	<b>3.00</b>	<b>3.00</b>	
<b>Fineness</b>	824	824	823	823	823	830	823	999	941	997	991	975	991	647	
	Vein gold														
	85	86	87	88	89	90	91	92	93	94	95	96	97	98	
	<b>Weight %</b>														
Hg	0.10	0.10	0.09	0.08	0.07	0.08	0.08	0.11	0.10	0.10	0.07	0.07	0.07	0.07	
Ag	17.4	17.4	17.5	17.5	19.5	0.80	0.04	0.40	19.3	19.5	2.60	8.20	0.90	2.70	
Au	83.2	83.1	83.2	83.4	81.3	98.3	98.8	98.7	81.1	80.4	96.9	91.8	98.3	96.7	
<b>Sum</b>	<b>100</b>	<b>100</b>	<b>100</b>	<b>101</b>	<b>100</b>	<b>99.2</b>	<b>98.9</b>	<b>99.2</b>	<b>100</b>	<b>100</b>	<b>99.6</b>	<b>100</b>	<b>99.2</b>	<b>99.5</b>	
<b>Atomic %</b>															
Hg	0.09	0.09	0.08	0.07	0.06	0.08	0.08	0.11	0.08	0.08	0.07	0.06	0.07	0.07	
Ag	27.6	27.6	27.7	27.7	30.4	1.46	0.07	0.73	30.3	30.7	4.67	14.0	1.64	4.85	
Au	72.3	72.3	72.2	72.3	69.5	98.5	99.9	99.2	69.7	69.3	95.3	85.9	98.3	95.0	
<b>Sum</b>	<b>100</b>	<b>100</b>	<b>100</b>	<b>100</b>	<b>100</b>	<b>100</b>	<b>100</b>	<b>100</b>	<b>100</b>	<b>100</b>	<b>100</b>	<b>100</b>	<b>100</b>	<b>100</b>	
<b>Formula</b>															
Ag	0.83	0.83	0.83	0.83	0.91	0.04	-	0.02	0.91	0.92	0.14	0.42	0.05	0.15	
Au	2.17	2.17	2.17	2.17	2.09	2.95	3.00	2.97	2.09	2.08	2.86	2.58	2.95	2.85	
<b>Sum</b>	<b>3.00</b>	<b>3.00</b>	<b>3.00</b>	<b>3.00</b>	<b>3.00</b>	<b>3.00</b>	<b>3.00</b>	<b>3.00</b>	<b>3.00</b>	<b>3.00</b>	<b>3.00</b>	<b>3.00</b>	<b>3.00</b>	<b>3.00</b>	
<b>Fineness</b>	827	827	826	827	807	992	1000	996	808	805	974	918	991	973	

## APPENDIX

### Appendix 4b continued.

	Vein gold													
	106	107	108	109	110	111	112	113	114	115	116	117	118	119
<b>Weight %</b>														
Hg	0.07	0.07	0.07	0.07	0.07	0.10	0.07	0.09	0.08	0.07	0.08	0.08	0.07	0.07
Ag	18.3	18.1	18.0	18.0	17.8	4.60	17.3	18.0	18.1	18.1	18.0	18.0	18.0	18.1
Au	82.2	82.6	82.5	82.7	82.0	95.6	83.2	82.4	82.4	82.0	82.7	82.6	82.4	82.6
<b>Sum</b>	<b>100</b>	<b>100</b>	<b>100</b>	<b>100</b>	<b>99.9</b>	<b>100</b>								
<b>Atomic %</b>														
Hg	0.06	0.06	0.06	0.06	0.06	0.09	0.06	0.08	0.07	0.06	0.07	0.07	0.06	0.06
Ag	28.9	28.6	28.5	28.4	28.4	8.07	27.5	28.5	28.6	28.7	28.4	28.5	28.5	28.6
Au	71.1	71.4	71.5	71.5	71.6	91.8	72.4	71.4	71.3	71.2	71.5	71.5	71.4	71.4
<b>Sum</b>	<b>100</b>													
<b>Formula</b>														
Ag	0.87	0.86	0.85	0.85	0.85	0.24	0.83	0.85	0.86	0.86	0.85	0.85	0.85	0.86
Au	2.13	2.14	2.14	2.15	2.15	2.76	2.17	2.14	2.14	2.14	2.15	2.14	2.14	2.14
<b>Sum</b>	<b>3.00</b>													
<b>Fineness</b>	818	820	821	821	822	954	828	821	820	819	821	821	821	820

	Vein gold													
	120	121	122	123	124	125	126	127	128	129	130	131	132	133
<b>weight %</b>														
Hg	0.07	0.07	0.08	0.10	0.07	0.11	0.07	0.07	0.07	0.07	0.07	0.07	0.07	0.08
Ag	3.00	2.10	3.60	0.50	1.30	2.30	1.30	16.6	16.6	17.7	19.1	19.2	19.1	19.2
Au	96.4	97.5	95.9	98.7	98.1	96.9	98.0	84.2	83.8	82.4	81.2	81.3	80.9	81.2
<b>Sum</b>	<b>99.5</b>	<b>99.7</b>	<b>99.6</b>	<b>99.3</b>	<b>99.5</b>	<b>99.3</b>	<b>99.4</b>	<b>100</b>						
<b>Atomic %</b>														
Hg	0.07	0.07	0.08	0.10	0.07	0.11	0.07	0.06	0.06	0.06	0.06	0.06	0.06	0.07
Ag	5.37	3.78	6.41	0.92	2.36	4.15	2.36	26.5	26.6	28.2	30.0	30.1	30.1	30.1
Au	94.6	96.2	93.5	99.0	97.6	95.7	97.6	73.5	73.4	71.8	69.9	69.8	69.8	69.8
<b>Sum</b>	<b>100</b>													
<b>Formula</b>														
Ag	0.16	0.11	0.19	0.03	0.07	0.12	0.07	0.79	0.80	0.84	0.90	0.90	0.90	0.90
Au	2.84	2.88	2.81	2.97	2.93	2.87	2.93	2.20	2.20	2.15	2.10	2.09	2.10	2.09
<b>Sum</b>	<b>3.00</b>													
<b>Fineness</b>	970	979	964	995	987	977	987	835	835	823	810	809	809	809

	Vein gold									
	134	135	136	137	138	139	140	141	142	
<b>weight %</b>										
Hg	0.07	0.07	0.08	0.07	0.38	0.60	0.39	0.36	0.27	
Ag	19.1	19.1	18.0	17.9	24.3	46.6	32.3	26.1	28.9	
Au	81.6	81.1	82.1	82.6	75.5	52.8	67.9	73.6	70.9	
<b>Sum</b>	<b>100</b>									
<b>Atomic %</b>										
Hg	0.06	0.06	0.07	0.06	0.31	0.43	0.30	0.29	0.21	
Ag	29.9	30.1	28.6	28.3	36.9	61.5	46.3	39.2	42.6	
Au	70.0	69.9	71.4	71.6	62.8	38.1	53.4	60.5	57.2	
<b>Sum</b>	<b>100</b>									
<b>Formula</b>										
Hg	-	-	-	-	0.01	0.01	0.01	0.01	0.01	
Ag	0.90	0.90	0.86	0.85	1.11	1.84	1.39	1.18	1.28	
Au	2.10	2.10	2.14	2.15	1.88	1.14	1.60	1.82	1.72	
<b>Sum</b>	<b>3.00</b>									
<b>Fineness</b>	810	809	820	822	757	531	678	738	710	

## APPENDIX

**Appendix 5:** LA-ICP-MS analyses of pyrite and arsenopyrite from Batouri lodes

	Pyrite III										Pyrite II	
	1	2	3	4	5	6	7	8	9	10	11	12
<b>ppm</b>												
Ni	3.23	19.9	31.9	74.1	11.7	43.0	72.5	23.0	10.3	2.71	1.93	0.338
Ru	<0.048	<0.031	<0.046	<0.052	<0.046	<0.041	0.038	<0.041	<0.027	<0.052	<0.031	<0.033
Rh	0.229	0.200	<0.008	0.015	0.013	0.017	<0.005	0.059	0.014	0.055	<0.007	0.007
Pd	0.316	0.404	<0.029	<0.027	<0.031	<0.029	<0.042	<0.025	<0.026	0.037	<0.019	<0.019
Re	<0.028	<0.018	<0.021	<0.024	<0.023	<0.021	<0.023	<0.022	<0.023	<0.027	<0.017	<0.012
Os	0.079	<0.064	<0.043	<0.051	<0.059	<0.073	<0.059	<0.046	<0.059	<0.067	<0.039	<0.039
Ir	<0.028	0.013	0.014	<0.016	<0.016	<0.014	<0.013	<0.014	<0.013	<0.022	<0.015	<0.009
Pt	<0.044	<0.031	<0.031	<0.024	<0.029	<0.035	<0.032	<0.036	<0.029	<0.029	<0.038	0.042
Au	0.351	1.70	1.52	2.52	2.09	2.47	1.52	1.90	1.72	0.426	0.167	2.81
<b>cps</b>												
<b>Background subtracted</b>												
Co	9573	99118	213619	99143	583	10177	159079	139641	147491	11103	944	19537
Cu	742449	769674	7359	3489	15578	5158	1499	7020	177	1374	8	21
As	61657	24525	20115	13248	22260	19435	10639	26464	95176	81573	168599	302454
Ag	4663	6330	1543	1439	2471	1716	403	2474	638	592	0	2
Sb	2	4771	3465	3393	5781	3984	1023	4071	1337	24	0	0
Te	6	17	14	8	19	13	5	11	6	8	0	0
Bi	51	5113	6489	4471	8453	8559	814	9139	165	26	31	0
	Pyrite II						Pyrite I	Pyrite II			Pyrite I	
	13	14	15	16	17	18	19	20	21	22	23	24
<b>ppm</b>												
Ni	1.33	<0.358	<0.288	<0.249	<0.263	<0.302	25.3	<0.301	<0.252	42.8	55.5	27.6
Ru	<0.031	<0.034	<0.031	<0.029	<0.033	0.031	<0.029	<0.026	<0.029	<0.036	<0.033	0.034
Rh	<0.006	<0.005	<0.006	<0.005	<0.005	<0.005	<0.006	<0.005	<0.005	<0.005	0.037	<0.005
Pd	<0.022	<0.025	<0.019	<0.018	<0.025	<0.019	<0.023	<0.023	<0.025	<0.019	<0.031	0.032
Re	<0.019	<0.021	<0.017	<0.012	<0.018	<0.012	<0.022	<0.013	<0.018	<0.021	<0.025	<0.016
Os	<0.053	<0.039	<0.047	<0.041	<0.042	<0.037	<0.046	<0.044	<0.037	<0.049	<0.062	<0.041
Ir	<0.013	<0.013	<0.015	<0.009	<0.011	<0.011	<0.017	<0.011	<0.013	<0.011	<0.014	0.014
Pt	<0.025	<0.029	<0.025	<0.024	<0.024	<0.026	<0.029	<0.029	<0.021	<0.028	<0.026	<0.026
Au	5.48	8.11	<0.022	0.032	0.049	0.624	<0.021	2.29	0.764	3.08	0.044	0.041
<b>cps</b>												
<b>Background subtracted</b>												
Co	3958	561	462	7724	250	16	586	387	4	76388	35810	20455
Cu	119	623	0	0	0	26	40	25	66	876	106847	4739
As	185207	317026	40935	87075	53295	148218	11	201183	137975	158752	311	82
Ag	6	434	0	1	2	0	0	0	4	289	795	129
Sb	41	2831	2	0	0	17	11	0	0	669	574	93
Te	3	5	1	0	0	0	0	1	1	2	5	1
Bi	40	46	0	2	18	7	0	0	18	862	445	41

## APPENDIX

**Appendix 5** continued

	Pyrite I 25	Pyrite II										
		26	27	28	29	30	31	32	33	34	35	36
<b>ppm</b>												
Ni	101	12.0	2.56	6.22	6.75	13.3	82.9	21.9	44.8	41.4	3.31	1.92
Ru	<0.029	<0.025	0.066	<0.027	<0.041	<0.046	<0.043	<0.051	<0.047	<0.039	<0.049	<0.037
Rh	0.057	<0.005	0.015	<0.012	<0.008	<0.008	<0.006	0.010	<0.008	0.795	<0.007	<0.006
Pd	0.081	<0.019	0.063	<0.031	<0.028	<0.032	<0.034	<0.029	<0.027	<0.029	<0.036	<0.027
Re	<0.018	<0.014	<0.026	<0.031	<0.019	<0.023	0.019	<0.024	<0.022	<0.025	<0.022	<0.019
Os	<0.055	<0.031	<0.055	<0.031	<0.057	<0.053	<0.051	<0.059	<0.069	<0.057	<0.072	<0.062
Ir	<0.011	<0.009	<0.016	<0.008	<0.015	<0.013	<0.014	0.019	<0.014	<0.014	<0.013	<0.013
Pt	<0.029	<0.018	<0.039	<0.018	<0.027	<0.039	<0.028	<0.038	<0.036	<0.029	<0.032	<0.031
Au	0.306	2.43	0.503	<0.034	<0.023	<0.024	0.041	0.036	0.068	0.076	0.070	<0.019
<b>cps</b>	<b>Background subtracted</b>											
Co	11548	1903	14236	103	97	24	516	211	128	883	45	22
Cu	102909	19	37838	0	15	17	38	33	3596	31055	42	19
As	6709	351879	99223	46368	70098	70363	53595	73531	61388	44412	82858	87048
Ag	982	0	449	0	3	5	3	7	91	12699	12	0
Sb	1294	7	5	0	0	8	4	2	44	3100	45	0
Te	0	8	1	3	0	6	1	0	0	28	8	0
Bi	1025	21	11	3	8	11	20	0	118	46716	14	1
	Pyrite II 37	Pyrite I					Pyrite II					
		38	39	40	41	42	43	44	45	46	47	48
<b>ppm</b>												
Ni	13.1	<0.413	28.0	39.1	32.8	<0.303	8.66	23.8	20.3	1.55	4.89	6.01
Ru	<0.039	<0.037	<0.041	<0.035	0.035	<0.029	<0.048	<0.038	<0.032	<0.035	<0.042	<0.053
Rh	0.020	<0.006	<0.006	<0.005	<0.005	<0.006	0.104	<0.009	<0.006	<0.007	<0.007	<0.007
Pd	<0.024	<0.025	<0.025	<0.019	<0.017	<0.020	<0.033	<0.032	<0.021	<0.026	<0.024	<0.029
Re	0.034	<0.018	<0.021	<0.019	<0.014	<0.022	<0.024	<0.026	<0.16	<0.022	<0.024	<0.021
Os	<0.052	<0.056	<0.056	<0.049	<0.027	<0.038	<0.093	<0.081	<0.045	<0.063	<0.061	<0.072
Ir	<0.016	<0.011	0.013	<0.013	<0.011	<0.011	<0.019	<0.018	<0.011	<0.014	0.018	<0.019
Pt	<0.036	<0.033	<0.033	<0.023	<0.021	<0.020	<0.039	<0.039	<0.029	<0.028	<0.036	<0.031
Au	0.067	<0.019	0.027	0.027	0.048	0.241	0.694	0.730	2.07	0.841	1.37	1.21
<b>cps</b>	<b>Background subtracted</b>											
Co	212	5587	32191	53773	28973	13854	7989	34014	12311	398	1830	2383
Cu	118	940	296	168	377	18224	108	110	210	20330	355	67
As	65572	5	5	27	27	296	59328	106495	293569	113164	146055	169447
Ag	212	45	11	19	57	319	49	146	81	1415	83	2
Sb	271	1	1	338	54	108	335	40	34	193	224	4
Te	1	2	1	2	0	0	1	0	2	0	2	0
Bi	1281	2	0	30	65	78	0	5	9	15	0	10

## APPENDIX

**Appendix 5** continued

	Pyrite II											
	49	50	51	52	53	54	55	56	57	58	59	60
ppm												
Ni	0.925	10.7	838	24.9	36.3	1.22	28.6	56.6	19.0	6.64	5.31	10.5
Ru	<0.039	<0.041	<0.045	<0.041	<0.032	<0.035	<0.044	<0.037	<0.037	<0.043	<0.043	<0.041
Rh	<0.006	<0.008	<0.007	<0.006	<0.004	<0.006	<0.008	<0.007	<0.008	<0.006	<0.008	<0.007
Pd	<0.028	<0.028	<0.025	<0.028	<0.023	<0.023	<0.029	<0.022	<0.028	<0.034	<0.024	<0.027
Re	<0.018	<0.021	<0.016	<0.023	<0.018	<0.019	<0.024	<0.012	<0.022	<0.022	<0.017	<0.014
Os	<0.058	<0.049	<0.043	<0.047	<0.048	<0.061	<0.057	<0.051	<0.049	<0.069	<0.062	<0.061
Ir	<0.018	0.017	<0.013	<0.012	<0.014	<0.013	0.013	<0.014	<0.015	<0.016	0.020	<0.015
Pt	<0.036	<0.034	<0.032	<0.029	<0.027	0.032	<0.038	<0.032	<0.025	<0.036	<0.037	<0.032
Au	25.8	2.87	18.5	4.89	5.85	9.18	9.41	24.1	3.55	17.8	1.78	38.9
cps	<b>Background subtracted</b>											
Co	573	3306	295529	7995	10453	18	8028	25550	6899	2218	2113	2608
Cu	614	1283	2465	399	145	833	525	1980	100	331	191	789
As	106681	117128	262289	79585	91421	177148	42497	135765	232094	39113	63741	42723
Ag	0	351	496	18	47	93	91	54	1	3	278	34
Sb	0	642	1606	121	464	594	566	147	5	2	1997	1354
Te	4	0	0	0		0	0	4	5	0	1	0
Bi	0	148	16	0	7	0	23	10	0	7	13	5
	Arsenopyrite											
ppm	1	2	3	4	5	6	7	8	9	10	11	12
Ni	6.46	4.43	357	116	727	1081	195	61.1	<0.691	8.38	11.4	12.6
Ru	<0.084	<0.101	<0.081	0.153	<0.087	<0.149	<0.080	<0.101	<0.097	<0.075	<0.099	<0.059
Rh	<0.016	<0.017	<0.016	<0.018	<0.016	<0.023	<0.021	<0.015	<0.015	<0.011	<0.012	<0.014
Pd	0.053	<0.059	0.070	<0.055	<0.055	<0.096	0.064	<0.062	<0.057	<0.038	<0.062	<0.064
Re	<0.047	0.079	<0.042	<0.041	<0.051	<0.081	<0.051	<0.049	<0.054	<0.045	<0.044	<0.039
Os	<0.128	<0.155	<0.121	<0.097	<0.121	<0.177	0.263	<0.131	<0.086	<0.123	<0.111	<0.123
Ir	<0.034	<0.037	<0.032	<0.033	<0.029	<0.047	<0.036	<0.035	<0.027	<0.028	<0.031	<0.029
Pt	<0.071	<0.059	<0.074	<0.066	<0.075	<0.122	<0.091	<0.079	<0.062	<0.061	<0.078	<0.057
Au	2.40	1.26	1.28	0.177	0.380	0.965	0.584	0.499	0.254	0.203	0.720	1.89
cps	<b>Background subtracted</b>											
Co	2653	2535	40939	29317	90512	84180	29503	13248	44	6025	6062	5222
Cu	6236	20	23	0	21	0	0	27	58	0	0	6
As	$4.9 \times 10^6$	$4.4 \times 10^6$	$4.9 \times 10^6$	$5.3 \times 10^6$	$4.9 \times 10^6$	$2.9 \times 10^6$	$4.3 \times 10^6$	$4.6 \times 10^6$	$6.5 \times 10^6$	$5.1 \times 10^6$	$5.1 \times 10^6$	$5.3 \times 10^6$
Ag	1045	44	7	3	5	4	0	5	0	0	0	5
Sb	5025	5832	14163	18259	17212	6623	14680	19058	6933	21008	20434	12771
Te	0	1	0	4	2	4	3	0	0	5	0	1
Bi	44	0	2	3	1	15	9	13	0	9	16	0

## APPENDIX

**Appendix 5** continued

ppm	Arsenopyrite											
	13	14	15	16	17	18	19	20	21	22	23	24
Ni	6.03	4.16	2.29	10.7	5.48	71.5	42.9	<1.94	9.41	7.28	465	405
Ru	<0.082	<0.083	<0.083	0.082	<0.116	<0.061	<0.030	<0.092	<0.109	<0.089	<0.089	<0.103
Rh	<0.014	<0.014	<0.016	<0.012	0.270	0.131	0.033	0.055	1.71	0.022	<0.012	8.25
Pd	<0.056	<0.068	<0.055	<0.049	<0.058	<0.048	<0.029	<0.065	<0.061	<0.067	<0.072	0.067
Re	<0.038	<0.045	<0.043	<0.041	<0.41	<0.023	<0.015	<0.049	<0.041	<0.052	<0.043	<0.047
Os	<0.106	<0.122	<0.111	<0.095	<0.129	<0.099	<0.059	<0.092	<0.118	<0.116	<0.135	<0.125
Ir	0.024	<0.027	<0.031	<0.028	<0.037	<0.034	<0.013	<0.028	<0.031	<0.032	<0.021	<0.034
Pt	<0.067	<0.059	<0.069	<0.057	<0.077	<0.058	<0.025	0.099	<0.078	<0.067	<0.062	<0.075
Au	3.32	3.41	0.156	0.830	2.11	1.63	1.22	0.168	3.98	0.238	3.68	9.48
cps	<b>Background subtracted</b>											
Co	4262	3795	669	5119	3156	17503	30995	4326	2631	122	61160	57364
Cu	12	53	0	4	379	86	2114	14	3671	897	0	5255
As	$5.2 \times 10^6$	$5.2 \times 10^6$	$4.8 \times 10^6$	$5.9 \times 10^6$	$4.0 \times 10^6$	$5.7 \times 10^6$	$1.6 \times 10^5$	$6.3 \times 10^6$	$4.3 \times 10^6$	$4.6 \times 10^6$	$4.7 \times 10^6$	$3.6 \times 10^6$
Ag	8	13	8	9	997	170	272	87	3959	66	4	6675
Sb	12208	7644	4449	9182	6150	9906	619	14115	83201	5685	8780	13156
Te	3	0	3	0	0	3	0	0	4	1	0	8
Bi	14	0	6	16	82	18	22	35	1369	0	9	850

## Curriculum Vitae

<b>Personal Information</b>	Name : Asaah Victor Akwinga Nationality : Cameroonian Year of birth : 27.07.1977 Country of Residence : Germany Marital Status : Single Email : ava777@ymail.com Phone : 0049 (0)176 2746 4866
<b>Professional Experience</b>	15.01.2001 to 14.05.2004: Site Geologist, Cummingtonite Limited, Ibadan, Nigeria.  01.01.2002 to 24.05.2004: Research Assistant, Department of Geology, University of Ibadan, Ibadan, Nigeria.
<b>Education</b>	2006–2010: PhD Economic Geology, Clausthal University of Technology, Germany. <i>PhD Project:</i> Lode gold mineralisation in the Neoproterozoic granitoids of Batouri, southeastern Cameroon.  2002–2004: MSc Mineral Exploration/Geochemistry (PhD Grade), University of Ibadan, Nigeria. <i>MSc Project:</i> Heavy metal concentration and distribution in the soils of the Bassa Industrial Zone in Douala, Cameroon.  1997–2000: BSc Geology/Environmental Science (Second Class Upper Division), University of Buea, Cameroon. <i>BSc Project:</i> The geology of Bai Manya, Marumba I and II, and environs.  1994–1996: Advanced Level GCE (3 subjects): Geology, chemistry and Biology, Cameroon College of Arts, Science and Technology (CCAST) Bambili, Cameroon.
<b>Publications</b>	<p><i>Peer Reviewed Articles</i></p> <ol style="list-style-type: none"><li>1. Abimbola, A.F., Kolawole, T., Ajibade, M.O., Odewande, A.A. and Asaah, V.A. (2006): Heavy Metal in Cattle Market soils of Ibadan, southwestern Nigeria: is there any environmental risk? <i>Mineral Wealth</i> 138: 53-60.</li><li>2. Asaah, A.V., Abimbola, A.F. and Suh, C.E. (2006): Heavy metal concentrations and distribution in surface soils of the Bassa Industrial Zone I, Douala Cameroon. <i>The Arabian Journal for Science and Engineering</i> 31:2A, 147-158.</li><li>3. A.V. Asaah, B. Lehmann, C.E. Suh and D. Frei (2008): Lode Gold mineralization at Batouri, southeastern Cameroon. Conference Proceeding, SEG-GSSA 2008 Student Conference - <i>Africa Uncovered: Mineral Resources for the Future</i>, pp. 48-49, Johannesburg.</li></ol> <p><i>Conference Papers</i></p>

# Curriculum Vitae

## **Oral Presentations**

*Oral Conference Presentation* 06.07.2008: "Lode gold mineralization at Batouri, southeastern Cameroon." SEG-GSSA 2008 Student Conference - *Africa Uncovered: Mineral Resources for the Future*, Johannesburg, South Africa. 5<sup>th</sup> July to 6<sup>th</sup> July 2008.

*Scientific Lecture* 17.02.2010: "Mineral resources and investment opportunities in Cameroon." Interdisciplinary Conversations: Science, Technology and Ethics. Technical University of Clausthal, Clausthal-Zellerfeld, Germany.

**Professional Societies** Society of Economic Geologists (SEG), Society of Geology Applied to Mineral Deposits (SGA), International Medical Geology Association (IGMA).

**Awards** 2009: SGA stipend.  
2008: SEG Travel Grant to the SEG-GSSA conference in Johannesburg.  
2008: SEG-Hugh E. McKinstry Student Research Award.  
2006: Newmont Student Research Grant.  
2005-2009: German Academic Exchange Service (DAAD) Scholarship.  
2000: Senate, Pecten and Geoscience Society of Cameroon prizes for best graduating student in Geology, University of Buea.  
1999: Dean's List of Academic Excellence, University of Buea.  
1994: Prices for Best All-Round student, Best Biology, Chemistry, Physics, Religion and Best Science student, Allo Comprehensive College (ACC Mulang) Bamenda.